Prifysgol Abertawe
Swansea University

# Understanding Creep Deformation and Lifing Approaches for Advanced Nickel and Steel Alloys

by

**Meihui Chong**

A dissertation

presented to Swansea University

in fulfilment of the

requirements for the degree of

**Doctor of Philosophy, Ph.D.**

in

**Materials Engineering**

College of Engineering, Swansea University

© Meihui Chong, 2025

I

# AUTHOR'S DECLARATION

This work has not previously been accepted in substance for any degree and is not being concurrently submitted in candidature for any degree.

Signed... ................................................................................

Date............07/04/2025............................................................................

This thesis is the result of my own investigations, except where otherwise stated. Other sources are acknowledged by footnotes giving explicit references.    A bibliography is appended.

Signed.. ................................................................................

Date...........07/04/2025............................................................................

I hereby give consent for my thesis, if accepted, to be available for electronic sharing

Signed..... ................................................................................

Date...........07/04/2025............................................................................

The University's ethical procedures have been followed and, where appropriate, that ethical approval has been granted.

Signed... ................................................................................

Date............07/04/2025............................................................................

# Acknowledgment

First and foremost, I would like to express my sincere gratitude to my academic supervisor, Prof. Mark Whittaker, for his invaluable guidance and support. The expertise, patience, and advice provided by Mark have exerted a tremendous influence on my personal development. The valuable perspectives and guidance played a pivotal role throughout the many phases of my research and have facilitated my ongoing development. I express my gratitude for your presence and guidance in assisting me throughout my academic journey.

I would like to express my appreciation to my previous supervisor, Prof. Soran Birosca, whose guidance and support throughout the initial phase of my professional journey played a pivotal role in shaping my decision to pursue a doctoral degree. Your fervour and guidance have sparked my enthusiasm for scholarly inquiry.

In addition, I express my deep thanks to Dr. Geoff West and his team from the University of Warwick, Prof. Yu-Lung Chiu and his student Gokul Obulan Subramanian from the University of Birmingham for their generous assistance in conducting experiments and providing valuable TEM results.

Throughout this academic endeavour, it is imperative for me to convey my sincere appreciation to my parents, whose unwavering provision of financial assistance has allowed me to dedicate myself fully to my educational pursuits. I would not have been able to embark on this academic endeavour without the assistance provided by them.

I would like to express my heartfelt thanks to my friends for their invaluable presence in my life and unwavering emotional support. The support, comprehension, and camaraderie you have provided have contributed to the fulfilment and happiness I have experienced in both my academic and personal endeavours.

In closing, I would like to express my gratitude to all individuals who have contributed to my scholarly endeavours. The unwavering support and encouragement provided by you have served as consistent sources of motivation, facilitating the successful completion of this thesis. I anticipate the opportunity to further exchange intellectual and personal experiences with you in the forthcoming times.

# Abstract

This study explores the creep behaviour of three polycrystalline alloys—stainless steel 316, Haynes 282, and Inconel 713C—chosen for their varying precipitate volume fractions. The primary aim is to provide a comprehensive understanding of the underlying mechanisms that control creep behaviour in these alloys, with a particular focus on determining the creep activation energies ($Q_c$*) involved.

SS316 displays a gradual transition in $Q_c$* values (153–298 kJ/mol; up to 305 kJ/mol for plates), attributed to dislocation movement at low temperatures and twinning above yield stress at elevated conditions. Haynes 282 shows a wider range (276–427 kJ/mol), with $\gamma'$ precipitate resistance at low stress and forest hardening above yield strength.

In contrast, Inconel 713C with highest volume fraction of precipitates, exhibits a constant $Q_c$*, indicating creep governed by confined dislocation motion within $\gamma$ channels, with no clear transition.

To further examine deformation behaviour in SS316, cyclic creep tests were conducted between 600 °C/334 MPa and 700 °C/165 MPa. The results indicate that cyclic creep reduces the material's service life and that the transition from dislocation cell formation to twin boundary formation contributes to an increased creep rate as the temperature rises from 600 °C to 700 °C. Additionally, when cycling from 700 °C to 600 °C, the creep rate was found to be higher than expected. This may be attributed to the retrograde formation of dislocations during the recovery phase, which are rapidly disrupted upon reloading.

The findings reinforce the utility of the Wilshire equations in rationalising $Q_c$* values and linking them to microstructural mechanisms. This provides a robust framework for predicting creep behaviour, aiding alloy development and high-temperature material optimisation.

# Table of contents

# List of Figures

XIV

# List of Tables

# 1. Introduction

With the improvement in living standards, global energy demand has risen sharply. However, this trend increasingly conflicts with environmental concerns. The burning of fossil fuel produces a significant amount of pollutants, including nitrogen oxides (NOx) which are one of the main components of acid rain and are harmful to both the atmosphere and human health, as well as the greenhouse gas carbon dioxide ($CO_2$)[1]. To address the growing energy demand while meeting energy efficiency and emissions reduction targets, major emitters of pollutions such as fossil fuel power plants and the aviation industry, as well as some alternative generators including nuclear power stations and ultra-supercritical (USC) plants have raised their service temperature and stress requirements. For instance, the last steel-based USC power plant aims to produce steam at temperatures about 650°C, and the Advanced USC target to achieve a steam temperature of more than 700°C[2], [3]. In the aerospace sector, PW1133G-JM engine, produced by Pratt & Whitney, can reach turbine inlet temperatures of approximately 1083°C at rated thrust, and Rolls-Royce's Trent XWB97 engine can reach turbine inlet temperatures close to 1472°C[4]. However, long periods of high temperature and stress operation increase the risk of excessive structural deformation and premature failure. To ensure that materials have sufficient durability and longevity to ensure their reliability throughout their service life, the requirements for the materials have become increasingly stringent, especially the resistance to deformation and long-term failure of these materials.

Creep is the continuous deformation of materials when exposed to continuous mechanical loads and is one of the primary types of damage that leads to changes in engine component geometry and degradation of performance, followed by failure. It is particularly prevalent under conditions of elevated temperature and stress. The creep phenomenon has received increasing attention since the 1830s, and people have realized its importance and started developing new materials and techniques to resist its effects[5]. Currently, creep phenomena are an important research direction in the field of materials science and engineering and are essential for many applications in high-temperature and high-stress environments.

Although creep experiments are one of the most reliable methods for determining the creep behaviour of materials, they usually require long periods of loading to simulate the long-term stress history of the material and must be carried out at high temperatures. In addition, even when adequate creep experiments are carried out, the creep behaviour of a material can be influenced by a variety of factors such as stress state, temperature, test period, specimen geometry etc., all of which need to be carefully controlled and documented. This is time and cost intensive and places high demands on the experimental equipment and maintenance personnel. The Japanese National Institute of Materials Science (NIMS) has been conducting creep tests since the mid-twentieth century. As of 2019, its database includes 433 specimens with fracture times exceeding 100,000 hours and 326 specimens from interrupted tests running more than 100,000 hours, including 14 of those exceeding 300,000 hours[6]. This shows that it is impractical to perform creep tests for the entire life of some practical applications.

Therefore, creep prediction is of great importance for material design and engineering applications. It plays a vital role in enabling engineers and materials scientists to understand the deformation behaviour of materials under various operating conditions. It allows for the estimation of creep deformation and service life under practical working conditions, thereby guiding material selection and design, optimising service parameters, and informing reliable life assessment methodologies. In addition, creep prediction can help engineers and materials scientists to develop new materials and processes to improve the creep resistance and life of materials. Creep prediction can also help to reduce the risks and costs associated with the use of materials. Failure to accurately predict the creep behaviour and lifetime of materials can lead to unexpected failures during use, which can result in injury, death and property damage. Therefore, performing creep predictions can help to reduce these risks and costs and improve the safety and reliability of materials. Using creep extrapolation formulae to predict the creep behaviour of materials is a faster, more economical and more efficient method, especially where large amounts of material data are required[7]. Using these formulae, creep behaviour can be quickly predicted under different conditions based on known creep data and other material properties. This approach can reduce the number of creep experiments and reduce experimental time and costs, while also improving the efficiency and reliability of material design.

Material lifetime prediction has been extensively researched by numerous scholars and scientists, leading to the development of several scientific breakthroughs and the creation of various extrapolation models and theories, such as Larson-Miller (LM)[8], Manson-Haferd (MH)[9], Orr-Sherby-Dorn (OSD)[10], etc. These various extrapolation methods have been extensively discussed and critically reviewed for the purpose of finding a reliable predictive model for creep, but a general model that can be applied to a wide range of materials has not yet been established. Current methods are typically limited to narrow ranges of conditions, and none are capable of accurately predicting creep behaviour across the full spectrum of conditions. Moreover, most existing methods are empirical in nature and lack mechanistic evidence that reflects the actual behaviour of materials, making extrapolated results unreliable. In particular, the two 'constants', activation energy $Q_c$ and stress exponent n, proposed by the most traditional extrapolation methods— the power law equations—have since been shown to vary with testing conditions. These variations are linked to changes in the underlying creep mechanisms[11]. However, this has been questioned, as microstructural studies and creep curve analyses previously suggested that the dominant deformation and damage processes often remain unchanged over the studied stress-temperature range[12]. Therefore, changes in n may not always reflect a shift in mechanism. Meanwhile, n value is used as an indicator of the creep mechanism, with values around n = 1 typically associated with diffusional creep and n = 4–6 with dislocation creep[13]. In any case, this inconsistency highlights a fundamental limitation of traditional parametric methods: treating all data as a whole leads to significant errors when extrapolating beyond the specific range for different mechanisms[14]. As such, parametric correlations must be applied to distinct regimes individually, rather than across an entire dataset.

To address these limitations, Wilshire[15] proposed a new predictive formulation—the Wilshire Equations—which modify the traditional activation energy $Q_c$. Unlike the power law which normally calculated the $Q_c$ value at constant σ, the Wilshire Equations determine the creep activation energy $Q_c^*$ from minimum creep rate or rupture time at constant (σ/σ$_{TS}$), and changes in deformation mechanisms across stress regimes by region splitting. In some materials, $Q_c^*$ varies significantly on either side of a breakpoint, while in others, it remains relatively constant[16-19]. Although the

Wilshire Equations have been successfully applied to a variety of materials[20-25], the specific factors influencing activation energy still require further investigation.

To evaluate the reliability of the Wilshire Equations in linking micromechanical processes to creep behaviour, a series of creep tests will be conducted on three creep-resistant alloys with differing precipitate contents: IN713C with 60-70% γ', Haynes 282 with 15-25% γ', and stainless steel 316 nearly no precipitates. The resulting creep data will be analysed using the Wilshire Equations, alongside microstructural and dislocation observations, to explore the mechanisms governing activation energy and its relationship with deformation behaviour.

# 2. Literature Review

## 2.1 Fundamentals of Mechanical Behaviour

The mechanical behaviour of solids is governed by the balance between attractive and repulsive forces between atoms or ions.

Attractive forces arise from different mechanisms depending on bonding type. In ionic crystals, attraction is dominated by Coulombic forces between oppositely charged ions. In covalent and metallic systems, attraction primarily results from the interaction between valence electrons and atomic nuclei. Van der Waals forces may also contribute in non-ionic systems at longer distances.

Repulsive forces become dominant when atoms are brought very close together. These originate from the overlap of electron orbitals and the Pauli Exclusion Principle, which prevents electrons from occupying identical quantum states. As a result, a steep increase in repulsive energy occurs at short separations, ensuring atoms do not collapse into one another.

The balance of these two types of forces is typically represented by the interatomic potential energy curve, which shows how potential energy varies with interatomic separation, see Figure 2.1.
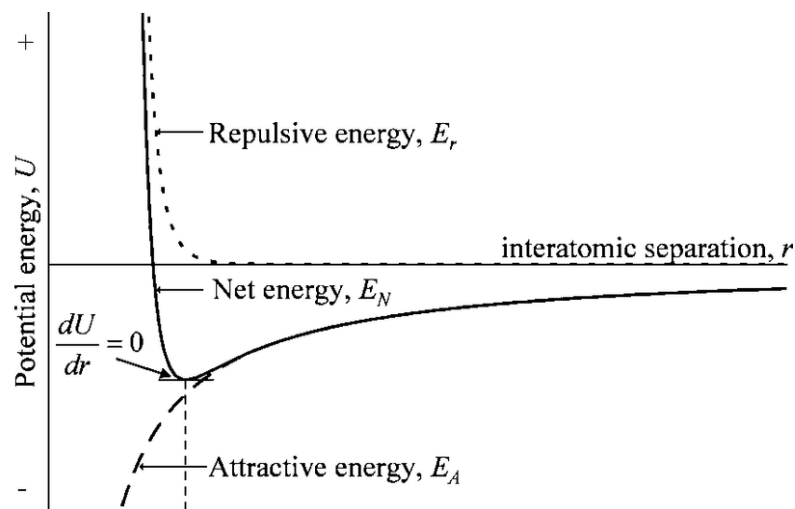


**Figure 2.1 Potential energy vs interatomic separation curve showing how the net effect of attractive and repulsive forces acting between a pair of atoms or ions[26].**

The curvature of the potential well at this minimum is the binding energy, and is directly related to bond stiffness, which defines how resistant atomic bonds are to stretching or compression[27]. Figure 2.2 shows the force-distance curve for two materials, showing the relationship between atomic bonding and the modulus of elasticity. A steep and deep potential well indicates strong interatomic bonding, means that a greater force is required to stretch the bond, thus the material has a high elastic modulus, while a shallow potential well corresponds to weaker bonds and lower stiffness.
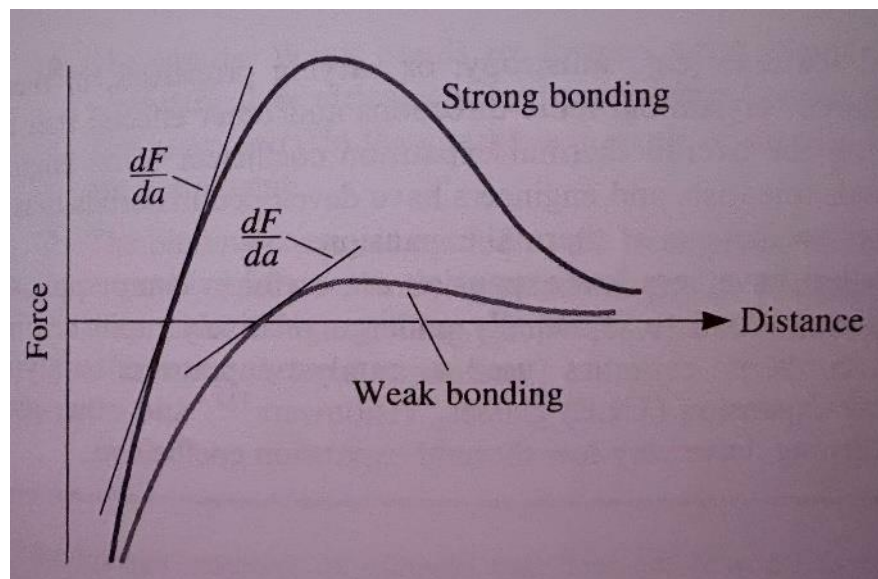


**Figure 2.2 The force-distance curve showing the relationship between atomic bonding and the modulus of elasticity**[27].

Thus, the connection between atomic interactions and bulk mechanical behaviour is established: bond stiffness at the atomic scale translates into resistance to deformation at the macroscopic material level.

When an external force is applied to a solid, the average separation between atoms changes slightly from the equilibrium bond distance, producing deformation. At the macroscopic level, this is described using the concepts of stress and strain.

Stress is the internal force per unit area within materials that arises from externally applied forces, temperature changes, or deformation.

$$\sigma = \frac{F}{A}$$

where F is the applied force and A the cross-sectional area.

Strain is the measure of deformation representing the displacement between particles in the material body.

$$\varepsilon = \frac{\Delta L}{L_0}$$

where $L_0$ the initial length and $\Delta L$ the change in length.

As fundamental descriptors of mechanical behaviour, stress and strain also serve as the basis of most mechanical testing; for example, the outcome of a tensile test is typically represented as a stress–strain curve, from which key material properties can be derived, as shown in Figure 2.3.
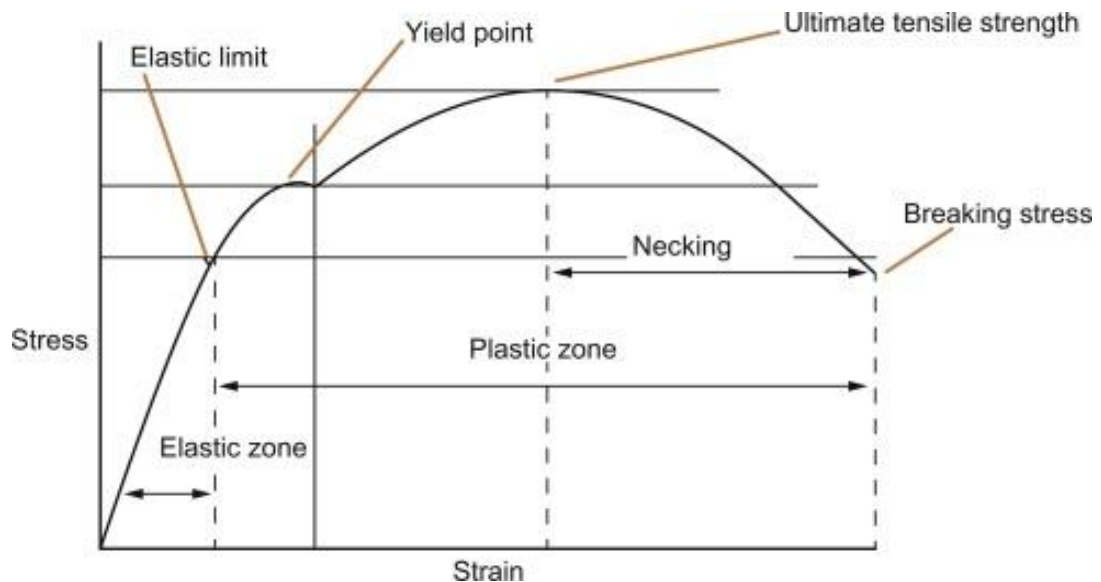


**Figure 2.3 Stress-strain curve**[28].

A tensile test provides several key mechanical properties:

- Yield strength ($\sigma_y$): the stress at which permanent plastic deformation begins, often determined using a 0.2% offset method.

- Ultimate tensile strength (UTS): the maximum stress a material can withstand before necking.

- Fracture strength: the stress corresponding to final failure.

- Ductility: the capacity for plastic deformation, usually expressed as percentage elongation or reduction in area at fracture, obtained directly from the strain at

fracture.

- Toughness: the total energy absorbed up to fracture, given by the area under the stress–strain curve, indicating resistance to crack initiation and propagation.

One of the most important properties that can be extracted from a stress–strain curve is the Young's modulus (E), which quantifies the stiffness of a material in the elastic regime[27]. It is defined as the ratio of stress to strain within the initial linear portion of the stress–strain curve, where the material returns to its original shape after the removal of the load.:

$$E = \frac{\sigma}{\varepsilon}$$

Hooke's law formalises this relationship:

$$\sigma = E \cdot \varepsilon$$

When the applied stress exceeds the yield strength, elastic deformation is no longer sufficient to accommodate strain, and the material undergoes plastic deformation. Unlike elasticity, which involves reversible stretching of interatomic bonds, plasticity results from permanent atomic rearrangements. At the microscopic scale, plastic deformation in crystalline solids is governed mainly by slip and twinning[29].

Slip is the primary mechanism in most metals and alloys. It occurs when the critical resolved shear stress (CRSS) is reached, allowing dislocations to move along specific crystallographic planes and directions, collectively known as slip systems[30]. The ease of slip depends strongly on the crystal structure. Face-centred cubic (FCC) metals, possess multiple slip systems, which makes them highly ductile. The primary slip system is the {111} plane in the <1-10> direction. Body-centred cubic (BCC) metals, have fewer slip systems at low temperatures, which can lead to higher strength but lower ductility. The {110} plane in the <111> direction is a common slip system, but several slip planes compete, including {1-10}, {11-2} and, less commonly, {12-3}. In contrast, hexagonal close-packed (HCP) metals, such as titanium and magnesium, have a more complex slip behaviour due to their lower symmetry, which tends to limit their ductility[31].

Twinning provides an alternative mode of deformation, involving a coordinated movement of atoms that reorients part of the crystal lattice into a mirror image of the

parent structure. Unlike slip, which produces continuous shear displacements, twinning generates a discrete reorientation, often at characteristic angles depending on the crystal structure. Twinning becomes significant when slip is restricted, for example at low temperatures or under high strain-rate conditions, and is recognised by the formation of twin boundaries[32].

In most metals, slip dominates under ambient conditions, while twinning becomes important under conditions where dislocation mobility is hindered. Both mechanisms are essential to understanding the transition from elasticity to plasticity and for interpreting the complex deformation behaviour observed in high-temperature creep.

Plastic deformation is also highly relevant to engineering applications. In metal forming, polymer processing, and composite design, the ability to predict and control plasticity is central to achieving the desired performance. Advanced techniques such as severe plastic deformation (SPD), which refine grain structures, are used to enhance strength and ductility simultaneously. These approaches extend beyond conventional metallic systems to include polymer-based nanocomposites, enabling the production of lightweight, high-strength components for aerospace, automotive, and power-generation applications[33].

## 2.2 Creep

At high temperatures, materials can undergo continuous plastic deformation over time, even when the applied stress is far below the elastic limit. This phenomenon is known as creep. Due to the more complex nature of plastic deformation in high-temperature environments, creep has become an important topic in fields such as materials science, mechanical engineering, and materials physics. The temperature at which creep occurs is typically above $0.4T_m$ (where $T_m$ is the absolute melting temperature)[34]. However, in practical engineering applications, such as turbine blades in jet engines, materials often need to withstand long-term exposure at temperatures exceeding $0.5T_m$[35], [36]. Under such prolonged high-temperature and high-stress conditions, materials are prone to creep deformation and even failure, which can adversely affect the performance and lifespan of engineering components. Therefore, the creep resistance of these high-temperature materials has become one of the fundamental and crucial

properties for their application and design, ensuring stability and reliability. Understanding the mechanisms of creep phenomena holds significant importance for material design, evaluation, and improvement.

Creep is defined as the tendency of a solid material to exhibit permanent deformation and failure over an extended period under the influence of continuous mechanical stress at high temperatures[37]. As shown in Figure 2.4 and Eq. 2-1 below, the load applied to a metal wire is insufficient to cause immediate failure, but it gradually extends the wire in a time-dependent manner.
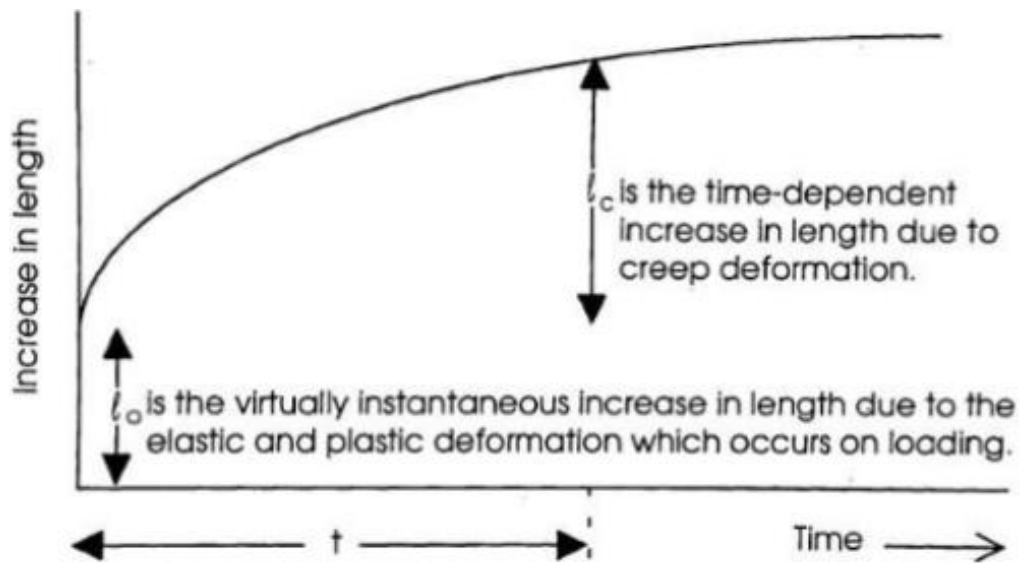


**Figure 2.4 The time-dependent increase in length of a wire due to creep deformation at low temperature**[37].

$$l - l_i = l_0 + l_c$$

**Eq. 2-1**

where $l_i$ is the original length of the wire, $l$ is the length after a time, $t$, $l_o$ is the virtually instantaneous increase in length which occurs on loading, and $l_c$ is the time-dependent increase in length due to creep.

During the creep process, materials undergo various phenomena such as work hardening and recovery due to the effects of high stress, temperature, and strain rate. Work hardening refers to an increase in dislocation density within the crystal structure of a material under stress, resulting in the formation of more dislocations and an increase in hardness and strength[38]. Recovery, on the other hand, refers to the rearrangement of the material's structure and the partial disappearance of dislocations

10

after experiencing certain stress or deformation, leading to a decrease in hardness and strength[39]. Work hardening and recovery are not independent processes but rather compete with each other. In the creep process, the balance between work hardening and recovery significantly influences the deformation behaviour and mechanical properties of materials.

## 2.2.1 Creep curve

In creep testing, specimens are heated to a certain temperature and then subjected to mechanical loading. The strain, $\varepsilon$, of the specimen is recorded as a function of time, t, at the given temperature and stress, yielding a strain-time relationship curve known as the creep curve. To measure the creep curve, continuous monitoring of the gauge length of the specimen is required, and the displacement of the specimen is recorded as a function of time until final fracture. Therefore, the creep curve can provide more comprehensive details of specimen changes during the test, rather than just measuring the time to failure and failure strain[37]. This means that more material characteristics can be plotted and described on the complete creep curve, beyond just creep fracture. The typical creep curve for high temperatures (i.e. $T/T_m > 0.4$) shown in Figure 2.5 demonstrates that materials usually go through three stages before fracture occurs, with different creep rate variations in each stage:
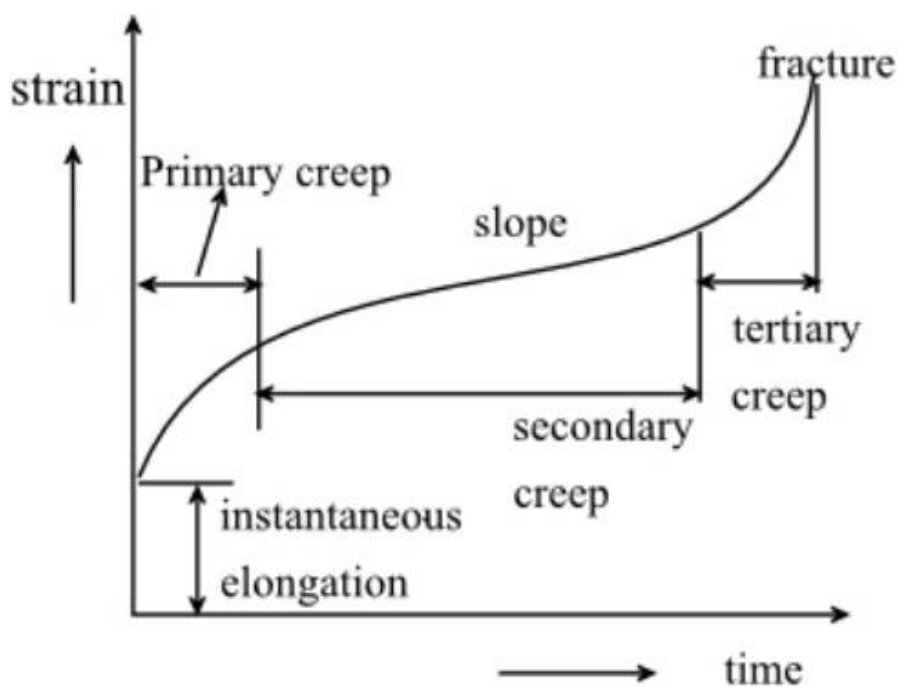


**Figure 2.5 A typical creep curve indicates three different stages**[40].

11

In the initial stage of the experiment, the mobility of atoms increases at high temperatures, making dislocation glide more likely to occur. Thus, even if the stress is below the yield stress, the elevated temperature is sufficient to cause plastic or non-elastic deformation. However, during plastic deformation, work hardening occurs, leading to an increase in deformation resistance. Therefore, in the primary stage, the strain rate decreases over time until the beginning of the secondary stage.

The secondary region is a steady-state stage where the strain rate remains relatively constant. This is because work hardening, recovery, and recrystallization occur simultaneously and reach a dynamic equilibrium, resulting in a constant creep rate. In creep-resistant materials, the occurrence of tertiary creep is earlier due to the loss of hardening caused by recovery, resulting in the contraction of the secondary stage to a specific point. This is known as the minimum strain rate, $\acute{\varepsilon}_m$[41].

In the third stage, damage through the formation of voids and cracks occurs, primarily at grain boundaries, causing an accelerated strain rate until the test specimen fails.
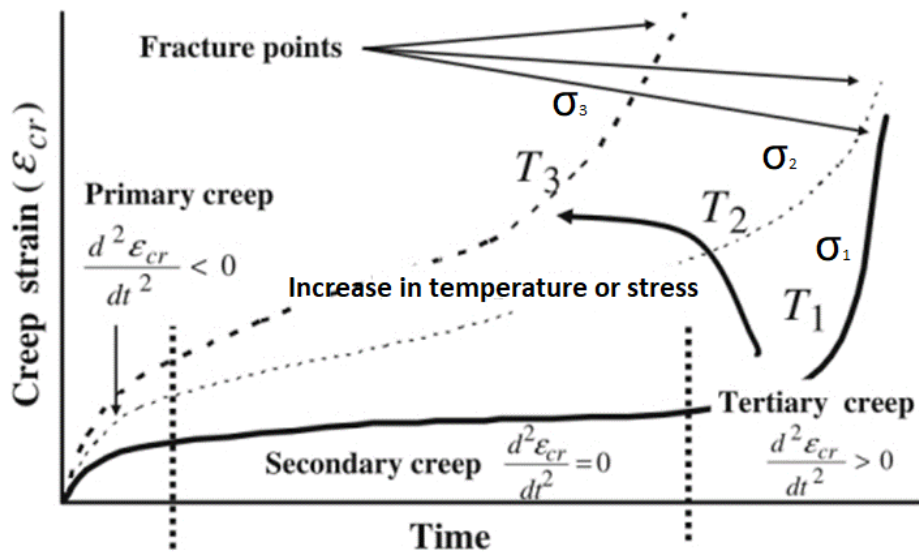


**Figure 2.6 Effects of temperature and stress on creep strain, where $T_1<T_2<T_3$ and $\sigma_1<\sigma_2<\sigma_3$[42], [43].**

From the perspective of creep characteristics, the effects applied within a certain time period are greatly influenced by the applied stress and operating temperature. Figure 2.6 shows that at low temperatures, creep strain gradually changes, and failures are rare. Conversely, at high temperatures, creep deformation occurs more rapidly and failure occurs after a certain time, denoted as $t_f$. The time to fracture decreases as the

temperature increases. Similarly to stresses, higher stress leads to shorter time to fracture.

It is reasonable to assume that on the basis of Figure 2.6 the creep rate should be dependent on both stress and temperature, and historically secondary creep rate behaviour has been considered to be critical in the understanding of overall creep deformation.

## 2.2.2 Creep mechanisms

For metallic materials, different combinations of stress and temperature lead to different creep deformation mechanisms. Common types of creep include diffusion creep, dislocation creep, and grain boundary sliding. These different types of creep exhibit variations in deformation mechanisms, rates of deformation, and temperature dependence. For instance, under high-stress conditions, slip mechanisms may dominate, while under low-stress conditions, diffusion mechanisms may be more significant. Additionally, temperature can also affect the creep mechanisms. Typically, high temperatures promote the diffusion mechanisms, while low temperatures are more likely to induce slip mechanisms. Regarding this, Ashby summarized a deformation mechanism map for creep, where the horizontal coordinate represents $T/T_m$ (current temperature/melting temperature of the metal), and the vertical coordinate is $\tau/\mu$ (shear stress/shear modulus)[52].
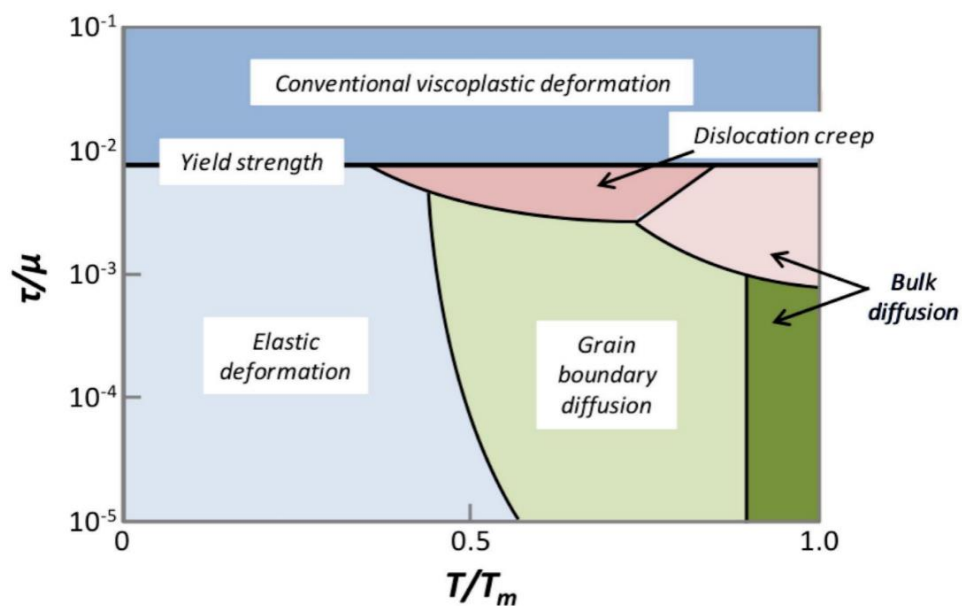


**Figure 2.7 Creep deformation mechanism map**[52].

13

Diffusional creep is a plastic deformation caused by the diffusion of atoms due to thermal motion and occurs mainly in metallic materials at high temperatures. Diffusional creep exists in a few types, including Coble creep[53] and Nabarro-Herring creep[54]. Creep due to the continuous diffusion of crystal defects at grain boundaries (e.g. unstable grain boundary energy, grain boundary dissolution, and stacking faults, etc.) at high temperatures, resulting in grain boundary movement and deformation, is known as Coble creep[53]. At higher temperatures, point defects within the crystal (e.g. vacancies, interstitial atoms, etc.) diffuse to their surroundings, causing changes in the crystal volume. This type of internal creep induced by volume diffusion mechanisms is known as Nabarro-Herring creep[53],[54]. Many experiments indicate that Coble creep typically occurs at lower temperatures, while Nabarro-Herring creep occurs at higher temperatures[55].

Dislocation creep is a plastic deformation caused by dislocation movement and primarily occurs in metallic materials under high-stress conditions. In dislocation creep, dislocations move along the mismatch direction within the crystal structure, but prevented by precipitates, grain boundaries, other dislocations and solute in solid solution[56].

The two creep mechanisms sometimes do not occur separately. The plastic deformation that incorporates both dislocation creep and diffusional creep mechanisms is known as mixed creep and occurs mainly in metallic and ceramic materials at high temperatures and high stresses. In mixed creep, dislocation and atomic diffusion act simultaneously, resulting in faster deformation rates but also making it more complex.

Grain boundary sliding is one of the main mechanisms for creep deformation under high temperature conditions. In this case, stress drives the grains to slide along the grain boundaries, and the atoms within the grain boundaries adjust their positions to accommodate this sliding by diffusion. This phenomenon, which involves a combination of relative sliding between grains and grain boundary diffusion to achieve material deformation, is also commonly observed in high-temperature plastic deformation and creep[57].

Mitchell summarized the damage mechanisms occurring during creep using the stress exponent as follows[58]:

n = 1: Harper-Dorn and viscous creep

n = 2: Coble creep

n = 3: Nabarro-Herring creep

n = 4-5: Climb-controlled or Weertman creep

However, it is recognised that this approach may be overly simplistic. Recent studies have found that creep behaviour can change under specific conditions, and this change is thought to be associated with the dominant creep mechanism. For instance, when the temperature drops below $0.7T_m$, a transition of creep mechanism of polycrystalline copper from Nabarro Herring to Coble creep occurs, leading to a reduction in activation energy from 200kJ/mol to below 130kJ/mol. Similarly, reducing the stress, resulting in a decrease in stress exponent from 4 to 1, implies a transition from dislocation-controlled creep to diffusion-controlled creep[59]. Foldyna et al.[60] therefore, suggested that creep or creep fracture data obtained under one creep mechanism cannot be used to predict creep behaviour that is controlled by a different creep mechanism. This is because when the conditions change, the predictions become unreliable due to the shift in dominant creep mechanism.

### 2.2.2.1 Diffusional creep

Diffusional creep refers to the deformation process of solid materials at high temperatures primarily achieved through atomic diffusion. Atoms migrate within the material via mechanisms such as vacancies and lattice defects, leading to material deformation. Diffusional creep typically occurs at temperatures above the yield point but below the melting point of the material. At elevated temperatures, atoms possess sufficient thermal energy to overcome the resistance of dislocations, surmounting lattice barriers and migrating from one position to another, resulting in plastic deformation, namely creep.

The rate of diffusional creep depends on factors such as temperature, stress, crystal structure, and diffusion mechanisms of the material. Generally, the diffusional creep rate increases with increasing stress, and higher stresses may lead to faster creep rates.

Activation energy refers to the energy barrier that atoms need to overcome during the diffusion process, which represents the minimum energy required for atomic migration

from one position to another. In solid materials, atomic migration requires surmounting lattice barriers, and the height of these barriers determines the rate of diffusion, as described in Figure 2.8. The higher the barrier, the more difficult for atoms to overcome it, resulting in slower diffusion rates. Conversely, lower barriers make it easier for atoms to overcome them, leading to faster diffusion rates.
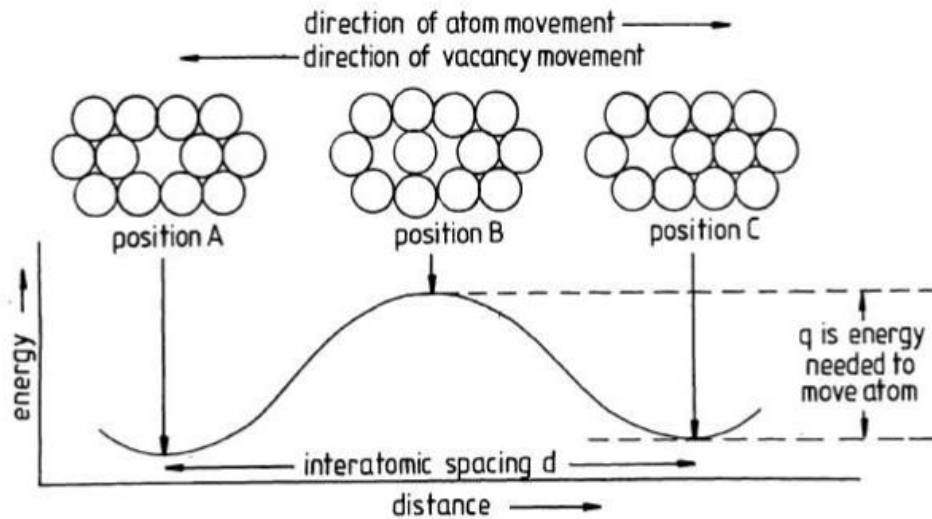


**Figure 2.8 A schematic diagram illustrating diffusion via vacancy movement, depicting the energy levels at various atomic positions**[37]**.**

Activation energy can also be described by the Arrhenius equation, which establishes the relationship between diffusion rate and activation energy as follows:

$$D = D_0 * \exp(-Q/RT)$$

**Eq. 2-2**

Here, D represents the diffusion coefficient, $D_0$ is a constant, Q represents the activation energy, R is the gas constant, and T is the temperature. According to this equation, higher activation energies correspond to lower diffusion coefficients, indicating slower diffusion rates.

Therefore, diffusional creep is closely related to activation energy. The activation energy determines the diffusion rate and creep behaviour of the material. At high temperatures, if the activation energy of the material is low, atomic migration is facilitated, resulting in faster diffusion rates and easier occurrence of creep deformation. Conversely, if the activation energy is high, atomic migration becomes difficult, resulting in slower diffusion rates and reduced creep deformation.

### 2.2.2.1.1 Coble creep

Coble creep is a form of creep in solid materials at high temperatures, primarily involving grain boundary diffusion[53]. In polycrystalline materials, there exist grain boundaries between grains, which are transitional regions of the crystal structure where atomic arrangement is relatively loose. Coble creep is accomplished through diffusion along grain boundaries, where atoms migrate from one grain to an adjacent grain.

At high temperatures, atoms on the grain boundaries possess sufficient thermal energy to overcome the energy barrier of the grain boundaries and migrate along them to neighbouring grains. When atoms migrate from the grain boundary to adjacent grains, it leads to the movement of dislocations within the grains, resulting in a rearrangement of atoms and causing slip. During the slip process, dislocations within the grains diffuse towards the grain boundaries, leading to changes in the shape of the grains, making them more flattened. The process is illustrated in the diagram below:
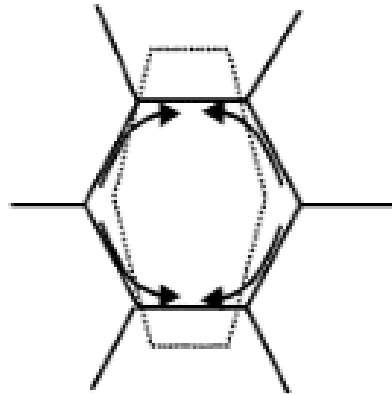


**Figure 2.9 Diagram illustrating Coble creep mechanism**[61].

The rate of Coble creep can be described by the Coble equation:

$$\dot{\varepsilon}_{CO} = A_{CO} \frac{\delta D_{gb} G b^2 \sigma}{d^3 kT}$$

**Eq. 2-3**

Where $D_{gb}$ is the grain boundary diffusion coefficient, G is the shear modulus, b is the Burgers vactor, $\sigma$ is the stress, d is the grain size, k is the Boltzmann constant, T is the absolute temperature, and $A_{CO}$ is a constant ($\approx 150/\pi$)

Coble creep is characterized by being more sensitive to grain size and grain boundary diffusion coefficient compared to bulk diffusional creep. Smaller grain sizes and higher grain boundary diffusion coefficients result in faster creep rates. Additionally, Coble creep is more significant under low-stress conditions, as grain boundary diffusion is more likely to occur[53].

**2.2.2.1.2 Nabarro-Herring creep (N-H creep)**

Nabarro-Herring creep is a creep behaviour that occurs at high temperatures primarily in crystalline materials and involves the diffusion process of lattice defects, such as vacancies, also known as volume diffusion. It was proposed by Nabarro and Herring[54] to describe creep behaviour under low stress conditions at high temperatures.

At temperatures above $0.7T_m$, atoms in the crystal have sufficient thermal energy, and some atoms may depart from their lattice positions, forming vacancies[34]. Vacancies migrate within the crystal through vacancy diffusion. By undergoing atomic jumps, vacancies move from one position to an adjacent one, resulting in a rearrangement of atoms in the crystal. This diffusion of vacancies leads to the reorganization of atoms within the crystal and causes creep deformation of the material. The process is illustrated in the diagram below:
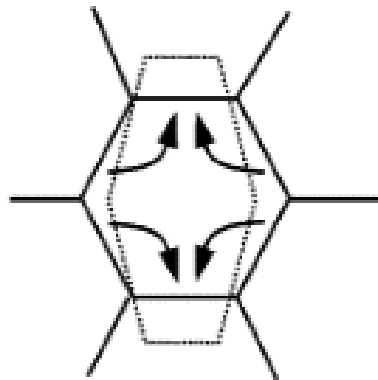


**Figure 2.10  Diagram illustrating Nabarro-Herring creep mechanism**[61]**.**

The rate of Nabarro-Herring creep can be described by the Nabarro-Herring equation:

$$\dot{\varepsilon}_{NH} = A_{NH} \frac{D_1 \Omega \sigma}{d^2 kT}$$

**Eq. 2-4**

Here, $D_1$ is the coefficient for lattice self-diffusion, $\Omega$ is the atomic volume, d is the grain size, k is Boltzmann's constant, T is the absolute temperature, and $A_{NH}$ is a constant with theoretical value that depends on the grain size and load distributions.

The strain rate in Nabarro-Herring creep is almost proportional to the stress and inversely proportional to the square of the average grain size.

### 2.2.2.2 Dislocation creep

Dislocation creep is a creep mechanism that primarily occurs under lower temperatures and higher stresses, and it is primarily driven by the motion and formation of dislocations. Dislocation creep typically occurs when the stress exponent (n) is greater than 4. In this process, dislocation glide and climb are two key modes of dislocation motion, as shown in Figure 2.11.
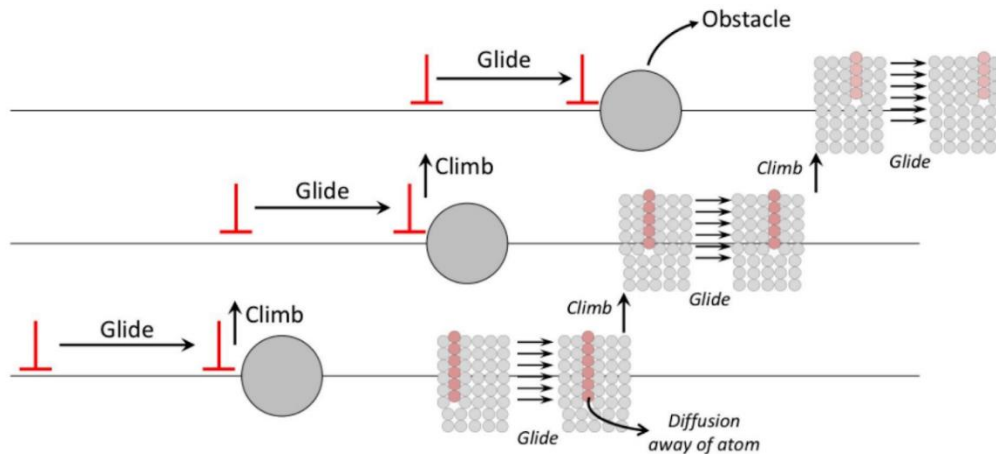


**Figure 2.11 The process of dislocation glide and climb in metals**[62].

**Dislocation glide:** Glide is the movement of dislocations along specific crystal planes in specific crystallographic directions. It is the fundamental mechanism and primary carrier of plastic deformation because it requires significantly lower stress compared to the stress required for shear deformation in an intact crystal. This is because dislocations only need to break and reform atomic bonds in localized regions rather than across the entire shear plane of the crystal. Dislocation glide occurs on specific

crystal planes known as glide planes. When an external stress is applied to the material, dislocations move along the glide planes in a direction known as the glide direction. During this process, one part of the lattice slides relative to another, resulting in permanent deformation of the material. The process is illustrated in the Figure 2.12:
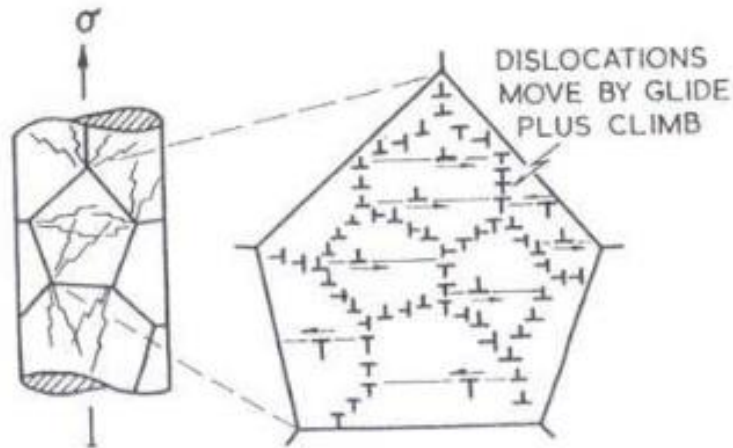


**Figure 2.12 Diagram illustrating dislocation glide and climb**[63].

Glide can occur at all temperatures and stress conditions, but it is particularly significant at lower temperatures and higher stresses.

**Dislocation climb:** Climb is a mode of dislocation motion that occurs at higher temperatures. In the climb process, dislocations move up or down along their dislocation lines by absorbing or emitting vacancies, transitioning from one slip plane to an adjacent one. Climb requires sufficient activation energy and primarily occurs at high temperatures. The process is illustrated in the Figure 2.13:
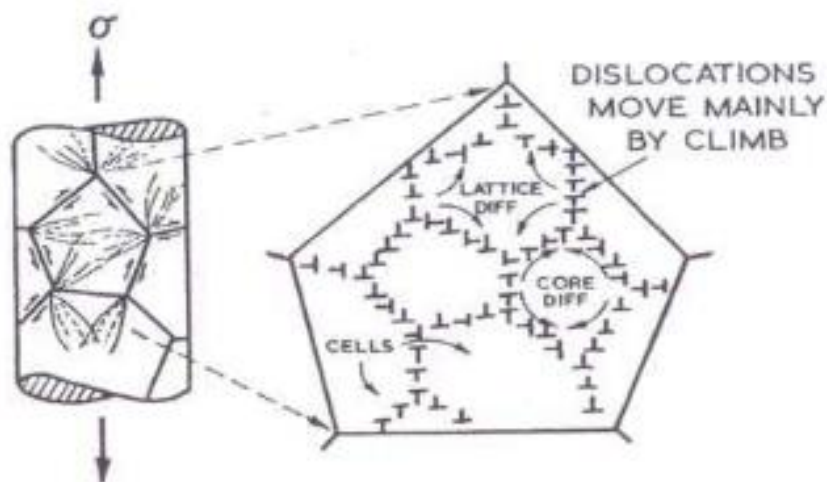


**Figure 2.13 Diagram illustrating dislocation climb**[63].

Glide and climb are both crucial steps in the dislocation creep process. Dislocation glide is the primary mechanism that leads to permanent deformation of the material, while dislocation climb allows dislocations to overcome obstacles such as grain boundaries, secondary dislocations and precipitates, continuing the deformation of the material.

The resistance to dislocation glide and climb primarily comes from the applied stress, so an increase in stress significantly increases the difficulty of dislocation motion, leading to an increase in creep rate. Conversely, when the stress is reduced, dislocation motion becomes easier, and the creep rate decreases.

### 2.2.2.3   Grain boundary sliding

Grain boundary sliding is a process where relative movement occurs between grains (individual crystalline regions) in solid polycrystalline materials. This process takes place at grain boundaries, which are the regions between different grains.

When a material is subjected to external forces, such as during heat treatment, mechanical stress, or other physical processes, grain boundary sliding may occur. In the process of grain boundary sliding, one grain slides over the adjacent grains, resulting in a change in the overall shape of the material. This process requires the elimination of space between the grains to prevent a change in the material's volume, which is typically achieved through diffusion. The likelihood of grain boundary sliding increases at high temperatures because the dynamic activity of grain boundaries increases, making it easier for atoms to diffuse along the grain boundaries.
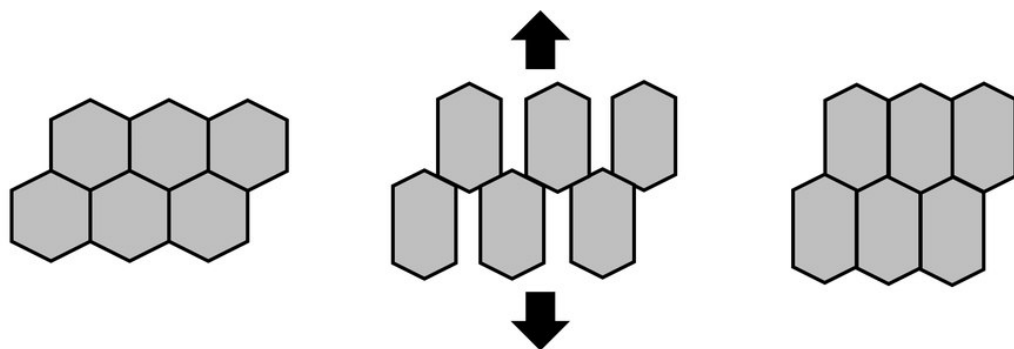


**Figure 2.14 Diagram illustrating the process of grain boundary sliding**[64]**.**

Figure 2.14 depicts the process of grain boundary sliding. When subjected to a tensile load, the grains undergo elongation, leading to the formation of gaps between them,

referred to as voids. In order to prevent the occurrence of voids within the material, the grains slide to fill the gaps.

The initial discovery of grain boundary sliding (GBS) was made by Moore et al.[65], who observed sharp displacements at the intersections of surface markings and grain boundaries in Pb-2%Sn alloy. Subsequent research on GBS revealed its significant influence on the overall strain during low-stress creep testing, as demonstrated by Bell et al[66]. After comparing four different metals, Gifkin et al.[67] concluded that the magnitude of sliding displacement is directly proportional to the shear component of the applied stress resolved in the boundary plane.

Langdon[68] summarized two distinct mechanisms that may occur in GBS. The first mechanism, known as Rachinger sliding, involves grains maintaining their original shape while experiencing relative displacement through intragranular motion of dislocations in neighbouring grains. The second mechanism, Lifshitz sliding, is based on the diffusion process of Nabarro-Herring and Coble creep, where grains elongate along the axis of tension.

Under external forces, sliding occurs along grain boundaries, causing relative displacement between grains on either side of the boundary. If this process cannot be accommodated properly, localized defects can form, leading to the initiation of cracks, as illustrated in the Figure 2.15.
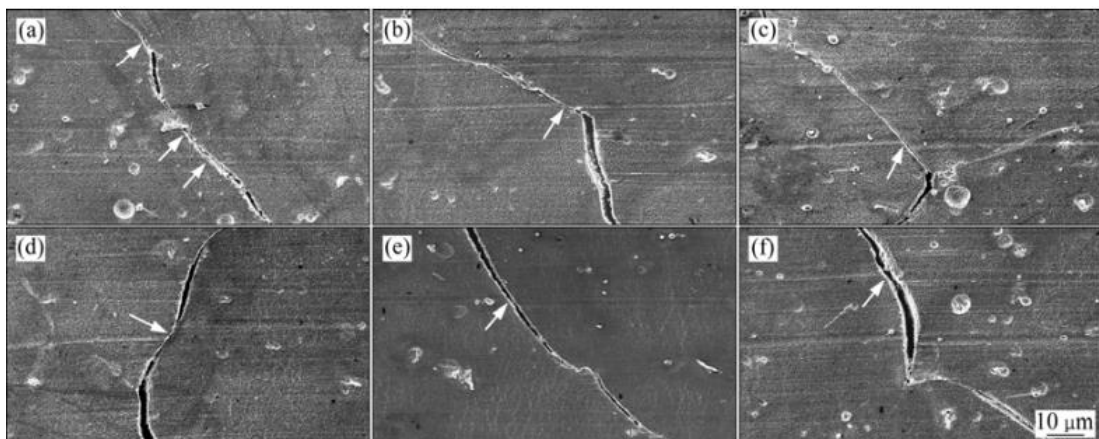


**Figure 2.15 The mechanism of crack formation by Rachinger grain boundary sliding**[69].

## 2.3 Fracture

Fracture is the process of material failure where it experiences a complete or partial separation into two or more pieces. In the context of creep deformation, fracture can occur as the final stage when the creep rate accelerates and reaches a critical point. Creep damage can appear within the grains, but primarily occurs at grain boundaries[70].

At higher stresses and lower temperatures, grain boundary sliding can be impeded at triple junctions where three grain boundaries meet, leading to stress concentration and the formation of voids. These voids connect with each other, forming wedge-shaped cracks. The wedge cracks formed at grain boundaries result in local separation of the grain boundaries, and subsequent interaction and connection of cracks lead to final fracture. When the stress is low and the temperature is high, creep damage manifests as protrusions on grain boundaries and the formation, growth, and coalescence of small voids near second-phase particles. The voids are formed and enlarged through grain boundary sliding, eventually leading to fracture[71].

Both crack formation mechanisms involve the nucleation of voids. It is evident that grain boundary voids play a critical role in the high-temperature range and lifetime of materials. Once cracks are formed, their further propagation relies on processes such as grain boundary sliding, vacancy diffusion, and void coalescence, ultimately leading to intergranular fracture. As creep fracture primarily occurs at grain boundaries, the morphology of grain boundaries, precipitation and segregation of impurities on grain boundaries, grain size, and grain size uniformity all have a significant influence on creep fracture[64-67].

### 2.3.1 Wedge Cracks (Triple Point Cracks)

Wedge cracks are a type of crack morphology that can form under creep conditions. They typically occur at grain boundaries. At high stresses and lower temperatures, grain boundary sliding and plastic deformation within grains can lead to the accumulation of dislocations in the grain boundary region, resulting in the formation of wedge cracks[76]. The shape of a wedge crack resembles a wedge, with a sharp tip at the end.

23

The formation of wedge cracks often initiates at microstructural defects within the material, such as grain boundaries, voids, dislocation clusters, and so on, particularly at trigeminal intersections where three grains converge. These microstructural defects can serve as nuclei for cracks under sustained stress. On the other hand, when materials are operated at high temperatures, the thermal motion of atoms can induce microstructural changes within the material, potentially facilitating crack formation. Once cracks are formed, they act as stress concentrators and gradually propagate under sustained stress, triggering crack extension. The enlargement of cracks typically occurs through a series of atomic displacements within the material. During this process, the stress concentration at the crack tip causes the rupture of atomic bonds surrounding it, driving crack propagation[77]. At high temperatures, crack growth may proceed through diffusion mechanisms, such as grain boundary diffusion and dislocation diffusion. As the crack extends along the path of the wedge crack, the fracture strength of the material (the maximum stress it can withstand) gradually decreases. When the crack reaches a critical size, the material may no longer sustain external stress, resulting in fracture. This process can occur suddenly, leading to abrupt material failure. Early work by Evans and Wilshire[78] provided a comprehensive overview of the mechanisms involved in wedge crack formation during creep. The microstructure of an alloy significantly influences the formation of wedge cracks. Alloys with extensive grain boundary areas are more susceptible to wedge crack formation[79]. In austenitic stainless steels, wedge cracks form at triple junctions at stresses above 200 to 250MPa and at temperature around 500 to 675°C[80], while in nickel-based superalloys, wedge cracks form at stresses over 150MPa and at temperature between 700 to 950°C[81].

## 2.3.2 Cavitation

During the creep process, internal voids or cavities, known as cavitation, can form in a material due to sustained stress. When a material is subjected to continuous stress, atomic diffusion occurs to reduce the internal energy of the material. If the diffusion is concentrated towards a particular region within the material, a void can form in that region, representing the initial stage of cavitation[82]. In some cases, cavitation may occur near grain boundaries, inclusions, or other defects where the stress state and/or diffusion characteristics may differ from the surrounding material. Once a void forms, the stress in the vicinity of the void becomes concentrated, driving further atomic

diffusion into the void and causing it to grow. Additionally, due to the lower pressure inside, this also causes gases or other materials to diffuse from the surrounding area into the cavitation zone, further increasing the cavitation[83], [84]. When the cavitation reaches a certain size, the load-bearing capacity of the material decreases because the material in the cavitation zone can no longer withstand the stresses. At this point, if external stresses continue to act, the material around the cavitation zone may fracture. The expansion and union of the cavitation may form cracks and eventually lead to the fracture of the entire material. Cavitation is often observed in the tertiary stage of creep[85]. It is a critical mechanism in the fracture of both metallic and non-metallic materials, and is particularly significant in materials with high ductility, where void growth can accommodate significant plastic deformation before fracture[86].
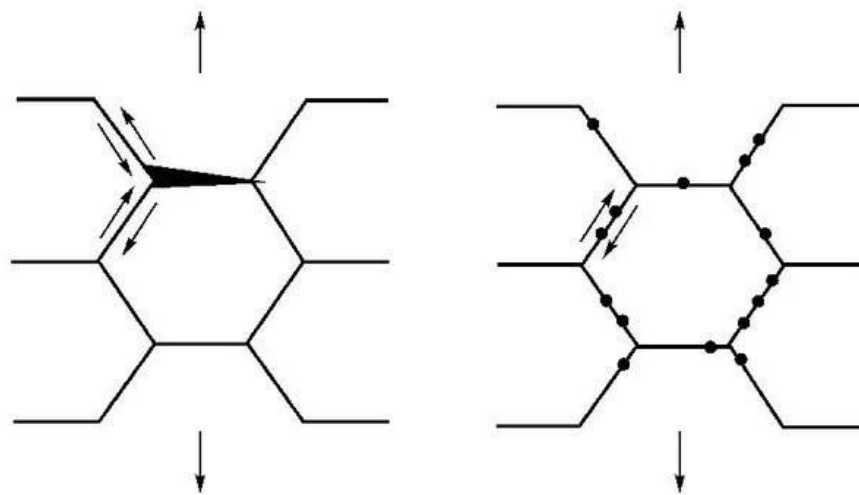


**Figure 2.16 The formation of wedge cracks and cavities**[71].

## 2.4  Predictive methods for determining creep life

Predicting the creep fracture life of materials is also an important direction of creep research. While creep testing is the standard method to determine material creep performance and lifing time, such tests often require hundreds of hours or even years, are costly, and demand a large number of specimens and complex equipment. Therefore, it is desirable to replace creep experiments with predictive models. The importance of creep life prediction lies in the fact that creep is a time-dependent material failure mode that results in permanent deformation and failure of materials under high-temperature and high-stress conditions. Therefore, for critical components

and structures that need to operate in high-temperature and high-stress environments for extended periods, such as in aerospace, nuclear industry, and power generation, creep life prediction is essential. Accurate creep prediction is crucial for preventing accidents, optimizing maintenance schedules, and extending component service life, which reduces costs and enhances safety[15], [79-82].

The long-term strength required for engineering design is the stress at which fracture occurs after 100,000 to 200,000 hours, particularly in the field of power generation. Obtaining such long-term experimental data directly through testing is extremely difficult. The commonly used approach is to increase the stress and temperature to obtain the relationship between short-term fracture time and stress/temperature, and then extrapolate this relationship to predict the long-term fracture time under specific stress and temperature conditions. This extrapolation is referred to as the extrapolation of the long-term strength.

Among many extrapolation methods for creep, the Time-Temperature Parameter (TTP) method, which relies on the influence of time and temperature on creep deformation, is one of the commonly used methods. The time and temperature variables are combined into a parameter P that relates to stress, i.e., $P(\sigma) = f(t_r, T)$. The short-term creep rupture data is overlaid to form a curve or a line, and the longer-term creep data is inferred based on the trend of the main curve. Typical TTP methods include Larson-Miller[8], Manson-Haferd[9], Manson-Succop[91], Orr-Sherby-Dorn method[10], etc. Using creep life prediction methods instead of creep testing not only reduces costs and shortens time but also plays an important role in ensuring the service life of specific high-temperature components, improving reliability, and optimizing design.

## 2.4.1 The Power Law

By considering the relationship between secondary creep rate and stress, Norton[14] was able to show linear relationship by plotting $\ln \dot{\varepsilon}_s$ vs $\ln \sigma$ where the gradient of the graph was given by n. Based on this relationship, Norton's law describes the relationship between creep rate and stress during the steady-state stage as follows[44]:

$$\dot{\varepsilon}_s \propto \sigma^n$$

**Eq. 2-5**

Where $\acute{\epsilon}_s$ is the creep rate, $\sigma$ is the applied stress and n is the stress exponent.

Simultaneously, the Arrhenius equation, initially used to determine the rate of chemical reactions, as proposed by Swedish scientist Svante Arrhenius, can be employed in the context of materials to express the relationship between temperature and creep rate[45] where plotting $\ln \acute{\epsilon}_s$ vs 1/T yields a straight line relationship where the gradient is given by -$Q_c$/R. Hence

$$\acute{\epsilon}_s \propto \exp\left(-Q_c/RT\right)$$

<div align="right">**Eq. 2-6**</div>

where $Q_c$ is the activation energy for creep, R is the universal gas constant with a value 8.3145J/(mol·K), and T is the absolute temperature.

By combining these two equations, the creep equation, also known as the Power law equation[46], can be derived into Eq. 2-7:

$$\acute{\epsilon}_s = A\sigma^n \exp\left(-Q_c/RT\right)$$

<div align="right">**Eq. 2-7**</div>

As stated, the equation illustrates a linear relationship between $\log\acute{\epsilon}_s$ and $\log\sigma$, with the slope representing the stress exponent n. This type of creep, which follows the linear relationship, is referred to as power law creep. Theoretically, the activation energy ($Q_c$) and stress exponent (n) are assumed to be constant. However, subsequent research has overturned this assumption[88]. Additionally, it is important to note that this equation is based on certain assumptions, such as the homogeneity of the material and the absence of other microstructural defects like voids or dislocations. Based on the creep equation, a relationship between the activation energy and temperature can be derived[47]:

$$Q_c = -\left(\frac{\partial \ln \acute{\epsilon}_s}{\partial \ln(1/RT)}\right)_\sigma$$

<div align="right">**Eq. 2-8**</div>

Eq. 2-8 revealing that the value of $Q_c$ varies with temperature.

Similarly, the value of n is also dependent on the applied stress, and there is a relationship between the stress exponent and the applied stress[48]:

$$n = -\left(\frac{\partial \ln \dot{\varepsilon}_s}{\partial \ln \sigma}\right)_T$$

**Eq. 2-9**

Both Eq. 2-8 and Eq. 2-9 indicate that $Q_c$ and n should not be treated as constants. This also leads to the power law approach being considered unsuitable for the prediction of creep behaviour.

In fact, in the study by Wilshire and Scharning on 9-12% chromium steel, it was found that these "constant" values strongly depend on the creep conditions, particularly the creep temperature and creep stress[24]. As shown in Figure 2.17(a), different values of $Q_1$ and $Q_2$ for the activation energy were found to be suitable for describing the relationship between strain rate, temperature, and either high or low temperatures. As shown in Figure 2.17(b), when applied to Eq. 2-9, both $n_1$ and $n_2$ describe the relationship between strain rate and stress.
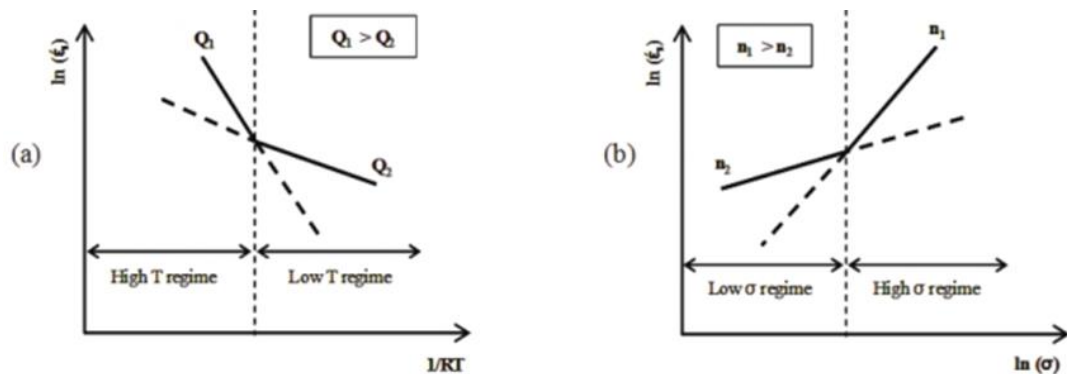


**Figure 2.17 Transition of (a) $Q_c$ and (b) n, relative to temperature and stress, respectively**[92].

Traditionally, the stress exponent, n, had also been used to describe the mechanism of the creeps, i.e. n = 1 is diffusional creep, n = 3 is dislocation glide, and n = 4-6 is dislocation climb mechanism[13].

As the stress reaches a certain level, especially for creep-strengthened alloys or those that have undergone precipitate hardening, the presence of additional precipitates significantly impedes dislocation movement within the lattice. The power law relationship alone is insufficient to accurately capture the complex interaction between dislocations and these obstacles, i.e. log $\dot{\varepsilon}_s$ and log $\sigma$ deviate from the linear relationship, leading to a phenomenon known as power law breakdown[8].

In the power law breakdown regime, the dominant mechanism transitions from dislocation climb control to glide control, significantly contributing to the observed breakdown of the power law due to altered stress dependence of the strain rate[49]. Experimental studies indicate that vacancy supersaturation in this regime enhances creep rates by reducing the activation energy for diffusion, thereby facilitating faster creep[49],[50]. The shift from lattice self-diffusion to dislocation pipe diffusion, associated with large strain plasticity, is a key factor in increased creep rates and is central to the power law breakdown mechanism[49],[50].

Typically occurring below approximately $0.6T_m$, the power law breakdown regime is characterized by decreasing activation energy for creep with lower temperatures or higher stresses, further disrupting the power law[50]. In practical applications, such as high-temperature deformation analysis in materials like Alloy 690, the power law creep model predicts steady-state creep rates and rupture times. Enhancements to this model, including optimized temperature-dependent parameters, improve prediction accuracy[51].

For this reason, the power law equation cannot accurately predict long-term fracture strength from short-term measurements, as the values of $Q_c$ and n were found to vary unpredictably, as summarized by Abdallah[92]. Therefore, the application of the power law relationship to infer actual long-term performance always leads to overestimation, which can result in significant errors and distort the predicted data to overestimate creep behaviour over time[23].

However, overestimation is the worst consequence of predictions because it leads to projected lifetimes longer than the time a component operates safely, running the risk of creep failure before reaching its intended design life. Hence, the power law approach is considered unsuitable for predicting creep behaviour.

## 2.4.2 The Monkman-Grant Relationship:

In the early 1950s, Monkman and Grant proposed a hypothesis that there exists a direct hyperbolic function relationship between the minimum creep strain rate and the time to rupture[93]. They suggested that the minimum creep rate is a function of stress and temperature. This relationship is typically expressed as:

$$\acute{\varepsilon}_m = M \mathbin{/} t_f$$

<div align="right">**Eq. 2-10**</div>

Where $t_f$ is the time to rupture (or failure time), M is a constant, and $\acute{\varepsilon}_m$ is the minimum creep rate.

The Monkman-Grant relationship indicates that materials with higher minimum creep rates have shorter rupture times. In other words, materials that exhibit faster creep deformation under creep conditions are more prone to failure. This relationship implies an inverse proportionality between the time to rupture and the minimum creep rate.

The Monkman-Grant relationship is commonly used in creep testing and analysis to estimate the long-term durability and reliability of materials under high-temperature sustained loading. It provides a useful tool for characterizing and comparing the creep resistance of different materials. However, it is important to note that this relationship is empirical and may have limitations in certain cases, as creep behaviour can be influenced by multiple factors other than the minimum creep rate.

## 2.4.3  The Larson-Miller (LM) Methodology

The Larson-Miller equation is one of the most commonly used empirical formulas for predicting creep life. It was proposed by scientists Larson and Miller [8] in the 1940s and derived from the Arrhenius equation under constant stress. In contrast to the power law, which assumes constant values for the stress exponent and activation energy, the Larson-Miller (LM) equation considers the activation energy as a variable. The basic principle of the Larson-Miller equation is to predict the creep life of a material under certain stress and temperature conditions using the LM calculation. The logarithmic term in the equation results in an exponential growth of life with time, providing higher accuracy even for relatively short time predictions. The general form of the Larson-Miller equation is as follows:

$$P_{LM} = f(\sigma) = T( C_{LM} + \log t_f )$$

<div align="right">**Eq. 2-11**</div>

where $P_{LM}$ is the Larson-Miller parameter, T is the absolute temperature, $t_f$ is the creep life, and $C_{LM}$ is a constant.

The Larson-Miller parameter ($P_{LM}$) is a parameter that combines temperature and time to describe the high-temperature creep behaviour of materials. A higher Larson-Miller parameter indicates a shorter creep life of the material.

The constant $C_{LM}$ in the Larson-Miller equation acts as a correction term to adapt to the creep behaviour under different materials and experimental conditions. The value of $C_{LM}$ depends on the specific material and experimental data and is typically determined through experimental testing and curve fitting. Larson and Miller[8] originally proposed a universal constant value of $C_{LM}$ as 20 for most metals. Pink[94] also explained that constant of Larson-Miller equation is related to the logarithm of the pre-exponential factor, which shows minimal variation, thus, $C_{LM}$ could be used as a universal constant.

However, subsequent research has shown that although the Larson-Miller method is widely used, its extrapolation accuracy has been questioned because the value of $C_{LM}$ can be influenced by factors such as processing and phase transformation, making it not a precise number. It has been found that the value of $C_{LM}$ for specific aluminium alloys can fluctuate between 13 and 27[95]. Zhao et al.[96] derived the range of $C_{LM}$ values for 1Cr0.5Mo steel from creep rupture data at different stresses, which ranged from 15.1 to 23.7. Wilshire et al.[24] also calculated the value of $C_{LM}$ for 9-12% chromium steel to be 36.

## 2.4.4 The Manson-Haferd (MH) Methodology

Manson and Haferd[9] analysed the creep performance data of over 40 heat-resistant steels and found that the L-M parameter had lower extrapolation accuracy for some materials, and the predicted results were not highly reliable. They observed that, for the same material under constant stress, there was a tendency towards a linear relationship between the temperature T and the logarithm of fracture time Log($t_r$), and these lines tended to intersect at a fixed point. To address this, they proposed a new model.

The Manson-Haferd method is also one of the most commonly used creep extrapolation methods. The equation for this method is as follows:

$$P_{MH} = f(\sigma) = (\log t - \log t_a)/(T - T_a)$$

<div align="right">**Eq. 2-12**</div>

Compared to the Larson-Miller equation, which has only one constant C, Manson and Haferd[9] introduced two constant terms, $T_a$ and $\log(t_a)$, in their formula. This improved the correlation of creep rupture data and the accuracy of life prediction. However, it also imposed certain limitations on its application.

The Manson-Haferd method provides improved accuracy in predicting creep life by incorporating additional parameters in the equation. It offers better correlation for certain materials compared to the Larson-Miller method. Nonetheless, it is important to note that both the Larson-Miller and Manson-Haferd methods are empirical and may have limitations in certain cases, as creep behaviour can be influenced by various factors beyond the minimum creep rate.

## 2.4.5  Wilshire Equations

Previously, although many computational methods were being adopted and used, it still took upwards of ten years of 'material development cycles' to determine the required long-term estimates. Predicting data through extrapolation of short-term property measurements was still a major challenge. This is because traditional methods for creep prediction, such as power-law equations, have long served as a basis for understanding deformation mechanisms at various stress and temperature conditions. However, Wilshire[59], [97] highlighted substantial limitations of these conventional approaches, particularly the use of variable constants stress exponent n and activation energy $Q_c$ to predict dominant mechanisms by assuming a transition across different stress/temperature regimes. This approach often conflicts with observed experimental evidence, especially in cases where n>4 and dislocation models are invoked to explain high-stress creep[98].

Wilshire[59] provided a comprehensive analysis of fine-grained copper over an extensive stress range (686–823 K), challenging the traditional view that dislocation-dominated creep transitions to diffusion-controlled creep at lower stress levels. Instead, dislocation processes are shown to dominate across all stress levels where significant creep affects most engineering applications. Consequently, Wilshire introduced an alternative methodology for interpreting both creep rate and creep life measurements

as part of a unified data trend, eliminating the need to assume mechanism changes to explain variability in primary creep mechanisms.

Wilshire normalised the stresses in the power law equation based on the Monkman-Grant relationship to give a formula for the minimum creep rate as a function of temperature, stress and time as follows:

$$\dot{\varepsilon}_m = M \, / \, t_f = A^* \left( \frac{\sigma}{\sigma_{TS}} \right)^n \exp \left( -\frac{Q_c^*}{RT} \right)$$

**Eq. 2-13**

where $A^* \neq A$ and $Q_c^* \neq Q_c$.

In traditional lifing theories, the value of $Q_c$ is dependent on the temperature, and can be obtained by fitting a minimum creep strain rate or time over a narrow temperature range at the same load. However, Wilshire[15] points out that in a reasonable approach to endurance assessment the activation energy and the tensile strength at different temperatures are correlated and subsequently introduces a temperature-dependent tensile strength correction to $Q_c$, presenting a corrected creep activation energy $Q_c^*$. The value of this parameter can be determined by plotting the modified creep activation energy against temperature for the same normalised stress ($\sigma/\sigma_{TS}$), in terms of minimum creep strain rate, by plotting $\ln(t_f)$ as the vertical coordinate and $1/T$ as the horizontal coordinate.

It has also been shown that normalising $\sigma$ by yield stress ($\sigma_y$) or ultimate tensile stress ($\sigma_{TS}$) provides a good description of the stress/creep rate relationship at different temperatures. The choice to use $\sigma_{TS}$ instead of $\sigma_y$ in this equation is because the ($\sigma_{TS}/\sigma_y$) ratio varies for different alloys and is more difficult to measure[97].

Wilshire[15] further identified that the anomalous variations in the stress exponent n and activation energy $Q_c$ values, derived from the standard power-law equation, do not signify a shift in the dominant creep mechanism. Instead, these anomalies arise from the complex dependence of creep rate and creep life on the shape of the creep curve, a relationship systematically influenced by changes in testing conditions. Wilshire observes that as test durations and temperatures increase, microstructural evolution and corresponding alterations in the shape of the creep curve contribute significantly to the observed variability in creep behaviour. When the normal creep strain/time

curves were plotted, it was found that the decaying primary curve was offset by tertiary accelerations. Therefore, in the Wilshire Equations, the minimum creep rate $\dot{\varepsilon}_m$ is used, instead of the steady-state rate $\dot{\varepsilon}_s$, which was often used as the basis of the creep study. The focus of the attention also changed from the mechanisms that control secondary creep stage to the process that control the creep strain accumulation, and the phenomena leading to the tertiary stage and failure[59],[99].
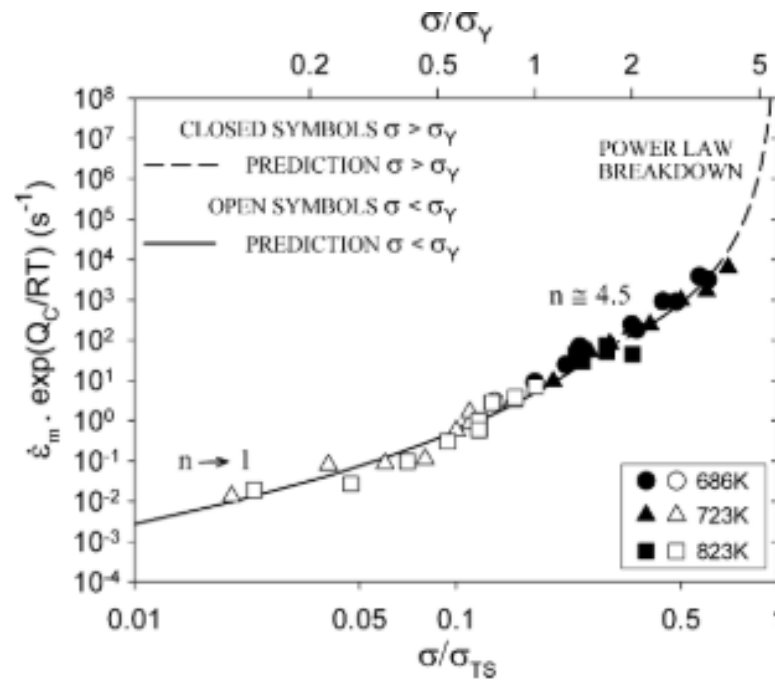


**Figure 2.18 The break curve predicted by the Wilshire Equation for polycrystalline copper at 686-823 K, Qc=110KJ/mol can fit n=1, n=4.5 or even power law breakdowns**[59].

As shown in the Figure 2.18, after rationalisation of the dataset, the predicted curves fit well and effectively capture the transition from n = 4.5 to n = 1 at a normalised stress of $\sigma_Y/2$. They also account for the "power-law breakdown" behaviour observed at high applied stresses, where n rises significantly above 4.5.

This insight underscores the limitations of traditional models when applied to complex materials like aluminium alloys[97], which undergo substantial microstructural transformations during prolonged creep exposure. Wilshire's revised approach to the standard power-law model incorporates a correction term that accounts for the lattice diffusion activation energy, thereby systematically elucidating the long-term creep behaviour of these alloys. This revised methodology allows for rationalisation of the complex creep curves observed under varying stress conditions and enables reliable

34

long-term predictions; for instance, it successfully extrapolates short-term test data (e.g., 1,000 hours) to forecast the 100,000-hour creep rupture strength of alloy 2124[97].

Any prediction method follows the fundamental rule that when the loading stress converges to the tensile strength $\sigma_{TS}$, it leads to almost instantaneous rupture, while the long-lasting fracture life $t_f$ tends to zero and the minimum creep strain rate $\acute{\varepsilon}_m$ tends to $+\infty$, making it impossible to predict the occurrence of creep rupture. Conversely, when the loading stress tends to zero, the long-lasting fracture life tends to $+\infty$ and the minimum creep strain rate $\acute{\varepsilon}_m$ tends to zero. In simple terms, this means that the material will not rupture without the applied stress and therefore the rupture life is infinite normalising the stress through the strength of the material. In contrast, in the theory of life prediction, a wide range of stresses from 0 to $\sigma_{TS}$ needs to be considered to obtain better extrapolation performance. Based on this idea, Wilshire improved on the equation above by proposing enduring life models for creep fracture life, minimum creep rate, and time and temperature dependence at specific strains to better meet the prediction needs, respectively:

$$\frac{\sigma}{\sigma_{TS}} = \exp\left\{-k_1\left[t_f \exp\left(-\frac{Q_c^*}{RT}\right)\right]^u\right\}$$

**Eq. 2-14**

$$\frac{\sigma}{\sigma_{TS}} = \exp\left\{-k_2\left[\acute{\varepsilon}_m \exp\left(-\frac{Q_c^*}{RT}\right)\right]^v\right\}$$

**Eq. 2-15**

$$\frac{\sigma}{\sigma_{TS}} = \exp\left\{-k_3\left[t_\varepsilon \exp\left(-\frac{Q_c^*}{RT}\right)\right]^w\right\}$$

**Eq. 2-16**

Where $t_f$ is the rupture life, $\acute{\varepsilon}_m$ is the minimum creep rate, $t_\varepsilon$ is the time to reach predefined creep strains, $k_1$, u are constants for Eq. 2-14 that can be determined by plotting $\ln[t_f \exp(-Q_c^*/RT)]$ against $\ln[-\ln(\sigma/\sigma_{TS})]$ graph. The intersection of the plots with y-axis shows the value of $\ln(k_1)$ and the gradient of the plots illustrates the value of u. $k_2$ and $k_3$, as well as v and w are constants for Eq. 2-15 and Eq. 2-16 and can be derived from similar plots. The value of $Q_c*$ can be obtained by plotting $\ln(t_f)$

and/or $\ln(\dot{\varepsilon}_m)$ against $1/T$ and the slope gives the value of $Q_c^*/R$, where R is the gas constant with a certain value 8.3145 J/mol·K.

When the Wilshire Equations was first employed to predict creep behaviour, researchers assumed that the activation energy remained constant and closely aligned with the material's lattice self-diffusion activation energy. However, subsequent investigations revealed significant scatter in the predicted data in later research[87],[100]. This discrepancy resulted in inaccurate predictions, highlighting the need for refined methodologies to account for the variations in activation energy during different creep regimes.

Zharkova[101] has shown that in long-term creep experiments, the fracture mechanism varies with stress and loading time. For example, intragranular fracture occurs at high stresses, intergranular fracture caused by wedge cracks at medium stresses and intergranular fracture at low stresses is caused by the formation and growth of pores along grain boundaries. The change in fracture mechanism leads to kinking of the stress profile. The known Time-Temperature Parameter (TTP) methods are based on the relationship between temperature, time, and fixed constants, ignoring changes in the fracture mechanism, and therefore generally have large errors in predicting creep performance. Bernstein[102] proposed a 'region splitting' method to address the difficulty of describing changes in the creep mechanism by traditional methods. In recent years there have also been a number of research teams that have improved on traditional methods by region splitting[95-102].

Users of the Wilshire Equations have learned from these experiences and have also improved the prediction model through a region splitting technique, i.e. a 'break point' is set to split the high and low stresses into two regions, and different values of constants from each region are calculated and fitted to the data so that the prediction curves match the actual measurements at both high and low stresses. Activation energy as a function of stress is obviously one of the main parameters for region splitting and is currently attempted to link to micromechanical behaviour. When the applied stress is below the yield stress, materials exhibit only elastic deformation, and creep is localized to the grain boundary regions. In this regime, mechanisms such as grain boundary sliding dominate. Conversely, when the applied stress exceeds the yield stress, plastic deformation occurs, and creep transitions to involve the generation and

movement of new dislocations at appropriate sources. This transition is accompanied by an increase in activation energy[88].

For instance, in 316H stainless steel, the activation energy shifts from 150 kJ/mol below the yield stress to 250 kJ/mol above it. The 150 kJ/mol value corresponds to grain boundary diffusion and the activity of dislocations near the boundaries, whereas 250 kJ/mol aligns with the activation energy for self-diffusion in the austenitic matrix[99].

Similarly, in Waspaloy, the activation energy increases from 340 kJ/mol to 400 kJ/mol. At low stresses, dislocations primarily climb around precipitates through diffusion. At higher stresses, forest hardening becomes significant, requiring additional energy for dislocation motion[19],[111].

In 22, 23, and 24 steels, three distinct activation energy shifts (280kJ/mol-230 kJ/mol -280 kJ/mol) are observed during long-term, high-temperature testing. These transitions are attributed to dislocation mechanisms evolving from grain boundary diffusion to intragranular diffusion with new dislocation formation. Additionally, microstructural transformations occur, including the bainite phase transitioning to ferrite and the formation of coarse molybdenum carbide particles during intragranular diffusion[88].

The successful application of the Wilshire Equations to the prediction of high temperature creep in different materials, including many industrially relevant metals, steels, titanium alloys, nickel-based superalloy, and single crystal alloys has proved its value[17],[20],[23],[24],[51],[79],[80],[89],[92],[103-109]. With further research and refinement, it is expected that the Wilshire Equations can be applied to a wider range of materials and conditions. The Wilshire Equations success in predicting high-temperature creep across various materials has demonstrated its practical value and robustness.

According to Vito Cedro III [21],[118],[119], after fitting the equation to multiple materials, the Wilshire Equations exhibits modular flexibility, allowing for numerous combinations of methods, which broadens its potential applications. In scenarios requiring only preliminary estimates of long-term creep strength such as during the early stages of new alloy development, the original form of the Wilshire Equations

may be sufficient. Conversely, when using the Wilshire Equations for precise component design or to establish long-term creep strength values in design codes—potentially replacing the current equations used across various standards—more complex analyses are required. This involves increasing the number of fitting constants, thereby enhancing the equation's adaptability and predictive power.

Evans[104],[110-114] has also proposed advanced methods for applying the Wilshire Equations to complex datasets across diverse materials including handling data collected from multiple sample batches, defining Qc as a function of temperature, statistically determining the number of stress regimes, and utilising additional batch-specific characteristics. Recently, Evans[124] combined the Wilshire Equations with an improved Kachanov-Rabotnov continuum damage mechanics (CDM) model, yielding a new approach that successfully predicts uniaxial creep curves inclusive of primary and tertiary stages. These developments highlight the equation's adaptability and potential for broader integration in material design and performance assessment.

With continued research and refinement, it is anticipated that the Wilshire Equations could be extended to a broader range of materials and operating conditions, enabling further advances in creep modelling. However, a deeper understanding of the underlying physical and microscopic mechanisms that inform the Wilshire Equations is necessary to improve its predictive accuracy for high-temperature creep behaviour.

## 2.5  Selected Testing Materials

The experiments conducted in this study utilized three different materials: stainless steel 316 and nickel-based superalloys Inconel 713 and Haynes 282. The primary aim of this investigation was to explore how the microstructure of these materials affects their creep behaviour, which in turn was linked to changes in activation energy.

The three materials are used in different applications: stainless steel 316 is commonly used in moderately high-temperature, corrosive environments such as pipework in power plants, while the two nickel-based alloys are mainly used in extremely high-temperature, high-stress environments, Inconel 713 typically in turbine blades for gas turbines and aero-engines, and Haynes 282 tends to be used more as a combustor alloys.

However, they all equally have to serve in harsh operating environments for long periods of time. And their different precipitation phase contents were used as the reason for the selection of materials for this study. As a γ' precipitation- hardened cast nickel- based superalloy, Inconel 713 typically contains a large volume fraction of γ' particles, as illustrated in the Figure 2.19(a)[125]. In contrast, Haynes 282 is a nickel-based superalloy that is also reinforced with the γ', but it has fine and diffuse γ' particles, with the volume fraction of approximately 15-25wt%, similar to that depicted in Figure 2.19(b)[126]. Stainless steel 316, on the other hand, has almost no precipitation, but twinning boundaries, as shown in Figure 2.19 (c)[127].
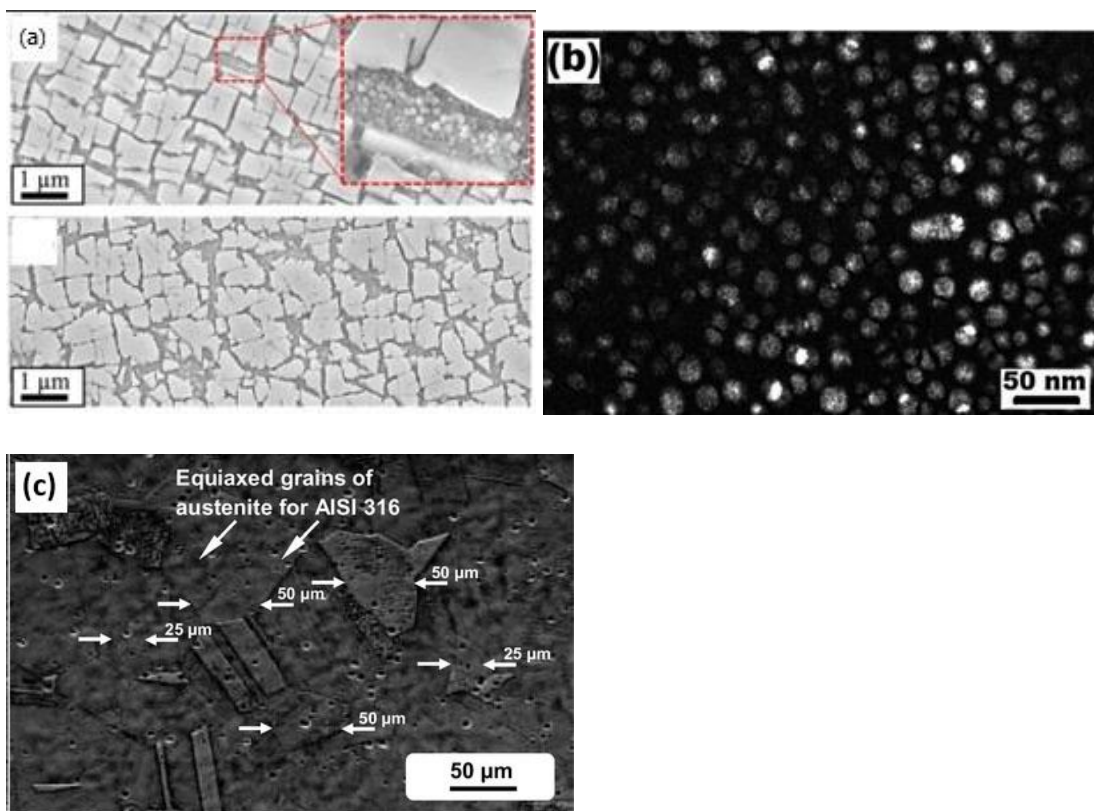


**Figure 2.19 (a) the γ' particles of IN713C**[125] **(b) the γ' particles of H282**[126] **(c) the twinning boundaries of SS316**[127].

In the subsequent subsections, a thorough examination of the fundamental properties of each material—stainless steel 316, Inconel 713C, and Haynes 282—will be presented, alongside a comprehensive review of relevant literature for linking material composition, precipitation phases, and creep performance across these distinct alloys, and a deeper understanding of activation energy variations among these materials will be considered.

## 2.5.1 316 Stainless steels

The typical austenitic stainless steel stainless steel 316, initially developed for paper mills, has become a versatile material widely used in various industries due to its excellent corrosion resistance, mechanical strength, and high-temperature stability. Common applications include everyday items such as exhaust pipes, valves, pumps, tanks, and heat exchangers, as well as components in the pharmaceutical and photography industries. The alloy's resilience in corrosive environments has also made it popular in the maritime industry and for food and beverage processing equipment, where it withstands acids and resists pitting and crevice corrosion in chloride-rich conditions. Additionally, 316 stainless steel is frequently utilised in medical devices, surgical instruments, and implantable equipment, prized for its biocompatibility and durability.

With the rapid growth in global energy demand, the nuclear power industry has become a crucial part of the energy sector. Initially, nuclear power plant piping was predominantly made of 304 austenitic stainless steel. However, this material's microstructure is susceptible to phase changes during welding thermal cycles. Over long service periods, chromium carbides may precipitate at grain boundaries, creating chromium-depleted areas that reduce the material's corrosion resistance[128]. To improve resistance to high-temperature intergranular stress corrosion, 316 stainless steels, containing 2-3% molybdenum, gradually replaced 304.

As energy-saving and emissions-reduction requirements have intensified, steel used in thermal and nuclear power plants must now withstand higher temperatures and stricter performance standards, demanding advancements in material development and high-temperature performance evaluation[2],[3]. Standard 316 stainless steel no longer meets these high-temperature demands, leading to modifications in element content to enhance specific properties. For example, 316H, with higher carbon content, is suited to high-temperature, high-stress environments, while the lower-carbon 316L variant is better suited to highly corrosive environments. Other variants, including titanium-stabilized 316 stainless steel (316Ti), nitrogen-reinforced 316 stainless steel (316N), and low-carbon, nitrogen-reinforced 316 stainless steel (316LN), offer further versatility[129],[130].

316 stainless steel and its variants are widely used in nuclear reactors, tanks, and power plant piping, where they provide long-term protection against corrosive substances like sulphur compounds and chlorides[131],[132]. This adaptability to extreme conditions has established 316 stainless steels as a cornerstone of the power generation industry. However, given the critical operating environment of power plant equipment, any severe failure can significantly impact daily life. Power outages can disrupt residential life and essential services, including hospital emergency equipment, public transportation, and industrial production. In the event of a major failure at facilities like nuclear power plants, leaks, contamination, or explosions could occur, posing long-term risks to human health and the environment. Consequently, as the second most commonly used stainless steel, in-depth research on 316 stainless steel is essential, particularly regarding its lifespan and performance under high-stress conditions.

### 2.5.1.1 Mechanical properties of 316 stainless steel

Stainless steel exhibits excellent oxidation and corrosion resistance, primarily due to the early addition of chromium (Cr) elements. When stainless steel contacts a corrosive medium, oxidation results in a dense oxide film (passivation layer), which prevents further corrosion. In addition to chromium, other alloying elements are added to strengthen stainless steel, including approximately 12% nickel (Ni) to maintain the austenitic structure and improve wear resistance and mechanical properties, 2-3% molybdenum (Mo) to enhance corrosion resistance, manganese (Mn) stabilizes austenite, while titanium (Ti) and niobium (Nb) prevent intergranular corrosion. Nitrogen (N) strengthens the austenite and improves corrosion resistance, and carbon (C) stabilizes austenite but may reduce corrosion resistance due to carbide formation. These elements significantly influence the properties and microstructure of stainless steel. The specific chemical composition of 316 stainless steesl is shown in the Table 2-1:

**Table 2-1 Chemical composition of 316 stainless steel** [133]

| Iron (Fe) | Balance |
|---|---|
| Carbon (C) | 0.0-0.07 |
| Manganese (Mn) | 0.0-2.0 |
| Silicon (Si) | 0.0-1.0 |
| Phosphorus (P) | 0.0-0.05 |
| Sulfur (S) | 0.0-0.02 |
| Chromium (Cr) | 16.5-18.5 |
| Molybdenum (Mo) | 2.00-2.50 |
| Nickel (Ni) | 10.00-13.00 |

316 stainless steels have been extensively researched due to its long history and proven properties. It is available in various forms to suit a wide range of applications, including large forgings, castings, rolled plates, welded tubes, and powder metallurgy components. Different manufacturing processes lead to variations in internal structure and grain size. Subsequent heat treatments, such as solution treatment temperature and holding time, also influence austenite grain size[134]. Although the Hall-Petch relationship suggests that reducing grain size increases yield strength, differences in deformation levels and internal structure from solution treatments can result in significantly varied mechanical properties in 316 stainless steels[135].

Solomon[136] found that deformation-induced martensite forms in 316 stainless steel during cold working, which reduces corrosion resistance, leading to pitting, cracking, and stress corrosion cracking. This is attributed to the instability of austenite near or below room temperature. Li et al.[137] evaluated the microstructure, elemental distribution, and creep properties of SLM 316L stainless steel over an annealing temperature range of 650-1050°C in their study. They found that annealing temperature significantly impacts microstructure, elemental segregation, and creep properties. Wang et al.[138] conducted a comprehensive study on primary strain-hardened F316 stainless steel, focusing on its unique microstructure characterized by austenitic equiaxed grains and wider annealed twin boundaries. They found that the creep resistance of primary strain-hardened F316 stainless steel is considerably

superior to that of non strain-hardened F316 stainless steel when subjected to similar conditions. This improvement in creep resistance can be attributed to the high density of deformation twins present in the material.

Tensile testing is one of the main methods for assessing mechanical properties, evaluating elasticity, strength, plasticity, work hardening, and toughness while also producing stress-strain curves that simulate the material's plastic deformation and fracture in service. Analysis of fracture surfaces and microstructures from tensile tests provides insights into the fracture mechanisms and deformation characteristics of 316 stainless steel under various thermal and mechanical conditions. Numerous studies have investigated the tensile deformation behaviour of 316, showing that at low temperatures, deformation occurs primarily through dislocation slip or deformation twinning[131-134]. The typical stress-strain curves of 316L is shown in Figure 2.20. Sun et al.[143] analysed the microstructure and slip band changes of 316 stainless steel during slow tensile testing at room temperature. They found that the number of slip bands increased with the increase in deformation during the tensile process. In the later stages of tension, multiple slip occurred due to grain rotation, resulting in increased surface roughness. Adjustments in chemical composition and variations in tensile temperature can significantly influence this deformation mechanism.
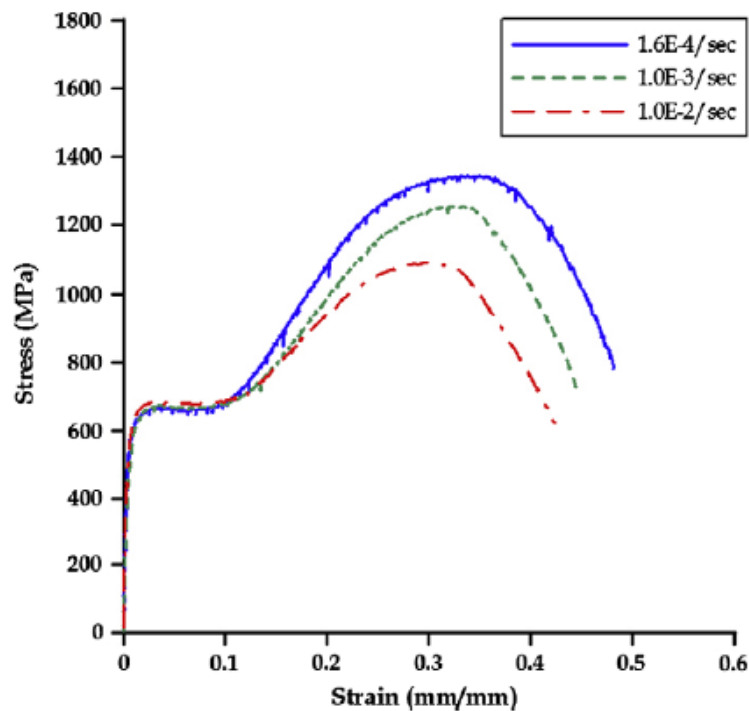


**Figure 2.20 Stress–strain curves of 316L obtained at different strain rates**[139].

43

In tensile tests conducted between 500-700°C, austenitic stainless steels often exhibit a serrated curve due to interactions between solute atoms and dislocation movements, known as dynamic strain aging, as shown in Figure 2.21. This effect has significant implications for the mechanical properties, fatigue resistance, and creep behaviour of austenitic steels at elevated temperatures [144].
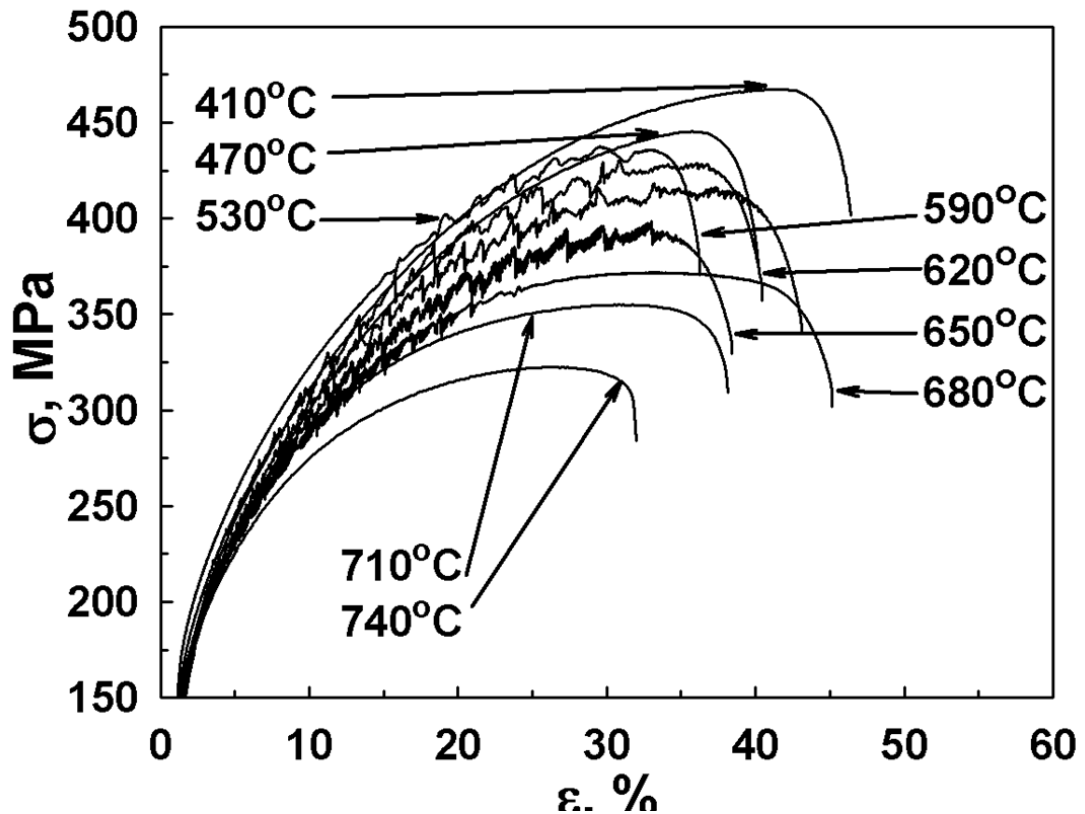


**Figure 2.21 Tensile stress–strain curves of an austenitic stainless steel at various temperatures illustrating serrated flow behaviour associated with dynamic strain ageing**[144].

The creep behaviour of austenitic stainless steels has been widely studied. As noted, the creep mechanism is often characterised by the stress exponent n, which for austenitic stainless steel ranges from 3 to 15[145][146]. This range indicates complex dislocation dynamics accompanied by the precipitation of secondary-phase particles. Zhang et al.[147] observed in nuclear class 316H steel plates after high-temperature creep that both the σ-phase and chain $M_{23}C_6$ precipitated at the δ-ferrite and austenite boundaries promote the formation of voids, while the Laves phase precipitated inside the δ-ferrite is the main strengthening phase of the metal at high temperatures. The internal dislocation structure undergoes complex transformations during sustained

creep. In single-phase solid solutions with sufficient solute and low initial dislocation density, dislocation density increases at the onset of deformation, forming tangles that evolve into cellular structures. Dislocations align at cell walls, forming sub granular boundaries, while dislocation networks appear in some areas due to dislocation movement. Cheng and Gao[148] investigated the influence of pre-creep on the microstructure of 316LN stainless steel and also studied the effect of dislocations on creep performance. They found that at 300°C/20MPa, the grain size remained unchanged. However, as the stress increased to 120MPa, a large number of dislocations slipped in different directions and accumulated at grain boundaries, gradually forming a dislocation network, which contributed to dislocation strengthening. At 600°C, dynamic recrystallization occurred, resulting in grain growth and the decomposition and disappearance of dislocations at grain boundaries, promoting grain boundary sliding and the formation of creep voids. Song et al. [149] found that 316L has an obvious temperature-dependent dynamic strain aging at a specific temperature range (723-923 K) with a strain rate of $1.3 \times 10^{-3} s^{-1}$. At elevated temperatures, dislocation climb is the main creep mechanism of 316L and can affect dislocation mobility. They established a dislocation-based crystal plasticity model to describe the relationship between the macroscopic mechanical responses and the underlying microscopic dislocation behaviours, especially that dislocation climb leads to the annihilation of monopolar dislocations and the formation of dislocation dipoles and helps monopolar dislocations surmount obstacles.

Due to the long service life and irreplaceability of 316 stainless steel in many applications, predicting its creep life has become a critical issue in engineering design and materials research. Yoda[150] used EBSD as the inspection method of plastic and creep deformation of 316 stainless steel in electric power plants, and indicated grain average misorientation (GAM) as one of the important parameters for creep life prediction. Esposito et al.[151] established the BE creep rate model by considering the deformation and damage mechanisms in the creep process, and successfully applied it to 316H stainless steel. Davies et al.[152] predicted the incubation time of 316H stainless steel at 500 °C with typical length increments Δa=0.2 and 0.5 mm for creep crack extension based on the time-dependent failure assessment diagram (TDFAD), and found that the creep fracture toughness of the material and the value of the reference stress would have a significant influence on the creep crack incubation time.

Boerman et al.[143] studied the creep fracture process of 316H stainless steel at temperatures above 800°C and calculated the activation energy of the steady-state stage to be approximately 374.1 kJ/mol at 1000°C and 1200/1300°C, which is slightly higher than the self-diffusion energy of iron atoms. While the activation energy of the acceleration stage was 1758.5 kJ/mol, which is approximately equal to the heat of sublimation of pure iron.

Although 316 stainless steels have been extensively studied across various aspects, the changes in internal creep activation energy calculated using the Wilshire Equations—from 150 to 300kJ/mol—have yet to be effectively correlated with microstructural features[115]. Addressing this gap will be one of the primary objectives of this study.

## 2.5.2 Nickel-based superalloys

A superalloy is a family of metallic materials that can operate at high temperatures (often surpassing 0.7 of the absolute melting point) under stress for long periods[153]. In 1929, superalloys were first 'developed' by Bedford, Pilling, and Merica,[154] who added small amounts of titanium and aluminium to "80/20" Nichrome and found that the creep strengthening was surprisingly improved. However, it was only in 1951 that Taylor and Floyd[155] finally discovered a tiny coherent phase after the invention of the electron microscope in 1931 and envisioned that the higher strength was caused by the precipitation of this phase. The phase, which is named γ' afterwards, will be described in detail later. Superalloys are primarily used in aerospace and marine turbine engines; thus, creep and oxidation resistance of the materials are crucial design considerations. This type of high-temperature alloy also exhibits excellent high-temperature strength, corrosion resistance, and good fracture toughness, and is widely utilised in the aviation, petroleum, and chemical industries. According to the base elements, superalloys can be categorised into three groups: iron-based, nickel-based, and cobalt-based. Iron-based superalloys are relatively weak and can be employed up to approximately 700°C[156], thus, are used in heat exchangers, piping, heat treatment equipment or other chemical processing applications[157]. The utilisation of nickel-based superalloys has become prevalent in situations where there is a need for substantial resistance to loading in static, fatigue, and creep conditions, particularly when operating temperatures exceed approximately 800°C. The production of high-temperature resistant materials for aircraft gas turbines, including turbine blades,

combustion chambers, turbine discs, turbine blades, exhaust systems, and other parts of the hottest end, heavily relies on the use of nickel-based superalloys. Cobalt-based superalloys have higher melting temperatures and corrosion resistance than both nickel and iron-based alloys. However, Cobalt's supply crisis in 1978 resulted in the destruction of cobalt demand, which allowing nickel-based superalloys to be more popular in markets[158]. The three classifications of superalloys are shown in Figure 2.22.
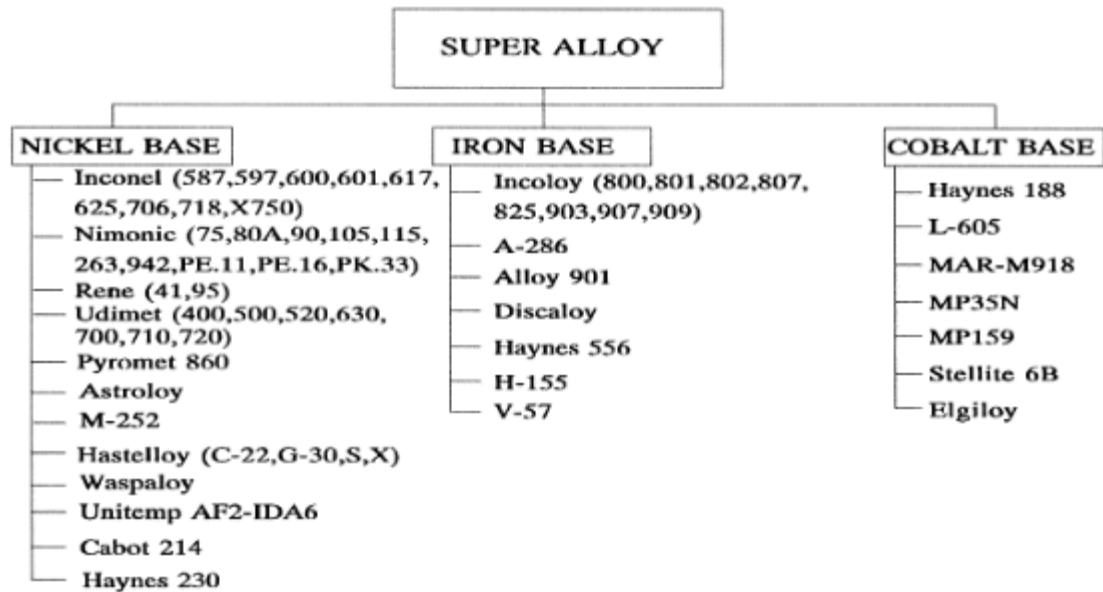


**Figure 2.22 Classification and examples of superalloys**[159].

### 2.5.2.1 Strengthening mechanisms of superalloys

The most commonly used strengthening mechanisms for superalloys are solid-solution strengthening, precipitation strengthening, oxide dispersion strengthening and carbide hardening[155].

**Solid-solution strengthening**: is caused by adding solute atoms of an alloying element to the atomic lattice, forming a solid solution. The solute atoms inhibit the movement of dislocation, which is the major problem in metals that cause plastic deformation. Therefore, once the dislocation motion is prevented, the strength of the material is increased. The austenitic $\gamma$ phase is mainly formed by the base metal of the superalloy but can also be stabilized by adding nickel, cobalt, iron, chromium, ruthenium, molybdenum, rhenium and tungsten, worked as solid solution strengthening elements.

**Precipitation strengthening**: is also called age hardening or particle hardening. In nickel-based superalloys, the precipitation strengthening elements such as aluminium, titanium, niobium and tantalum that have greater radii often form coherent secondary phases with γ-matrix during ageing. These precipitates, which are generated in the alloy matrix from solid solution during heat treatment, impede the movement of dislocations or crystal defects. The size of precipitates can be varied by controlling the ageing temperature, and further, affect the strength of the materials.

Precipitates can be categorised as carbides, geometrically close-packed (GCP), and topologically closed-packed (TCP). GCP phases such as γ′ and eta are usually advantageous for mechanical characteristics, whereas TCP phases like μ, σ, Laves, etc. make superalloys prone to brittleness as they are incoherent with the γ matrix and combine elements from the GCP phases.

**Oxide dispersion strengthening:** similar to precipitation strengthening, but instead of forming precipitates from the matrix, oxide particles are added to the alloy directly to inhibit the movement of dislocations.

**Carbide hardening**: because of the limited solubility of solid solution hardening elements such as molybdenum, tungsten, titanium and niobium, carbides with the formula $M_{23}C_6$, which is transformed from MC and $M_6C$ at high temperatures, form in grain boundaries to restrain the sliding of grain boundaries. This mechanism is particularly used for improving creep strength as high-temperature creep processes mostly occur at grain boundaries. Carbides can occur within the grain to act similarly to precipitates.

### 2.5.2.2 Phases of superalloys

Basically, the microstructure of a typical superalloy is composed of the disordered austenitic fcc matrix, γ, and a variety of precipitations that contain ordered fcc γ' phase, body-centred tetragonal (BCT) γ″ phase, hexagonal close-packed (HCP) η phase, orthorhombic δ phase and carbides (borides and nitrides)[155]. Although TCP phases are undesirable, they usually occur in the service-aged condition and can be found in certain superalloys[160]. Below gives the details of the common phases that can be observed in superalloys:

**The gamma (γ) matrix**[147], [153-156]**:** The γ matrix possesses a disordered face-centred cubic (FCC) structure and typically constitutes a continuous matrix within which other phases coexist. Typically, it comprises a substantial proportion of solid solution elements like cobalt, chromium, or molybdenum. These elements act as γ-phase stabilizers due to their closely matching atomic radii with that of nickel, enhancing their likelihood of dissolution into the austenitic γ phase. The γ phase serves as the foundational matrix for all nickel-based superalloys.

**The gamma-prime (γ')**[147], [153-156]**:** Gamma prime (γ') is an ordered face-centred cubic (FCC) precipitate phase that can be found in nickel-base or nickel-iron-base superalloy, forming $Ni_3(Al, Ta, Ti)$, and possessing an L12 crystal structure. The enriched elements like aluminium, titanium, and tantalum atoms typically occupy the unit cell corner, while nickel atoms occupy the faces. These γ' precipitates are frequently coherent with the austenitic γ matrix. In numerous nickel- and nickel-iron-based superalloys, this primary strengthening phase possesses a crystal structure with a slight variation (0 to 0.5%) from the austenite matrix. In contrast to the elements dissolved within the austenitic γ phase, aluminium, titanium, and tantalum possess larger atomic radii than nickel. Consequently, these elements facilitate the formation of the ordered γ' phase, which serves as the primary high temperature strengthening phase. In most nickel-based superalloys, three types of γ' phase exist, contingent on their size. Precipitates larger than 100 nm are referred to as primary γ' and predominantly locate themselves at the triple junctions between grains. Those in the range of 50-100 nm are termed secondary γ', and precipitates ranging from 20-50 nm or smaller are referred to as tertiary γ', as shown in Figure 2.23.
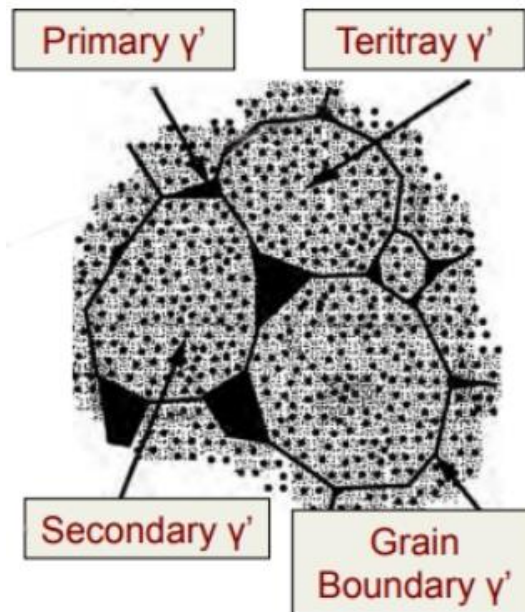
**Figure 2.23 Different types of γ' phase**[161].

Furthermore, the morphology of γ' precipitates primarily depend on three factors: composition, the matrix-precipitate lattice mismatch, and the degree of aging. Experiments have shown that modifications in molybdenum content and the aluminium-to-titanium ratio can alter the morphology of the gamma prime phase. The shapes that change as the lattice mismatch (γ / γ') increases include spherical, globular, blocky, and cuboidal, see Figure 2.24. The characteristics of superalloys have been seen to be significantly influenced by the coherency of the γ / γ' contact, defined as δ, and can be calculated by the formula:

$$\delta = \frac{2\left(A_{\gamma'} - A_\gamma\right)}{\left(A_{\gamma'} + A_\gamma\right)}$$

**Eq. 2-17**

where δ is the lattice misfit, and A is the lattice parameter.

Typically, spherical γ' shapes prevail for mismatches within the range of 0-0.2%. As mismatch grows to approximately 0.5-1% it transitions to a cuboidal shape, and above 1.25% it develops into a plate shape.
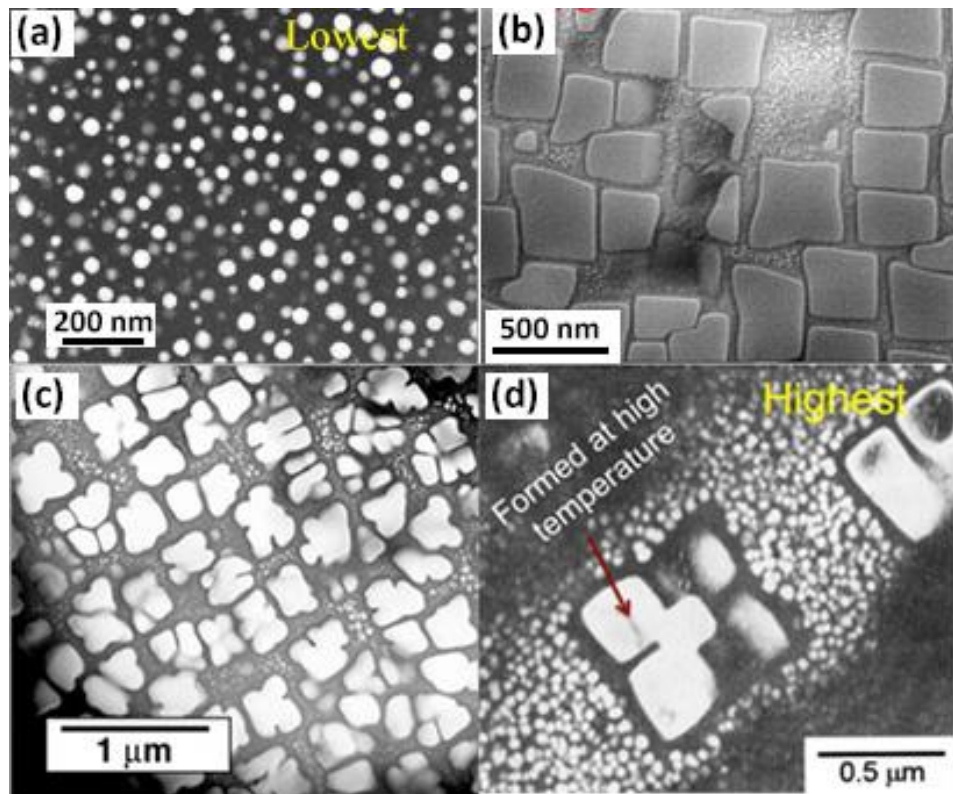
**Figure 2.24 The different mismatch of γ / γ' showing different shape, with the lowest mismatch showing at (a), to the highest at (d)**[161], [165], [166].

**The eta phase (η)**[161]**:** The η phase exhibits an hcp (D0$_{24}$) structure and can be found in superalloys with relatively high titanium/aluminium ratios after prolonged exposure. The possibility of cellular structures forming along grain boundaries or needle-shaped plates adopting the Widmanstätten pattern within grains.

**The gamma double prime (γ'')**[163], [164]**:** The gamma double prime phase (γ'') is a finely dispersed precipitate that forms within the gamma (γ) matrix of certain nickel-based superalloys. The coherent precipitate possesses a composition of Ni$_3$Nb and exhibits a body-centred tetragonal (BCT) crystal structure known as D0$_{22}$. This phase plays a pivotal role in enhancing the mechanical properties of these alloys. It forms during controlled heat treatment or aging process and maintains coherence with the γ matrix, signifying a well-defined interface, and is usually observed to form on the {100} planes. These precipitates have an average diameter of roughly 600 angstroms and a thickness ranging from 50 to 90 angstroms. This coherency contributes to the alloy's strength by impeding dislocation motion.

**The delta phase (δ)**[153-156]**:** The δ phase exhibits a distinctive orthorhombic structure with the chemical formula Ni$_3$Nb. It is observed in some overaged

51

superalloys such as Inconel 718, taking on an acicular shape when formed between 815 and 980°C. Its formation occurs through cellular reactions at low aging temperatures and intragranular precipitation at high aging temperatures. These phases have the potential to be utilized for grain size control and refinement, consequently enhancing the alloy's tensile properties, fatigue resistance, and resistance to creep fracture. Nonetheless, this phase's formation is usually discouraged due to its inherent hardness and its lack of compatibility with the gamma matrix.

**The carbide**[147], [153], [154], [156], [159-161]: Carbides are a common presence in many non-single crystalline alloys, and their classification varies based on alloy composition, processing methods, and working conditions. The most common types include MC in the Cubic structure, $M_{23}C_6$ and $M_6C$ in the fcc structure, and $M_7C_3$ in the hexagonal structure. These carbides exhibit varying shapes and colours, with the M atom representing one or more distinct metal atoms within different carbides. The importance of these carbides lies in their effect on the mechanical properties associated with grain boundaries during high-temperature service, which is as important as the strengthening effect of $\gamma'$ within the grains, and is known as a grain-boundary strengthener. MC carbides typically precipitate from the alloy's liquid phase at elevated temperatures, forming globular, irregularly shaped particles with colours ranging from grey to mauve. This phenomenon typically takes place during heat treatment or alloy aging. These carbides are distributed within the intergranular regions, which correspond to the spaces between the grains of the alloy. They lack a clearly defined orientation relationship with the $\gamma$ matrix in the alloy. M elements can be titanium, tantalum, niobium, hafnium, thorium, or zirconium, and titanium carbide has a certain degree of solubility for nitrogen, zirconium, and molybdenum. In the course of processing or utilization, MC carbides may undergo decomposition into alternative carbide forms, such as by exposure to temperatures from about 790 to 816°C, the presence of $M_{23}C_6$ carbides tends to increase, leading to their precipitation in various forms, including thin films, globules, plates, flakes, and cells. Typically, these precipitates form at grain boundaries. Similarly, the $M_6C$ type typically forms randomly distributed $M_6C$ carbides within the temperature range of approximately 816 to 1038°C, often exhibiting a pink colouration. The fine and dispersed $M_6C$ precipitates effectively hinder dislocation movement, thereby preventing the shearing of the $\gamma'$ phase and ultimately enhancing the fatigue properties of high-temperature

alloys. $M_7C_3$ is typically encountered in large intergranular formations and is rarely observed in high-temperature alloys following exposure to temperatures exceeding 1000°C. These carbides obstruct grain boundary slip during deformation, consequently improving the creep properties of high-temperature alloys. However, the presence of high concentrations of carbides or the formation of continuous carbide chains at grain boundaries along grain boundaries may contribute to crack initiation and propagation during aging or high-temperature exposure. Therefore, in order to maintain the excellent mechanical properties of high-temperature alloys, good control of the amount of carbides, typically below 2%, is essential.

**The borides and nitrides ($M_3B_2$ and MN)**[161], [164]**:** Similar to carbides, borides also serve to enhance the strength of grain boundaries and play a crucial role in enhancing the resistance to creep-rupture. They also exhibit precipitation at γ-grain boundaries, but in a tetragonal crystal lattice structure, and in a smaller volume fraction than carbides. "M" elements in borides can be nickel, iron, molybdenum, tantalum, niobium, etc.

Nitrides are commonly found in alloys that incorporate titanium, niobium, or zirconium. These compounds exhibit limited solubility at temperatures lower than their respective melting points. They can be readily identified by their polished appearance, which typically manifests as square to rectangular shapes, and their colouration, which ranges from yellow to orange.

**The TCP phases**[161], [164], [170]**:** TCP phases (Topologically Close-Packed Phases), are common precipitation phases in nickel-based, cobalt-based, iron-based high-temperature alloys as well as austenitic stainless steel, usually formed at high temperatures. The principal constituents responsible for solid solution strengthening inside the alloy are comprised of a majority of elements involved in TCP phase formation. The presence of TCP phases leads to a reduction in the effectiveness of solid solution strengthening in the substrate. In addition, it is important to note that the TCP phase exhibits inherent characteristics of rigidity and brittleness, making the process of dislocation propagation during creep particularly difficult. The presence of accumulated material at the interface between the TCP (topologically close-packed) and γ' (gamma prime) phases results in the concentration of stress, which in turn promotes the development of cracks and their subsequent rapid propagation.

53

Ultimately, this leads to a significant deterioration in the creep resistance of the alloy. σ, μ, R, Laves phases, etc., belong to this classification.

### 2.5.2.3 Nickel-based superalloys

Nickel is a silvery-white metal, discovered by Axel Fredrik Cronstedt in 1751 [171], with ductile, hard, and malleable properties. It is one of the most abundant elements, expressed with the symbol Ni, atomic number 28, atomic weight 58.71. It is a transition metal, the outer d electrons provide a strong cohesion and form a small interatomic distance, thus, rather dense. Nickel has excellent corrosion and high-temperature oxidation resistance and is an important engineering metallic material, can also be used in food processing equipment and for plating. The crystal structure of nickel is a face-centred cubic (FCC) lattice (Figure 2.25), with strong plastic deformation ability, and has good pressure processing properties in both hot and cold conditions. However, the use of nickel is largely influenced by its higher density ($8907kg/m^3$) compared with Ti ($4508kg/m^3$) and Al ($2698kg/m^3$) and price.

To further improve the corrosion resistance and mechanical properties and increase some special physical properties, nickel can be alloyed with other metals such as chromium, iron, copper, cobalt, aluminium, titanium, molybdenum, etc.[172]. According to their characteristics and application fields, nickel alloys are classified into commercially pure nickel, nickel-copper alloys, nickel-chromium alloys, nickel-based superalloys and nickel-iron superalloys.
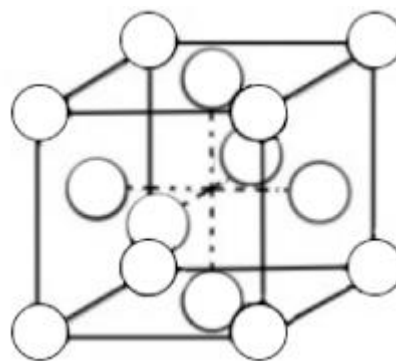


**Figure 2.25 The crystal structure of Ni.**

Nickel-based superalloys have a complex chemical composition as they are often containing more than ten different alloying elements with up to 60% nickel as solvent[173]. Most of the alloying elements are taken from the d block of transition

metals and each alloy has its own effect on microstructure and phase stability, as shown in Figure 2.26.
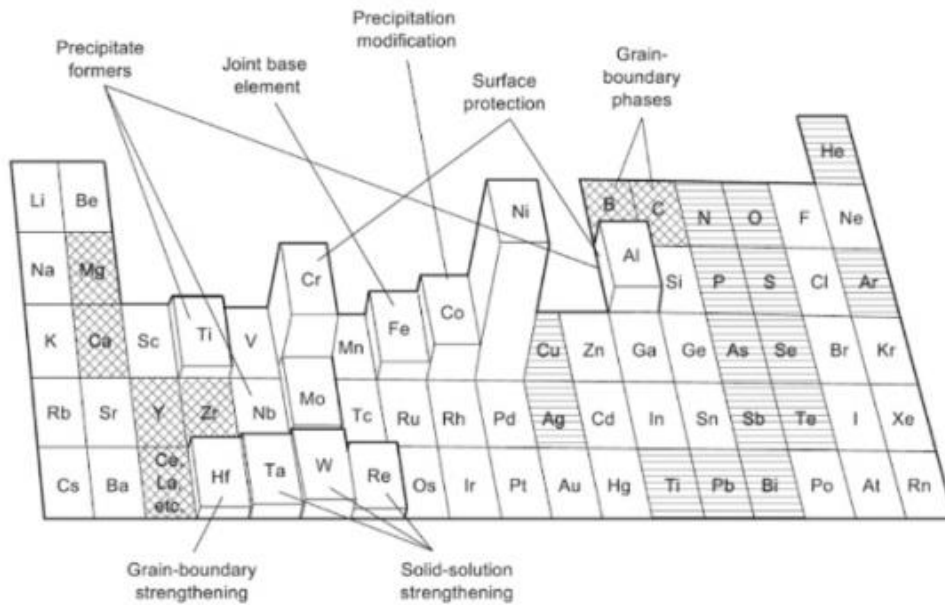


**Figure 2.26 Main elements and their roles in nickel-based superalloys** [174].

As previously mentioned, nickel-based superalloys contain a stable, continuous $\gamma$ matrix made up of nickel atoms. The additions of Ti, Al and Nb, in turn, precipitate a $\gamma'$ phase in the $\gamma$ matrix. $\gamma'$ phase has an ordered $L1_2$ crystal structure with Ni atoms at the centres of the cube surface and Al/Ti atoms at the corners of the cube, see Figure 2.27.
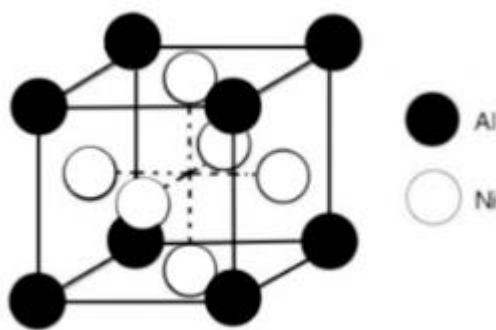


**Figure 2.27 The crystal structure of $\gamma'$ ($Ni_3Al/Ti$).**

$\gamma'$ is an important phase as it affects the high-temperature strength and creep resistance of nickel-based superalloys. Tian et al.[175] has found that the higher the volume fraction of the $\gamma'$ phase, the better creep resistance of the superalloys. However, the amount of $\gamma'$ depends not only on the chemical composition but also on the temperature

55

– the fraction of γ′ decreases with increasing temperature. This phenomenon can be used to produce a fine and homogeneous dispersion of strengthening precipitates by dissolving the γ′ at a sufficiently high temperature and then ageing at a lower temperature.

With increasing ageing time, the development of γ′ morphologies from spheres to cubes, to arrays of cubes, and finally to solid-state dendrites is shown in Figure 2.28. The top line illustrates the projection along <111>, and the bottom line shows the projection along <001>.
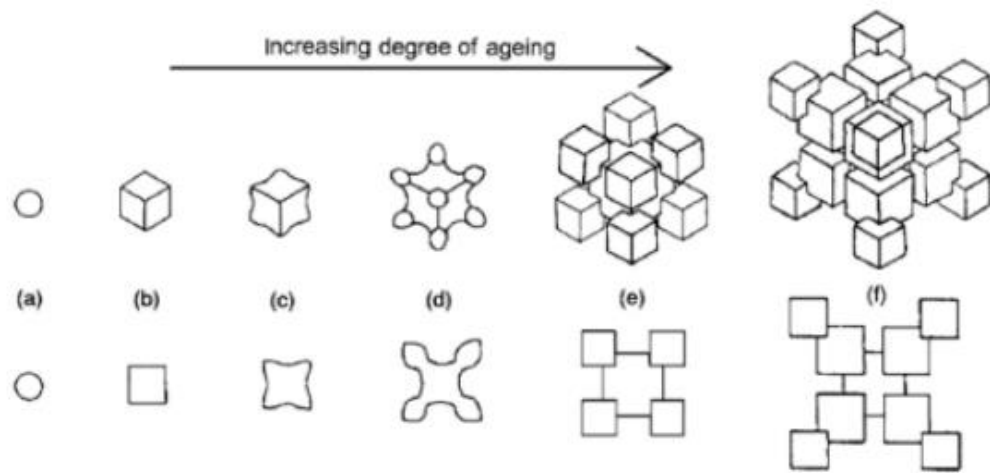


**Figure 2.28 The development of strain-induced, faceted γ' morphologies during ageing**[176].

Although γ'and γ are coherent when the size of precipitates is small, dislocations in γ find it challenging to penetrate γ'. The ordered fcc lattice structure of γ' results in this interruption of movement of dislocations. Dislocations have to crawl past these precipitates by Orowan bending/looping, climbing around, or cutting through the particles, which makes dislocation movement more difficult. Hence, the strength of the superalloy depends on the precipitation of γ' in the matrix[153][25]. Figure 2.29 demonstrates the SEM images of cubic morphology of the γ′ phase in the γ phase matrix for an Inconel 713C superalloy.
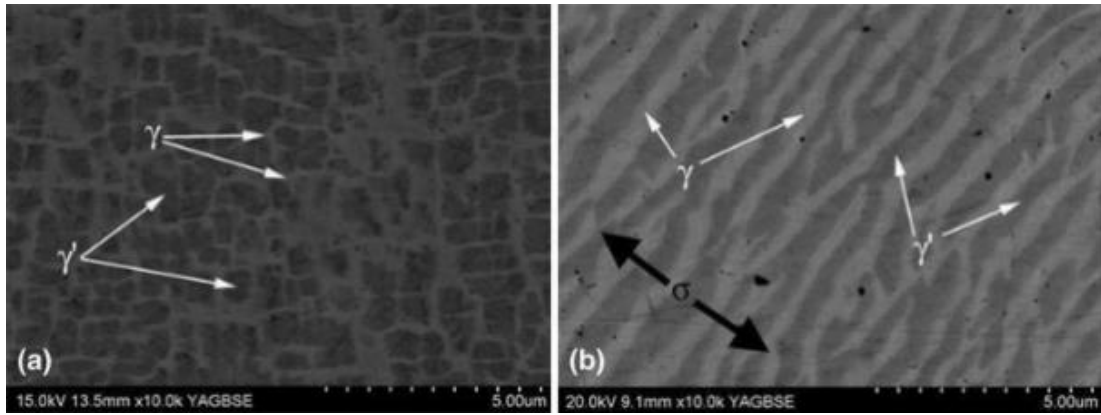
**Figure 2.29 The microstructure of γ and γ' phase for the IN713C nickel-based superalloy** [177].

A small amount of carbon, often present at concentrations up to 0.2wt%, combined with other reactive elements including chromium, molybdenum, tungsten, niobium, tantalum and titanium, to produce a network of carbide particles such as TiC, BC, $Mo_6C$, $Cr_7C_3$, $Cr_{23}$, etc.[178]. Carbides such as $M_{23}C_6$ form at temperatures around 750°C via reactions:

$$MC + \gamma \rightarrow M_{23}C_6 + \gamma'$$
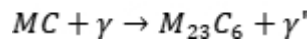
Those elements with very different atomic sizes from that of nickel, especially carbon and boron, are also known as grain boundary strengtheners as they protect grain boundaries from sliding.
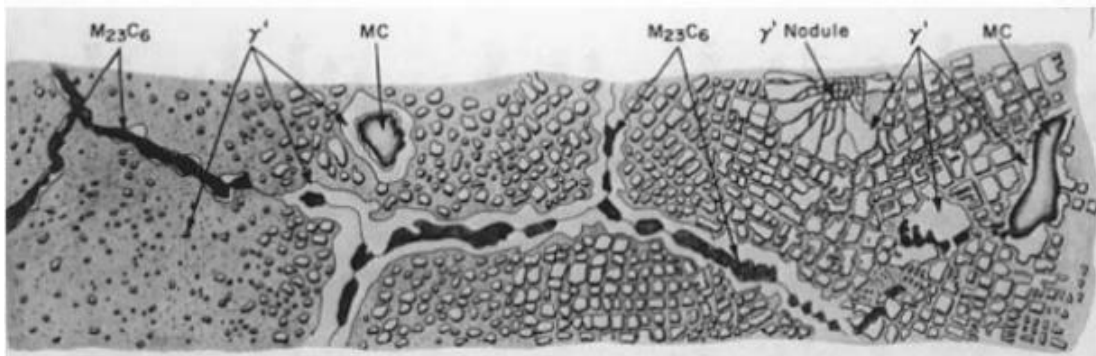


**Figure 2.30 Microstructure of a superalloy labelled with different carbides at the grain boundaries and some γ' precipitates in the matrix**[164].

Figure 2.30 illustrates a schematic of the microstructure of IN713C superalloy labelled with different carbides at the grain boundaries and other secondary precipitates.

Nickel-based superalloys are produced as wrought superalloys, cast superalloys and powder metallurgy nickel-based superalloys by different manufacturing processes. Investment casting is the primary process for nickel-based superalloys with high content of aluminium and titanium, and a high-volume fraction of $\gamma'$ phase to fabricate complex final shapes, such as turbine blades and vanes[179]. With the development of casting technology and higher requirements of turbine blades for advanced engines, nickel-based casting superalloys have been gradually developed from equiaxed crystal alloys to directionally solidified alloys and, currently, single-crystal alloys. Compared to equiaxed superalloy blades, directionally solidified superalloy blades have columnar grains whose orientation is aligned. On account of the elimination of transverse grain boundaries that are perpendicular to the principal stress axis, the physical properties such as fatigue and creep strength in high temperatures are significantly improved. In addition, the operating temperature is also increased by approximately 50°C. Since the single-crystal superalloy blades eliminate the grain boundary, the properties are further improved, and the working temperature has been increased up to 1100°C[178]. Figure 2-21 shows the evolution of turbine blades in the (a) equiaxed, (b) columnar and (c) single-crystal forms.
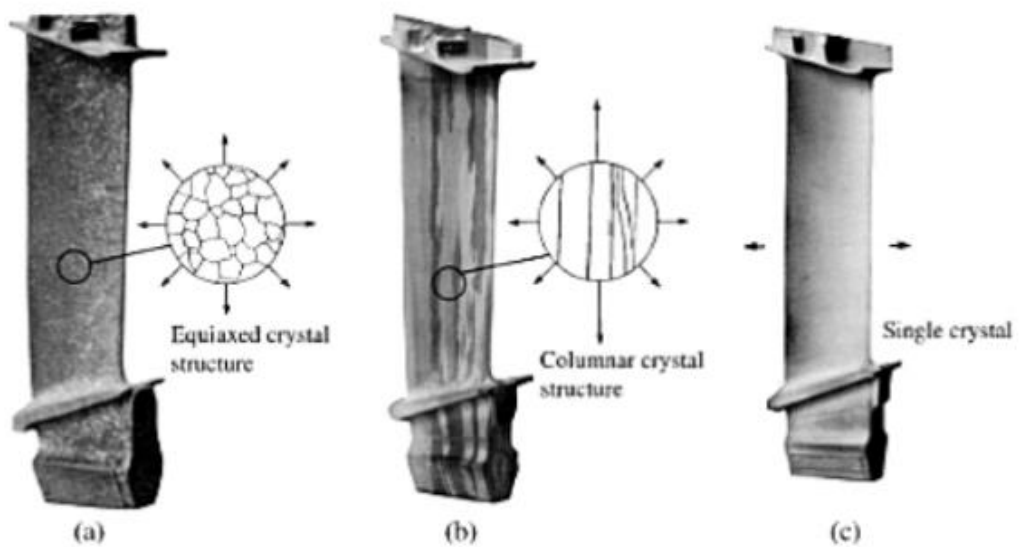


**Figure 2.31 Turbine blades with different morphologies with (a) Equiaxed, (b) Columnar, (c) Single crystal structure**[180].

Wrought superalloys including Inconel, Rene, Hastelloy, Nimonic, Astroloy, Udimet and other series are generally formed by hot working methods such as hot forging, hot rolling, and hot extrusion. Inconel 718 is a typical wrought superalloy which is widely

used in aerospace, jet engine and gas turbine operations. Most wrought superalloys require vacuum induction melting (VIM) as the primary melting process to form an ingot or powder for the following manufacture.

The use of γ′-forming elements increases the strength of superalloys but also results in segregation on macro-component because the structural properties of nickel-based superalloys are very sensitive to the chemical inclusions and the change of microstructure. To produce turbine disks and compressor discs, powder metallurgy processes (such as hot extrusion + isothermal forging) are used to avoid macro segregation in large ingots and to obtain uniform fine-grained structure, thereby, significantly improving their properties. Therefore, has started to replace the nickel-base superalloy that is produced by casting process. IN 100, Rene ′ 95, Merl 76, etc. are widely used examples of powder metallurgy superalloys[178].

### 2.5.2.4  Inconel 713C

Inconel is a family of the austenitic nickel-chromium-based superalloys and was first developed in the 1940s to support the Whittle Jet Engine by Wiggin Alloys (Hereford, England), which was later adopted by SMC (Special Metals Corporation)[181]. Inconel 713C (also referred to IN713C) was one of the first of several precipitation hardened, cast nickel-based superalloys developed during the 1950s[177].

Like all the other nickel-based superalloys in the Inconel series, IN713C is widely used in some challenging applications such as rocket engines, power generation turbines etc. because of their superior mechanical properties, heat resistance, high-temperature corrosion resistance, good castability and acceptable cost[182]. The outstanding properties of IN713C are mainly due to the addition of elements including aluminium, titanium and chromium and the full composition is given in Table 2-2.

**Table 2-2 Composition of Inconel 713C**[183]

| Nickel | Balance |
|---|---|
| Carbon (C) | 0.08-0.20 |
| Manganese (Mn) | 1.0 max |
| Boron (B) | 0.015 max |
| Silicon (Si) | 1.0 max |
| Chromium (Cr) | 11.0-14.0 |
| Molybdenum (Mo) | 3.5-5.5 |
| Titanium (Ti) | 0.25-1.25 |
| Aluminium (Al) | 5.5-6.5 |
| Iron (Fe) | 5.0 max |
| Columbium + Tantalum (Cb + Ta) | 1.0-3.0 |

### 2.5.2.5 Mechanical properties of Inconel 713C

IN713C is a precipitation hardened alloy which offers outstanding resistance to thermal fatigue and excellent rupture strength properties at 927°C (1700°F) and up to 982°C (1800°F)[182], [183]. The improved vacuum technology also increased the level of high temperature properties and led to a melting range of 1260-1288°C (2300-2350°F). As Nickel is the main component, IN713C therefore, has a relatively high density of 7.913g/cm$^3$.

As Inconel 713C alloy is normally used in high temperature conditions, the mechanical properties have been tested over various temperatures by the Nickel Institute[182]. Table 2-3 represented the effect of heat treatment on tensile properties of IN713C.

**Table 2-3 Tensile properties of cast alloy Inconel 713C by Nickel Institute**[182]

| Test Temp, °F | 0.2% Yield Strength, psi | Tensile Strength, psi | Elong, % | Red. Area, % |
|---|---|---|---|---|
| 70 | 106,600 | 123,000 | 7.9 | 11.6 |
| 1000 | 102,200 | 125,600 | 9.7 | 17.0 |
| 1200 | 104,200 | 125,700 | 6.7 | 10.5 |
| 1400 | 108,000 | 136,000 | 5.9 | 10.5 |
| 1500 | 95,100 | 120,500 | 6.0 | 11.5 |
| 1600 | 72,100 | 105,400 | 13.9 | 20.0 |
| 1700 | 55,800 | 85,300 | 11.8 | 17.7 |
| 1800 | 44,200 | 68,400 | 19.7 | 25.0 |

Inconel 713C is well-regarded for its high-temperature strength and excellent creep performance, making it ideal for demanding environments. Research indicates that both the alloy's microstructure and composition significantly influence its mechanical properties. The primary mechanism by which precipitate phases enhance metal strength is through inhibition of dislocation movement. According to Orowan theory[184] , if the precipitate phase particles dispersed in the matrix have higher strength and hardness than the matrix itself, or if the particles are spaced sufficiently apart with incoherent interfaces, dislocations struggle to cut through them. Instead, dislocations must bend around the particles, eventually forming dislocation loops, which contributes to overall strength. This theory shows that material strength correlates with the average particle spacing: the closer the particles, the greater the strengthening effect. Increasing the volume fraction of particles has a similar effect by reducing the particle spacing, thus also enhancing strength.

Tian et al.[175] has also found that the higher the volume fraction of the $\gamma'$ phase, the better creep resistance of the superalloys. Li et al.[185] also mentioned that the properties of superalloys mainly depend on the size and volume fraction of the precipitation phase, i.e. $\gamma'$ particles, which are generally formed by Aluminium and Titanium. Therefore, the content of Al and Ti are closely controlled to approximately 7wt% or less as too many $\gamma'$ particles affect the castability of the materials. Therefore, IN713C with more than 60% $\gamma'$ would be expected to have high creep strength.

Columbium and Tantalum are the weakest γ′ formers, however, Brinegar et al.[186] examined IN713C with varying content of Tantalum and Columbium to determine the effect of those chemical compositions on 713C alloy. The results showed that the Tantalum increased the secondary precipitates, γ′, and carbide stability but formed an unexpected TCP phase which is known as the sigma phase. Also, the substitution of Ta and Cb leads to an improvement in heat treatment response after hot isostatic pressing (HIP) and ageing, especially at 760°C (1400°F) and 980°C (1800°F). The addition of Chromium is to increase the resistance to corrosion and oxidation with Aluminium by forming oxides $Cr_2O_3$ and $Al_2O_3$[187], [188]. The addition of Boron and Carbon play an important role in grain boundary hardening to prevent dislocations from slipping. The function of each element can be roughly summarized in Table 2-4 below.

**Table 2-4 Summary of the main roles of alloying elements in In713C**

| Influence | C | B | Cr | Mo | Ti | Al | Cb+Ta |
|---|---|---|---|---|---|---|---|
| Matrix strengthening | | | √ | √ | | | √ |
| γ′ formers | | | | | √ | √ | √ |
| Carbide formers | | | √ | √ | √ | | √ |
| Grain boundary strengthening | √ | √ | | | | | |
| Oxidation resistance | | | √ | | | √ | |
| TCP promoters | | | √ | √ | | | |

Mohammad[189]carried out creep experiments on IN713C to investigate the effect of stress level on creep properties. The results showed a significant effect of stress on the carbide, which was elongated in a direction parallel to the force as time increased. Marie et al.[190] compared the creep behaviour of INC713LC, B1914 and MAR-M247 and concluded that dislocation glide and climb were their main creep mechanisms by calculating the stress exponent. He et al.[191] found that all the dislocations in γ' originated from the γ matrix, <110> type super dislocation and <010> type super dislocation are the two common dislocations. They also pointed out that suppression of <112> slip is beneficial for improving low temperature creep performance. Farahani[192] investigated the difference between IN713C reflowed material and its properties in a recent study of the returned gating and feeding system.

The results showed that the addition of reduced material had no significant effect on the key elements in the alloy's organisation and the γ mass precipitation phase. However, it did lead to an increase in the volume fraction of oxide and nitride inclusions due to the presence of oxygen, nitrogen and other contaminants in the reducing material. It was also shown that the addition of reflowed material does not alter the mechanical properties of the material at room temperature, but affects the mechanical properties of the material at elevated temperatures (T = 600 ° C), particularly the yield strength. Creep properties, which are critical to the performance of high-temperature alloys, decreased by 14% as the percentage of reflowed material in the alloy increased.

Although numerous studies have examined the creep behaviour of IN713C, none have applied the Wilshire Equation to model or predict its performance, particularly regarding creep activation energy. This represents a research gap in understanding IN713C.

**2.5.2.6   Haynes 282**

Haynes 282 alloy is a new type of γ′ strengthened nickel-based superalloy developed by Haynes International Inc. in 2005 for high-temperature structural applications, specifically for use in aerospace and land-based gas turbines in the hot section components[193].  It has a considerable improvement in creep strength, especially in the temperature range 649-927 ℃[194]. Its key advantages include comprehensive creep strength, weldability, and thermal stability[195]. Haynes 282 can be manufactured through both wrought and casting processes. Casting is a manufacturing process where molten metal is poured into a pre-made mold and allowed to cool and solidify to obtain the finished product. The casting process enables the production of complex geometries and large-sized parts. Wrought, on the other hand, is a process of changing the shape of the metal by applying pressure, usually done in the semi-solid or hot state of the metal. Wrought improves the material's toughness and strength by breaking down the cast structure and deforming the grains into shapes that are more favourable for withstanding mechanical stress. Therefore, casting is typically chosen for manufacturing complex aerospace components or large gas turbine components using Haynes 282. If the parts require higher mechanical performance, wrought Haynes 282 may be selected. Compared to other nickel-based superalloys, for example,

René-41 and Waspaloy alloy that have similar creep strength to Haynes 282, the new alloys also offering excellent formability and weldability because of the relatively lower volume fraction of γ′. In addition, it has higher allowable stress than Inconel 740 and better thermal stability[196], so has been considered to become one of the important candidate materials for advanced ultra-supercritical unit (A-USC) steam turbines[197]. The compositions of Haynes 282 alloys are shown in Table 2-5 below.

**Table 2-5 Composition of Haynes 282 adapted to '*Haynes 282 alloy*'** [198]

| | |
|---|---|
| Nickel (Ni) | 57 Balance |
| Chromium (Cr) | 20 |
| Cobalt (Co) | 10 |
| Molybdenum (Mo) | 8.5 |
| Titanium (Ti) | 2.1 |
| Aluminium (Al) | 1.5 |
| Iron (Fe) | 1.5 max |
| Manganese (Mn) | 0.3 max |
| Silicon (Si) | 0.15 max |
| Carbon (C) | 0.06 |
| Boron (B) | 0.005 |

The development of nickel-based super alloys is a matter of adjusting the content on the basis of Cr20Ni80, with additional elements. Thus, Haynes 282 unsurprisingly has a very high content of chromium, reaches to 20% and provides an excellent corrosion resistance to high temperature mechanism. As γ′ phase, the main strengthening phase of nickel-based alloys, increases in content, the stronger the alloy, but also decreases machinability. Therefore, to improve the weldability and fabricability, the volume fraction of the potent strengthening phase, γ′, has been controlled within 19 vol% since the amount of aluminium and titanium has been carefully balanced at approximately 3.6wt%. Molybdenum is a well-known solid solution strengthening element which provides good creep strength below 700°C but may reduce at 800°C or above[198]. Mo is mostly dissolved in the γ matrix, increasing the lattice constant of the matrix solid solution to improve creep properties. A small amount of Mo is dissolved in the γ′ phase, reducing the mismatch between γ/γ′ and reducing the rate of coarsening of γ′ at elevated temperatures to improve the strength of alloys. Considering the cost of the

material, only 10% cobalt has been added to help the solvus of $\gamma'$ precipitates since cobalt is relatively expensive. The additional carbon and boron, as mentioned in the last section, forms $M_{23}C_6$ at grain boundaries to enhance the mechanical properties. The microstructure of Haynes 282 is represented in Figure 2.32. It can be seen that the microstructure of Haynes 282 is heterogeneous, with a mixture of coarse grains and fine grains.
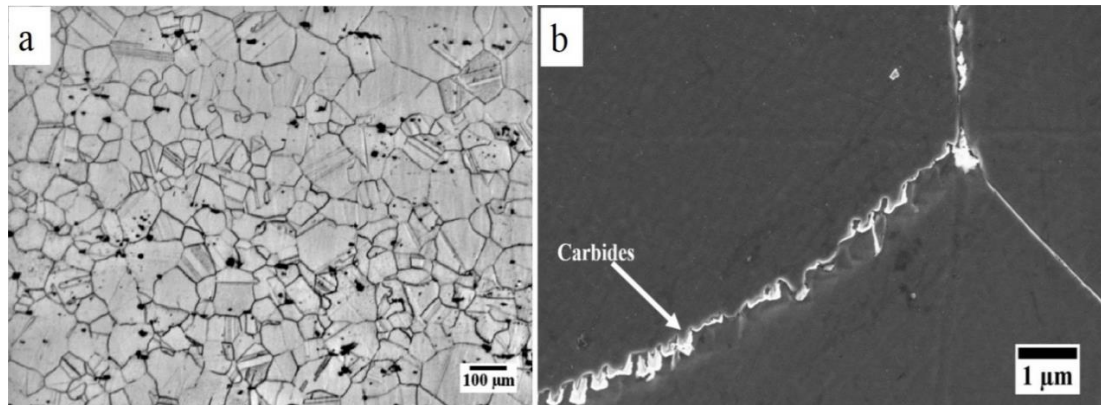


**Figure 2.32 (a) Optical microstructure of Haynes 282 sheet; grain structure and presence of inter and intragranular MC carbides. (b) SEM of grain boundary carbides**[199].

### 2.5.2.7 Mechanical properties of Haynes 282

The $\gamma'$ phase is the primary strengthening phase in Haynes 282, providing stability at high temperatures. Additionally, carbides along grain boundaries play a critical role in resisting grain boundary sliding, a key creep deformation mechanism. The types and distribution of these carbides vary with manufacturing methods, such as casting or direct metal laser sintering (DMLS), influencing the alloy's creep properties[200], [201].

Kelly[202] suggests that when the volume fraction of precipitate particles remains constant, needle-shaped or lamellar particles reduce the average particle spacing more effectively than spherical particles, thereby enhancing matrix strength. Thus, IN713C, which has a higher $\gamma'$ content, a lower $\gamma/\gamma'$ mismatch, and square-shaped $\gamma'$ particles, would theoretically exhibit higher mechanical properties than Haynes 282, which has a lower $\gamma'$ content and round $\gamma'$ particles. However, dislocation movement involves complex interactions with other dislocations, such as kinks and steps, as observed in studies on Waspaloy[19], [111]. During deformation, dislocations interact and entangle,

65

forming dislocation cells or walls[64]. As deformation progresses, higher external stress is needed for dislocations to overcome obstacles, resulting in higher yield strength and increased resistance to plastic deformation[65].

Grain size significantly impacts the creep behaviour of Haynes 282. Cast Haynes 282 typically has larger grains than wrought forms, which can affect the creep rate and failure mechanisms. Larger grains tend to reduce the creep rate due to fewer grain boundaries, which act as sites for creep deformation[201]. Wang et al.[203] conducted tensile and creep tests on sand-cast Haynes 282 specimens to investigate the influence of heterogeneous grain sizes. The results showed that sand-cast Haynes 282 has coarser grain sizes and a bimodal distribution of γ' precipitates, resulting in lower tensile strength and ductility compared to wrought Haynes 282. However, based on the Larson-Miller parameter, the creep rupture times of cast and wrought Haynes 282 were found to be similar, and the dominant creep mechanism for sand-cast Haynes 282 at temperatures of 704-788°C and stresses of 190-431 MPa was diffusional creep. Microstructural observations revealed that at room temperature, dislocation slip bands in cast Haynes 282 exhibited non-uniform distribution, and the dominant strengthening mechanisms were dislocation pile-up and tangled dislocations interacting with clustered carbides. However, at elevated temperatures up to 816 °C, γ' precipitates served as major obstacles to the dislocation network.

The production method—casting or additive manufacturing—affects Haynes 282's microstructure and, consequently, its creep properties. Additively manufactured Haynes 282 often exhibits higher yield and tensile strengths compared to cast forms, attributable to finer microstructures and differing grain and precipitate orientations[200].

As for its tensile properties, Kruger[198] pointed out the benefits of the first step of aging on the ductility at high-temperature, but it has been offset by higher strengths of general yields in the aged conditions of the single-step. On the basis of the promising result, the aging treatment of single step has been pursued for Code Case development of ASME. Pike[204] mentioned that alloy of Haynes 282 features exceptional creep strength in the range of temperatures from 1200 to 1700°F. In spite of its exceptional fabricability for 282 alloy, it has compared well to alloys which are less fabricable designed for high creep strength. At temperatures of 1500-1700°F, 282 alloy features

creep strengths which have been equivalent to that of R-41 alloy. Boehlert[205] compared the effects of thermomechanical processing (TMP) on the microstructure, creep, and fatigue properties of Haynes 282 and Haynes 230, and demonstrated that Haynes 282 exhibits superior creep resistance. By calculating the creep exponent, it was found that at a temperature of 1033 K, the n-value is 6.9 (baseline) and 6.1(TMP), suggesting dislocation creep as the dominant deformation mechanism. Santella et al.[206] studied the creep properties of aged wrought Haynes 282 using the L-M and Wilshire Equations. The results showed that the L-M expression provided better predictions of creep rupture data compared to the Wilshire Equation, but the Wilshire Equation was more conservative. They also noted that since smaller grain sizes generally increase tensile strength but decrease diffusion-controlled creep resistance, an appropriate modification should be made to the direct proportionality between creep rupture time($t_f$) and ultimate tensile strength ($\sigma_{TS}$) in the Wilshire Equation.

The use of Direct Metal Laser Sintering (DMLS) has been shown to produce Haynes 282 with superior mechanical properties compared to traditional casting. The finer microstructure and controlled orientation of grains and precipitates in DMLS samples contribute to enhanced yield strength and tensile strength, which are advantageous for creep resistance[200].

Although Santella[206] has fitted Haynes 282 using the Wilshire Equation and observed the influence of grain size on activation energy, no study has yet investigated the relationship between dislocation motion and activation energy in this alloy. This study will utilise Santella's experimental data to perform a detailed analysis of the microstructure in crept Haynes 282.

## 2.6 Cyclic Creep

In many high-temperature applications, alloyed components are subjected simultaneously to static and cyclic stresses. The resulting deformation differs from that observed under pure creep (static loading) or pure fatigue (cyclic loading), instead reflecting a complex interaction of both mechanisms. For example, during service, turbine blades in aircraft engines undergo rapid start-up, steady-state operation, and emergency shutdowns, reaching temperatures as high as 1100 °C. During these phases,

blades are exposed to varying aerodynamic loads and fluctuating centrifugal forces, leading to alternating stress and fatigue damage, while also experiencing average stress (or strain) and associated creep damage[207]. Similar creep-fatigue interactions occur in other critical systems such as automotive exhaust components and power plant equipment. Therefore, understanding the deformation and fracture behaviour of alloys under combined creep-fatigue loading is vital for improving the reliability and service life of high-temperature components.

Cyclic creep is one of the forms of creep-fatigue interaction and involves the gradual accumulation of mean strain during cyclic plastic deformation under cyclic stress and thermal conditions. Cyclic creep can induce significant microstructural evolution, including dislocation annihilation, rearrangement of dislocations, and the buildup of inelastic strain. These changes often result in cyclic softening, a phenomenon where a material's resistance to deformation progressively decreases under cyclic loading. The interaction of creep-fatigue can notably reduce serving life, as seen in tempered martensite-ferritic steels like P92[208]. Under stress-controlled cyclic loading, dislocation creep dominates. Conversely, in strain-controlled conditions, stress relaxation facilitates diffusional flow, significantly influencing creep behaviour. During unloading, anelastic recovery slows down strain accumulation. Dislocation motion and back stress govern this recovery, which varies with unloading rates and affects both elastic and plastic strain components.

Cyclic creep behaviour can be influenced by different factors, including experimental temperature, applied stress, hold time, cyclic frequency, load waveform and many other factors that directly affect the cyclic creep behaviour of materials[209], [210], [211]. The amplitude and frequency of stress and thermal cycles significantly influence cyclic creep. Longer hold times and higher stress changes can lead to increased creep deformation and longer rupture times. The inherent properties of the material, such as its microstructure and composition, play a crucial role in cyclic creep as well. For instance, the tempered martensite structure in Gr. 91 steel, strengthened by carbides, shows specific responses to cyclic loading[212]. To describe cyclic creep behaviour, several models have been developed. The equivalent cyclic creep model incorporates stress control and strain-hardening indices to capture cyclic accumulation and hardening characteristics[213]. Additionally, the unified creep-fatigue equation offers

a comprehensive framework for predicting material response under combined creep and fatigue conditions[214].

316 stainless steel is extensively used in industries where materials are exposed to cyclic thermal and mechanical loads, making cyclic creep a significant factor in determining component reliability and safety. Understanding cyclic creep behaviour is essential for developing mitigation strategies, including optimizing material composition and processing techniques. Experimental studies have been central to investigating the cyclic creep behaviour of 316 stainless steel, often involving cyclic stress-induced creep tests where the material is subjected to controlled stress cycles to assess deformation patterns. Key findings indicate that cyclic loading parameters, such as stress amplitude and frequency, substantially affect both the creep rate and failure time[215]. Morris et al.[216] showed that the cyclic creep of 316 stainless steel is affected by the cycling frequency, and the transition from accelerated cyclic creep to decelerated cyclic creep occurs at high frequencies, whereas the intergranular cracking damage is independent of the frequency. An increase in average stress within the range of 550 °C to 650 °C causes a shift in the cyclic creep fracture mode of 316 stainless steel—from fatigue-dominated to creep-dominated damage. The threshold average stress at which this transition occurs is strongly influenced by the experimental temperature[217], [218]. Transmission electron microscopy observations on 316 stainless steels revealed that the dislocation grouping pattern evolved from low-energy dislocation lines to high-energy dislocation tangles and dislocation cells during cyclic creep[219]. At a certain maximum applied stress, the higher the average stress the lower its cyclic creep rate, which is directly related to the increase of dislocation dipole walls within the grain[220].

Conventional cyclic creep testing typically involves either maintaining a constant temperature while varying the stress or holding the stress constant while adjusting the temperature. However, in practical service conditions, both temperature and stress may change simultaneously. Therefore, it becomes important to determine how these combined changes affect the position on the creep curve, enabling further analysis and understanding of material behaviour. A more advanced cyclic method involves adjusting both temperature and stress simultaneously while keeping the creep rupture life constant. This approach is referred to as the life-fraction hardening method, and it has been successfully applied to alloys such as Waspaloy[221].

Compared to conventional creep tests, cyclic creep testing enables a more efficient evaluation of material behaviour. Numerical simulations further enhance these studies by providing detailed insights into cyclic creep mechanisms across various scales. For example, crystal plasticity modelling helps clarify the influence of prior cyclic plasticity on subsequent creep deformation[222], while finite element analysis (FEA) is used to simulate cyclic behaviour, assisting in fatigue life prediction and material design[223].

## 2.7 Summary

316 stainless steels, an austenitic alloy, demonstrates notable creep resistance. Its face-centred cubic (FCC) crystal structure provides a high number of slip systems, imparting exceptional toughness and deformation capacity at elevated temperatures. Furthermore, the stability of the austenitic phase, which does not undergo transformation at high temperatures, ensures structural integrity. Grain boundaries act as barriers to creep deformation, further enhancing the material's high-temperature performance.

IN713C and Haynes 282 are nickel-based high-temperature alloys whose creep deformation is influenced by factors such as stress, temperature, time, and the material's microstructure and composition. The $\gamma'$ precipitate phase plays a critical role in improving the creep resistance of these alloys by pinning dislocations and inhibiting their movement. However, differences in $\gamma'$ content, arising from distinct compositional designs and application requirements, result in varying creep properties between the two alloys.

Long-term exposure to high temperatures can alter the microstructure of these materials, affecting their creep resistance. For example: the $\gamma'$ phase may coarsen or dissolve, facilitating dislocation movement and increasing the creep rate. Alternatively, the formation of a huge amount of new dislocations which are then entangled, and subsequent dislocation cells or forest hardening can impede dislocation movement, improving creep resistance.

Understanding the creep process in these materials requires advanced analytical techniques and experimental methods. A key parameter in creep studies is the

activation energy, which varies with the governing creep mechanism. Studies have shown that the activation energy for a given material can shift significantly under different experimental conditions. These shifts are attributed to transitions in creep mechanisms driven by changes in stress, temperature, or loading time.

To improve the accuracy of creep life prediction models, researchers have adopted regional segmentation techniques. These methods allow models to better align with experimental observations by accounting for transitions between mechanisms. However, direct microstructural evidence linking activation energy variations to specific creep mechanisms remains limited.

This study examines the creep properties of Inconel 713C, Haynes 282, and 316 stainless steel, with a focus on their microstructures and activation energies calculated using the Wilshire Equation. The goal is to validate the relationship between creep mechanisms and activation energy, providing deeper insights into their high-temperature deformation behaviour.

# 3. Experimental Procedure

## 3.1 General Introduction

The experimental programme in this study comprises a series of mechanical tests and microstructural characterisations aimed at understanding the creep behaviour of selected high-temperature alloys. The materials—316 stainless steel, Haynes 282, and Inconel 713C—were chosen for their widespread use in high-temperature environments such as power plants and aerospace systems. These alloys exhibit distinct microstructural and compositional characteristics, from the precipitate-free austenitic structure of 316 stainless steel to the $\gamma'$-strengthened microstructures of Haynes 282 and IN713C. This selection enables a comprehensive investigation of how microstructural features influence creep mechanisms, particularly the relationships between dislocation motion, $\gamma'$ content, and activation energy.

The mechanical testing programme includes tensile testing to determine fundamental mechanical properties, alongside constant load and cyclic creep tests to evaluate time-dependent deformation under different loading conditions. These tests provide essential data on the creep resistance of the selected materials.

Following mechanical testing, the study is divided into two sections. The first focuses on microstructural characterisation, where specimens with different microstructures are examined using optical microscopy (OM), scanning electron microscopy (SEM), and transmission electron microscopy (TEM). These techniques facilitate detailed analysis of grain structures, carbide distributions, twin boundaries, and deformation mechanisms, offering crucial insights into the role of microstructural evolution in creep resistance.

The second section involves data analysis, incorporating both experimental results from this project and datasets from literature and the National Institute for Materials Science (NIMS) database. A key objective is to assess the applicability of creep prediction models, with particular emphasis on the Wilshire Equations. By fitting experimental data to Wilshire Equations, the study evaluates their effectiveness in

describing the creep behaviour of different alloys. Ultimately, by correlating the activation energy ($Q_c^*$) with microstructural and mechanical observations, this research aims to rationalise the creep mechanisms in these alloys. This approach enhances the fundamental understanding of creep deformation, improves long-term extrapolation accuracy, and aids in predicting the behaviour of new alloys under elevated temperature conditions.

## 3.2 Selected Materials

### 3.2.1 316 Stainless Steel

**316 stainless steel (SS316)** was selected due to its widespread industrial use, especially in power plants, where high temperature and oxidative environments are prevalent. It is known for its good creep resistance and corrosion properties, making it an ideal candidate for comparison with more advanced alloys. Additionally, it has been extensively studied in the existing literature, providing a lot of data for comparison. Moreover, SS316 is essentially free of significant precipitates, but commonly characterised by relatively low stacking fault energy (SFE), which substantially affects the dislocation motion [224]. This makes it an ideal reference material for examining the role of γ' precipitates in the other two alloys.

The data for 316 stainless steel were obtained from the National Institute for Materials Science (NIMS) creep data sheets[6], which provide detailed mechanical and creep property measurements for multiple product forms. These include six batches of bar [225], two batches of plate [226], and nine batches of tube [227], tested across the temperature range 873–1123 K (600–850 °C). The bar specimens (ADA–ADF) were hot rolled and then subjected to different heat treatments, including (i) 2 h at 1353 K (1080 °C), (ii) 70 min at 1373 K (1100 °C), or (iii) 110 min at 1333 K (1060 °C), all followed by water quenching. The plate specimens (AaA–AaB) were hot rolled and held at 1323 K (1050 °C) for either 40 or 80 minutes before water quenching. The tube specimens (AAA–AAN) were processed in three variants: (a) rotary pierced and cold drawn, followed by water quenching from 1373 K (1100 °C); (b) hot extruded and cold drawn, followed by water quenching from 1403 K (1130 °C); and (c) hot extruded and cold drawn, followed by solution treatment.

73

NIMS data sets report a wide range of properties, including 0.2% proof stresses (PS), ultimate tensile strengths (UTS), minimum creep rates ($\dot{\varepsilon}_m$), rupture times ($t_f$) and etc. In the present study, the datasheet values are primarily used as a contextual baseline, and no distinction was made between individual batches; instead, the data were grouped according to product form (tube, bar, or plate). Among these, the bar and plate datasets were analysed in detail to evaluate creep behaviour using the Wilshire Equations, while the tube data were only processed as supplementary reference points. This grouping strategy reflects the focus of the study on comparing product forms rather than processing variations within each form. More importantly, the Wilshire Equations are applied to analyse and compare the different forms of 316, thereby demonstrating the reliability of the Wilshire approach across material variants.

316 specimens used for creep tests in this study were originally prepared as part of a previous research study under the supervision of Prof. Mark Whittaker. Their availability provided a valuable foundation for the experimental work conducted in this research.



**Figure 3.1 SS316 test specimens in SS10259 type**

## 3.2.2  Haynes 282

Two nickel-based superalloys, Haynes 282 and Inconel 713C were chosen due to their differing levels of γ' precipitates, which play a critical role in enhancing creep resistance. Haynes 282 features a moderate volume fraction of γ' precipitates, optimised for long-term thermal stability, while IN713C has a significantly higher γ' content. The variation in precipitate content offers an opportunity to systematically investigate how γ' precipitates interact with dislocations during creep deformation and influence the activation energy of the process.

The wrought Haynes 282 was supplied by Haynes International and was sectioned into smaller pieces with the help of the Swansea University workshop and remanufactured into subsequent specimens for further studies.

**Figure 3.2 The wrought Haynes 282 material**

### 3.2.3 Inconel 713C

The Inconel 713C samples used in this study were produced via investment casting at Cummins Turbo Technologies at Huddersfield, UK. The cylindrical bars consist of three batches, each with distinct microstructures: fully equiaxed, fully columnar, and transition from equiaxed to columnar, as illustrated in the accompanying Figure 3.3. While columnar and equiaxed are distinct microstructures, the term "transition" refers to the gradual morphological change between equiaxed and columnar grains rather than a discrete microstructure.

This design was chosen to reflect the microstructural variations observed in actual turbine blades. Specifically, equiaxed grains are typically found near the blade tip, columnar grains dominate toward the root, and transitional grains form in the regions between these two zones. These variations are inherent to the casting process and play a crucial role in defining the mechanical properties and creep behaviour of the alloy in service.
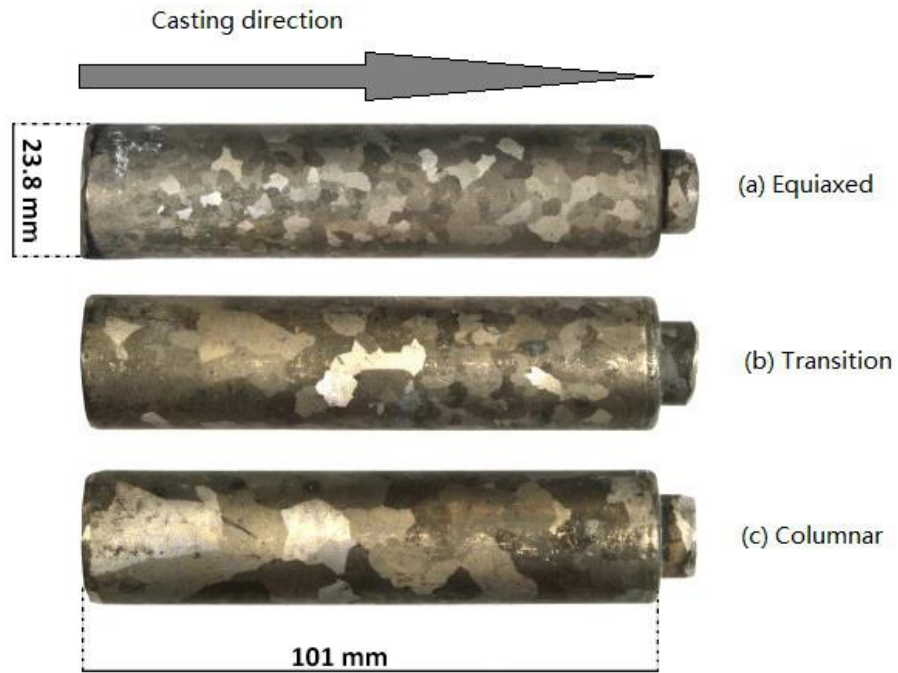
**Figure 3.3 Three batches of IN713C specimens with different microstructural conditions (a) equiaxed, (b) transition, (c) columnar.**

To better study how the grains change, the specimen was cut along the casting direction, as shown in the Figure 3.4.
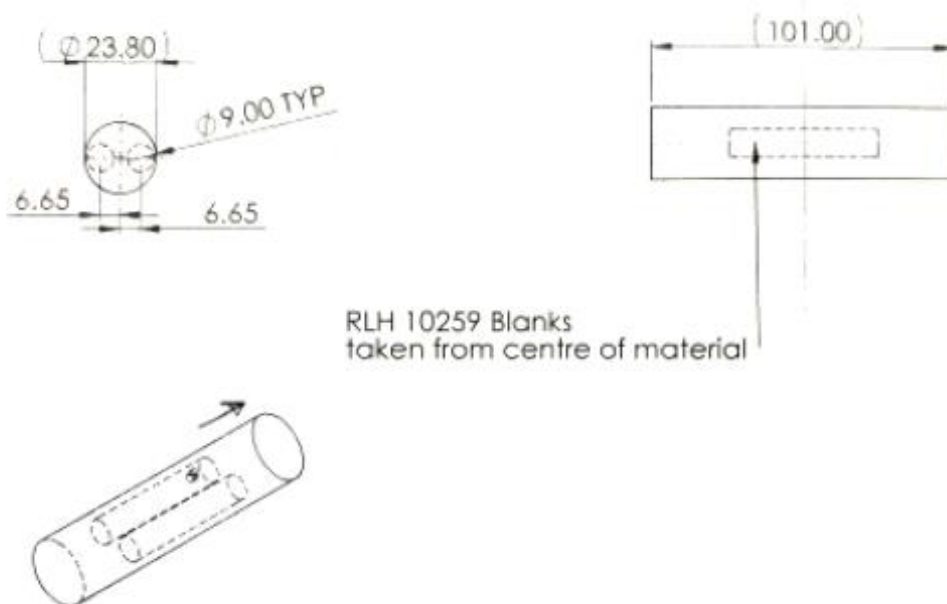


**Figure 3.4 The cutting direction of the IN713C specimens, aligned with the casting direction, indicating the orientation used during creep testing.**

The differences between the equiaxed and columnar microstructures are clearly illustrated in Figure 3.5 under optical microscopy. Diameters of the equiaxed grains, measured using ImageJ software, range from approximately 0.6 mm to 5 mm. The grain sizes of columnar are considerably larger, ranging from 3 mm to 9.6 mm, as shown in Table 3-1.
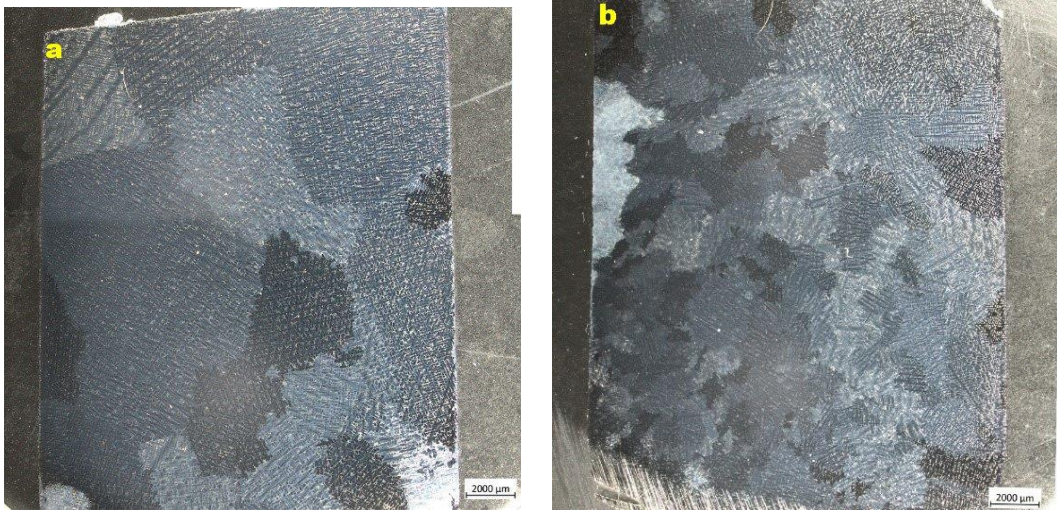


**Figure 3.5 Macrostructure of IN713C with (a) columnar and (b)equiaxed structure.**

**Table 3-1 The summary of the measurements of columnar IN713C**

| IN713C | Mean | SD | Min | Max |
|---|---|---|---|---|
| Equiaxed Area /$\mu m^2$ | 6545.5 | 4784.9 | 620.7 | 21791.1 |
| Equiaxed Length /$\mu m$ | 1577.9 | 963.4 | 594.6 | 4920.4 |
| Columnar Area /$\mu m^2$ | 34489.2 | 14272.5 | 17011.7 | 54002.0 |
| Columnar Length /$\mu m$ | 6114.2 | 2540.8 | 3021.7 | 9609.1 |

## 3.3  Mechanical testing

### 3.3.1  Tensile testing

Four tensile tests were conducted to determine the mechanical properties of the tested materials, specifically Haynes 282 at 650°C and 750°C, as well as IN713C equiaxed specimens at 650°C and 750°C. All tests were performed in a laboratory air

environment, with a soaking time of 30 minutes to ensure thermal equilibrium before testing. The tests were carried out under displacement control at a strain rate of 0.005 mm/mm/min. These conditions were selected to ensure consistency across all tests and to align with standard tensile testing procedures.

## 3.3.2 Creep testing

In most conventional creep experiments, including those performed in this study, a constant-load approach is employed. In such tests, the applied load remains fixed; however, as creep deformation proceeds, the reduction in specimen cross-sectional area results in a progressive increase in the true stress. Thus, while test data are traditionally reported using the initial nominal stress, the actual stress borne by the specimen is not strictly constant during the test. This effect becomes increasingly significant in materials that exhibit large creep ductility, where constant-load tests tend to accelerate deformation and shorten rupture life compared to tests under true constant-stress conditions.

By contrast, constant-stress creep testing incorporates mechanical systems such as profiled cams, which continuously adjust the applied force to compensate for specimen elongation and maintain a constant true stress. Although this methodology provides a more rigorous measure of creep response, it is technically more complex and remains less widely implemented. Accordingly, the vast majority of published datasets, including those from the NIMS database, and all experimental results generated in this project, are based on constant-load testing. This ensures internal consistency across the present work and with the broader literature. Moreover, in cases where total creep strains to failure are small, the differences between constant-load and constant-stress tests are negligible, further justifying the use of the constant-load approach in this study.

### 3.3.2.1 Creep testing by SMaRT

The creep testing of stainless steel 316 and parts of Inconel 713C was performed using a constant load creep machine at Swansea Materials Research & Testing (SMaRT) Ltd. The testing materials were cylindrical creep specimens with a gauge length of approximately 20 mm and a diameter of 4 mm, designated as SS10259 (Figure 3.6). These specimens were machined by the Institute of Structural Materials (ISM) Workshop.
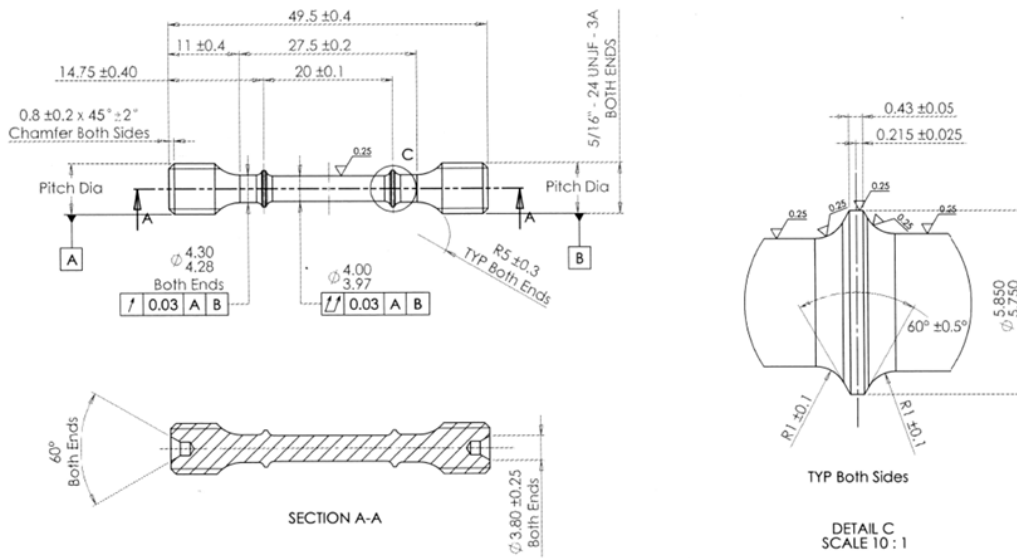
**ALL DIMENSIONS AND TOLERANCES ARE IN mm, EXCEPT WHERE STATED.**

**Figure 3.6 Geometry of SS10259 specimens.**

The diameter of each specimen was measured accurately using a shadowgraph technique with the HB400 optical comparator. The specimens were cleaned with alcohol wipe to remove any contaminants, such as grease or debris, to avoid affecting the light projection. The specimen was placed securely on the comparator's adjustable stage, where the key regions, such as the gauge length, diameter, and transition zones, were accessible for measurement. Then turned on the light source and adjusted its intensity and moved the stage to align the specimen perpendicular to the light source so that the full shadow of its profile is projected onto the viewing screen. A magnification of 10X was selected to clearly see and measure features. Each specimen's dimensions were measured three times from different places of the specimen to take the minimum value, and pip-pip length (gauge length) were measured twice from different directions to find the average. The maximum coaxial variation was also confirmed to be less than the limit by measuring the geometric centre of the thread with the central axis of the specimen to ensure that the threads are accurately positioned relative to the main axis.

All creep tests in this study were conducted using lever-arm testing rigs. Before setting up the constant load creep test, it was confirmed that machine frame, extensometry, temperature logging system and loading masses has been calibrated, and the position of the fulcrum knife edges was moved into the appropriate place so that the lever can

freely move. The applied load was measured using load cells calibrated to BS EN ISO 7500-2, class 1, which corresponds to an accuracy of ±1%. Strain was measured via extensometry calibrated to BS EN ISO 9513, class 1, also providing ±1% accuracy. Class 1 certification therefore guarantees that both load and strain measurements are accurate to within 1% of the true value. The temperature at the machine was recorded as room temperature by a digital room thermometer (DRT). Temperature inside the machine was controlled using thermocouples in direct contact with the specimen gauge section, with fluctuations limited to ±2 °C.

First of all, the test specimens were installed into the creep machine. A high-temperature anti-seize adhesive was applied to the specimens and collet threads to prevent thread seizing during high-temperature tests. The test specimen was then inserted into the top collet of the testing machine with care to ensure proper alignment. A small initial mass, typically between 10 g and 30 g, was added to the load pan to allow the testing machine's lever to find its balanced position, ensuring stability in the load train setup. The bottom rod was carefully attached to the lower thread of the specimen. Using the load train capstan, the bottom ram or universal joint assembly was adjusted to meet the rod, completing the connection of the load train. This step was crucial for maintaining an accurate and stable load path during testing. All adjustments were verified to ensure the system's alignment, minimising potential sources of error in the application of the test load. The auto level feature was then turned on. To maintain the load train in self alignment, the specified 20N mass was placed onto the load pan.

Following this, extensometry was added to the test setup. The threaded pins were used to secure the top extensometer cage piece to the specimen's higher crest and the bottom section to the lower crest. To make sure the cage is firmly fastened to the specimen, a single loop of wire was wrapped over the crests of each cage component. It was ensured that the extensometer cages, which contained linear variable differential transformers (LVDT), allowed sufficient clearance for specimen elongation.

The test temperature was controlled and measured using type R thermocouples connected to a Dirlik temperature logger. The type R thermocouples were connected to the top and bottom of the gauge section of the test specimens separately, and the control thermocouple was assembled onto the lower grip after filling the superwool

into the extensometer cages, so that the thermocouple bead is around the same height as the specimen gauge section's centre.

The furnace was lowered to the centre of the hot zone and insulated with high-temperature insulation materials.

The cold modulus measurement was conducted to verify the proper installation and operation of the extensometer system at room temperature. An initial mass was carefully selected and placed on the load pan, ensuring that the applied stress on the specimen ranged between 2% and 12% of the target test stress. The extension data from the LVDT system, transmitted as voltage signals, were converted into corresponding displacement values by the control system. To ensure accuracy, four additional incremental masses were applied sequentially. After each increment, the extension values were recorded, and the calculated modulus was monitored. The average modulus values from the left and right sides of the extensometer arms were compared with the expected modulus. The process was repeated until the difference between the measured average modulus and the expected value was within 10%, confirming the system's proper alignment and calibration. This step ensured that the extensometer would provide reliable measurements during the high-temperature creep test.

Once the specimen was heated to the target temperature and soaked for an hour, the hot modulus was similarly measured under the same load as cold modulus.

Following the hot modulus check, the required load was applied while maintaining a constant temperature to simulate high-temperature deformation conditions. Specimen elongation was recorded using the LVDT system, and time and temperature data were logged continuously. The experiment lasted for a specified duration to capture sufficient data on creep deformation.

### 3.3.2.2   Creep testing by Westmoreland

The creep experiments on Haynes 282 and some Inconel 713C with equiaxed microstructure were carried out by Westmoreland. The specimens were machined into a custom plate geometry, as shown in Figure 3.7. Those specimens were originally prepared as part of a previous PhD project under the supervision of Prof. Soran Birosca.

Testing was conducted at various temperatures and stress conditions to assess their relative creep behaviours under simulated service conditions.
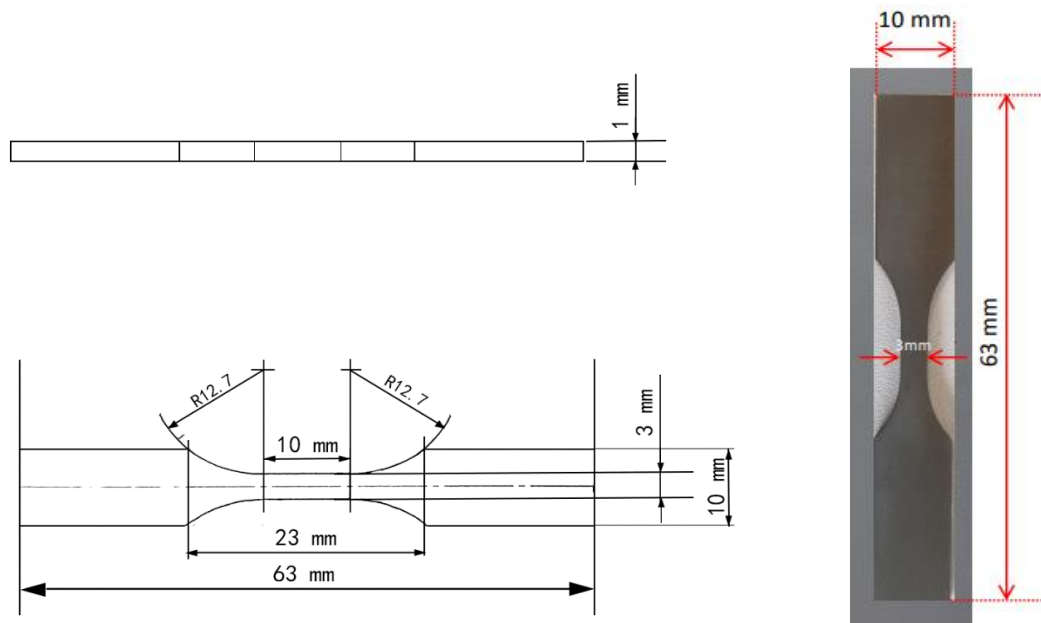


**Figure 3.7 The specimen and sample dimension of Haynes 282 and Inconel 713 used for creep tests at Westmoreland.**

### 3.3.2.3   Creep testing by The Open University

Inconel 713C samples with columnar and transition microstructures were tested using a constant load creep machine equipped with a digital image correlation (DIC) device at The Open University.

The creep specimen used for testing is a plate-shaped geometry with threaded ends at both sides, which are designed to facilitate easy assembly into the creep testing machine. The gauge region is rectangular, providing a consistent cross-sectional area for strain measurement. Refer to Figure 3.9 for the detailed geometry of the specimen.
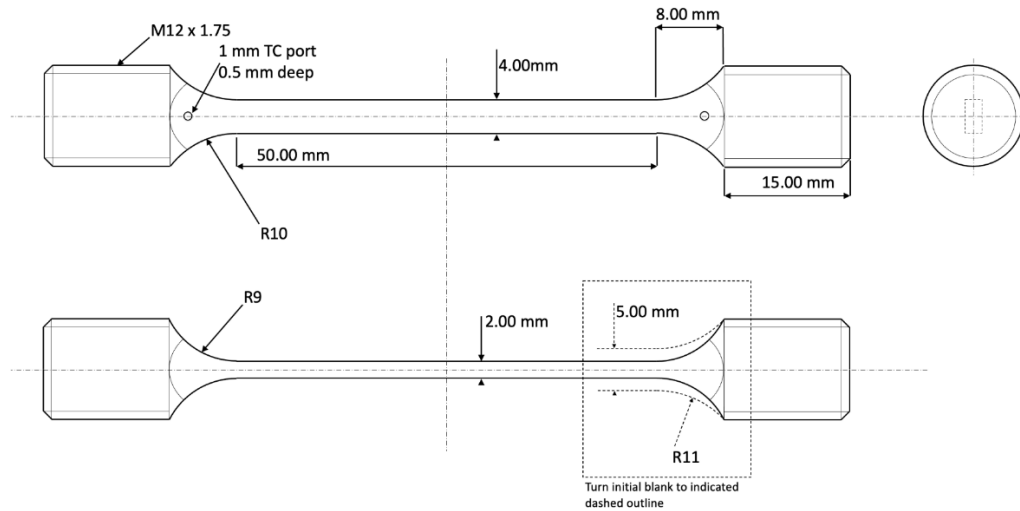
**Figure 3.8 Technical drawing of the IN713C creep specimen used at The Open University, showing key dimensions.**



**Figure 3.9 Image of the specimen surface prepared with a speckle pattern for DIC analysis during creep testing.**

The specimens were polished to remove surface imperfections and ensure a uniform reflective finish. A high-contrast speckle pattern, as shown is Figure 3.9, was then applied by using matte white paint as a base layer, followed by fine black spray paint. This pattern provided randomised features necessary for the DIC software to accurately track displacement and strain.

The DIC camera system comprised a Nikon D810 digital single-lens reflex (DSLR) colour camera with a complementary metal-oxide-semiconductor (CMOS) sensor. It was positioned 250 mm in front of the specimen and perpendicular to the gauge length within the test setup. High-temperature creep testing required the camera to be placed

at a safe distance from the furnace while maintaining a clear view of the specimen. To achieve this, heat-resistant windows, approximately 20 mm wide and 40 mm high, were used to protect the camera from thermal effects. For magnification, a Nikon Nikkor 200 mm Micro f/4 IF-ED macro lens was mounted on a Novoflex Ballpro bellows set at a 100 mm extension. This setup provided the required magnification and focus for detailed surface analysis. Illumination was provided by a 1/4-inch diameter fibre optic light, optically coupled to the camera's built-in flash. The flash was manually set to its maximum illumination setting to ensure consistent and adequate lighting for capturing high-quality DIC images.

Specimen installation was largely unchanged from the procedures before. However, instead of using the Creep Load Pan Calculator (CAT) before applying weights, a load cell was connected to the testing machine and a data acquisition system to ensure precise load application. This step was essential for maintaining constant load conditions, a critical requirement for creep experiments.

The DIC system was calibrated before the test to ensure accurate strain measurements by capturing test images to confirm the clarity and visibility of the speckle pattern. Once assembly was complete, the creep test was initiated by applying a constant load to the specimen while maintaining the target temperature. The DIC system continuously recorded high-resolution images of the specimen surface throughout the test. These images were analysed using the DaVis software to calculate strain distributions across the gauge section.

While the LVDT measured the overall displacement of the specimen, producing a single creep curve representing its average behaviour, the DIC system provided a more detailed analysis. It generated real-time strain data, capturing localised deformation and strain concentrations within the specimen. Since deformation under creep conditions is often non-uniform, with the specimen's centre typically deforming faster than the edges, the DIC system produced multiple creep curves from different regions of the same specimen. This capability facilitated a nuanced understanding of localised strain behaviour and heterogeneity, offering deeper insights into creep mechanisms.

### 3.3.2.4 Summary of creep test conditions

Creep tests were conducted on different materials and geometries under varying conditions to investigate the material deformation behaviour. The tests covered a range

of temperatures, stresses, and microstructure types, including columnar, equiaxed, and transition microstructures for IN713C. Digital image correlation (DIC) was used for strain field analysis in select tests, or extensometers with linear variable differential transformers (LVDT) were utilised for overall displacement measurements.

Specimens with differing geometries were employed to accommodate the testing capabilities of various experimental facilities, although these morphological differences may influence the testing results. Flat specimens, such as plates, may introduce slight variations in stress distribution—particularly at edges or corners—which can result in localised creep deformation. In contrast, RH10259 specimens, due to their cylindrical shape, tend to exhibit a more uniform stress distribution under both tensile and compressive loading.

Although the shape differences between plate and RH10259 specimens could potentially affect stress distribution and, consequently, creep behaviour, it is important to note that the creep tests did not extend to the final fracture stage. Moreover, since the analysis focused on the centrally stressed region of the specimens, the influence of geometric effects on the overall conclusions regarding creep response is considered minimal.

Table 3-2 below summarises the specific creep test conditions used:

**Table 3-2 The summary of creep tests**

| Specimens | Temperature (°C/K) | Stress (MPa) | Specimen Type | Test Setup |
|---|---|---|---|---|
| SS316 | 600/873 | 125 | RH10259 | LVDT |
| SS316 | 600/873 | 175 | RH10259 | LVDT |
| SS316 | 600/873 | 225 | RH10259 | LVDT |
| SS316 | 600/873 | 275 | RH10259 | LVDT |
| SS316 | 700/973 | 100 | RH10259 | LVDT |
| SS316 | 700/973 | 125 | RH10259 | LVDT |
| SS316 | 700/973 | 175 | RH10259 | LVDT |
| SS316 | 700/973 | 225 | RH10259 | LVDT |
| Haynes 282 | 650/923 | 500 | Plate | LVDT |
| Haynes 282 | 650/923 | 800 | Plate | LVDT |
| IN713C (E) | 650/923 | 500 | Plate | LVDT |
| IN713C (E) | 650/923 | 650 | RH10259 | LVDT |
| IN713C (E) | 650/923 | 700 | RH10259 | LVDT |
| IN713C (E) | 650/923 | 750 | RH10259 | LVDT |
| IN713C (E) | 650/923 | 800 | Plate | LVDT |
| IN713C (E) | 750/1023 | 500 | Plate | LVDT |
| IN713C (E) | 750/1023 | 800 | Plate | LVDT |
| IN713C (C) | 650/923 | 500 | Plate | DIC |
| IN713C (C) | 650/923 | 650 | Plate | DIC |
| IN713C (T) | 650/923 | 650 | Plate | DIC |
| IN713C (T) | 650/923 | 700 | RH10259 | LVDT |
| IN713C (T) | 650/923 | 750 | RH10259 | LVDT |
| IN713C (T) | 650/923 | 800 | Plate | DIC |

### 3.3.3 Cyclic creep testing

Cyclic creep testing was conducted exclusively on 316 stainless steel with the assistance of technicians from SMaRT at Swansea University. This test can be regarded as a special case of the previously performed constant load creep tests, with the primary distinction being that the test conditions were varied while the experiment was

still in progress. In other words, the test commenced under a specified stress level at a given temperature, and after a predetermined period, the stress and/or temperature were adjusted, allowing the specimen to continue creeping under the new conditions.

Cylindrical specimens RH10259 were used for the cyclic creep tests. The initial setup followed the same procedure as the previous constant load creep tests. The experiment commenced under controlled conditions of 600°C and 334 MPa. After 22 hours, the applied load was reduced to 165 MPa, followed by an increase in furnace temperature to 700°C, soaking for an hour.

The sequence of these adjustments was carefully designed to prevent premature fracture. If the temperature had been raised to $T_2$ (700°C) before unloading to $\sigma_2$ (165 MPa), the specimen could have failed due to $\sigma_1$ (334 MPa) potentially exceeding the ultimate tensile strength (UTS) at $T_2$.

After another 22 hours, the furnace temperature was lowered back to $T_1$ (600°C), and the applied load was restored to $\sigma_1$ afterwards. This cycle was repeated until specimen failure, ensuring that stress adjustments were performed in a controlled manner to avoid exceeding the UTS at elevated temperatures.

Additionally, a second set of cyclic creep tests was conducted under the same conditions but initiated at 700°C and 165 MPa. To provide a comparative basis, two additional isothermal creep tests were performed under 600°C, 334 MPa, and 700°C, 165 MPa, respectively.

## 3.4 Metallographic Preparation and Microstructural Observation

The specimens were sectioned into smaller pieces using a Brillant 220 precision cut-off machine. Typically, the two ends of the tested specimens were removed, preserving the central region for analysis. Cylindrical specimens were further split along the testing direction, ensuring that the most valuable experimental cross-section was retained for examination.

The sectioned samples were then mounted in black conductive bakelite resin using a hot mounting press (OPAL 410) to facilitate handling, subsequent processing, and microscopic analysis.
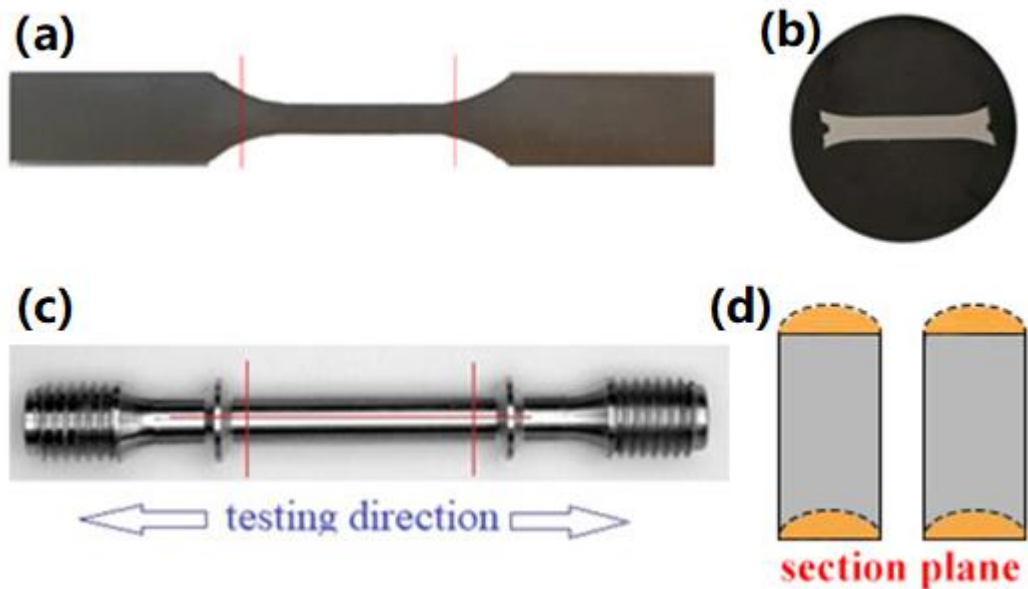


**Figure 3.10 (a) Macro image of the flat specimen, with red lines indicating the selected sectioning plane (b) Mounted cross-section of the specimen embedded in resin for metallographic preparation (c) Macro image of the cylindrical specimen (d) Schematic showing the cross-sectional plane used for microstructural characterisation.**

To prepare the surface for analysis, the initial grinding was carried out on the grinding machine using 320 grit sandpaper at 300 rpm to remove residual phenolic and markings from the surface. After rinsing off the abrasive particles, the surface was then finely ground with successively finer grit papers (#600, #1200 and #2400) to obtain a scratch-free surface. The surface was cleaned and sterilized with ethanol and then, polished successively using 6μm, 3μm and 1μm diamond lubricant for 10-15 minutes under 20N, with a Saphir 520 automatic polishing machine. Samples for EBSD analysis require a clean surface free of surface stress. Thus, the surface was finally polished for 15-20 minutes under 10N by OP-A suspension.

Although sufficiently fine polishing can reveal grain boundaries and other microstructural details, etching significantly enhances the clarity of these features. The etchants used in this study were placed in the Table 3-3 below.

**Table 3-3 Etchants used in this study**

| | | |
|---|---|---|
| **Carpenter Etchant** - for SS316 | Ferric chloride (FeCl$_3$) | 8.5gm |
| | Cupric chloride (CuCl$_2$) | 2.4gm |
| | Ethanol (C$_2$H$_6$O) | 122ml |
| | Hydrochloric acid (HCl) | 122ml |
| | Nitric acid (HNO$_3$) | 6 ml |
| **Kalling' No. 2** -for nickel-based superalloy | Cupric chloride (CuCl$_2$) | 1gm |
| | Hydrochloric acid (HCl) | 20ml |
| | Ethanol (C$_2$H$_6$O) | 20ml |

To minimise the risk of over-etching, the smearing method was used during the etching process. This approach involved directly applying the etchants onto the polished surface of the specimen while holding it flat. Unlike immersion, smearing allowed real-time observation of the surface as the etching progressed. This ensured precise control over the etching duration, typically limited to seconds. Immediately after etching, the specimen was rinsed with hot water, followed by ethanol, to remove residual etchant and halt the reaction. Finally, the sample was dried to prevent further chemical interactions.

## 3.4.1  Optical Microscopy

The macrostructural analysis of the samples was conducted using a Zeiss Stemi 508 and Primotech optical microscopes. These instruments were employed to examine the general grain structure, identify key features such as grain boundaries, and provide an overview of the material's microstructural characteristics. Optical microscopy served as a foundational step in the analysis, offering insights into grain size and phase distribution prior to more detailed investigations using advanced techniques.

## 3.4.2  Scanning Electron Microscopy (SEM)

Detailed microstructural observations, including the identification of twin boundaries and precipitates, were performed using a SU3500 and JEOL 7800 scanning electron microscopes (SEM). These instruments were equipped with Energy Dispersive Spectroscopy (EDS) and Electron Backscatter Diffraction (EBSD) detectors for

comprehensive analysis. Imaging voltages typically ranged from 10 kV to 20 kV, with working distances between 5 mm and 25 mm, depending on the resolution and depth of focus required.

Further EDS and EBSD analysis were processed by AZtec, Oxford Instruments. EDS provided elemental composition maps for precipitates and carbides, while high-resolution SEM imaging was instrumental in visualising fine features such as twin boundaries. SEM's versatility in magnification and resolution made it indispensable for detailed characterisation of both grain interior features and grain boundary phenomena.

Grain size measurements and particle analyses, including the evaluation of size, shape, and distribution, were conducted using EBSD mapping. The EBSD system was integrated with commercial software to generate grain orientation maps and assess microstructural parameters. However, manual analysis was often preferred for certain features, such as precipitates, due to the following limitations of EBSD:

- Precipitates are not always easily recognisable in EBSD maps.

- The method struggles with analysing large features accurately.

- EBSD sample preparation and map acquisition are highly time-intensive.

To overcome these challenges, supplementary analyses were conducted using micrographs obtained from optical microscopy or SEM. These were analysed manually with the open-source software ImageJ, which is widely used across various scientific fields, including metallurgy, biology, and geology[228].

Figure 3.11 illustrates an example of the calculation process with ImageJ for the volume fraction of the $\gamma'$ phase in IN713C. (a) shows the acquired SEM micrograph; (b) demonstrates the threshold adjustment to retain only the $\gamma'$ phase; ultimately, only the bright white particles are included in the area fraction calculation.

Manual analysis inherently carries a degree of subjectivity. To minimise bias, multiple fields of view were analysed, and the variation between measurements was used to estimate confidence bounds. The reported results, especially the volume fraction of $\gamma'$ are therefore expressed together with a $\pm$ value corresponding to the 95% confidence interval, reflecting the uncertainty inherent in image analysis at different scales. In

addition, repeated measurements on the same images were performed to ensure consistency and mitigate this limitation. The comparison of manually measured grain sizes with EBSD-derived values showed good agreement, validating the reliability of the approach.
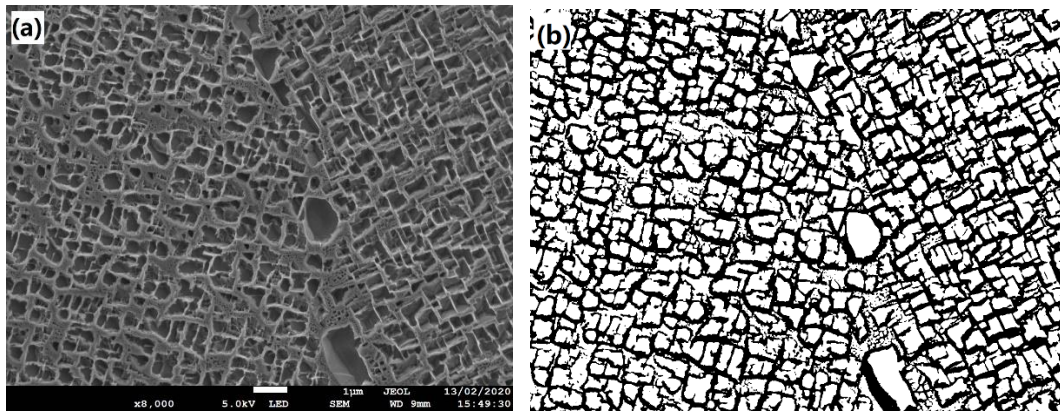


**Figure 3.11 Example of image analysis with ImageJ from a (a) SEM micrograph, and (b) threshold selection.**

## 3.4.3 Transmission Electron Microscopy (TEM)

Transmission electron microscopy (TEM) was used to investigate the deformation mechanisms, dislocation structures, and other microstructural features resulting from the creep tests.

The TEM requires a high level of sample preparation. Electrons have very little penetrating power, and transmission electron microscopy often uses high energy electron beams of several hundred kV, but still requires the sample to be ground or ionically thinned or ultra-thinly sliced to micro-nanometre scale thickness and placed on a 3mm diameter copper grid for observation.

The crept specimens were cut in the gauge region by low-speed cutter to make disc specimens of around 0.5 mm thickness. The specimens were then polished to further reduce the thickness to 0.1 mm thickness using #1200 - #4000 grit papers. It was then followed by twin-jet electro-polishing in a solution of methanol and perchloric acid (9:1 ratio) at 20V and -30°C.

The microstructural analysis results of the specimens after creep testing will be presented and discussed in the Chapter 4.

# 4. Results

As outlined in Chapter 3, this study investigates the creep behaviour of three alloys—316 stainless steel, Haynes 282, and Inconel 713C—under different test conditions, focusing on their microstructural characteristics. By analysing creep data using the Wilshire Equations, this study aims to assess variations in activation energy and their correlation with microstructural features.

This chapter presents the complete set of experimental data and its correlation with the Wilshire Equations. Creep test results for all investigated conditions are provided, along with fitted curves to evaluate the model's predictive capability. Additionally, basic microstructural observations illustrate differences in grain structure among the three materials. However, detailed TEM analysis of dislocation behaviour is beyond the scope of this chapter and will be discussed in Chapter 5, where its implications for creep mechanisms are examined.

## 4.1 Microstructural characterisation of materials

### 4.1.1 316 Stainless steel

Stainless steel 316 (SS316) was selected as a benchmark material in this study due to its widespread use in high-temperature applications such as power plant tubing and piping, where creep resistance is essential. Unlike nickel-based superalloys, SS316 contains negligible volume fractions of strengthening precipitates, and its creep behaviour is therefore governed primarily by dislocation motion and twinning. Understanding its microstructural features is important, as these directly influence deformation mechanisms. The as-received SS316 microstructure was examined to provide baseline data on grain size, morphology, and characteristic features such as twin boundaries, which will later be linked to its creep performance. The results of this characterisation are summarised below.

The microstructure comprises equiaxed austenitic grains with an average grain size of approximately 50μm, measured by ImageJ. A summary of the grain size measurements

is presented in Table 4-1, offering a comprehensive overview of the microstructural parameters.

**Table 4-1 The summary of the grain sizes measurements of SS316**

| SS316 | Mean | SD | Mini | Max |
|---|---|---|---|---|
| Area/$\mu m^2$ | 54.3 | 23.3 | 15.0 | 105.0 |
| Length/$\mu m$ | 53.4 | 23.3 | 13.9 | 103.9 |

No significant inclusions or precipitates were observed, as shown in Figure 4.1, however, twin boundaries, a notable feature of austenitic stainless steels, are evident by EBSD maps in Figure 4.1(c) and (d). These boundaries provide insight into the deformation mechanisms and contribute to the understanding of the material's mechanical behaviour.
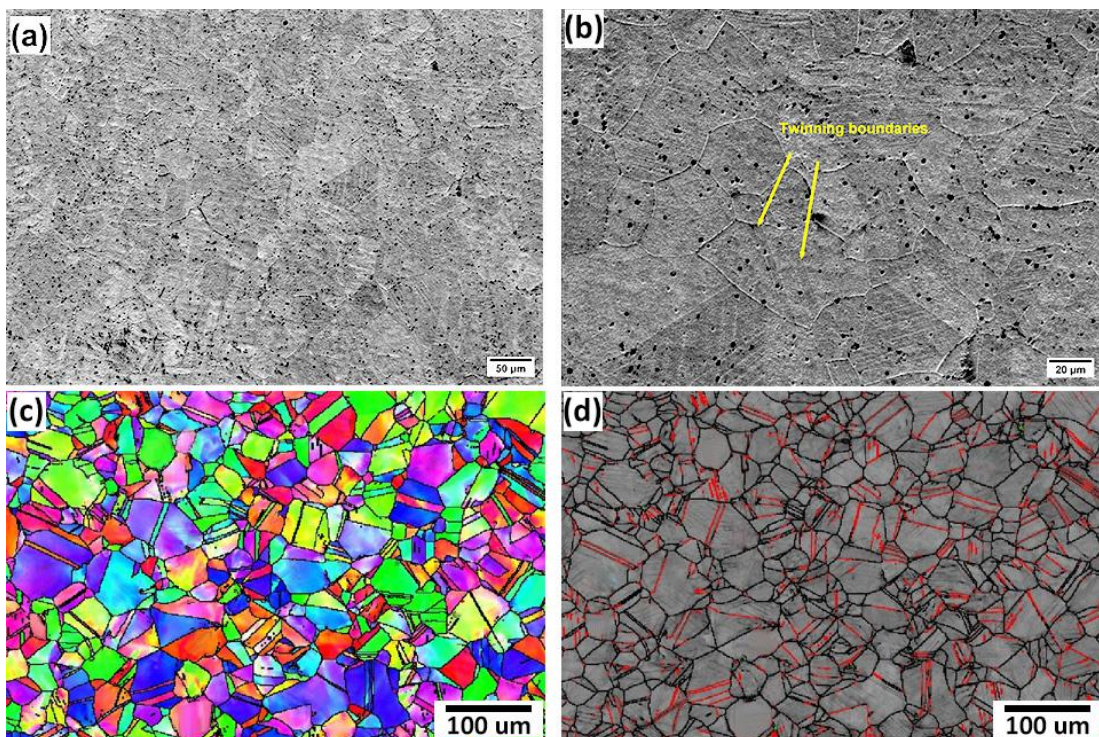


**Figure 4.1 SEM images of the austenitic grains of as-received SS316 at (a) x200 (b)x500 magnification and EBSD maps of (c) in IPF Z direction (d) twinning boundaries.**

## 4.1.2 Haynes 282

Haynes 282 exhibits a diverse and heterogeneous microstructure, characterized by a wide variation in grain sizes, ranging from very fine to very coarse. Optical microscopy, as shown in Figure 4.2, reveals this heterogeneity, with grain sizes manually measured using ImageJ. The largest grains reach approximately 300 μm, while the smallest measure around 6 μm, as summarized in Table 4-2. This variation is a result of the alloy's processing and heat treatment history, which significantly influences its mechanical properties. Larger grains are typically associated with improved ductility, whereas smaller grains contribute to higher strength[229].

**Table 4-2 The summary of the grain sizes measurements of H282**

| H282 | Mean | SD | Mini | Max |
|---|---|---|---|---|
| Area/μm$^2$ | 111.8 | 119.5 | 9.4 | 387.5 |
| Length/μm | 88.1 | 95.6 | 6.2 | 308.5 |
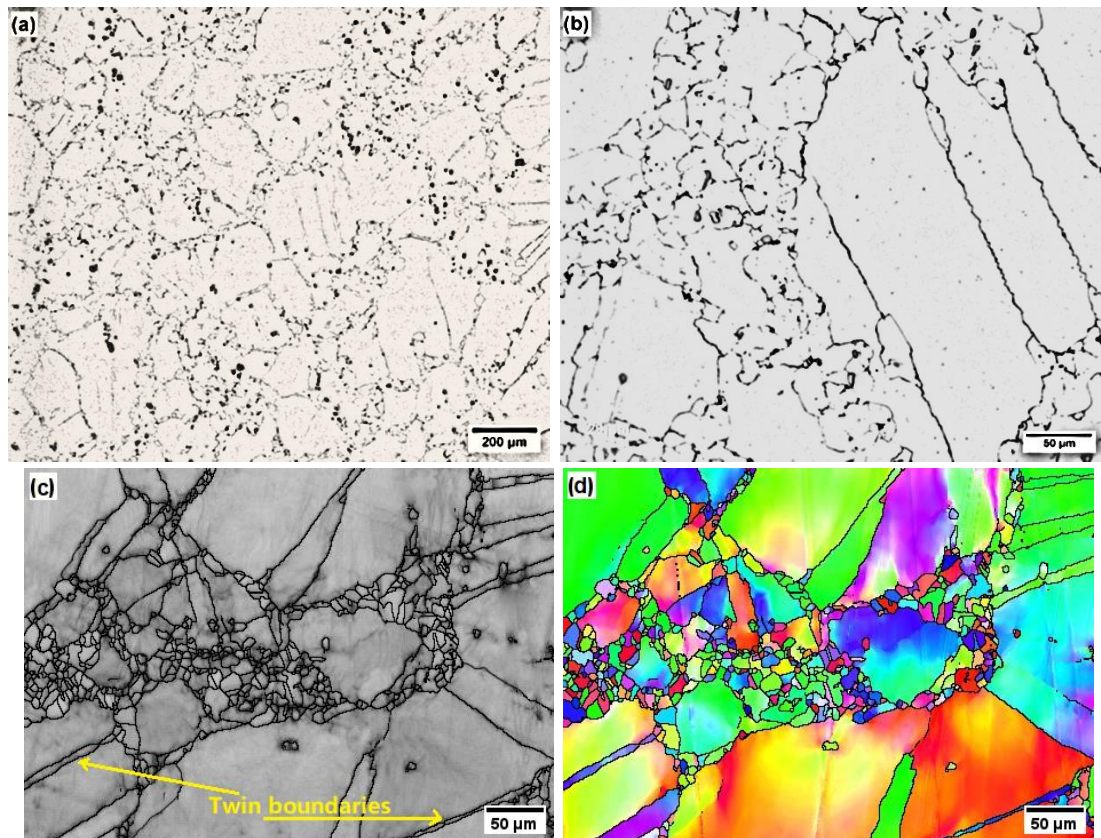


**Figure 4.2 Optical images of heterogeneous structures of Haynes 282 at (a) x5 (b) x20 magnifications, and EBSD maps of (c) band contrast at x30 magnifications and (d) in IPF X direction.**

94

Further microstructural analysis using EBSD mapping (Figure 4.2(d)) confirms the variation in grain size and highlights the presence of twin boundaries. These twin boundaries provide additional insight into the material's deformation behaviour under mechanical and thermal conditions, emphasizing the complexity of Haynes 282's microstructure.

In addition to the grain structure, Figure 4.3(b) illustrates the uniform dispersion of spherical precipitates within the $\gamma$ matrix, indicating a homogeneous distribution of secondary phases. The $\gamma$ matrix of Haynes 282 is reinforced by the spherical $\gamma'$ phase, which constitutes approximately 16% ($\pm 3.8\%$, 95%CI) of the microstructure. Despite its relatively low volume fraction, the $\gamma'$ phase plays a critical role in strengthening the alloy.
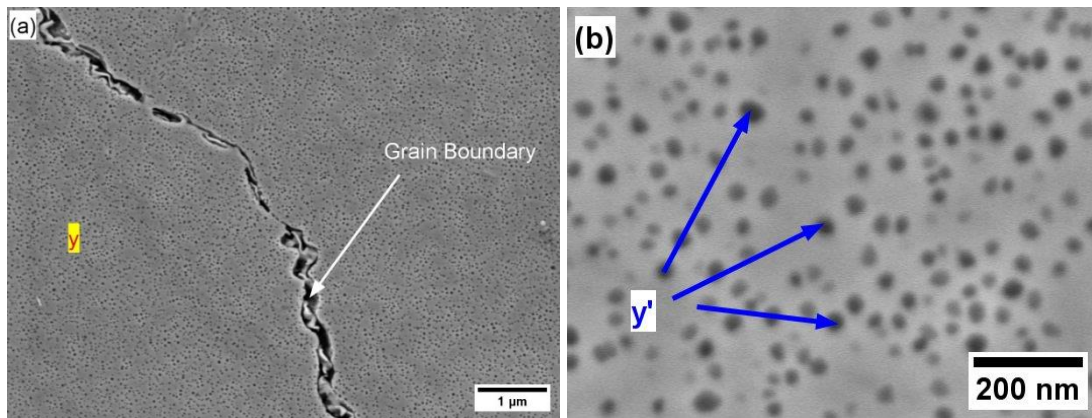


**Figure 4.3 SEM images of the grain boundaries and gamma prime precipitates of H282 at (a)x15000 (b)x50000 magnifications .**

Large carbides are observed at the grain boundaries, potentially playing a crucial role in impeding grain boundary sliding and improving high-temperature performance, as shown in Figure 4.4(a). Figure 4.4(b) shows that carbides exist along grain boundaries, which likely enhance creep resistance by strengthening grain boundaries.
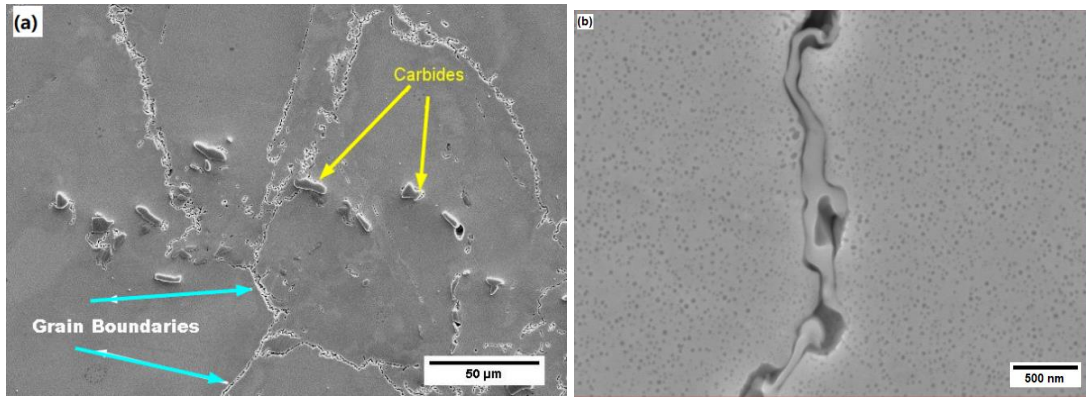
**Figure 4.4 SEM images of different carbides in Haynes 282 at (a)x500 (b) x30000 magnifications.**

EDS analysis (Figure 4.5) reveals that the larger carbides near the grain boundaries are rich in Ti, Mo, and C, while deficient in Ni, Cr, Co, and Fe. In contrast, the carbides filling the grain boundaries contain higher amounts of Cr, Mo, Ti, and C, as shown in Figure 4.6. These compositional differences suggest that the larger carbides are MC-type, primarily stabilized by Ti and Mo, whereas the grain boundary carbides are likely $M_{23}C_6$, commonly associated with grain boundary strengthening.
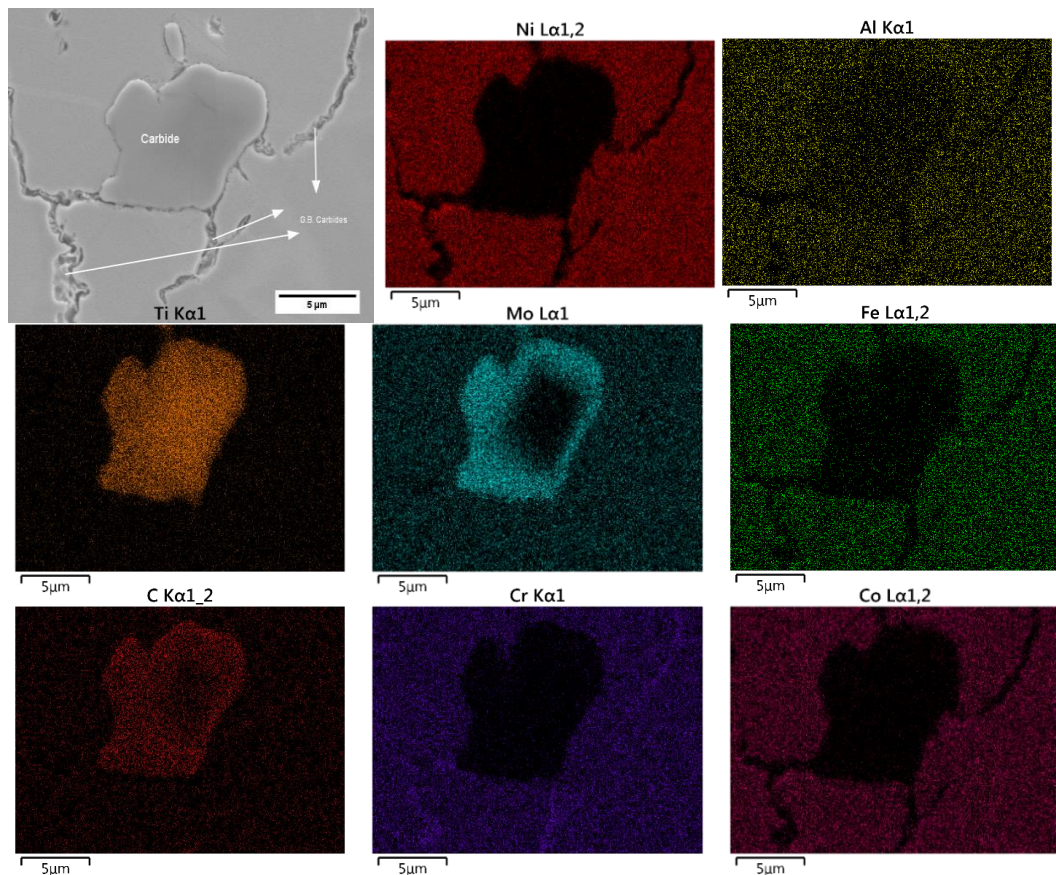


**Figure 4.5 SEM image and EDS maps of MC carbide in Haynes 282 at x5000 magnification.**
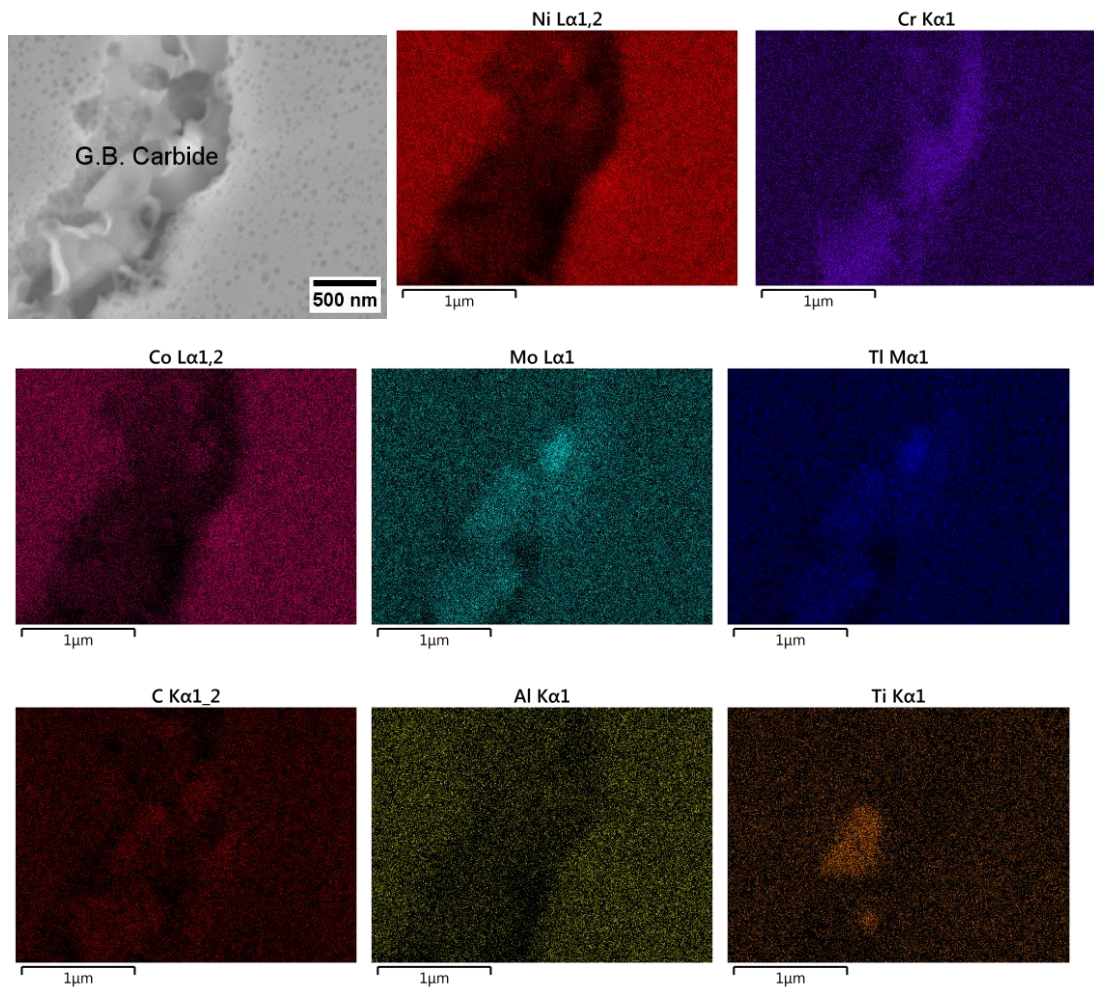
**Figure 4.6 SEM image and EDS maps of M₂₃C₆ carbides in Haynes 282 found inside the grain boundaries at x40000 magnification.**

This complex microstructural arrangement, including heterogeneous grain sizes, the presence of twin boundaries and the distribution of carbides and γ' precipitates, highlights the intricate balance between different strengthening mechanisms in Haynes 282.

### 4.1.3 Inconel 713C

The microstructure of cast IN713C, as shown in Figure 4.7, is characterised by a dendritic structure with MC-type carbides. These dendrites form during solidification and exhibit varied orientations within each grain due to differences in crystallographic directions. The dendrite length correlates with the grain size, while the primary dendrite arm spacing significantly influences the alloy's mechanical properties. A smaller arm spacing is generally associated with improved mechanical

97

performance[230]. However, due to its highly irregular and varied nature—ranging from 390 μm to 1 mm, as reported in the literature—detailed analysis of this effect remains challenging[125]. In contrast, the secondary dendrite arm spacing appears to be more consistent. Overall, dendritic structures constitute approximately 54.2% of the microstructure.

At higher magnifications, significant carbide precipitation is observed in the interdendritic regions, primarily concentrated along grain boundaries (Figure 4.7(d). EDS analysis (Figure 4.8) reveals that these carbides are primarily composed of Nb, Mo, and Ti. Electron microscopy further highlights the role of carbides in outlining the dendritic structure, as they align along the dendrite arms, visually representing the solidification process. Dendritic orientation varies significantly between grains, reflecting differences in crystallographic alignment. This variation becomes particularly pronounced at grain boundaries, where adjacent grains exhibit distinct dendritic orientations.
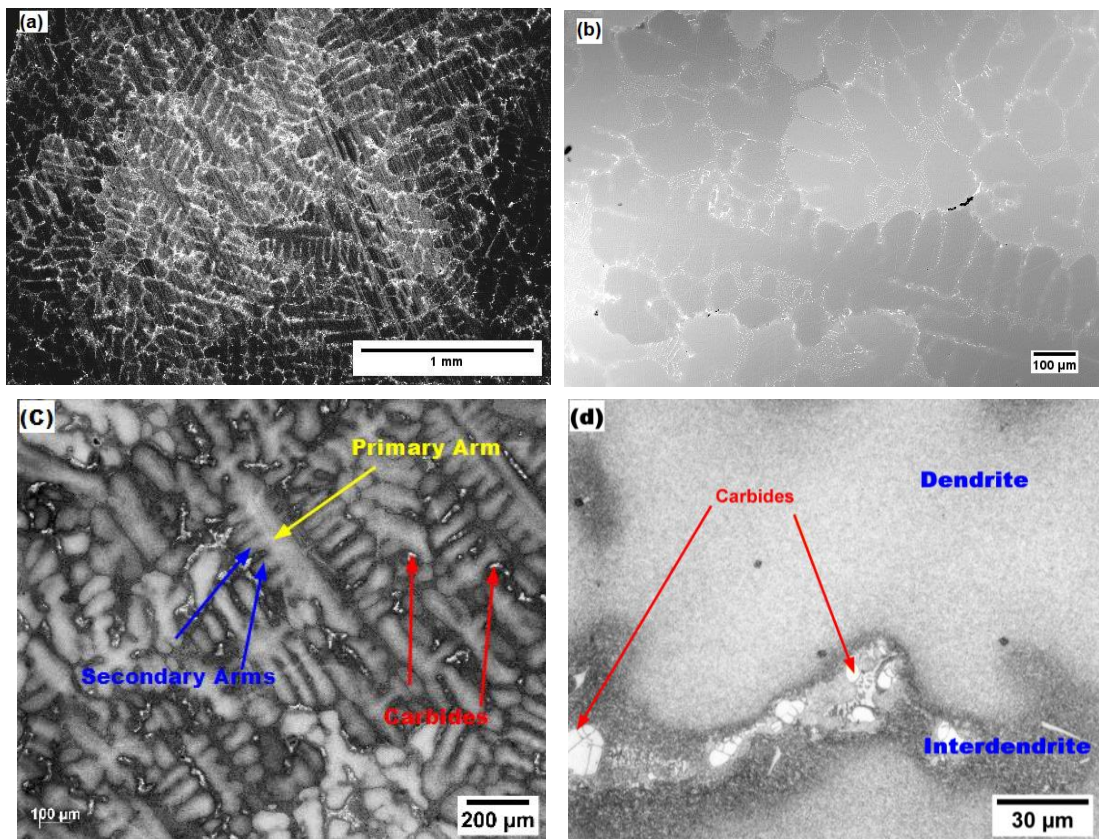


**Figure 4.7 SEM images of dendritic structure at (a) x40 (b) x100 magnifications, and optical images of dendritic structure and carbides at (c) x5 (d) x50 magnifications.**
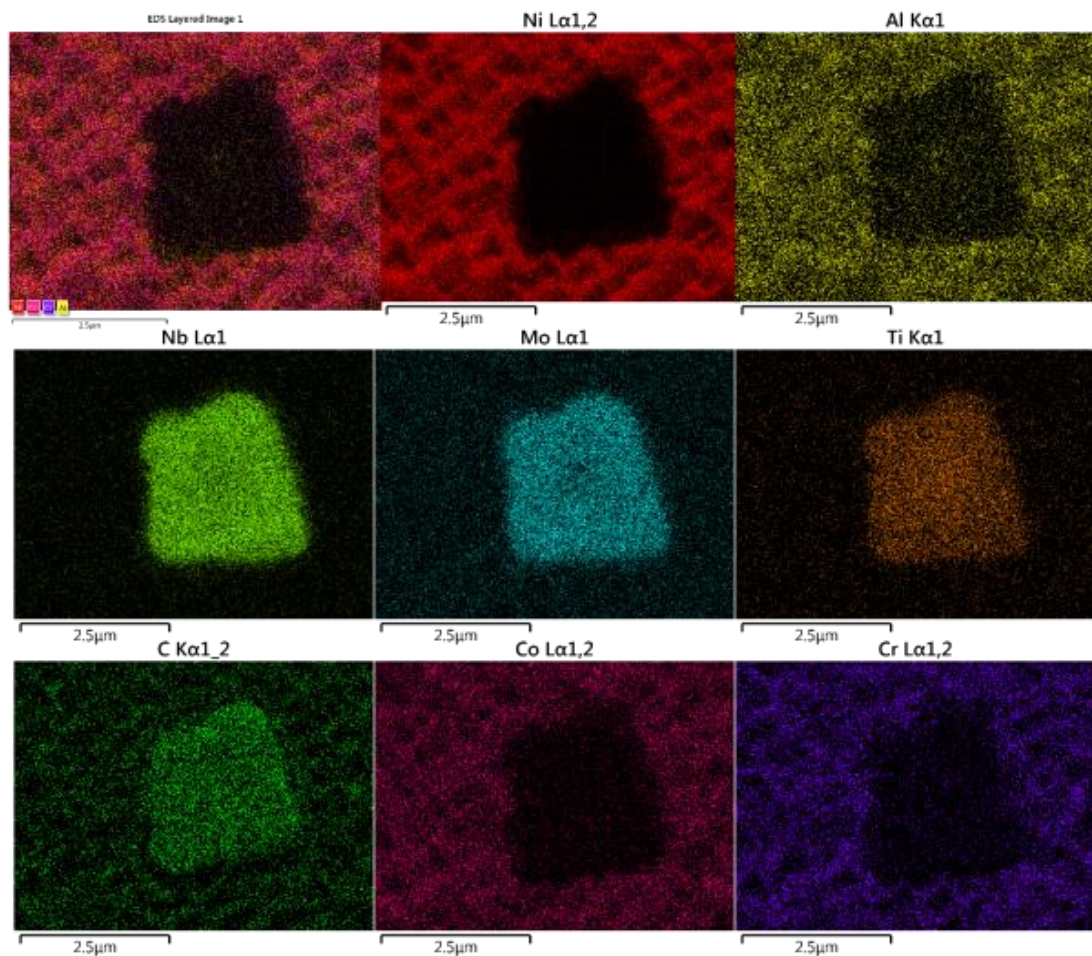
**Figure 4.8 EDS maps of MC carbide in IN713C.**

The γ matrix, which serves as the primary phase in IN713C, consists mainly of nickel (Ni) with solid solution elements such as chromium (Cr), aluminium (Al), and molybdenum (Mo). 'These elements are retained in solid solution within the γ matrix upon solidification. Subsequent heat treatment facilitates the precipitation of the γ' phase from the supersaturated solid solution. This precipitation is a key factor in strengthening the alloy, which relies on γ' hardening mechanisms. The γ' phase, the primary strengthening phase in IN713C, appears predominantly in a cuboidal shape (Figure 4.9(b)), and accounts for approximately 64% (±4.6%, 95% CI) of the microstructure, appearing in both dendritic and interdendritic areas. Coarse γ' precipitates are frequently found at boundaries (Figure 4.9(a)). This is consistent with the tendency of γ' to coarsen or cluster at grain boundaries during solidification.
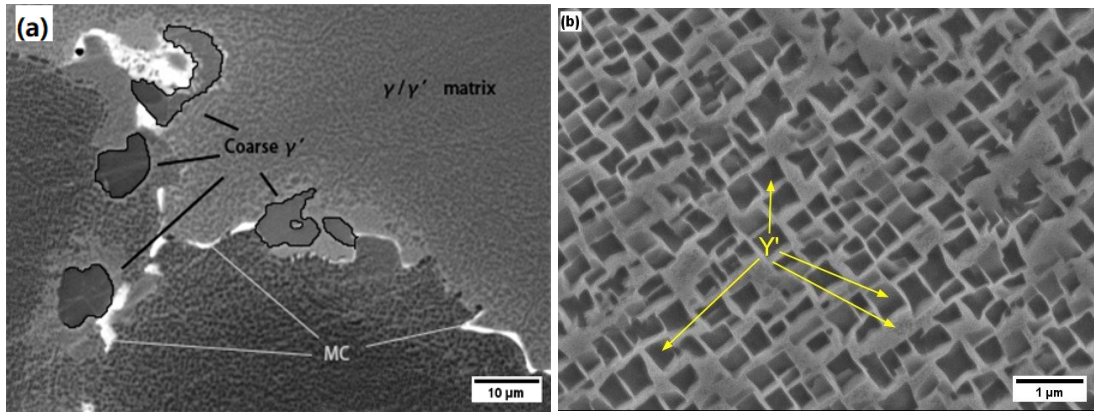
**Figure 4.9 SEM images of precipitates including γ' and carbides at (a) x500 (b) x15000 magnification.**
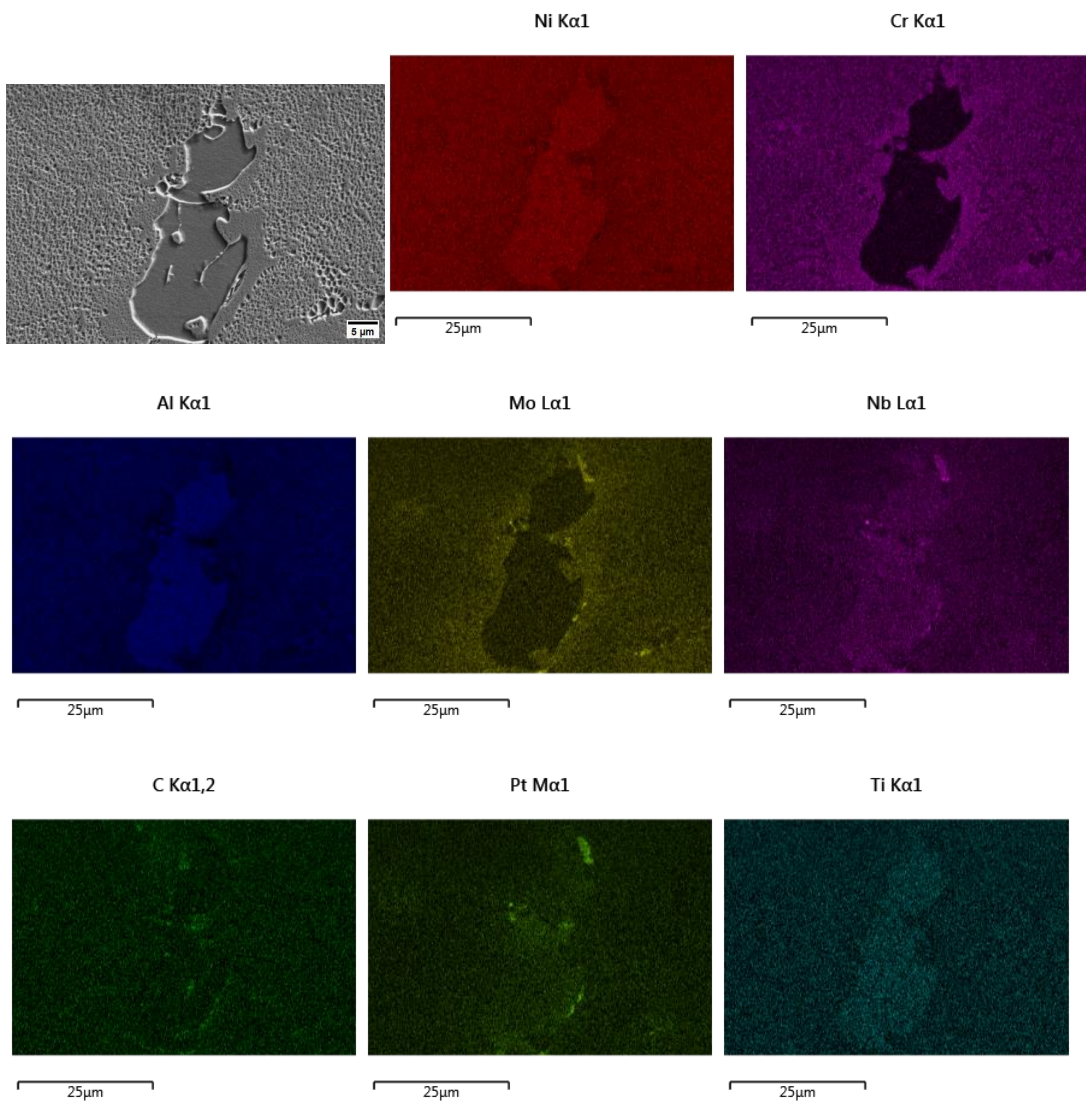


**Figure 4.10 SEM images and EDS maps of coarse gamma prime in IN713C at x2000 magnification.**

Figure 4.11 below presents SEM images and EDS maps of IN713C at a magnification of x2000, illustrating the presence of needle-shaped MC-type carbides within the alloy. The EDS analysis confirms that these carbides are enriched with molybdenum (Mo), niobium (Nb), carbon (C), and titanium (Ti), consistent with the composition of MC carbides typically observed in nickel-based superalloys. This highlights the significant role of these elements in the carbide formation and their contribution to the alloy's microstructural stability and mechanical properties.
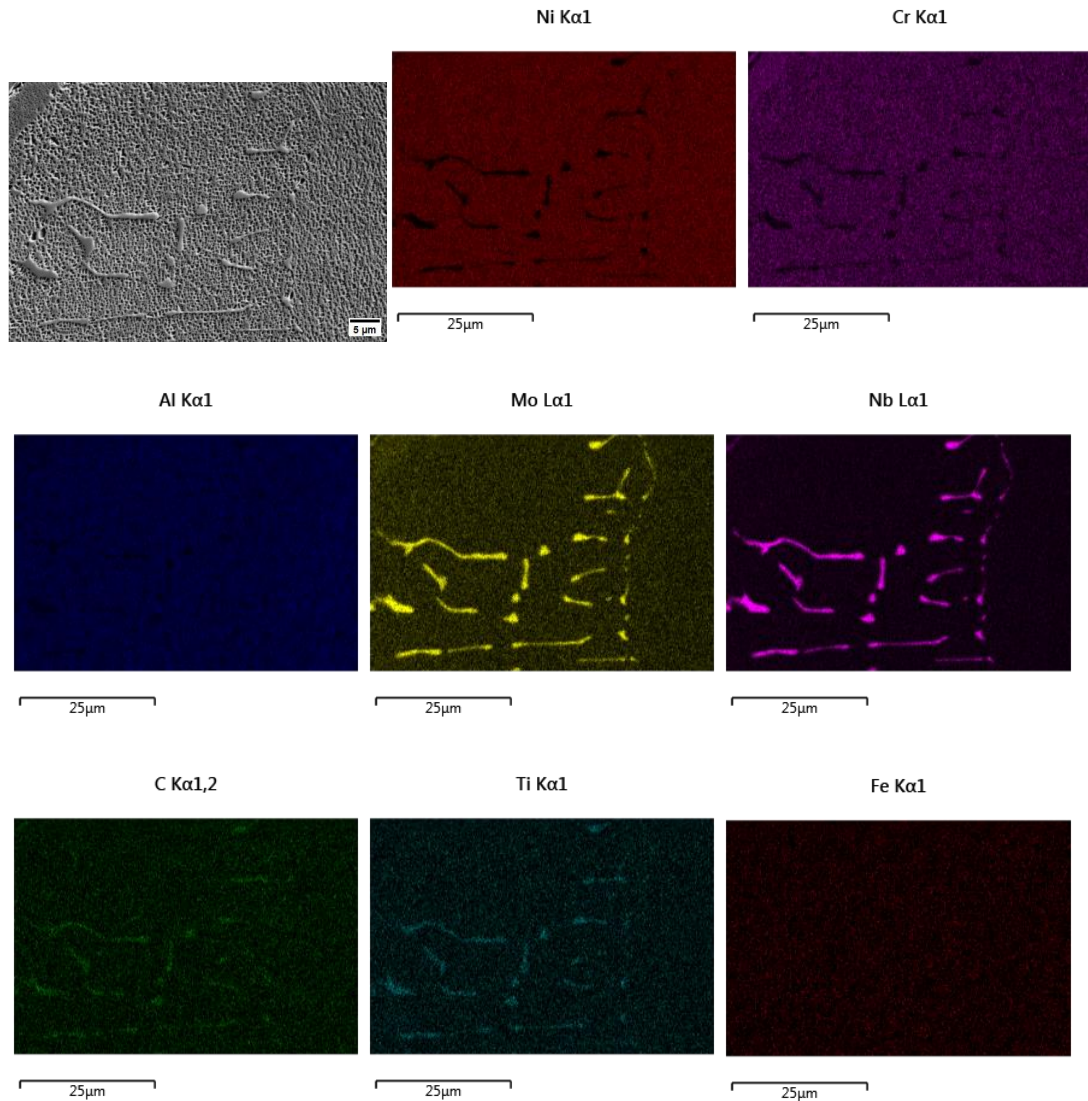


**Figure 4.11 SEM and EDS graphs showing MC carbides of IN713C at x2000 magnification.**

Furthermore, an additional precipitation phase has been identified, distinct from γ' and carbides. This phase forms clusters of coarse γ' containing significant amounts of Ni and Al, surrounded by fine Nb- and Mo-rich carbides. However, this phase exhibits a

lower concentration of Ni and Al while being enriched in Cr, as shown in the EDS maps (Figure 4.12). This composition raises the possibility that the phase could be a topologically close-packed (TCP) phase, which may contribute to alloy degradation by promoting fracture, creep, and reduced fatigue resistance.
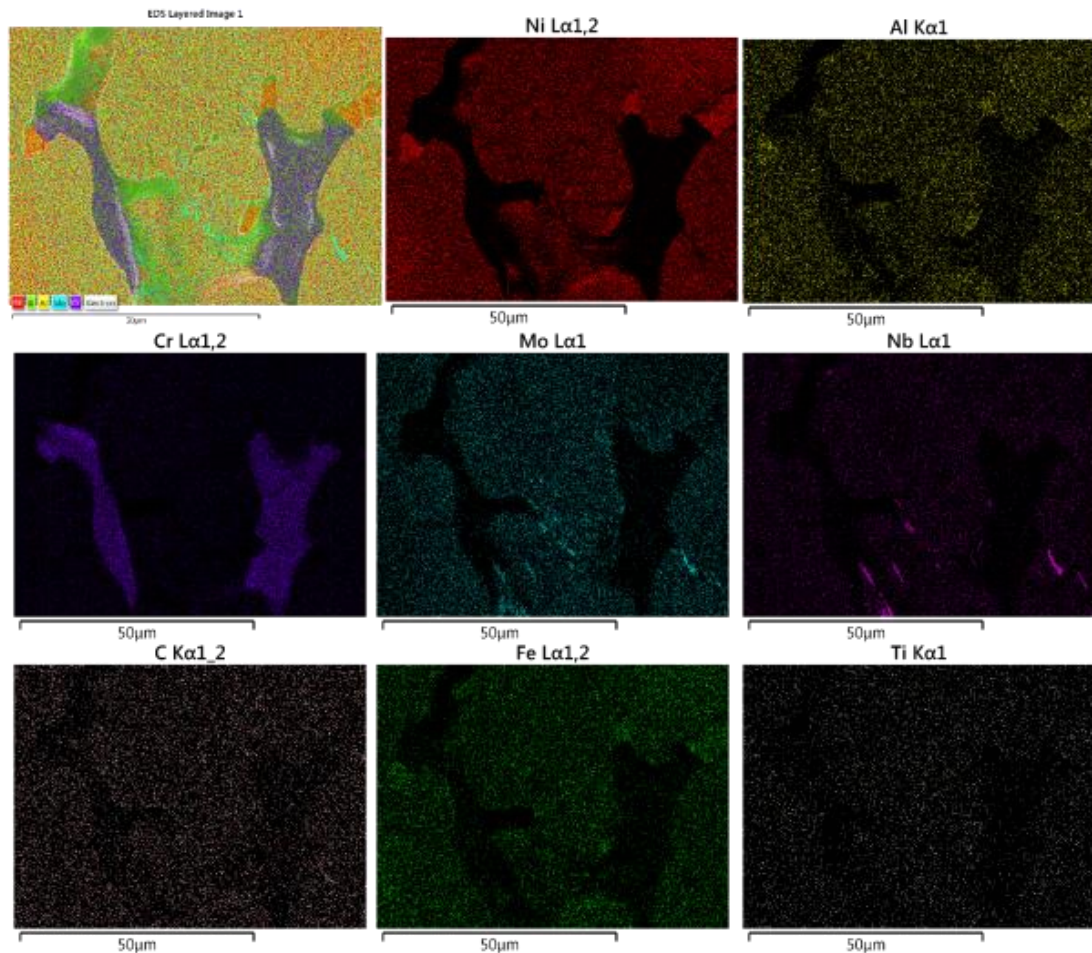


**Figure 4.12 EDS maps of TCP phase found in IN713C.**

As stated before, the microstructure of IN713C can be classified into three distinct grain morphologies: equiaxed, columnar, and transition grains, as shown in Figure 4.13. These variations arise due to differences in solidification conditions and influence the alloy's mechanical performance, particularly creep resistance and grain boundary behaviour. For instance, the lack of grain boundaries of columnar solidified alloys always gives a better creep resistance[161].
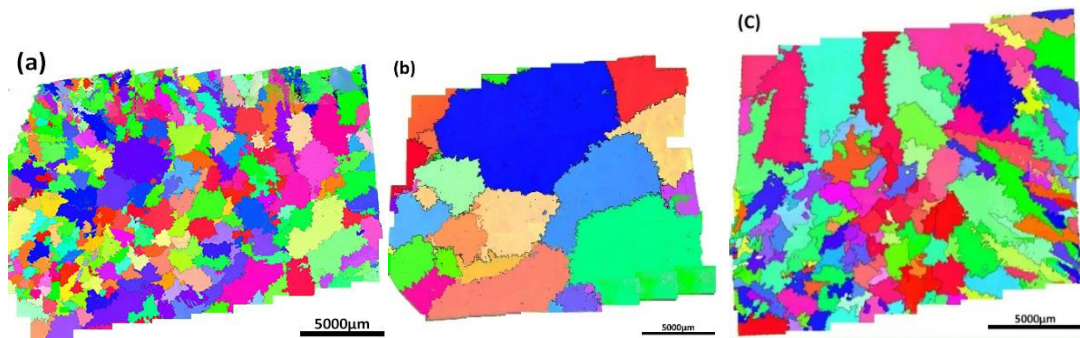
**Figure 4.13 EBSD maps of IN713C in IPF-X direction with (a) equiaxed (b) columnar (c) transition structures.**

According to Konrad et al.[231] and Pollock et al.[232], grain size and secondary dendrite arm spacing (SDAS) are highly dependent on solidification parameters. Higher mould temperatures and thicker ceramic shells slow down the solidification process, resulting in larger grains and wider SDAS.

The equiaxed grains form under near-equilibrium solidification conditions, typically aided by the addition of a grain nucleation promoter in the ceramic shell. These grains are relatively uniform in size and promote isotropic mechanical properties. However, the increased grain boundary area can reduce creep resistance.

Columnar grains are formed by withdrawing the ceramic shell, containing a columnar grain promoter, from the furnace's hot zone into a cooler zone. This directional solidification reduces transverse grain boundaries, typically improving creep resistance and making the structure more suitable for high-temperature applications.

Transition grains are mixed structures exhibiting features of both equiaxed and columnar grains, transition regions develop under intermediate solidification conditions. The presence of partially aligned grains may result in anisotropic mechanical behaviour.

These variations in grain morphology, as revealed through EBSD, significantly influence the alloy's high-temperature performance, particularly its creep resistance. Columnar grains, with their reduced grain boundary area, provide superior resistance to grain boundary sliding and damage, while equiaxed grains offer better toughness but may be more susceptible to creep deformation[233]. Transition regions, depending on their distribution, can introduce localised mechanical heterogeneity.

## 4.2 Tensile Properties and Fractography

### 4.2.1 Tensile properties of 316 stainless steels

Although no direct tensile tests were conducted on 316 stainless steels within this study, tensile data was obtained from the National Institute for Materials Science (NIMS)[225]. This data serves as a reference point for interpreting the alloy's high-temperature performance and contextualising the creep behaviour reported later in this chapter. In particular the proof stress and UTS, offer insights into the initial load-bearing capacity of the material at elevated temperatures.
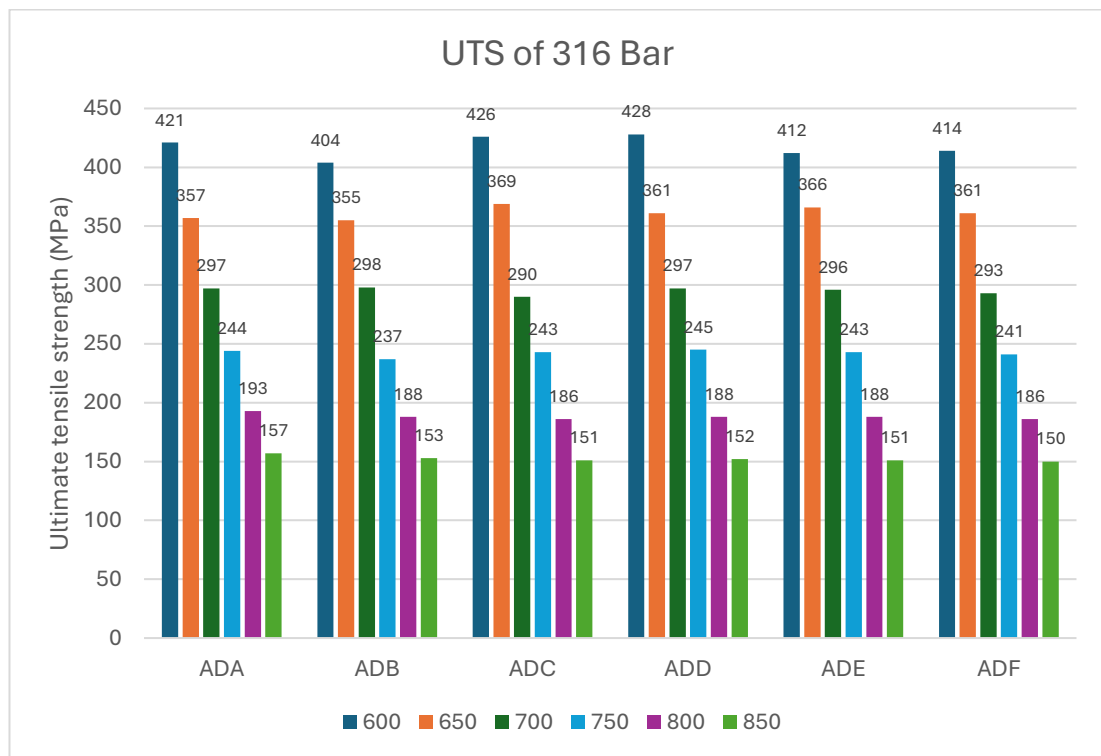


**Figure 4.14 Bar chart illustrating the UTS of 316 stainless steel at various temperatures, based on NIMS data.**

Figure 4.14 illustrates the ultimate tensile strength (UTS) of 316 stainless steel bars with different batches (ADA, ADB, ADC, ADD, ADE, and ADF) at various temperatures ranging from 600°C to 850°C. The UTS values exhibit a decreasing trend from above 400MPa to approximately 150MPa with increasing temperature, indicating the expected thermal softening effect.
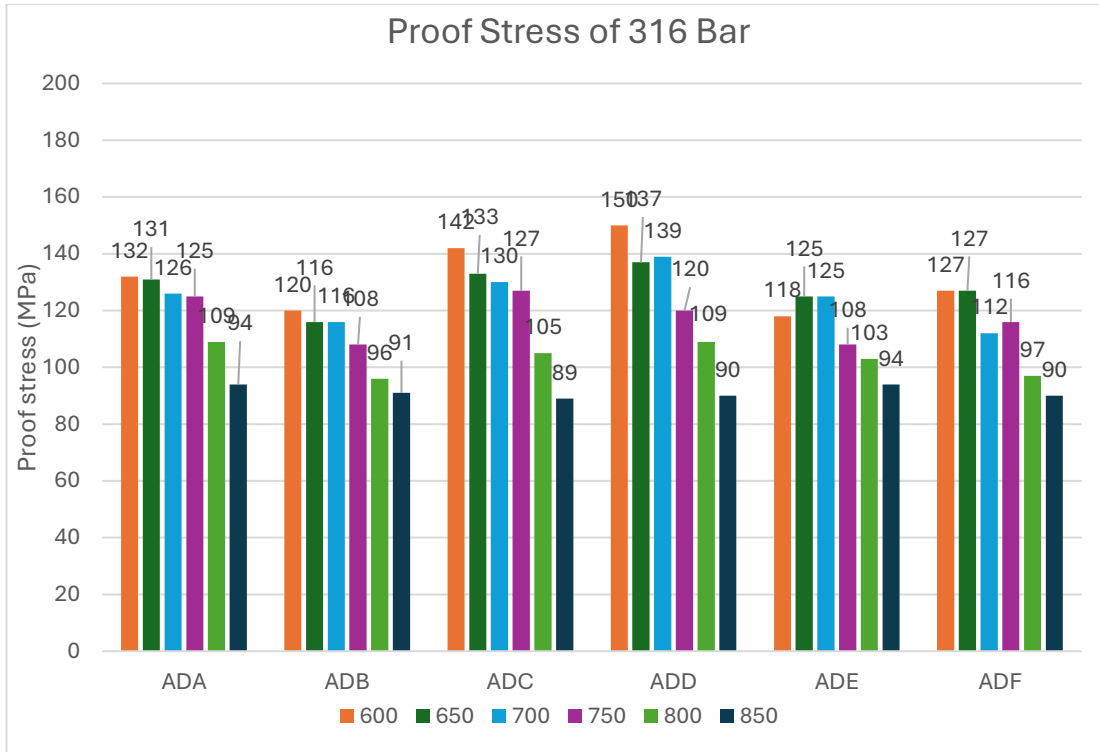
**Figure 4.15 Bar chart illustrating the 0.2% proof stress of 316 stainless steel at various temperatures, based on NIMS data.**

Figure 4.15 presents the 0.2% proof stress of 316 stainless steel bars. The proof stress generally decreases as the temperature increases, indicating a reduction in yield strength at elevated temperatures. However, the downward trend from 600℃ to 700℃ is not obvious, and some batches even have a reverse change. The proof stress declines more gradually than UTS at high temperatures because it primarily reflects initial yielding, which is less sensitive to strain-hardening loss and void formation. In contrast, UTS experiences a steeper reduction because it depends on strain hardening, dislocation interactions, and fracture mechanisms, which are more temperature-dependent. This behaviour is typical for austenitic stainless steels like 316, making them more ductile at high temperatures, where they retain some plasticity before complete failure.

While the general trend remains consistent among different 316 bars, slight variations exist among different material batches (ADA to ADF), potentially due to microstructural differences, prior processing conditions, or compositional variations. The resulting physical property differences are not significant; therefore, treating all batches as a single dataset in this study is considered reliable. These results also

highlight the substantial impact of elevated temperatures on the mechanical integrity of 316 stainless steel, reinforcing its suitability for applications up to 650–700°C before experiencing significant strength degradation.

### 4.2.2 Tensile tests of nickel-based superalloys

Samples of IN713C and Haynes 282 sent to Westmoreland for creep testing were first subjected to tensile tests to determine their mechanical properties. The information that is relevant to this study is reported in Table 4-3 , and the complete results are presented in the appendix.

**Table 4-3 The monotonic tensile properties of IN713C and H282**

| Sample | Temp. (°C) | UTS (MPa) | 0.2%YS (MPa) | Elong. (%) | Modulus (GPa) |
|---|---|---|---|---|---|
| IN713C#1 | 650 | 885 | 765 | 10 | 159 |
| IN713C#2 | 750 | 930 | 785 | 14 | 189 |
| Haynes 282#1 | 650 | 1060 | 750 | 18 | 165 |
| Haynes 282#2 | 750 | 885 | 790 | 14 | 171 |
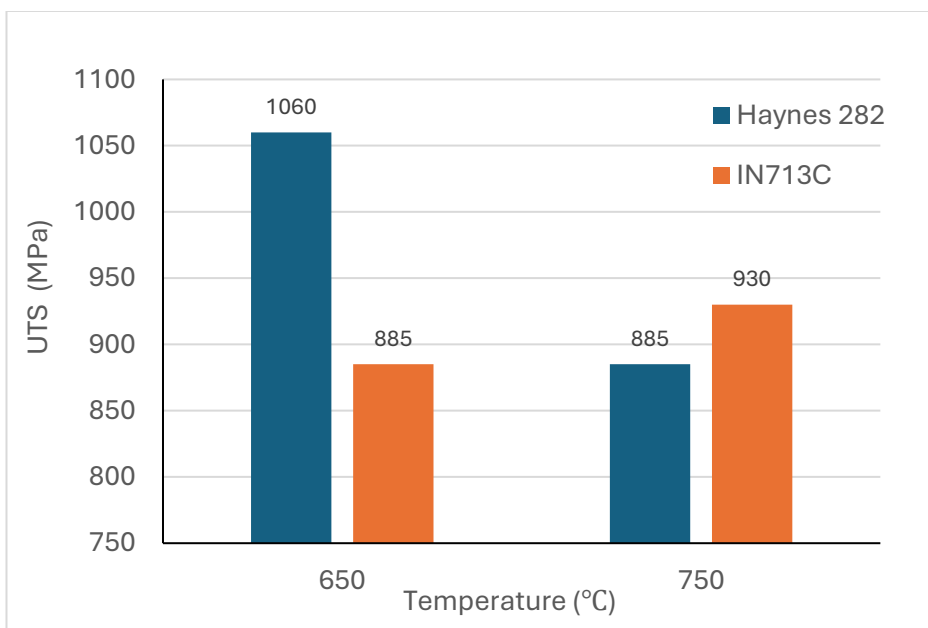


**Figure 4.16 Bar chart illustrating the UTS of IN713C and Haynes 282 at 650°C and 750°C.**

106

Based on the tensile test results, it is evident that temperature has a minor impact on the yield strength of the two nickel-based alloys. Generally, the ultimate tensile strength (UTS) of metallic materials decreases with rising temperatures - the experimental data from Haynes 282 is a good example of this. This phenomenon occurs due to the increased ductility or plasticity of the material at higher temperatures. As the temperature rises, the mean distance between atoms increases and bond strength reduces, and it requires relatively lower stress to undergo deformation. However, IN713C exhibited an unexpected strength outcome - displaying higher strength at 750°C compared to 650°C (Figure 4.16). This phenomenon is not unprecedented, as Cantó[234] observed a UTS of 940MPa for IN713C at 650°C, which was 90MPa higher than the material's strength at room temperature. Similarly, Cieśla et al.[235] conducted a test on IN713C at 800°C and found a higher UTS than at room temperature. Cantó[234] attributed this disparity to a higher hardening rate at 650°C compared to room temperature. The outcomes of this experiment are consistent and can also be explained by the fact that IN713C demonstrates a higher hardening rate at 750°C.

It was also observed that the modulus of both materials increased with rising temperature, which is a relatively uncommon phenomenon. Typically, an increase in temperature leads to enhanced atomic or molecular vibrations and a weakening of interatomic forces, resulting in a decrease in the material's elastic modulus. At elevated temperatures, thermal motion intensifies, and the movement of dislocations and lattice defects becomes easier, further reducing the material's stiffness and, consequently, its modulus[236]. The unexpected increase in modulus observed in this study may be related to precipitation hardening effects. However, this aspect was not explored in detail, as tensile testing was not the primary focus of the study and was conducted solely to provide baseline characterisation of the specimens.

### 4.2.3  Fractography of Inconel 713C

The fracture surfaces after the tensile tests were examined using scanning electron microscopy (SEM). The notable dissimilarities were seen between the left and right sides of the cross section, suggesting varied failure mechanisms. The depicted cross-section in Figure 4.17(b) illustrates the left side, which has a flatter surface and showcases a significant abundance of cleavage river patterns. The right half, depicted

in Figure 4.17(c), exhibits a mostly uneven fracture pattern, characterised by fractures that are oriented nearly perpendicular to the direction of tensile stress. Additionally, minor dimples, indicative of localized ductile deformation, were observed. The presence of a more prominent dendritic structure is a prevalent characteristic observed in cast alloys, as shown in Figure 4.17(d).
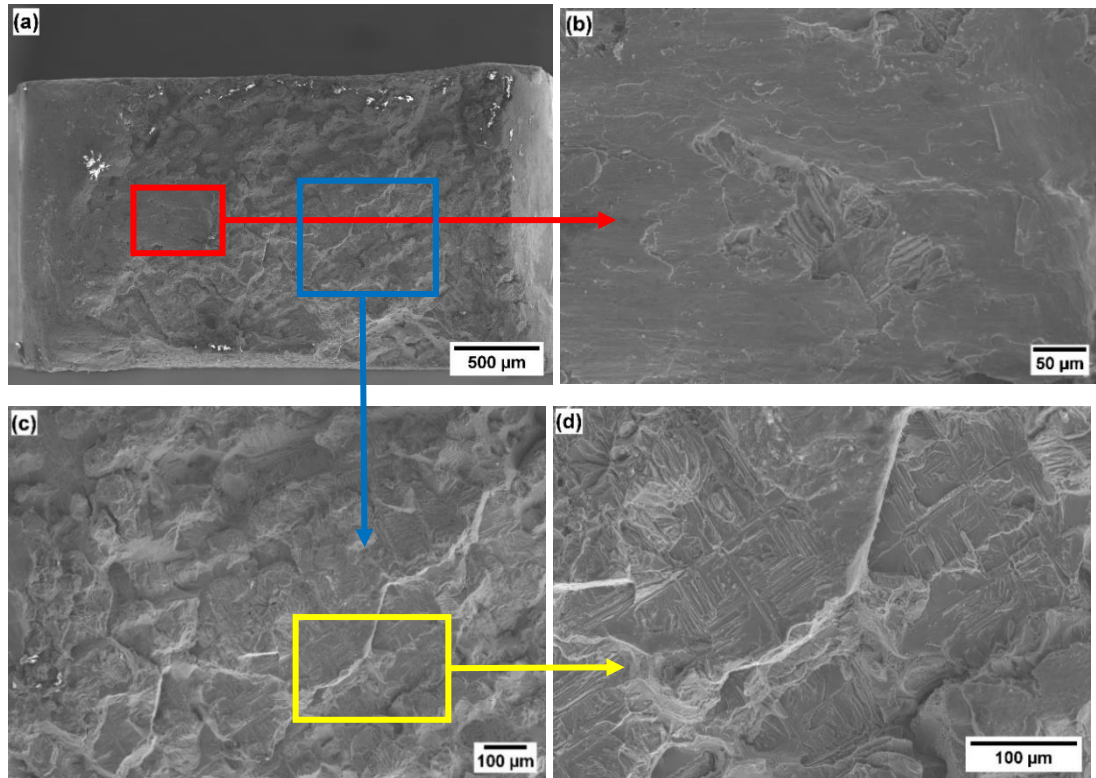


**Figure 4.17 Fractography of IN713C after tensile testing at 650°C, observed using SEM at different magnifications: (a) x40, (b) x250, (c) x100, and (d) x250.**

The fracture characteristics of the IN713 tensile specimen at a temperature of 750°C exhibit similarities to those seen at 650°C. The left portion of the cross-sectional analysis, as shown in Figure 4.18(b) exhibits a somewhat smoother surface, albeit still rougher than the outcome observed at 650°C, characterised by a clear increase in the prevalence of dimples and tear ridges. (c) and (d) exhibit discernible dendritic structures and cleavage steps.
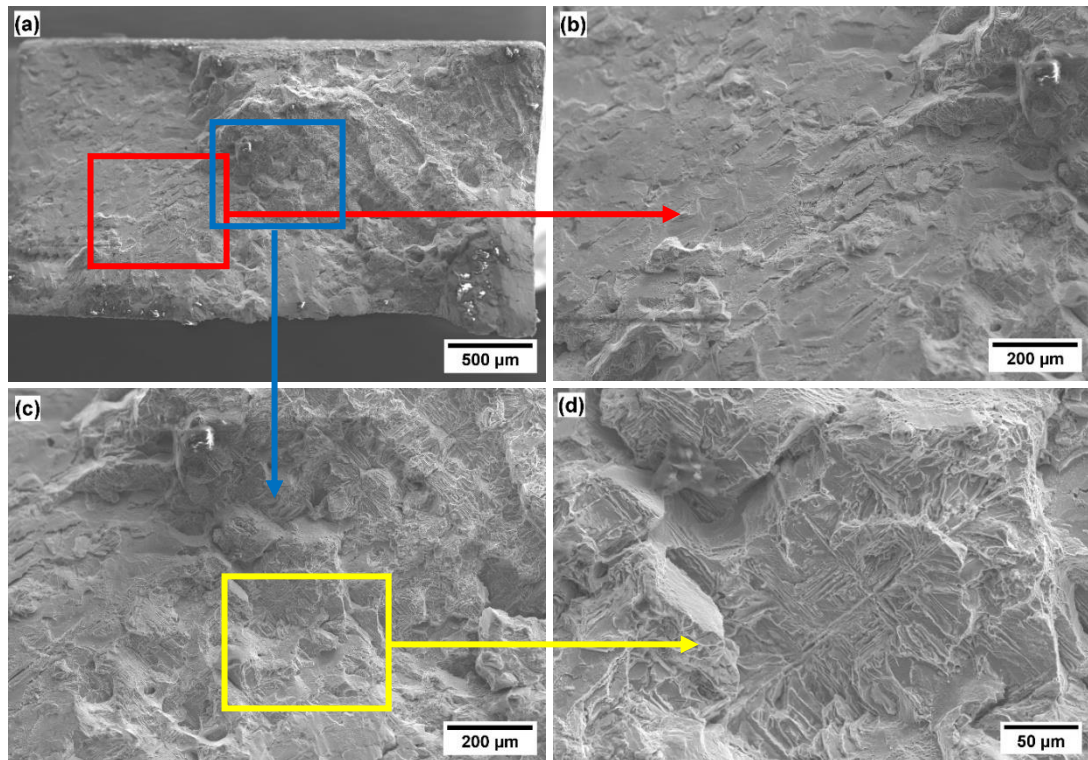
**Figure 4.18 Fractography of IN713C after tensile testing at 750°C, observed using SEM at different magnifications: (a) x40 (b) x100 (c) x100 (d) x350.**

## 4.2.4  Fractography of Haynes 282

The fracture surface of Haynes 282 exhibits a rugged, uneven terrain with characteristics of a combination of dimples. Unlike IN713C, no distinct left and right zones are observed, as evident in Figure 4.19 and Figure 4.20.

At a temperature of 650°C, the initial fracture initiates at the midpoint of the edge of the specimen, as depicted in Figure 4.19(b). This region displays a notable presence of tearing and secondary tearing fracture features. The specimen undergoes plastic deformation under axial tensile stress, resulting in the formation of fractures through the aggregation and enlargement of microvoids. Figure 4.19(c) shows that the fracture surface exhibits numerous variably sized equiaxed circular or elliptical voids and dimples, underscoring the material's retention of reasonably good plasticity at elevated temperatures. However, towards the upper-right corner of the fracture surface, where higher loading stresses prevail in the later stages of fracture, rapid crack propagation occurs. Stress concentration near the vicinity of microvoids impedes the formation of dimples, resulting in a smaller, smoother region on the surface.

109
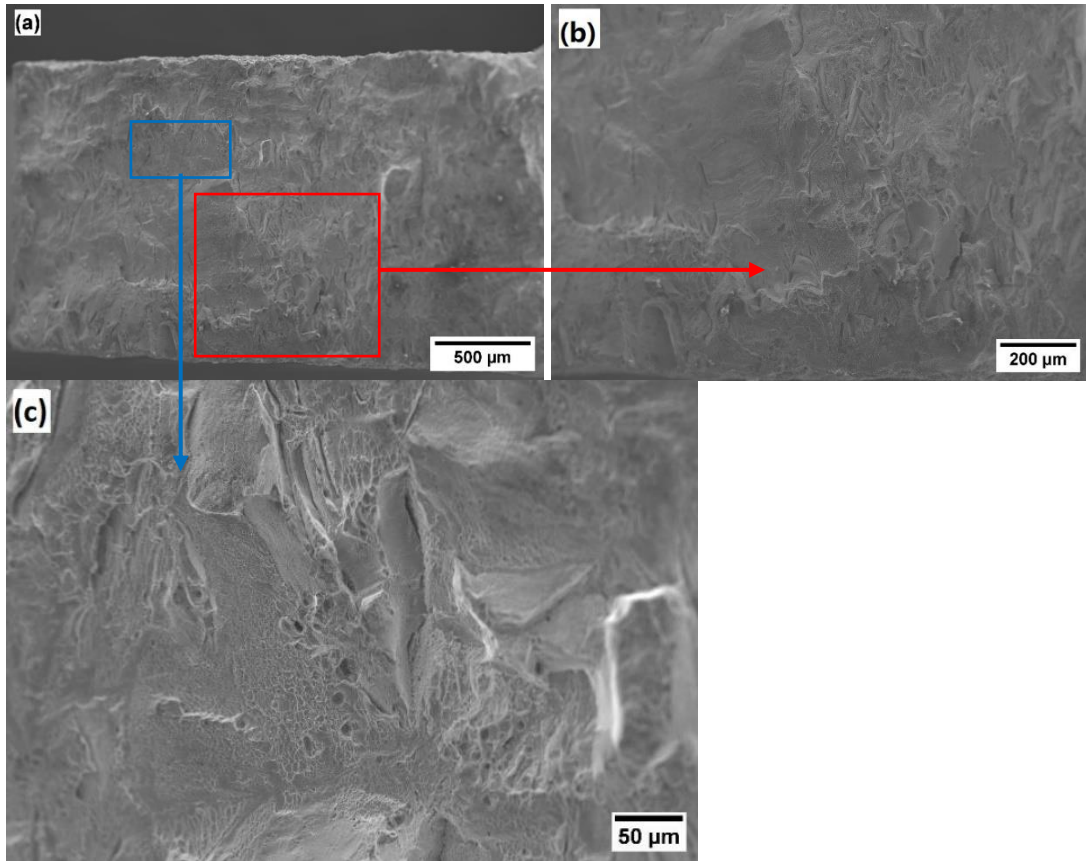
**Figure 4.19 Fractography of H282 after tensile testing at 650°C, observed using SEM at different magnifications: (a) x45 (b) x90, (b) x250.**

With a further increase in temperature to 750 °C, fracture continued to initiate at the midpoint along the edge of the specimen. The cross-section exhibited a pronounced central depression, accompanied by substantial and frequent tearing in the surrounding edges, as shown in Figure 4.20(a). As illustrated in Figure 4.20(b) and(c), tearing in this area appears to diminish, while both the number and size of dimples increase significantly. This observation suggests the presence of ductile void formation at the centre of the specimen, followed by the development of shear lips at the edges—characteristic of ductile fracture through void coalescence and tearing.
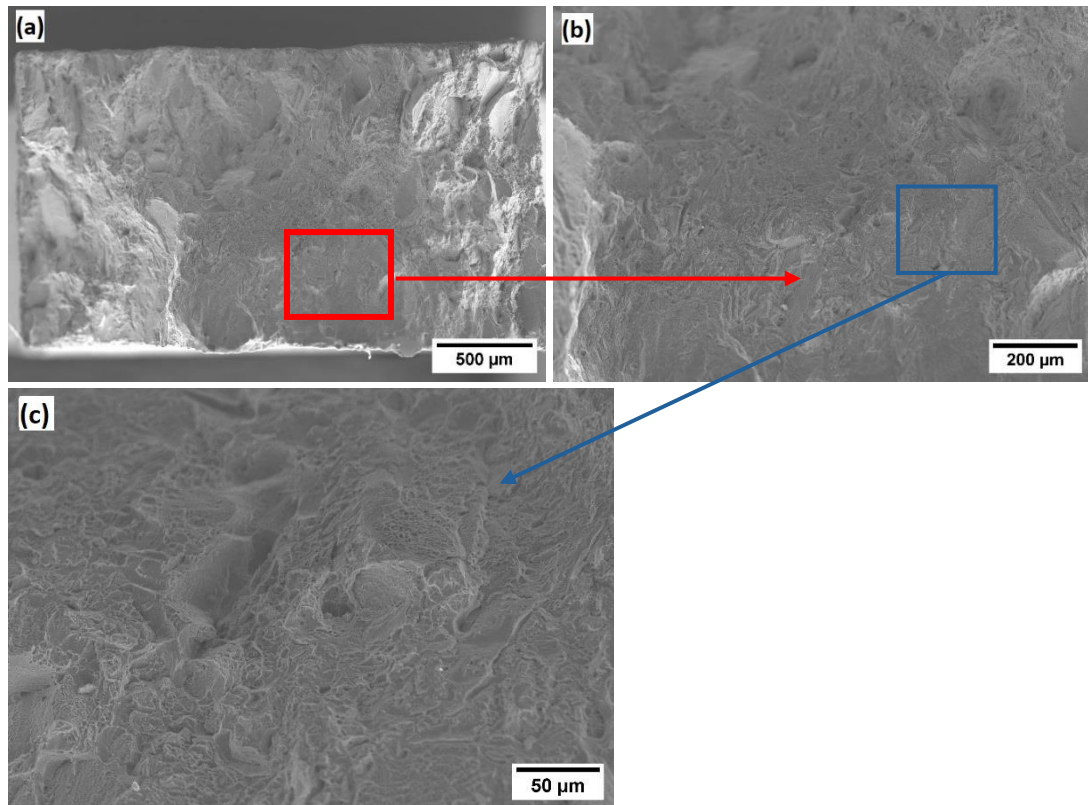
**Figure 4.20 Fractography of H282 after tensile testing at 750℃, observed using SEM at different magnifications: (a) x45 (b) x100 (c) x350.**

## 4.3  Creep Tests Results and Microstructural Evolution

The creep properties of stainless steel 316, a material characterised by a negligible volume fraction of precipitates, have been extensively tested by the National Institute of Materials Science (NIMS) in Japan. 316 stainless steel is widely used in practical engineering applications and is manufactured in various forms to suit different service environments. Although the chemical composition remains consistent across these forms, differences in geometry can lead to variations in mechanical behaviour; for example, cross-sectional differences may result in different stress distributions under identical loading conditions. To investigate these effects, a Japanese research organisation conducted creep tests on 316 stainless steels in three different forms: bar[225], plate[226], and tube[227]. Bar stock is typically used in general applications, plates are commonly employed in reactor vessels, and tubes are utilised in boilers and heat exchangers. This creep data has been made publicly available, providing a valuable resource for both academia and industry. Different creep prediction formulae

were applied to this dataset to explore the creep behaviour of stainless steel 316. Particular attention is given to the application of the Wilshire Equation creep model to the Stainless steel 316 dataset provided by NIMS as this datasheet is complete, comprehensive and detailed.

Building upon previous research[99], the aim is to uncover the underlying reasons for the significant shift in activation energy observed in Stainless steel 316 as it transitions from low-stress to high-stress regions. Through this analysis, the objective is to gain a deeper understanding of how microstructural differences affect the creep response of SS316, alongside two other materials, Inconel 713C with a high volume of precipitates and Haynes 282 with a low volume fraction of precipitates and to assess the predictive reliability of the Wilshire Equation in this context. By contrasting the creep behaviour with IN713C and H282, the study aims to elucidate the role of microstructural variations in shaping activation energy as calculated by the Wilshire Equations and contribute to the broader understanding of materials science and engineering.

## 4.3.1  316 Stainless steel

### 4.3.1.1  Creep data

The creep experiments for Stainless steel 316 were conducted at the Swansea Materials Research & Testing Ltd (SMaRT), involving a test temperature of 600°C and stress levels spanning 125 MPa, 175 MPa, 225 MPa, and 275 MPa, for at least 50 hours. The resulting creep curves, depicted in Figure 4.21, provide a graphical representation of the material's time-dependent deformation under these varying stress conditions, and Figure 4.22 shows the creep rate curves of creep test at 600°C with varying stresses.
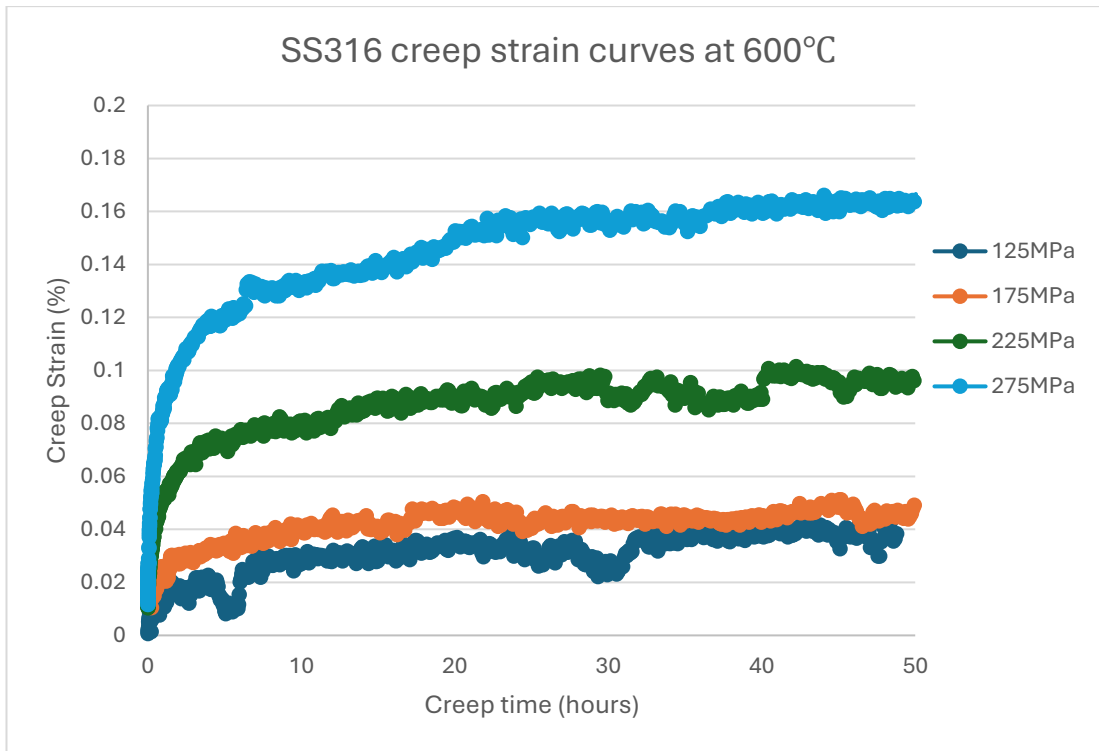
**Figure 4.21 Creep strain curves of SS316 tested at 600℃ under applied stresses ranging from 125MPa to 275MPa.**



**Figure 4.22 Creep rate curves of SS316 tested at 600°C under applied stresses ranging from 125MPa to 275MPa.**

113

From the analysis of both creep strain and creep rate curves, it can be observed that during the primary creep stage, the duration is relatively short and increases in time with increasing stress. This phenomenon can be attributed to the fact that, at the outset of creep, the metal's resistance to deformation is comparatively lower, thereby resulting in an elevated creep rate. As the deformation progresses, a subsequent phase is initiated where the metal undergoes work hardening, leading to a gradual decreasing of the creep rate, coupled with a progressive increase in the recovery rate. By the time the creep experiments were carried out for few hours, all four experiments have transitioned into and sustained secondary creep, characterized by a steady-state regime.

As the creep experiments extended to 50 hours, there was an absence of any noteworthy increase in the creep rate across all experiments, signifying a lack of progression into the tertiary stage.

The creep strain curves and creep rate curves for 316 stainless steels at 700°C, presented in Figure 4.23 and Figure 4.24. Due to the early interruption of the experiments, the creep curves do not exhibit the typical three-stage behaviour. In the primary stage, a rapid increase in strain is observed, reflecting initial microstructural adjustments and work-hardening effects. This is followed by a secondary, or steady-state, phase in which the creep rate stabilises as a result of the dynamic balance between strain hardening and recovery mechanisms.

The data show that at lowest applied stresses (e.g., 100 MPa), steady-state creep is reached at lower strain rates and sustained for a longer duration, indicating a relatively stable deformation process. In contrast, at higher stresses (125 MPa, 175 MPa, and 225 MPa), the primary creep phase extends to higher strain levels, and the creep rate increases markedly with stress, potentially leading to accelerated failure.

A comparison with data obtained at 600 °C under the same stress levels shows that both the initial strain and creep rate are significantly higher at 700 °C, highlighting the strong dependence of creep behaviour on temperature and stress.
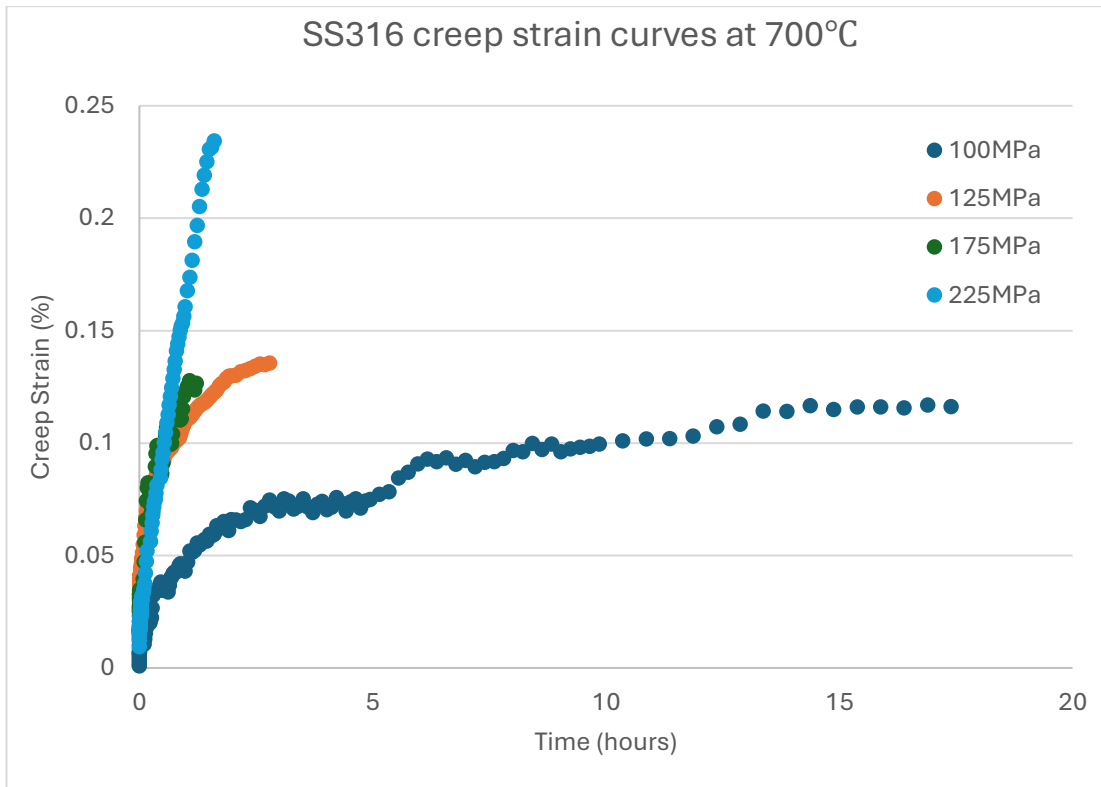
**Figure 4.23 Creep curves of SS316 tested at 700°C under applied stresses ranging from 100MPa to 225MPa.**
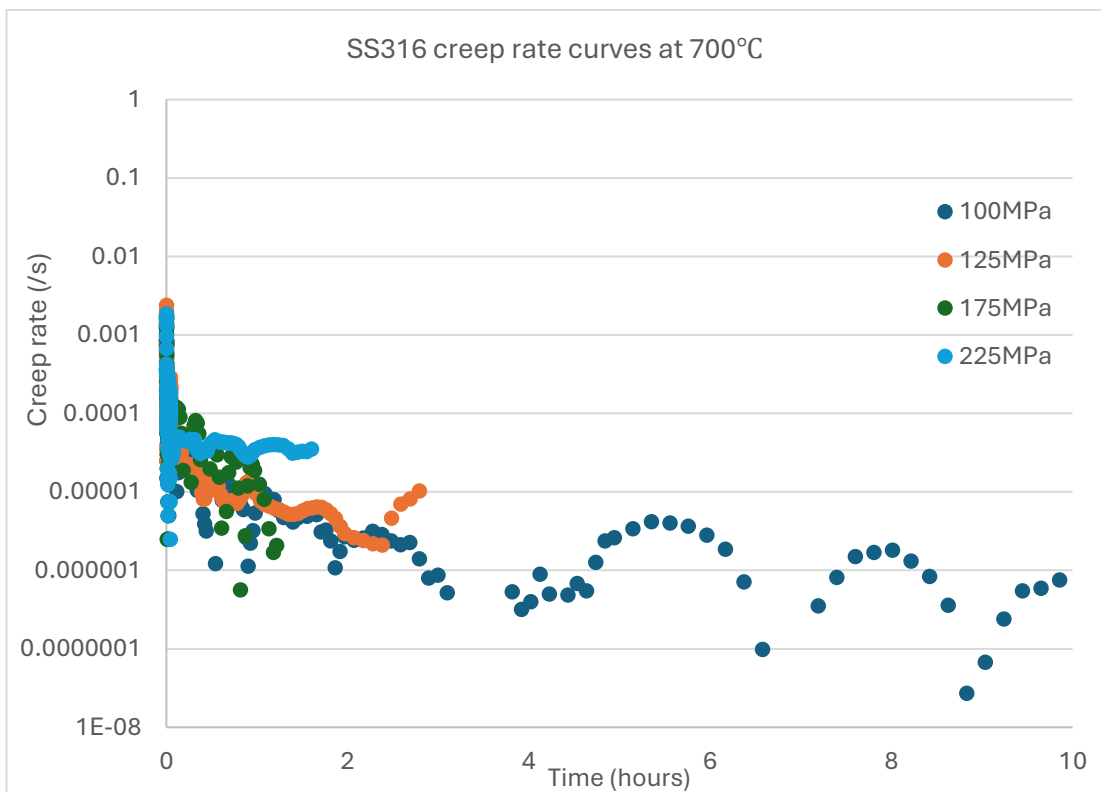


**Figure 4.24 Creep rate curves of SS316 tested at 700°C under applied stresses ranging from 100MPa to 225MPa.**

115

### 4.3.1.2  EBSD of crept samples

The EBSD maps of crept SS316 specimens tested at 600°C under different stress levels (125 MPa, 175 MPa, 225 MPa, and 275 MPa) are presented in Figure 4.25. The maps show the grain structure and twin boundary distribution after creep deformation. Despite increasing stress levels, the quantity of twin boundaries does not exhibit a significant increase. The Channel 5 software provides an imprecise identification of twin boundaries. This inaccuracy arises from residual stress and local misorientation, which can result in the software either failing to fully recognise actual twin boundaries or incorrectly identifying other boundaries as twins. Consequently, it cannot reliably determine the number of twins. However, manual counting has been conducted, and the number of twins observed is approximately consistent across the maps. Therefore, the twin boundaries, marked in red, appear to remain relatively stable quantities across all tested conditions, suggesting that deformation mechanisms at 600°C primarily involve dislocation motion and grain boundary sliding, rather than extensive twinning. This indicates that at 600°C, the stress levels applied may not have been sufficient to trigger significant twin formation.
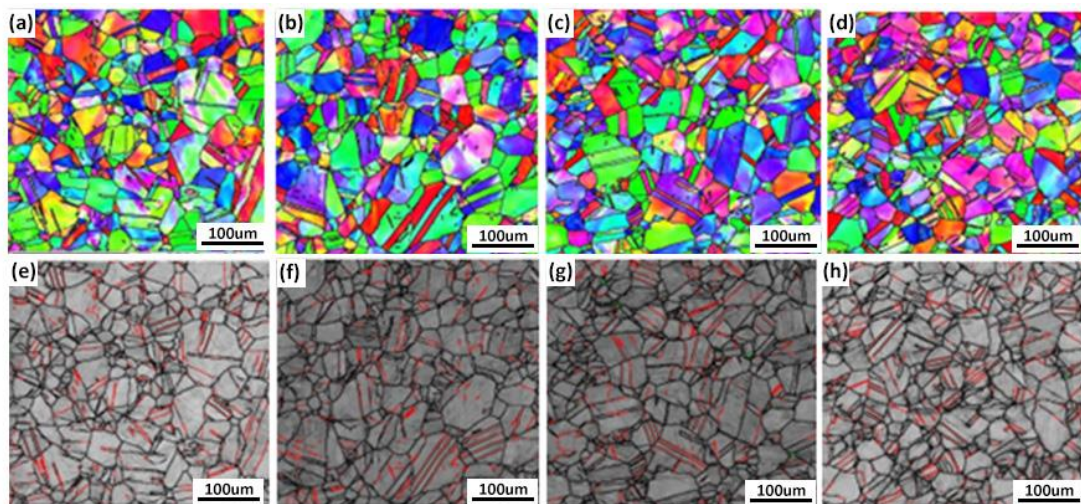


**Figure 4.25 EBSD maps of crept SS316 specimens tested at 600°C (a) 125MPa (b) 175MPa (c) 225MPa (d) 275 MPa, with twin boundaries showing at (e)-(f).**

In contrast, the EBSD maps of crept SS316 specimens tested at 700°C under stress levels of 100MPa, 125 MPa, 175 MPa, and 225 MPa (Figure 4.26) appear to show a noticeable trend of increasing twin boundary formation with increasing applied stress. At lower stresses (100MPa and 125 MPa), the twin boundaries are sparse, resembling the behaviour observed at 600°C. However, as the stress increases to 175 MPa and 225

MPa, the number of twin boundaries becomes more pronounced, indicating an enhanced role of twinning in the creep deformation process at 700°C. This suggests that at higher temperatures, twinning becomes an increasingly important deformation mechanism under elevated stress conditions.
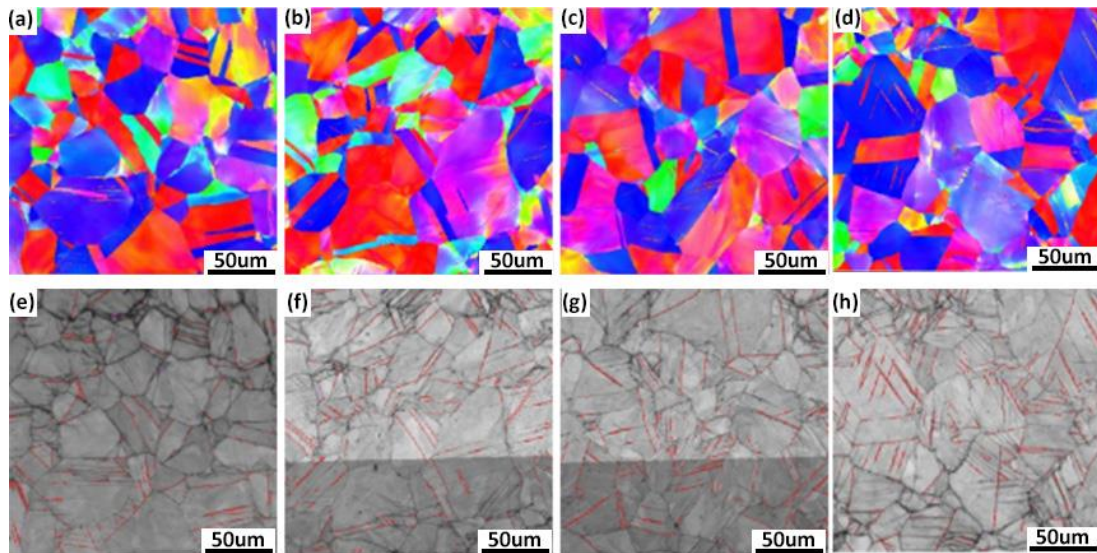


**Figure 4.26 EBSD maps of crept SS316 specimens tested at 700°C (a) 100MPa (b) 125MPa (c) 175MPa (d) 225 MPa, with twin boundaries showing at (e) – (f).**

## 4.3.2 Haynes 282

### 4.3.2.1 Creep data

Two creep tests for Haynes 282 were conducted with the support of Westmoreland under the conditions of 650°C and 500MPa, and 650°C and 800MPa, respectively. The resulting creep curves are presented in the Figure 4.27 below. The curve corresponding to 500MPa exhibits a gradual increase in strain, characterised by an initial primary creep stage followed by a relatively steady secondary creep phase. The strain accumulation remains minimal throughout the 50-hour duration, with a final strain below 2%. In contrast, the specimen tested at 800MPa displays significantly higher strain accumulation. The initial primary creep stage is followed by a well-defined secondary creep phase, after which the strain rate increases markedly, indicating the onset of tertiary creep. This transition occurs after approximately 20 hours, leading to a rapid escalation in deformation, with the final strain exceeding 7%. The pronounced difference in creep behaviour between the two conditions underscores the substantial

influence of applied stress on creep deformation, particularly in accelerating the transition to tertiary creep at higher stress levels.
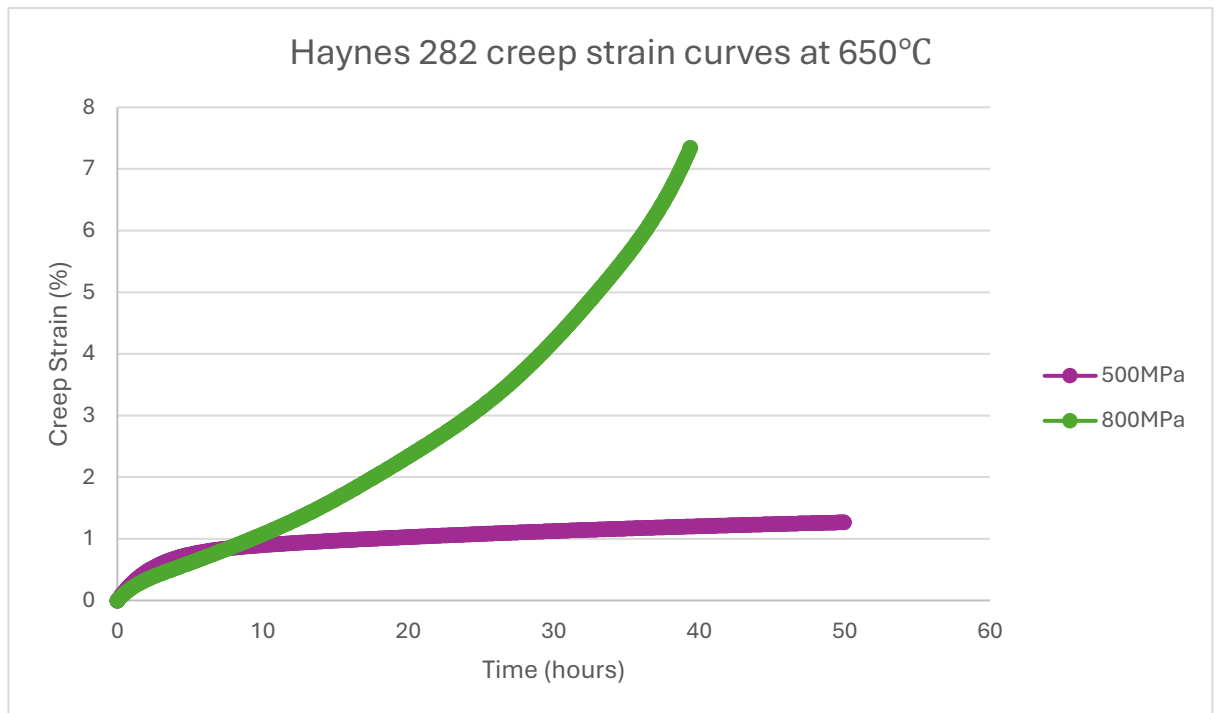


**Figure 4.27 Creep strain curves of H282 tested at 650°C under applied stresses of 500MPa and 800MPa.**

### 4.3.2.2    EBSD of crept samples

The 650°C, 800MPa creep test on Haynes 282 exhibited a typical and complete creep curve, leading to EBSD analysis of the fractured sample, as shown in Figure 4.28. The misorientation map provides insight into the strain distribution across the sample, with the fracture zone located on the left side.

The grains appear elongated in the direction of creep strain, compared to the EBSD map of as-received Haynes 282.  The EBSD misorientation map reveals a pronounced gradient of local misorientation, particularly near the fracture region, where elevated misorientation levels (indicated by intense contrast or colour variations) suggest significant localised plastic deformation and strain accumulation. Moving away from the fracture surface towards the centre and right side of the map, the misorientation gradients diminish, suggesting comparatively lower levels of deformation. However, strain accumulation is primarily concentrated at the grain boundaries, suggesting that grain boundaries of Haynes 282 were key contributors to the creep damage process. In contrast, the interior of grains exhibits lower misorientation levels, indicating that

118

intragranular dislocation activity, while present, played a secondary role in the final fracture.
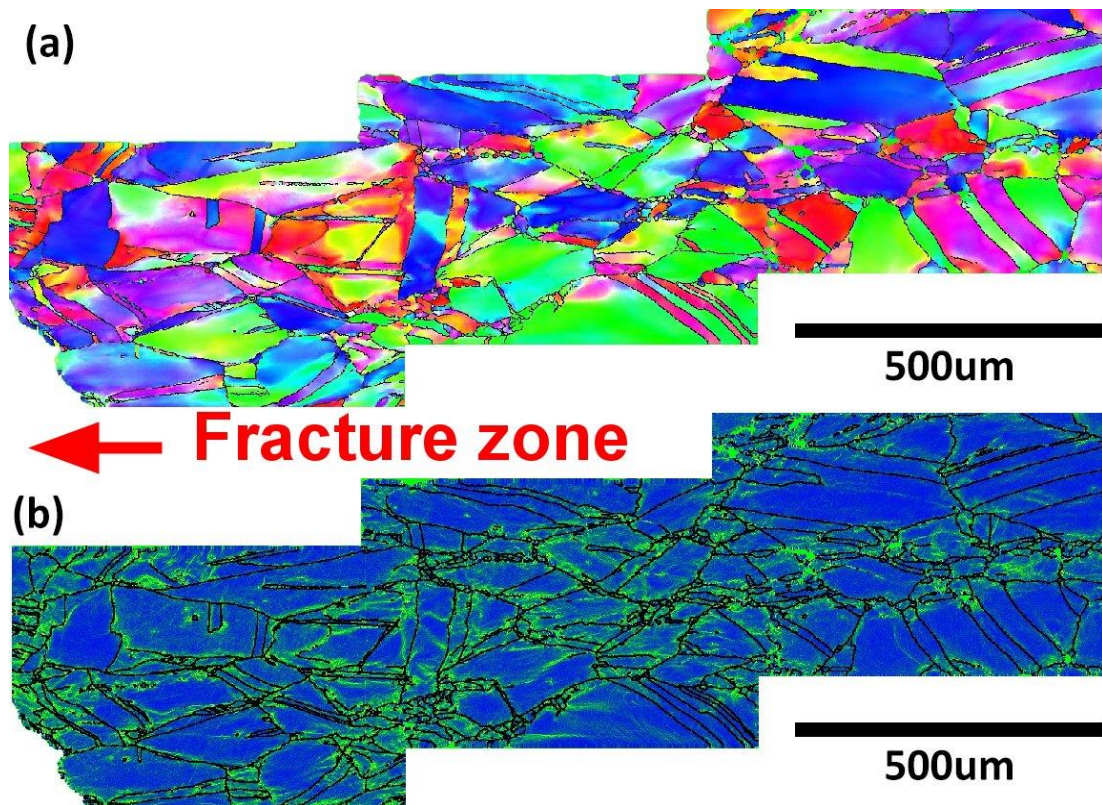


**Figure 4.28 EBSD maps of Haynes 282 after creep at 650°C, 800MPa, calculated by Channel 5 HKL (a) IPF map, (b)misorientation map.**

### 4.3.3 Inconel 713C

#### 4.3.3.1 Creep data

Due to the varying microstructural characteristics of the IN713C specimens, including equiaxed, columnar, and transition structures, additional creep tests were conducted on IN713C at temperatures of 650°C and 750°C, with applied stresses ranging from 500MPa to 800MPa. The specific microstructural features and experimental conditions were summarised in experimental procedure chapter.

The creep curves presented in Figure 4.29 illustrate the strain evolution of IN713C specimens with different microstructural conditions at 650°C under varying stress levels.
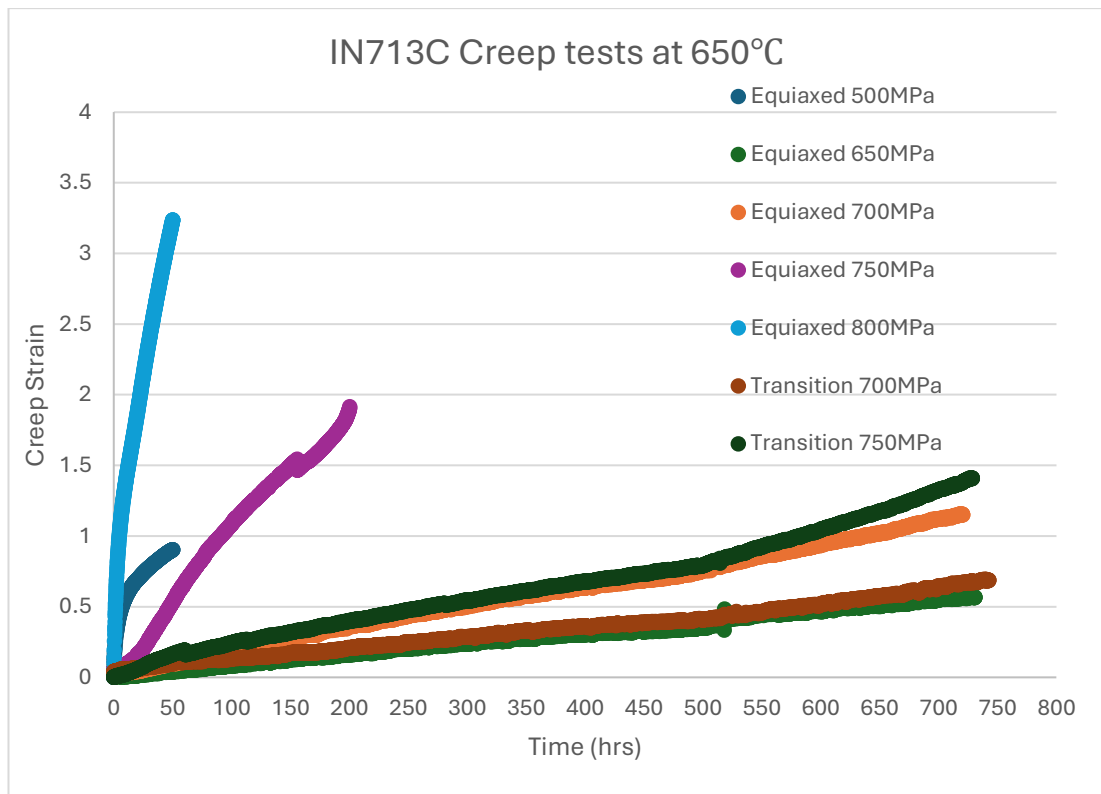
**Figure 4.29 Creep curves of IN713C with different grain morphology tested at 650°C under applied stresses ranging from 500MPa to 800MPa.**

The equiaxed 500MPa creep curve exhibits unusual strain behaviour, likely due to differences in specimen geometry. The samples sent to Westmoreland were in plate form, whereas the creep specimens tested at SMaRT were cylindrical bars. The stress distribution in plates is less uniform than in bars due to their geometry because plates typically have thinner cross-sections, greater width, and a rectangular profile, which can result in complex force and stress distributions under constant loading. Stress concentrations are more likely to occur near the support regions, particularly at the ends. In contrast, bars with uniform circular cross-sections tend to provide more homogeneous stress distribution, contributing to more consistent creep behaviour. Due to the short experimental time and the absence of comparative experiments, the results of the experiments under this experimental condition will not be considered subsequently.

At higher applied stresses (800MPa and 750MPa), the equiaxed specimens exhibited significantly higher creep strain and shorter test durations, with rapid primary and tertiary creep stages leading to early failure. The specimen tested at 800MPa experienced the highest strain accumulation, exceeding 3% within approximately 50

120

hours, followed by the 750MPa test, which nearly reached 2% creep strain before fracture.

For lower stress conditions (650MPa to 700MPa), the creep strain evolution was more gradual, with an extended secondary creep stage. The equiaxed specimens tested at 650MPa demonstrated relatively slow creep progression, with strains remaining below 1% even after 600–700 hours of testing. The transition specimens at 700MPa and 750MPa accumulated less strain than the equiaxed specimens at the same stress conditions, suggesting a potentially longer creep life.

These results suggest a strong dependence of creep behaviour on both stress levels and microstructural characteristics, with higher applied stress leading to accelerated creep deformation and failure, particularly in equiaxed specimens. The transition microstructure appears to enhance creep resistance under intermediate stress conditions, as indicated by the longer test durations and lower accumulated strain.

The creep curves in Figure 4.30 present the strain evolution of equiaxed IN713C specimens tested at 750°C under applied stresses of 500MPa and 800MPa.
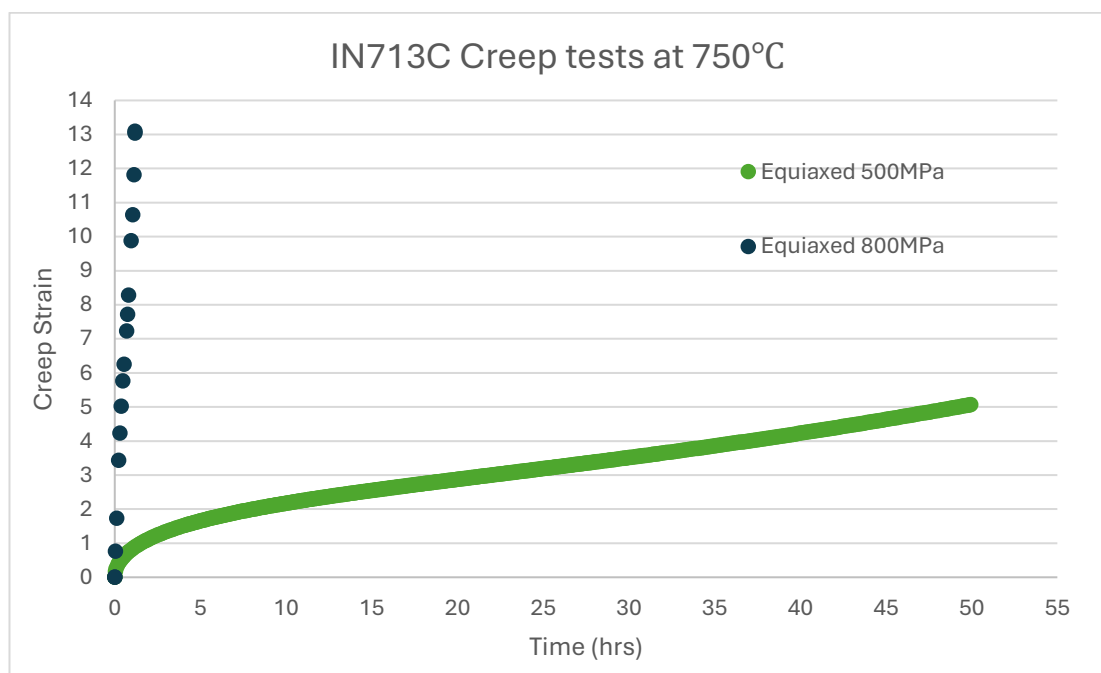


**Figure 4.30 Creep curves of IN713C with equiaxed grains tested at 750°C under applied stresses of 500MPa and 800MPa.**

The specimen tested at 800MPa exhibited rapid creep deformation, reaching a strain of approximately 13% within a very short duration (less than 5 hours), indicating a

predominance of tertiary creep and early failure. This suggests that at this stress level, the creep resistance of the equiaxed microstructure is significantly reduced, leading to a rapid loss of mechanical integrity.

Conversely, the specimen tested at 500MPa demonstrated a much slower strain accumulation, with a gradual increase over time. The creep strain remained around 5% even after 50 hours of testing, indicating an extended secondary creep stage with lower strain rates. This suggests that at moderate stress levels, the material retains its creep resistance for a longer duration, delaying the onset of tertiary creep.

### 4.3.3.2 Microstructure analysis of crept samples

### 4.3.3.2.1 Equiaxed microstructure

Under the testing condition of 650°C and 750MPa, the creep curve of equiaxed IN713C transitions rapidly from the primary stage into an accelerated tertiary stage, culminating in early fracture. The fracture surface, shown in Figure 4.31, confirms this observation: a dendritic morphology is clearly visible, with predominantly flat fracture surfaces and steps, and minimal plastic deformation of the dendrites as the dendritic arm lines as well as their intersection are very visible across this fracture surface. No dimples are present, indicating a very low fracture resistance and severely reduced strength and ductility at this stage. Furthermore, higher-magnification observations reveal shrinkage porosity resulting from the solidification process, which may partly explain the catastrophic failure within such a short time.
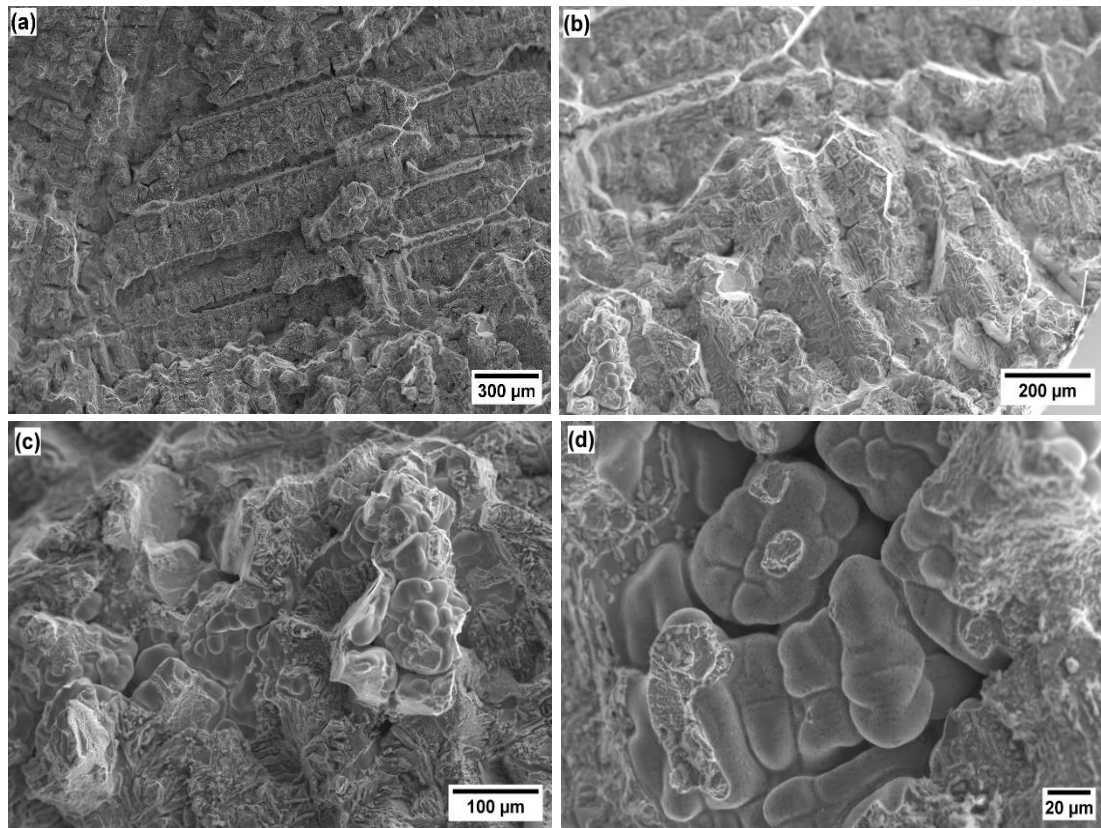
**Figure 4.31 Fractography of crept equiaxed IN713C specimen tested at 650°C and 750MPa at (a)x50 (b)x100 (c)x200 and (d)x500 magnifications.**

The interdendritic areas often exhibit higher concentrations of alloying elements rejected by the growing dendrites, leading to the precipitation of carbides[237]. The presence of these phases can either strengthen or weaken the material, depending on factors such as carbide type, size, and distribution[226-228]. However, under high-temperature creep conditions, these regions become preferential sites for micro-crack and void initiation, as carbides introduce local stress concentrations due to their stiffness mismatch with the matrix, as shown in Figure 4.32 where crack and voids formed on the carbides. As creep deformation progresses, voids coalesce and cracks propagate along the matrix-carbide interfaces, ultimately forming intergranular cracks that significantly reduce the alloy's load-bearing capacity. This behaviour is further illustrated in Figure 4.33, where cracks nucleate at carbide particles and subsequently extend along grain boundaries, confirming the role of carbides in creep damage accumulation and failure.
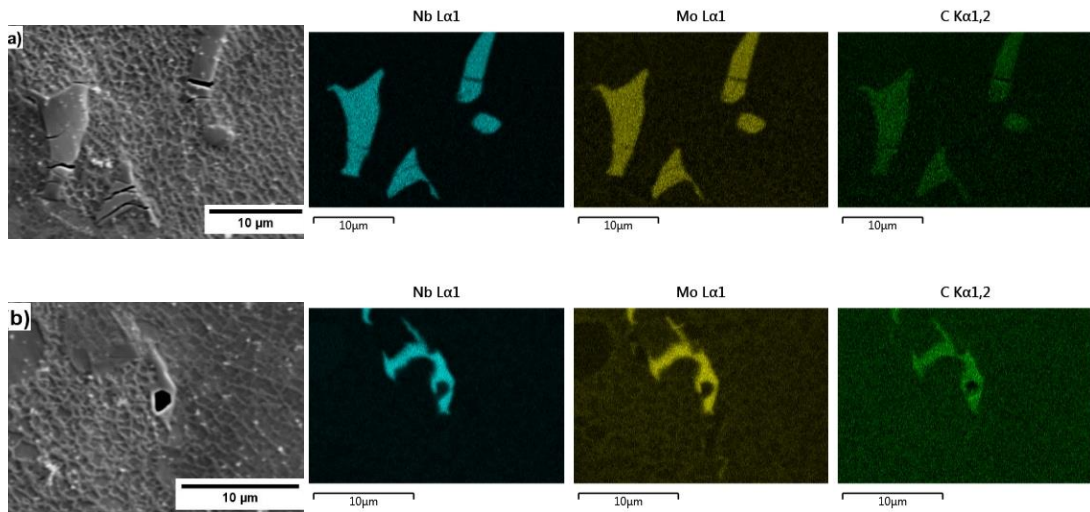
**Figure 4.32 SEM images and EDS maps of carbides illustrating the formation of (a) cracks and (b) a void.**
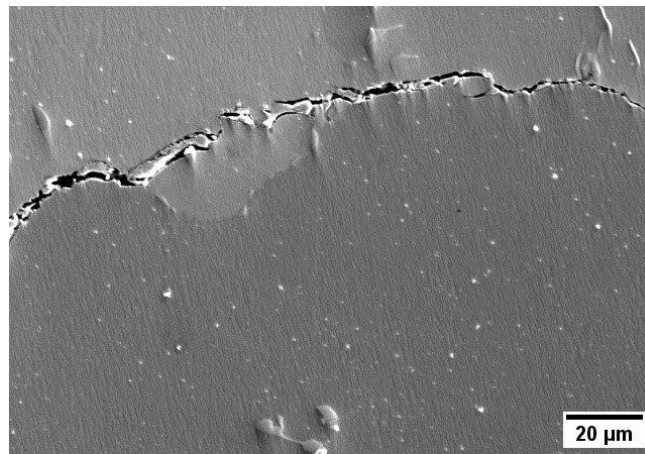


**Figure 4.33 SEM image of an intergranular crack in crept equiaxed IN713C specimen after testing at 650°C and 750MPa.**

A creep specimen tested at 650 °C and 750 MPa, where fracture occurred, was selected for EBSD analysis to investigate localised strain accumulation as shown in Figure 4.34. The grain size appeared similar to that of an equiaxed structure; however, the grain morphology was more elongated, resembling small columnar grains rather than equiaxed. No distinct intergranular fracture was observed at the fracture zone. The grains that were presumed to be columnar may have resulted from a manufacturing issue, leading to unexpected grain morphology. Nevertheless, since the grain size did not reach that typically associated with columnar grains, the impact on the mechanical data is likely negligible.

One region located further from the fracture zone was selected for misorientation analysis. Unlike in Haynes 282, strain accumulation was observed within the grains rather than along the grain boundaries, and the distribution appeared to follow a certain pattern.
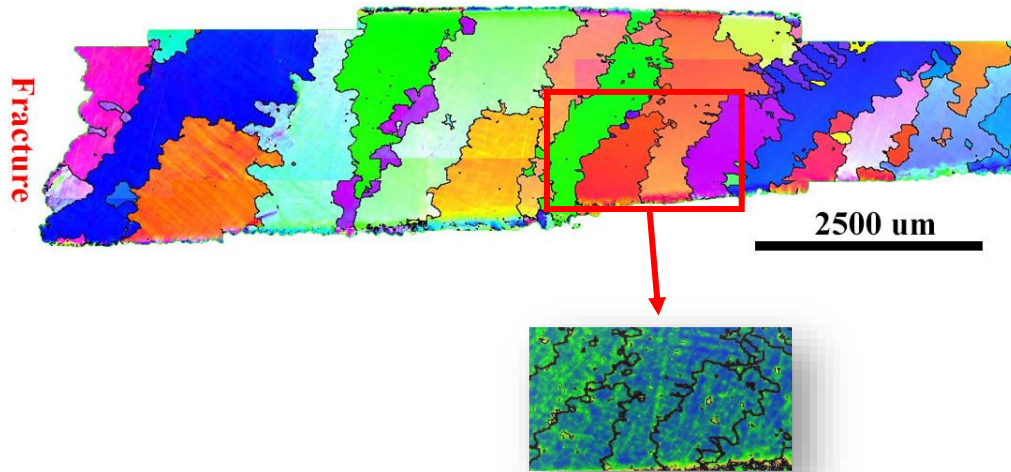


**Figure 4.34 EBSD map at IPF Z direction of equiaxed IN713C crept at 650℃ 750MPa.**

### 4.3.3.2.2 Columnar microstructure

Although no complete fracture was observed in the columnar-grained specimens, the presence of cracks and voids was detected in the central region of the specimen. The voids, shown in Figure 4.35, were found to be located along the grain boundaries, with EDS maps confirming that these voids originated around the coarse gamma prime precipitates. These defects indicate the onset of creep damage accumulation, likely initiated by stress concentrations near the grain boundaries and coarse gamma prime. While these cracks have not yet propagated to cause complete failure, their presence highlights the progressive nature of creep deformation and suggests that extended exposure under these conditions could eventually lead to intergranular crack coalescence and final rupture.
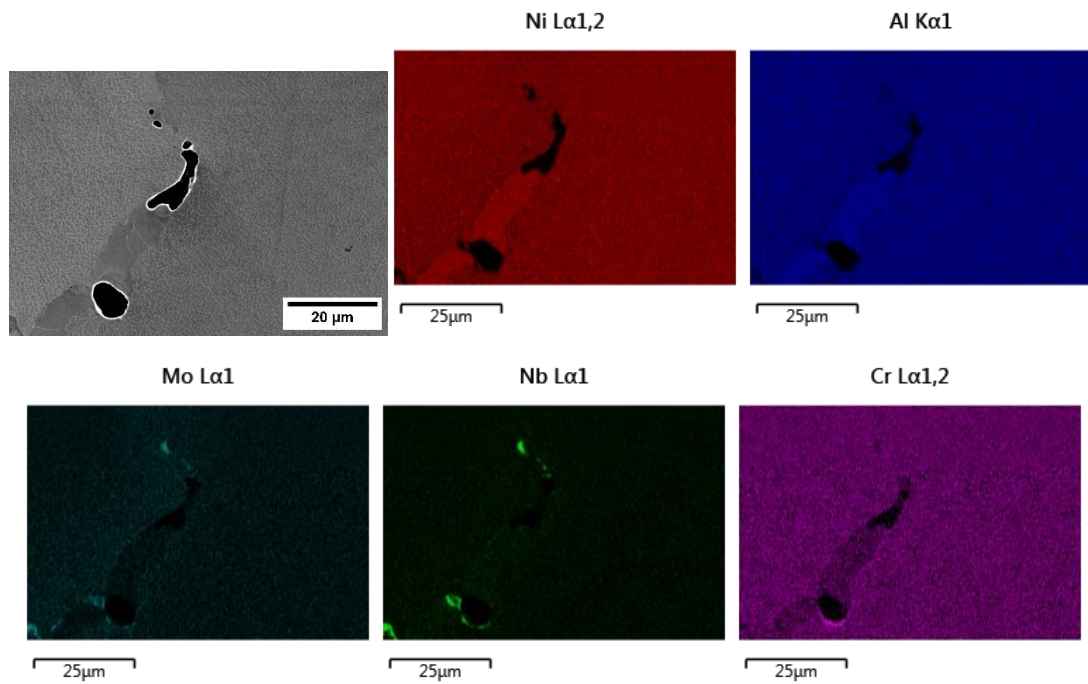
**Figure 4.35 EDS maps of a crack in crept columnar IN713C specimen after testing at 650°C and 500MPa.**

Columnar grains are typically very large—reaching millimetres or even centimetres in length. Due to specimen size constraints, no intact columnar grains were retained in the processed samples as shown in Figure 4.36. Furthermore, the solely columnar specimens did not fracture during testing and were therefore excluded from further EBSD analysis.
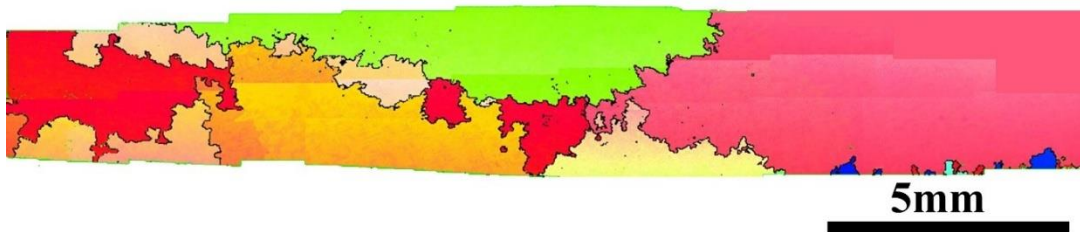


**Figure 4.36 EBSD map at IPF Z direction of Columnar IN713C crept at 650℃ 500MPa.**

#### 4.3.3.2.3   Transition microstructure
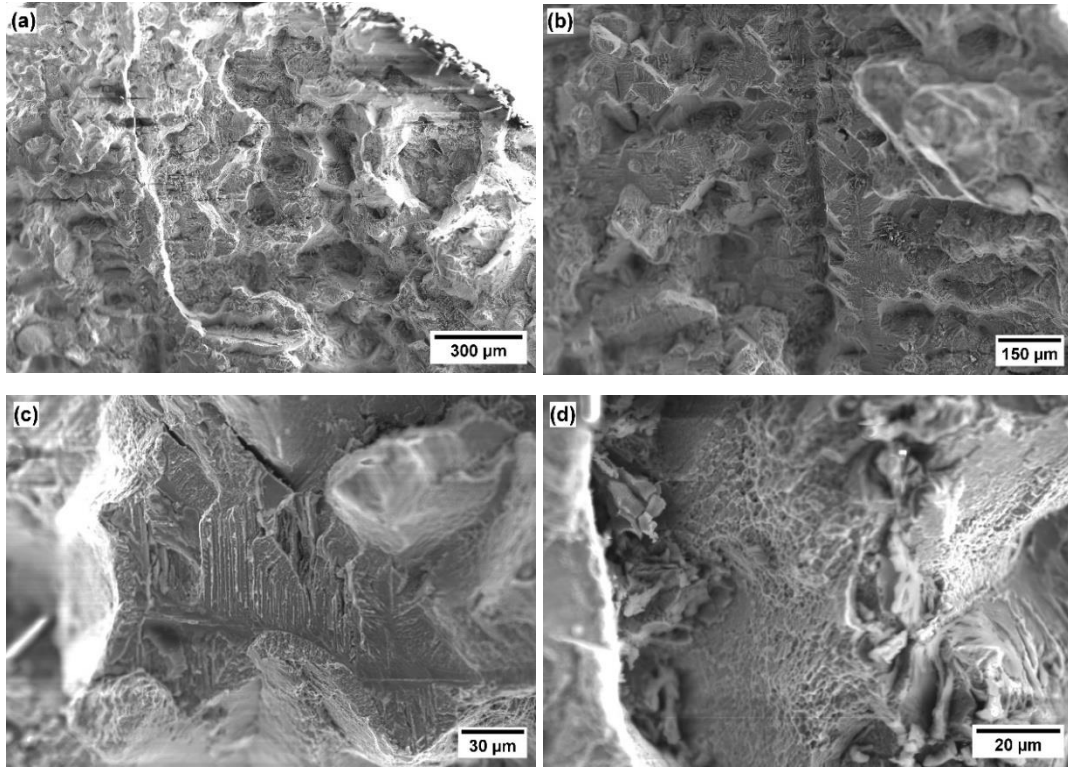


**Figure 4.37 Fractography of crept transition IN713C tested at 650°C, 800MPa at (a) x70, (b) x100, (c) x500, and (d) x1000 magnifications.**

The fracture surface of the specimen exhibits distinct morphological features indicative of high-temperature creep failure, as observed at varying magnifications. At low magnification (Figure 4.37(a) and (b), 70x–100x), the fracture surfaces appeared highly irregular and were marked by disintegration steps. Traces of dendritic arms were observed, although in significantly reduced numbers.

At higher magnification (Fig. 4.36(d)), the fracture surface exhibited fine cratering features, indicative of limited ductile tearing in certain regions. However, the overall morphology lacked evidence of extensive microporous coalescence, supporting the conclusion that the dominant fracture mechanism was predominantly brittle.

One creep test on IN713C with a transition microstructure at 650°C and 650MPa was conducted with support from The Open University, the creep curve is shown in Figure 4.38. This dataset was not included in earlier creep curve comparisons, as The Open University employed the digital image correlation (DIC) method, producing data in a different format than the LVDT-based measurements.
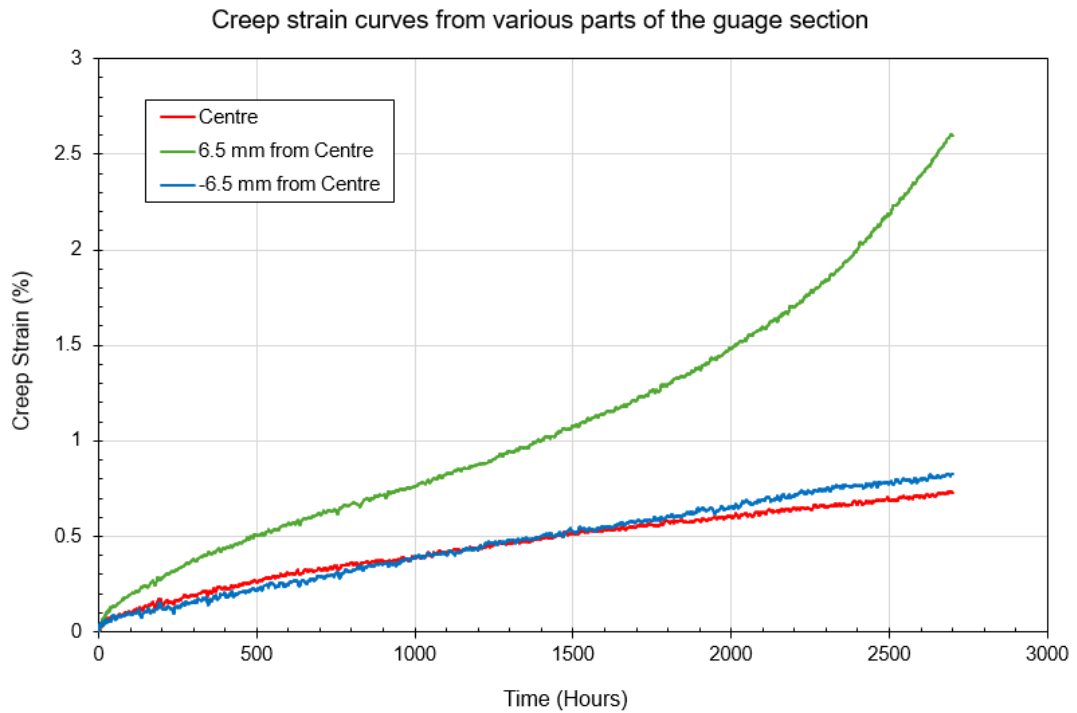
**Figure 4.38 Creep strains curves obtained from a constant creep test of IN713C with transition microstructure with test conditions at 650℃ and 650MPa.**
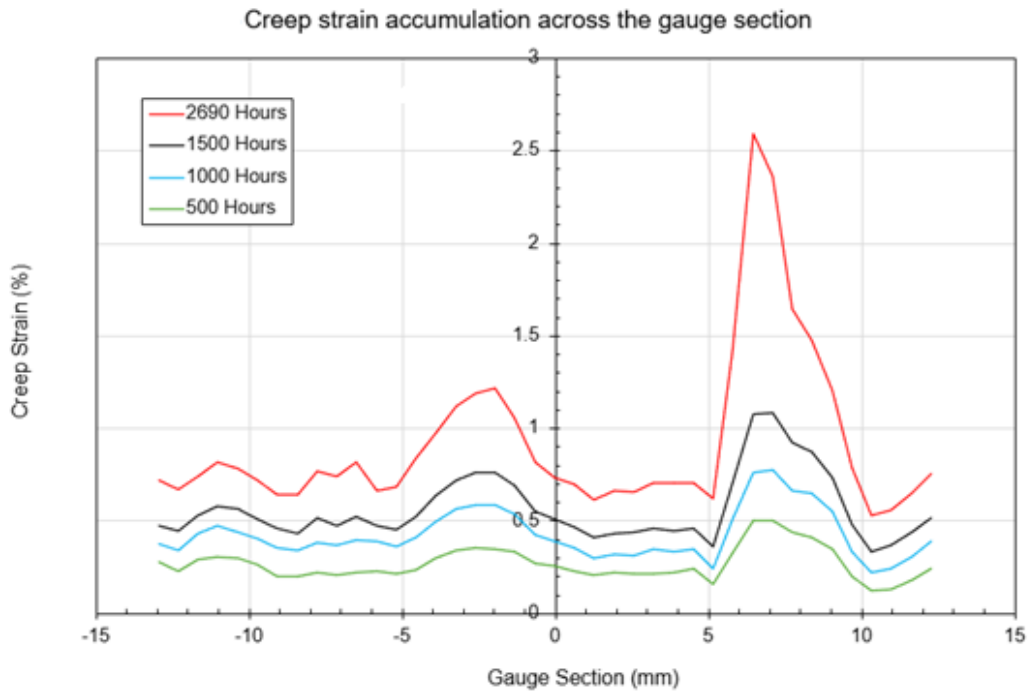


**Figure 4.39 Creep strain accumulation graph across the gauge section obtained from a IN713C specimen with transition microstructure, with test conditions at 650℃ and 650MPa.**

The DIC results indicated that strain accumulation in the transition-structured sample was not centred, but instead localised toward one side, see Figure 4.38 and Figure 4.39. Based on comparisons with other datasets, it is believed that this localisation occurred in the equiaxed region. This assumption is supported by the observation that equiaxed specimens exhibited higher creep strain and creep rates than transition specimens under identical conditions, suggesting greater susceptibility to stress accumulation and creep fracture.

Figure 4.40 shows the EBSD image of IN713C with a transition microstructure after creep testing at 650 °C and 800 MPa. However, this map of the fractured specimen revealed that the fracture more likely occurred within the columnar region, contradicting the initial assumption and highlighting the need for further investigation.

Misorientation analysis was performed on this partially fractured specimen. As expected, significant strain accumulation is observed in the fracture zone. However, the regions of high misorientation—indicated by highlighted areas—are predominantly located within the grains rather than along the grain boundaries. These regions also exhibit a clearly dendritic morphology. The specific mechanisms underlying this behaviour will be explored further in the discussion chapter.
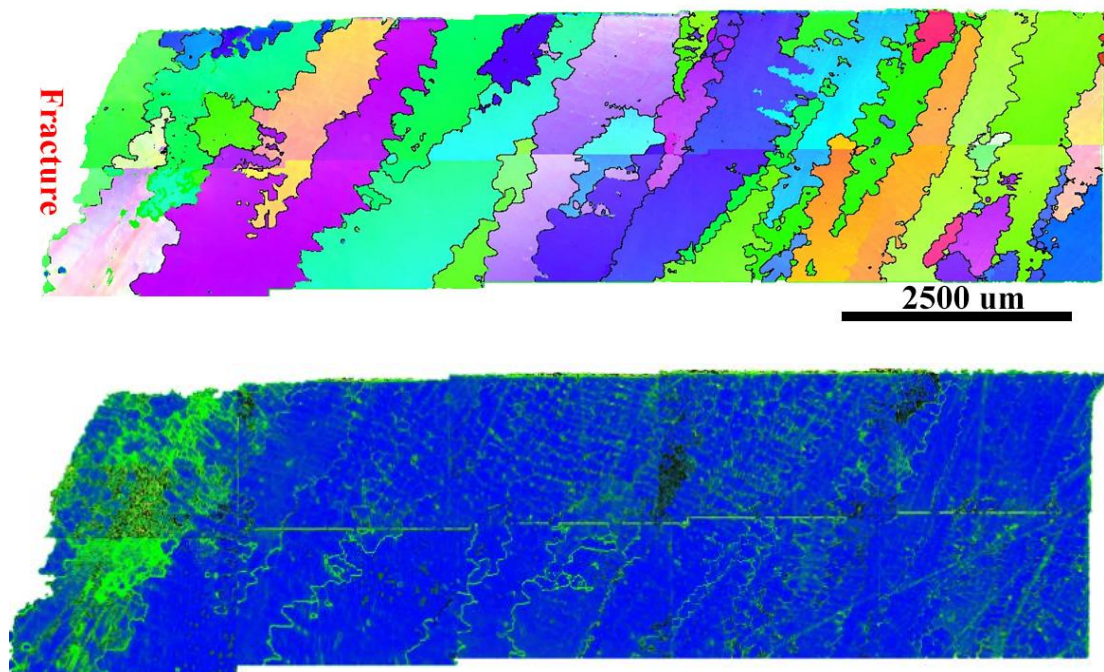


**Figure 4.40 EBSD map at IPF Z direction of transition IN713C crept at 650℃ 800MPa.**

## 4.4 Wilshire Analysis of Creep Data

### 4.4.1 316 Stainless steel

The Wilshire Equations require an initial rearrangement to obtain a linear form. Given that the Wilshire model consists of three distinct equations, the equation for time to rupture $t_f$ will be used as an example:

$$\ln\left(-\ln\sigma/\sigma_{TS}\right) = u\ln\left(t_f \exp\left(-\frac{Q_c*}{RT}\right)\right) + \ln k_1$$

<div align="right">**Eq. 4-1**</div>

The activation energy $Q_c*$ in the Wilshire Equations is illustrated through a scatter plot of $\ln(t_f)$ versus $1/RT$ in relation to $\sigma/\sigma_{TS}$. The slopes of these plots yield $Q_c*$. The constants u and $\ln k_1$ correspond to $\ln(-\ln \sigma/\sigma_{TS})$ plotted against $\ln(t_f \exp(-Q_c*/RT))$, represented by the slopes and y-intercepts of the plot.
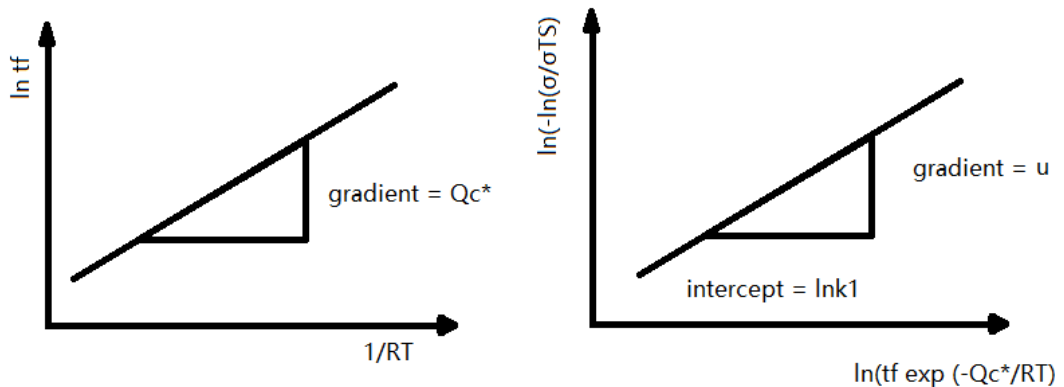


**Figure 4.41 The linear relationships to determine $Q_c*$ and constants u and k.**

To quote the selected activation energy $Q_c*$ to a certain level of accuracy, the regression coefficient ($R^2$) was plotted as a function of assumed $Q_c*$ (Figure 4.42 and Figure 4.43). The maximum $R^2$ was obtained at $Q_c* \approx 205$ kJ/mol for 316 bars and $Q_c* \approx 235$ kJ/mol for 316 plates, which was taken as the optimum value for subsequent analysis. The relatively narrow plateau around the peak indicates that the fitted results remain robust within $\pm 15$ kJ/mol.
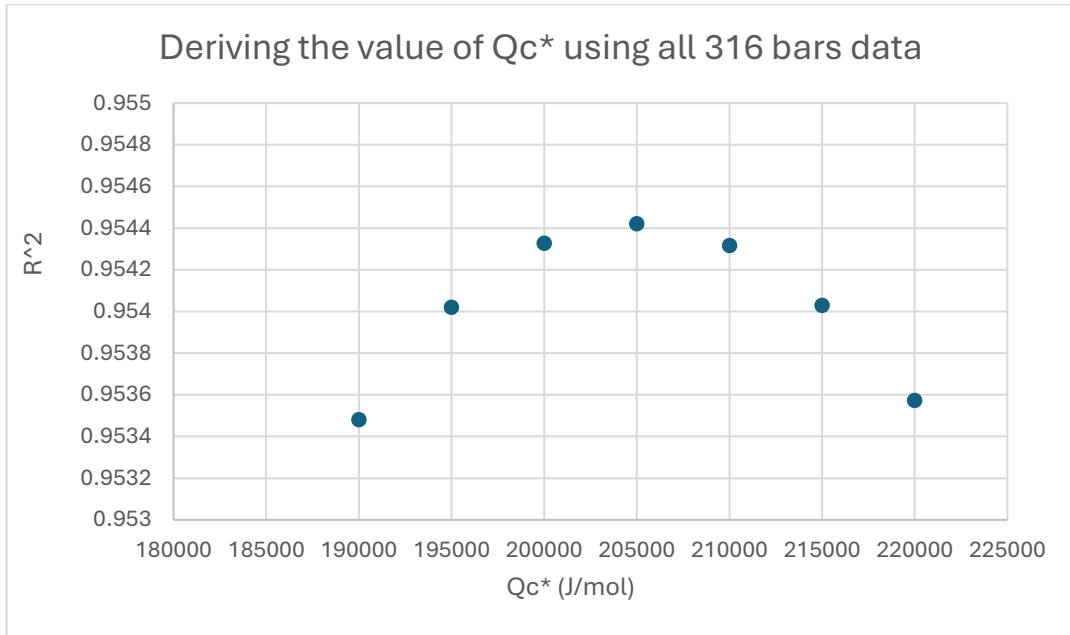
**Figure 4.42 Determination of the optimum activation energy ($Q_c$) for SS316 bars using the Wilshire Equations.**
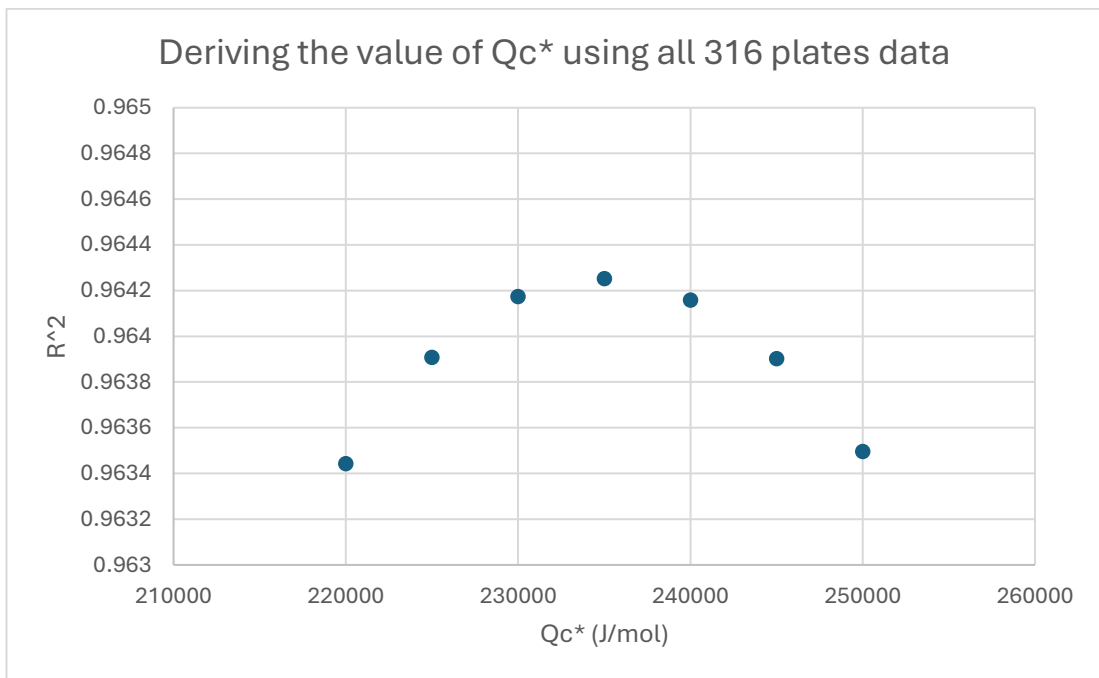


**Figure 4.43 Determination of the optimum activation energy ($Q_c$) for SS316 plates using the Wilshire Equations.**

In the case of using different creep activation energies, the change in constants u and $k_1$ would be shown in the Table 4-4:

131

**Table 4-4 Wilshire Equations parameters ($Q_c^*$, u, $k_1$) for 316 bars and plates with selected values and ±15 kJ/mol bounds.**

|  | Lower bounds (+15kJ/mol) | | Selected $Q_c^*$ | | Upper bounds (-15kJ/mol) | |
|---|---|---|---|---|---|---|
|  | **Bar** | **Plate** | **Bar** | **Plate** | **Bar** | **Plate** |
| $Q_c^*$ (kJ/mol) | 190 | 220 | 205 | 235 | 220 | 250 |
| **u** | 0.159 | 0.153 | 0.153 | 0.148 | 0.147 | 0.143 |
| $k_1$ | 20.5 | 22.0 | 17.5 | 26.0 | 14.4 | 30.6 |

These values reflect the equations being optimised in respect of the change in $Q_c^*$, and would provide relatively accurate version of the Wilshire Equations. However, for the remainder of this work the decision is made to use the value of $Q_c^*$ optimised by maximising the $R^2$ value, whilst recognising that this value comes with a degree of uncertainty, and described above.

A key feature of the Wilshire Equations is region splitting. This approach was introduced after previous researchers observed that variations in stress and temperature can lead to shifts in the dominant creep mechanism, resulting in data that are not uniformly predictable[60]. Kimura et al.[95-101] applied region splitting to a wide range of steels under both high and low stress conditions using the Larson-Miller method, and identified the half-yield point as a consistent 'breakpoint'. This finding was successfully applied to other steels for improved modelling accuracy.

However, the region splitting method used by Kimura et al. [103] was primarily focused on enhancing predictive capability and did not allow for a rigorous microstructural investigation to confirm whether the creep mechanism had changed. In contrast, the Wilshire approach integrates microstructural considerations by allowing the experimental data itself to determine the breakpoint. This breakpoint often coincides with a physically meaningful value—such as the yield stress or a stress level associated with microstructural transitions like overaging.

These 'breakpoints' or 'kink points' divide the dataset into high- and low-stress regions. The activation energy $Q_c^*$, as well as the constants $k_1$ and u, varies across these breakpoints. The impact of these distinctions is demonstrated in the following results:

As shown in Figure 4.44 and Figure 4.45, the breakpoint, indicated by the cross of the green lines, separates the high-stress and low-stress regimes, reflecting a distinct change in creep mechanism.
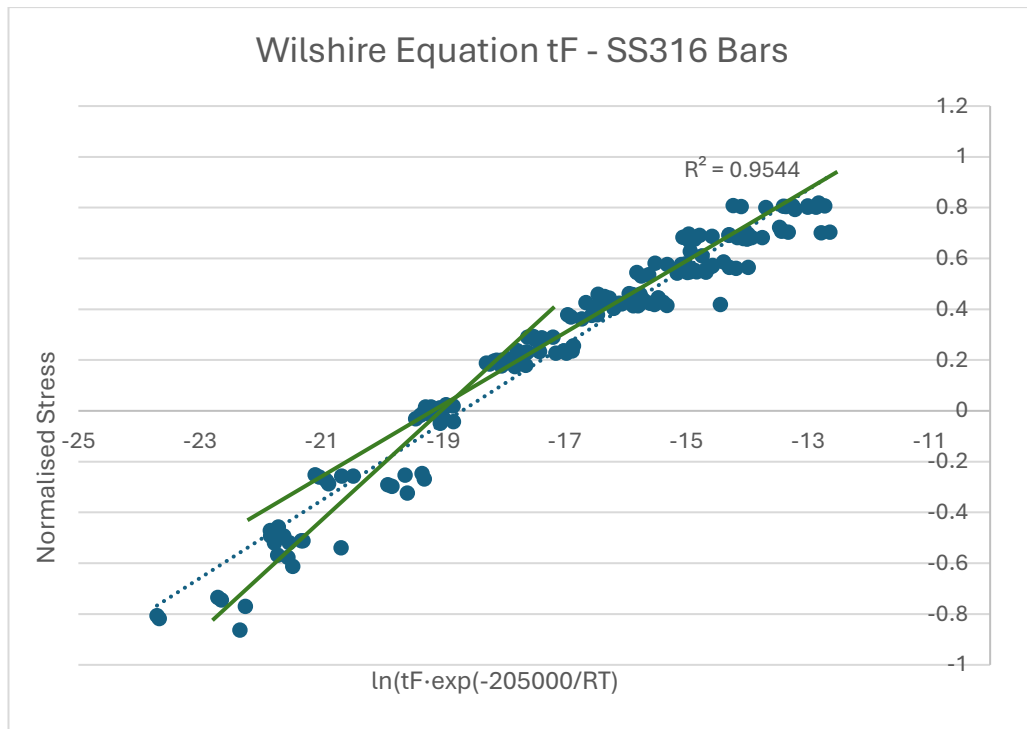


**Figure 4.44 Determination of the breakpoint in SS316 bar.**
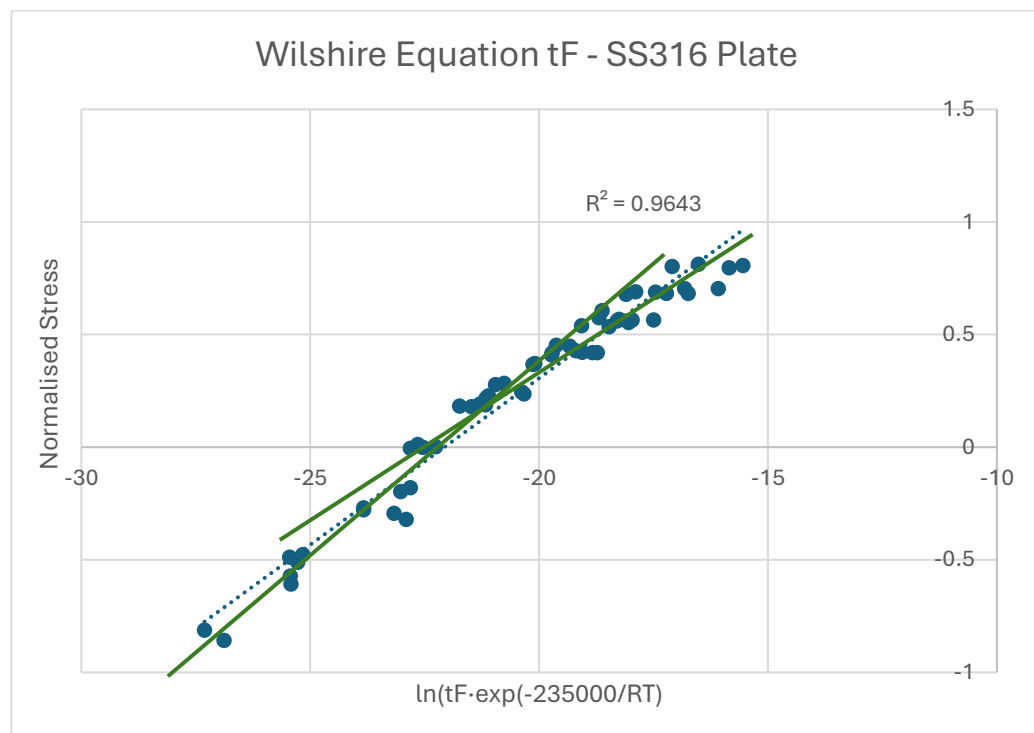


**Figure 4.45 Determination of the breakpoint in SS316 plate.**

**Table 4-5 Results after splitting regions for SS316 bar and plate**

| | High Stress | | Low Stress | |
|---|---|---|---|---|
| | **Bar** | **Plate** | **Bar** | **Plate** |
| $Q_c^*$ **(kJ/mol)** | 298 | 298 | 153 | 181 |
| **u** | 0.146 | 0.132 | 0.144 | 0.131 |
| $k_1$ | 85.6 | 49.4 | 6.36 | 8.50 |

The experimental data from the high and low stress regions of stainless steel bar and plate were fitted using different activation energy values obtained, as shown in Figure 4.46 and Figure 4.47.
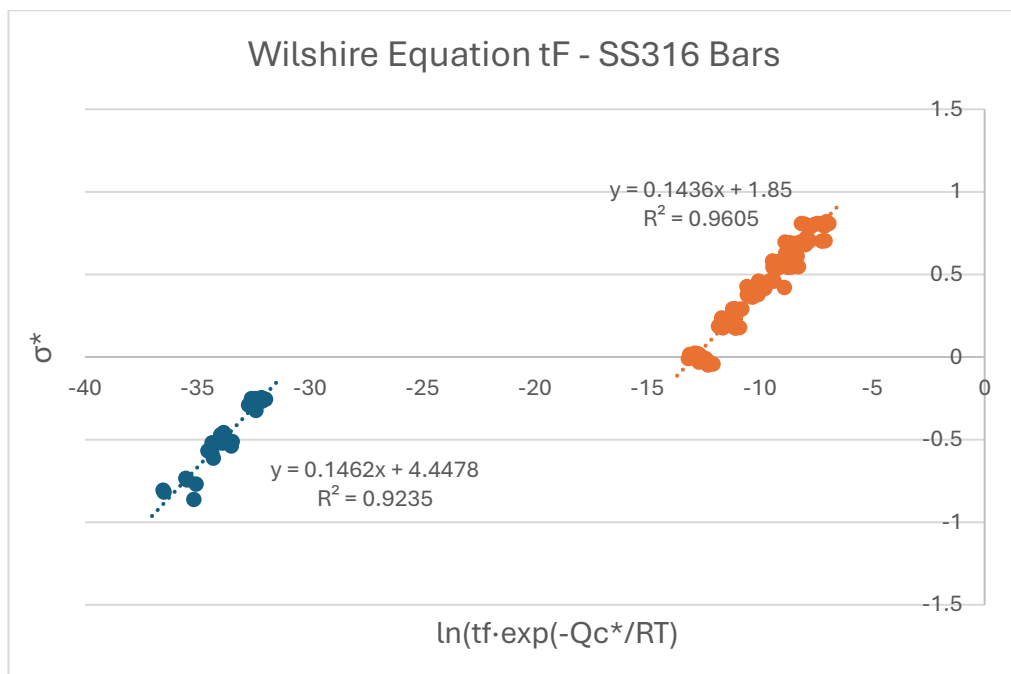


**Figure 4.46 Region splitting of the Wilshire Equations for SS316 bars.**
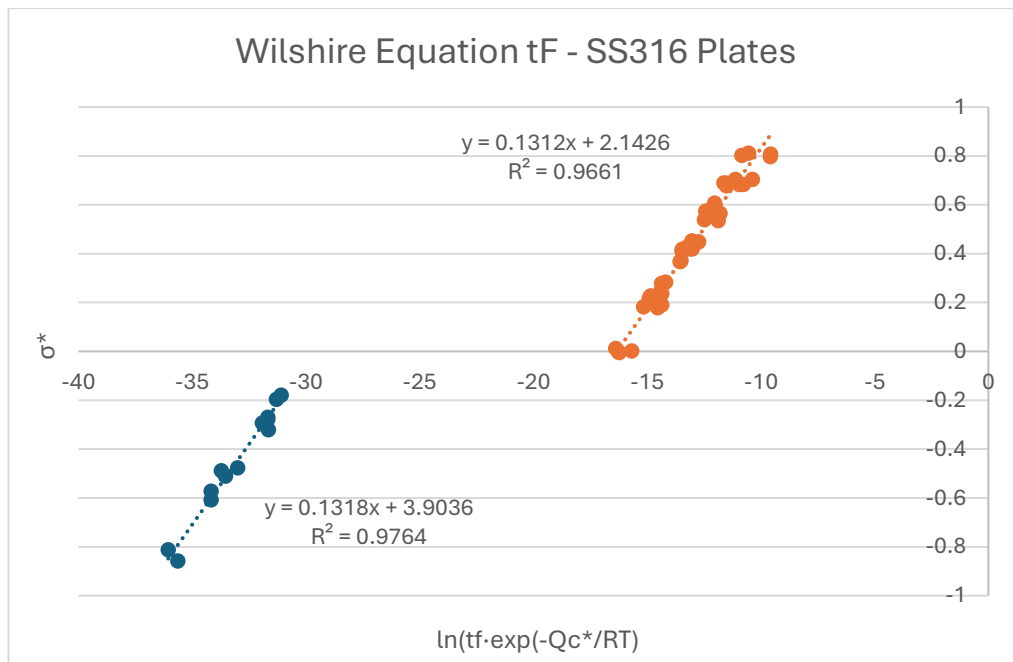
**Figure 4.47 Region splitting of the Wilshire Equations for SS316 plates.**

## 4.4.2 Haynes 282

While the current programme did not have the capability to collect substantial volumes of data, it is feasible to utilise the findings of other studies. The study conducted by Santella et al.[206] observed that Haynes 282, which contained a minor quantity of precipitation-hardened phase, exhibited a modification in activation energy. A series of tensile and creep experiments were conducted on Haynes 282 specimens from three furnaces throughout the temperature range of 593-927 °C, see Figure 4.48.

To enable direct comparison with published datasets, the experimental results obtained in this study have been superimposed onto the literature plots. The rupture data (650℃, 800MPa) are represented by solid brown star markers, showing that the specimen fractured at 39.4h, while the creep test with 650℃, 500MPa did not fracture and is plotted as a right censored point with brown line. This overlay confirms that the current results are consistent with the overall trends reported in the literature.
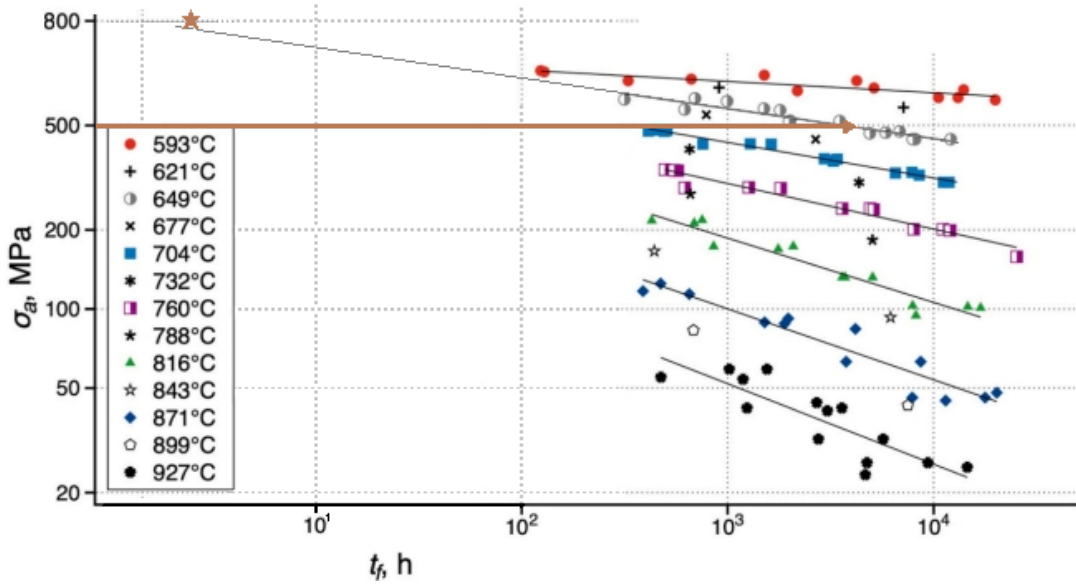
**Figure 4.48 Stress vs. rupture time for H282[5]. Solid brown star symbol shows the data of 650°C, 800MPa test conditions of this study, and the right-censored point with brown line shows the 650°C, 500MPa data.**

The obtained values were subsequently normalized using the Wilshire Equation, yielding an activation energy value of 301 kJ/mol, as depicted in Figure 4.49.
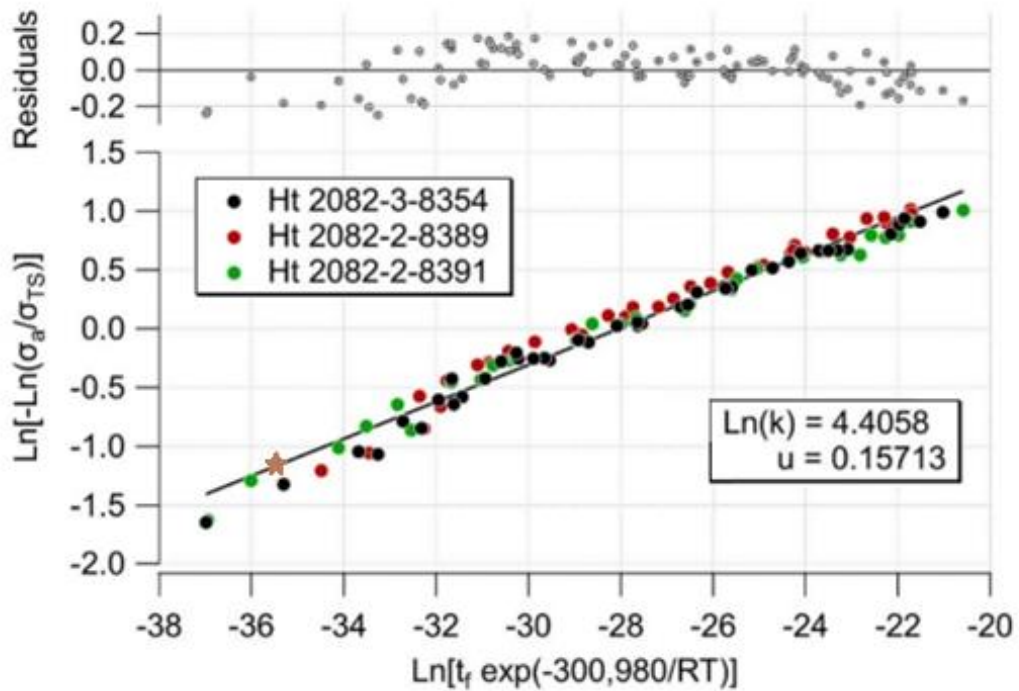


**Figure 4.49 Determination of the breakpoint for the Wilshire Equations in H282[206]. Solid brown star symbol shows 800MPa results from this study.**

The solid brown star represents the result of the present 800 MPa test, which was analysed using an activation energy of 301 kJ/mol within the Wilshire Equation. When plotted alongside the literature dataset, this point falls on the same trend line as the published results, indicating that the creep behaviour observed in this study is consistent with established data.

However, it can be observed from both the residual plot at the top and the scatter plot below that the single linear regression model may not be entirely appropriate. There appears to be a distinct change in the relationship between the variables, indicating the presence of a kink point. To further investigate this, the test samples were divided into two groups based on stress levels. Subsequently, a linear regression analysis was performed on each group separately (Figure 4.50). The results revealed that the activation energy varied between 277 and 427 kJ/mol, which is similar to the creep activation energy results of Waspaloy [19].
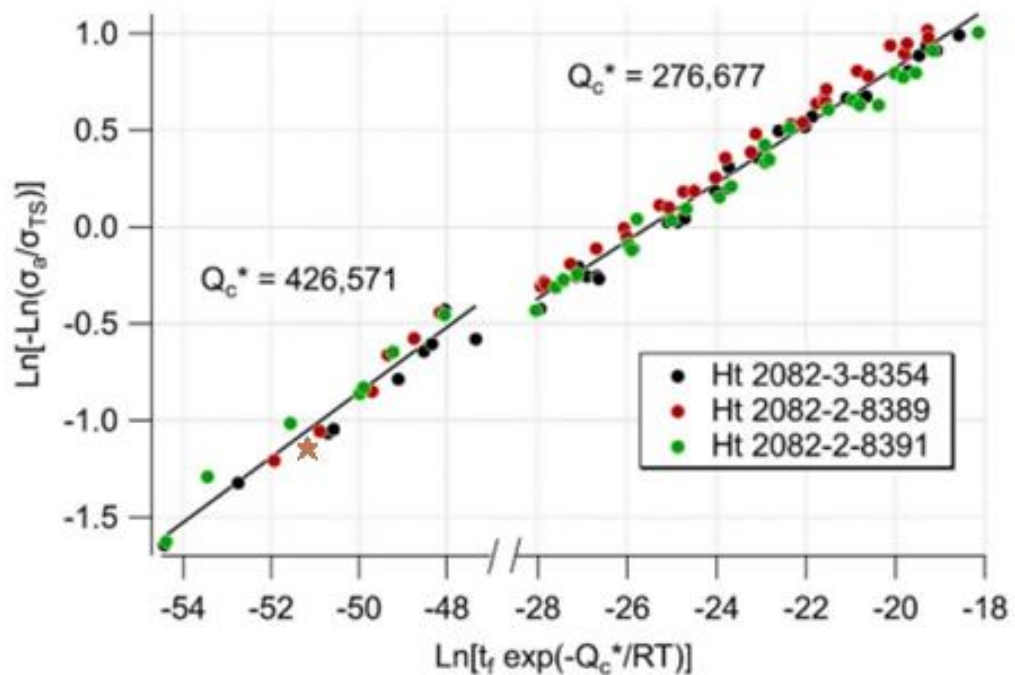


**Figure 4.50 Region splitting of the Wilshire Equations for H282**[206]. **Solid brown star symbol shows 800MPa results from this study.**

In the present study, the condition of 800 MPa was treated as a high-stress regime, and an activation energy of 427 kJ/mol was therefore adopted for the Wilshire equation region-splitting analysis. The corresponding experimental result, shown as a solid brown star, also lies close to the literature trend line. This agreement demonstrates that

the current high-stress rupture behaviour aligns well with previously reported data, thereby providing strong validation that the literature dataset can be reliably used to support the findings of this study.

### 4.4.3 Inconel 713C

The dataset from creep experiments conducted on INC713LC acquired by Kvapilová et al. [190], as shown in Figure 4.51 and Figure 4.52, was utilised to fit the experimental results to the Wilshire Equation, enabling a comparative analysis of creep behaviour. The data was fitted using two Wilshire Equations, specifically for rupture time and minimum creep rate.
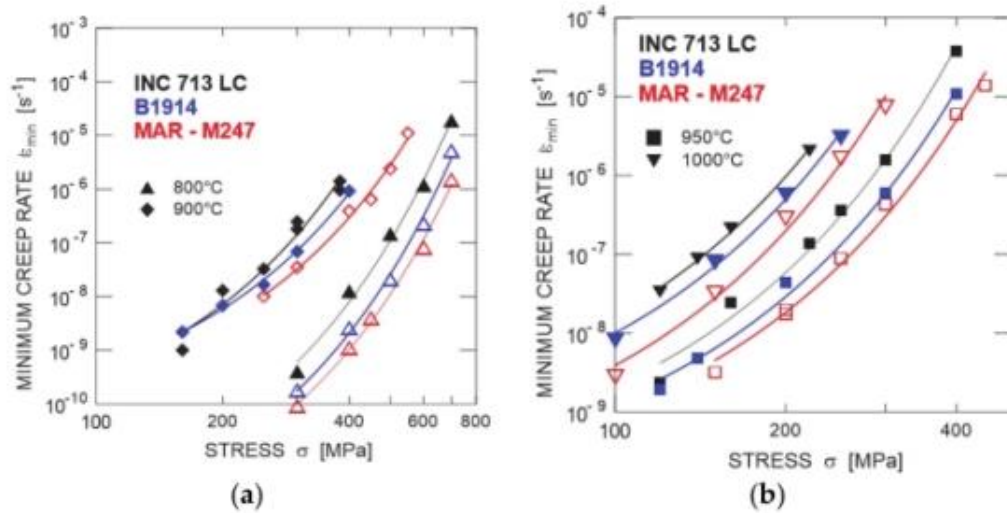


**Figure 4.51 Minimum creep rate VS stress plot of cast nickel-based superalloys[8].**
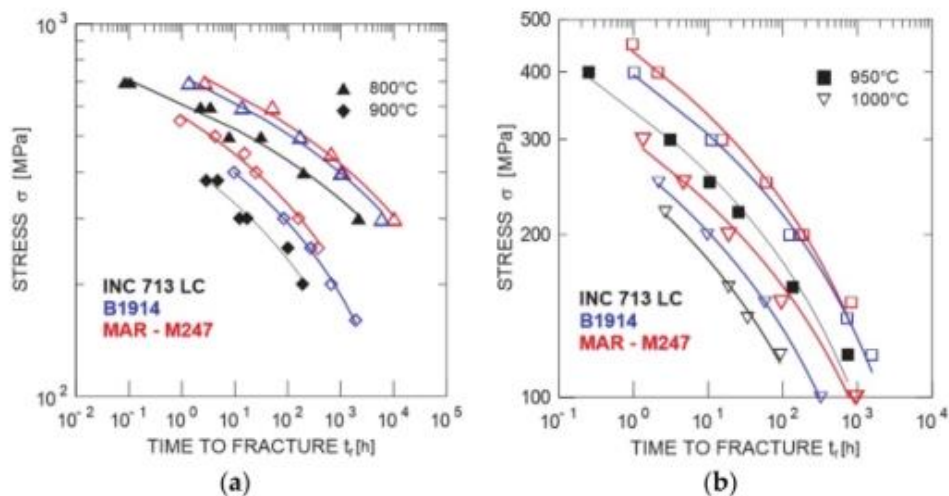


**Figure 4.52 Stress vs rupture time plot of cast nickel-based superalloys[190].**

138
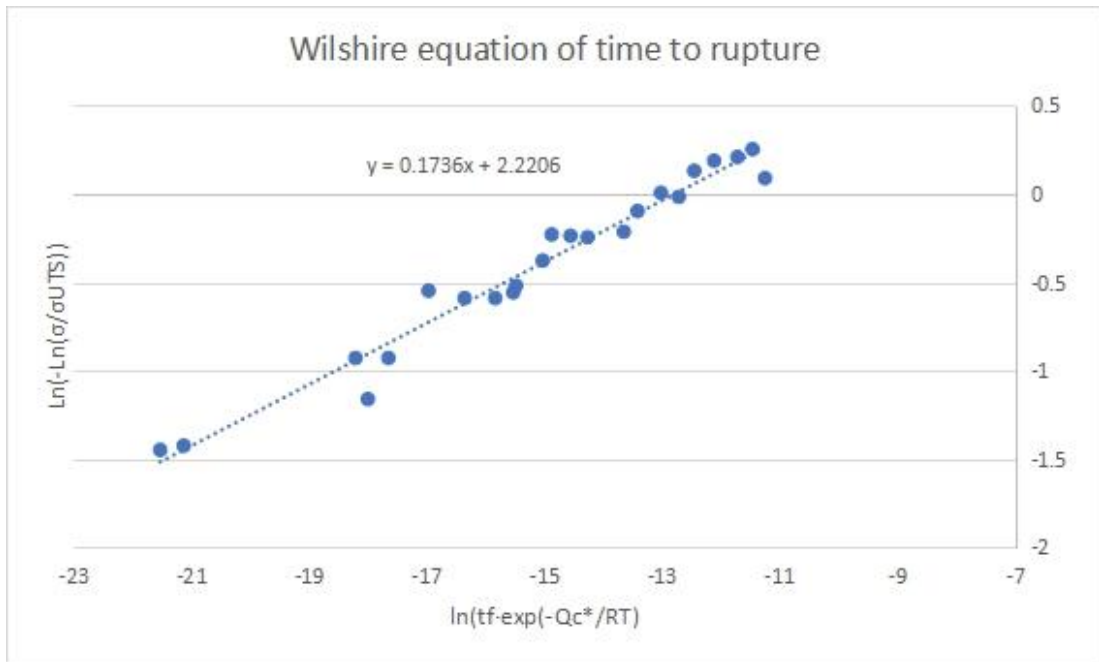
**Figure 4.53 Deriving the parameters Wilshire Equation of rupture time of INC713LC.**
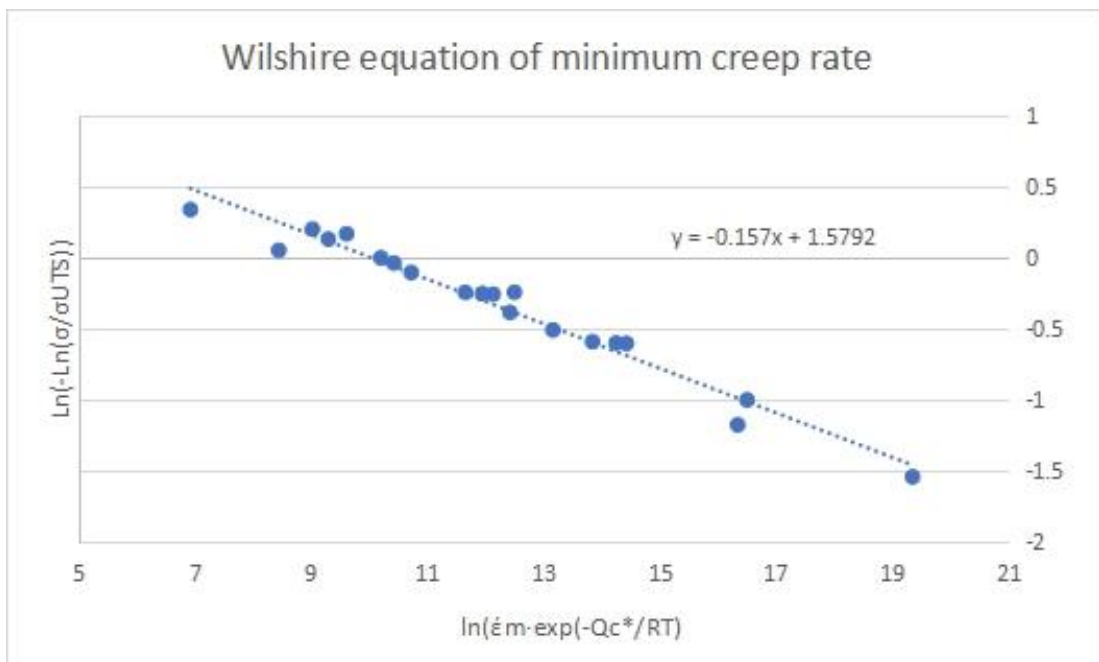


**Figure 4.54 Deriving the parameters of Wilshire Equation of minimum creep rate of INC713LC.**

**Table 4-6 Wilshire Equation results of INC713LC**

| INC713LC | Rupture time | Minimum creep rate |
|----------|--------------|--------------------|
| Qc* (kJ/mol) | 169 | 270 |
| u | 0.174 | 0.157 |
| $k_1$ | 9.21 | 4.85 |

The analysis reveals that a singular activation energy adequately aligns with the observed data, and no discernible breakpoints are evident. Nevertheless, the two distinct equations exhibit a substantial disparity in terms of activation energy. Considering the proximity of the minimum creep rate equation to the self-diffusion energy of pure nickel, which is around 276 kJ/mol, and less scatter in minimum creep rate data compared to that of rupture time, it can be argued that the former would offer greater reliability compared to the outcomes derived from the rupture time equation.

## 4.5 Cyclic tests

As stainless steel 316 exhibits distinct microstructural features, i.e. dislocation cells at 600 °C and twinning boundaries at 700 °C, this behaviour was investigated in greater detail through cyclic creep testing.

In order to conduct the experiments, a stress/temperature pairing was required to be determined for tests at 600°C and 700°C which would allow for comparison on a life fraction basis. Conditions were sought that would provide isothermal failures of around 240 hours, so that 10% of life fraction could be utilised by applying a daily cycle, allowing for practical considerations within a laboratory environment. The closest match was achieved between the conditions of 600 °C/334 MPa and 700 °C/165 MPa, which were ultimately used for comparative analysis.

The constant-stress and cyclic creep curves for 316 stainless steel under two different testing conditions are presented in Figure 4.55. The constant-stress creep curves of 700°C/165MPa are characterised by tertiary dominated creep while the curve obtained of 600°C/334MPa is characterised by more secondary creep. However, both of them

display similar levels of plastic strain during the primary creep stage, as the two curves are nearly identical. After several tens of hours, the curves begin to diverge. The high-temperature/low-stress condition (700 °C / 165 MPa) exhibits a rapid increase in strain and ruptures after approximately 400 hours. In contrast, the low-temperature/high-stress condition (600 °C / 334 MPa) enters tertiary creep more gradually and was interrupted after approximately 450 hours.
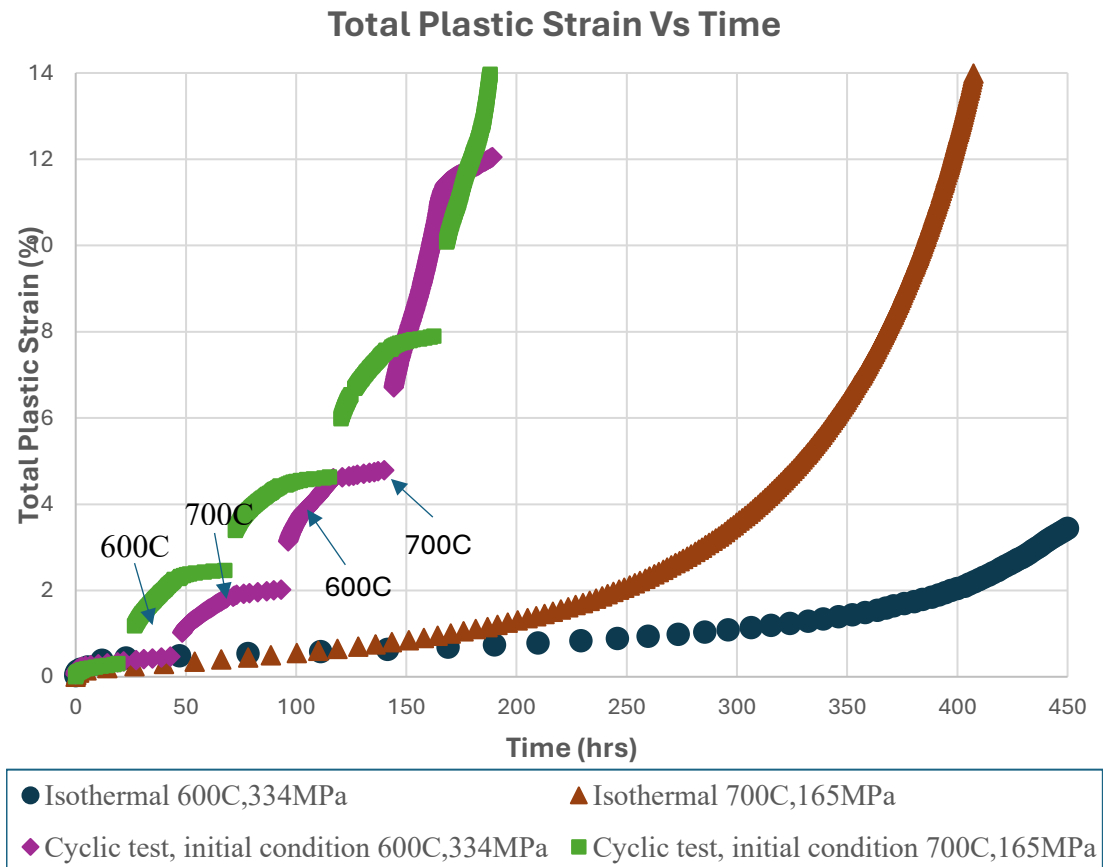


**Figure 4.55 SS316 creep curves obtained from two constant creep tests with test conditions 600℃/334MPa and 700℃/165MPa, and two cyclic creep tests cycled between these conditions every 22 hours.**

The two cyclic creep curves exhibit nearly identical initial creep strains to their corresponding constant-stress curves, which is expected. However, significant changes are observed after the first adjustment of the test conditions. The temperature reduced from 700 °C to 600 °C and the stress increased from 165 MPa to 334 MPa results in a noticeable acceleration of plastic strain accumulation, which only slightly slows after the second adjustment. For the test initiated at 600 °C/334 MPa, the first

temperature/stress adjustment produces little strain response. However, a marked increase in strain is observed following the decreased temperature and increased stress.

Interestingly, both cyclic creep tests result in similar rupture times, regardless of whether they began at high temperature/low stress or low temperature/high stress. Additionally, each subsequent cycle showed the same characteristics, i.e., a significant increase in strain at 600°C, and a more moderate trend during 700°C period. In both cases, rupture occurs much earlier than under constant-stress conditions.
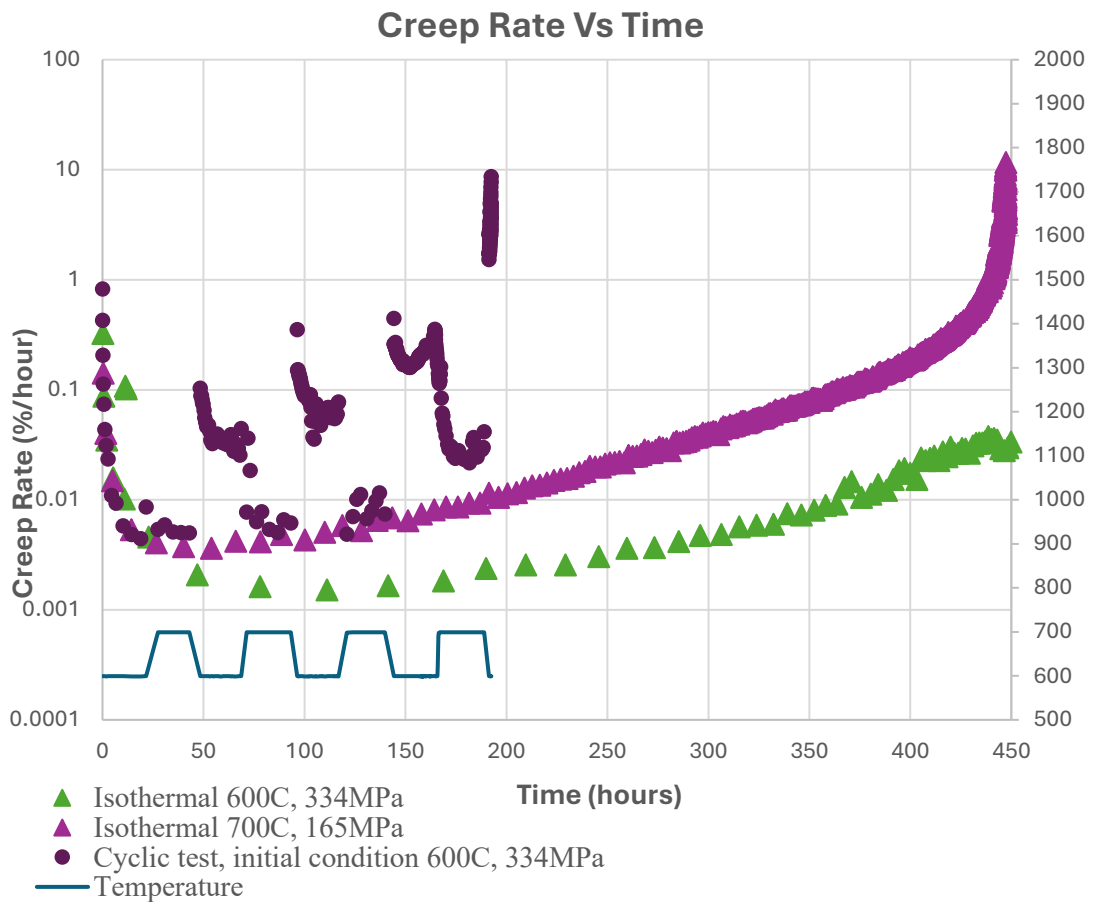


**Figure 4.56 Creep rate obtained from the cyclic creep test started from 600℃ /334MPa, with two creep rate curves obtained at two constant creep tests.**

Creep rate curves further clarify these differences. Figure 4.56 compares the creep rate of the 600 °C/334 MPa cyclic test with those of the two constant-stress tests. During the 'heating procedure' (test condition changed from 600 °C/334 MPa to 700 °C/165 MPa), the creep rate increases slightly with rising temperature, then stabilises close to that of the 700 °C/165 MPa constant-stress test. A sharp increase in creep rate is observed during the first 'cooling procedure' (test condition changed from

142

high temperature/low stress to low temperature/high stress). Once the temperature stabilises again at 600 °C, the specimen enters a stage resembling initial creep, which is called 'pseudo' primary creep, and the creep rate gradually declines toward a new minimum that is much higher than that of constant creep tests. Following the second temperature increase, the creep rate returns to levels comparable to the high-temperature/low-stress constant test. However, after the fourth temperature increase, the minimum creep rate becomes significantly higher than in the constant-stress test, and fracture occurs after a further stress increase, around 200 hours into the test.
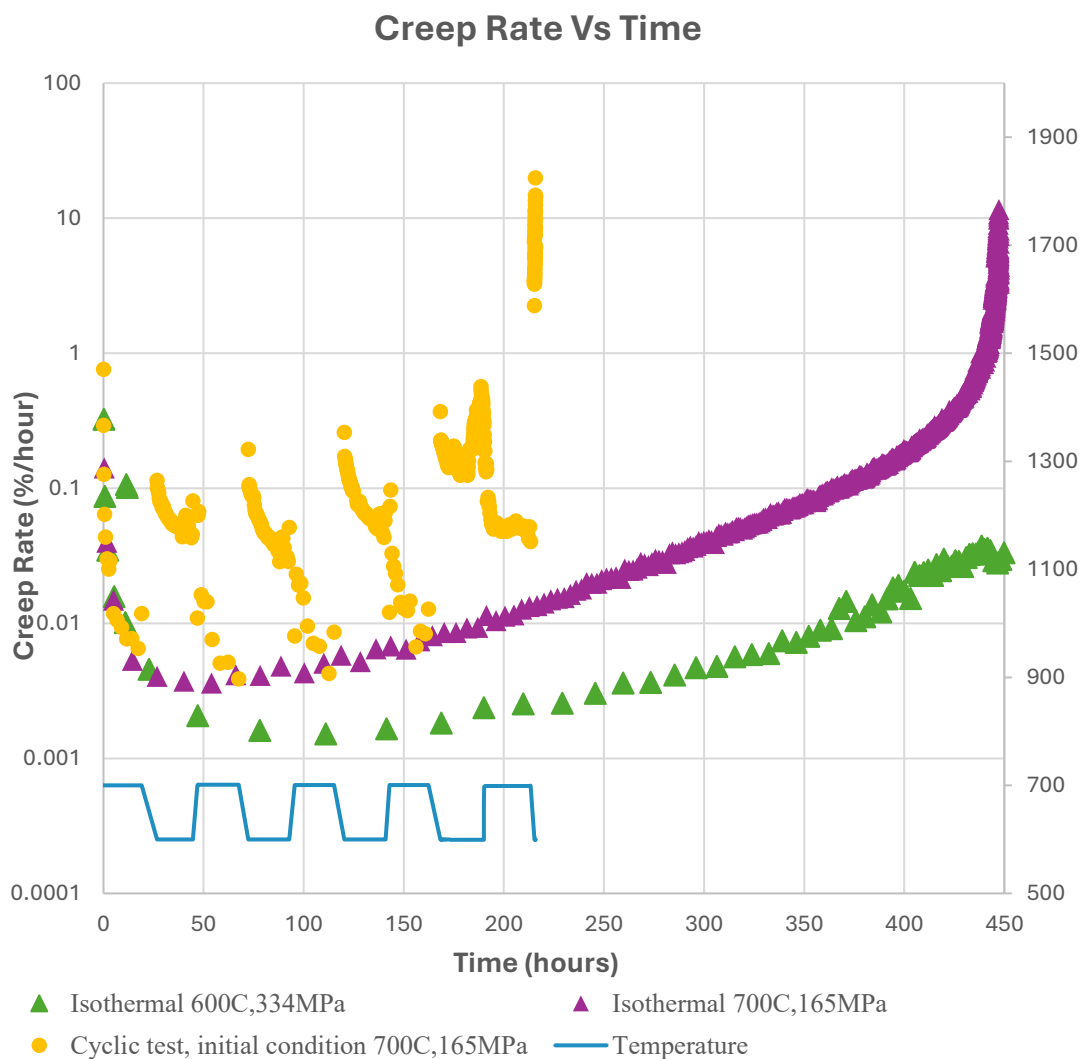


**Figure 4.57 Creep rate obtained from the cyclic creep test start from 700℃ /165MPa, with two creep rate curves obtained at two constant creep tests.**

Figure 4.57 shows the creep rate for the 700 °C/165 MPa cyclic test in comparison to the constant-stress curves. A sharp rise in creep rate also occurs following the initial temperature reduction and stress increase. This transient behaviour repeats after

143

subsequent changes in temperature and stress. The minimum creep rate of the cyclic tests at 700 °C is nearly identical to that of the constant-stress creep tests, as indicated by the overlap of yellow and purple data points. However, at 600 °C, the minimum creep rate during cyclic testing is significantly higher than in both constant-stress creep conditions. Fracture occurs following the fifth temperature decline, at approximately 220 hours.

# 5. Discussion

This chapter examines the creep behaviour of three alloys—316 stainless steel, Haynes 282, and IN713—with a focus on their activation energy (Qc*) values and the underlying dislocation mechanisms. It begins by reviewing traditional creep models, such as the Power Law and Larson-Miller methods, which have shown limitations in accurately predicting creep life. These models often fail to account for the complex microstructures of high-performance alloys, leading to inaccurate predictions. To address these issues, the Wilshire Equations are introduced as a more robust approach, offering improved accuracy in determining Qc* by accounting for stress partitioning and temperature standardisation.

The chapter then discusses experimental findings, including TEM analyses, to explore how microstructural evolution influences creep behaviour and Qc* in each alloy. Finally, the chapter concludes by discussing the results of cyclic creep tests and the implications of moving between different Qc* regions.

## 5.1  Revisiting Creep Models

### 5.1.1  The Power Law

The Power Law serves as the cornerstone for the conventional model's development. Despite its demonstrated inaccuracy, this model was utilized in this study to predict and simulate creep life. Primarily, the creep rate "$\dot{\varepsilon}_s$" in the original Power Law equation was substituted with time to fracture "$t_f$" through the Monkman-Grant relationship, leading to the following alteration:

$$\dot{\varepsilon}_s = M \, / \, t_f = A\sigma^n \exp\left(-\frac{Q_c}{RT}\right)$$

**Eq. 5-1**

A final form will be given by re-arranging equations:

$$t_f = D\sigma^{-n}\exp\left(\frac{Q_c}{RT}\right)$$

<div align="right">**Eq. 5-2**</div>

Where D is a constant equal to M/A.

The influence of stress and temperature on material fracture life is investigated by plotting a scatter plot of the time to fracture of SS316 bars at a specific temperature but varying stress levels, as shown in Figure 5.1. A logarithmic time scale is employed for enhanced representation across a wide time range. The findings demonstrate a pronounced linear correlation between stress and time to fracture across all tested temperatures. The logarithm of time to fracture shows a decreasing tendency as stress increases. This indicates that heightened stress intensifies the material's propensity to fracture at a consistent temperature, thereby elevating the strain rate. An interesting observation is that the time to fracture decreases as temperature rises. Moreover, the decreasing trend in fracture time is more pronounced under high-stress, low-temperature conditions, whereas it is more gradual under low-stress, high-temperature conditions. This can be attributed to the fact that, under high stress, the material is more susceptible to localised stress concentrations, particularly at grain boundaries, defects, and precipitates. These concentrations accelerate local deformation and crack propagation, ultimately leading to premature failure. In contrast, under high-temperature and low-stress conditions, the material tends to exhibit more ductile fracture behaviour. Although the applied stress is lower, the elevated temperature enhances the material's plasticity, allowing for greater deformation and relatively slower crack growth. As a result, the reduction in fracture time occurs more gradually[146]. Both phenomena align with the equation Eq. 2-8 and Eq. 2-9.
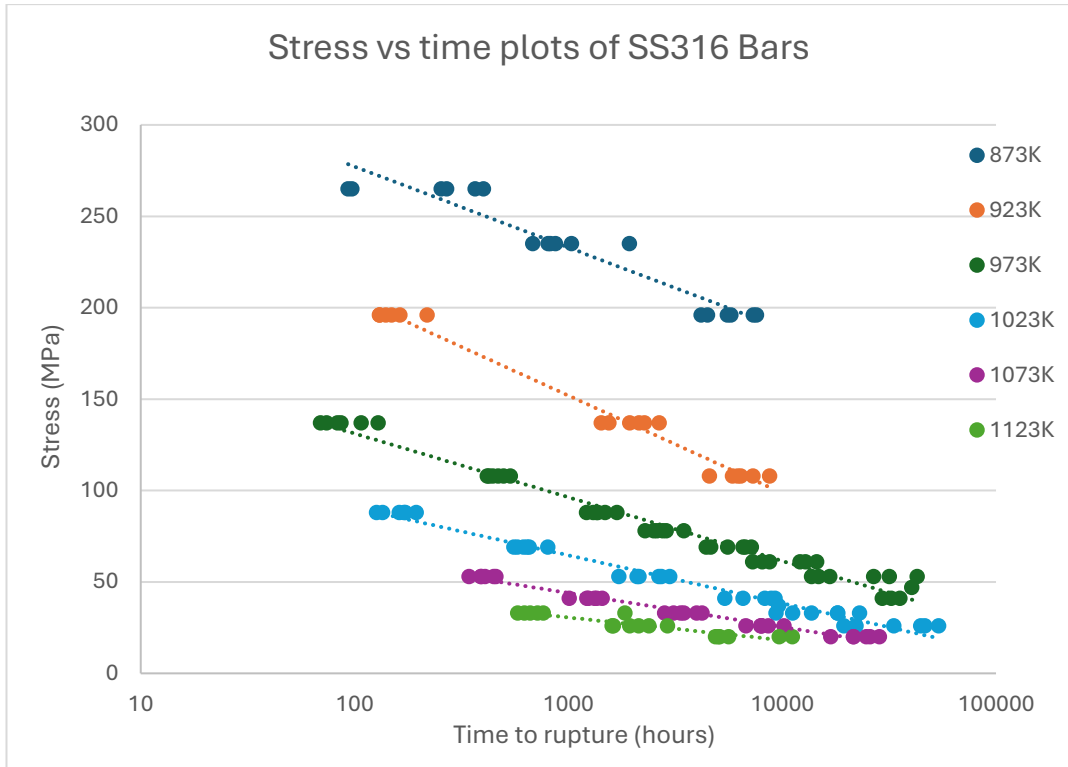
**Figure 5.1 Stress against rupture time plot of SS316 bars based on NIMs datasheet**

This equation can be further simplified into a linear form by taking the natural logarithm of both sides to give:

$$\ln t_f = \ln D - n\ln\sigma + (Q_c/RT)$$

<div align="right">**Eq. 5-3**</div>

In accordance with this equation, the value of "n" in the Power Law equation can be determined by plotting ln(tf) against ln(σ) at a constant temperature, yielding a slope of -n, see Figure 5.2.
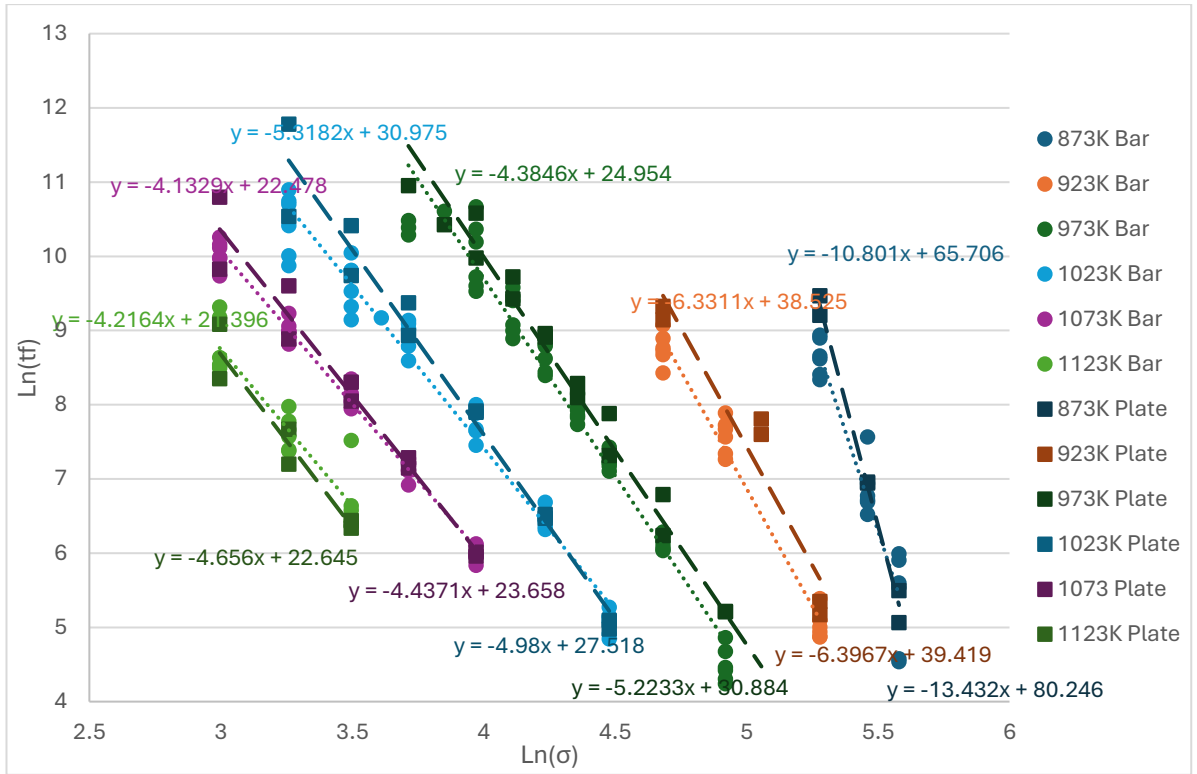
**Figure 5.2 The ln(t_f) against ln(σ) plots determining the n values of SS316 bars and plates.**

The calculated value of "n" for three types of stainless steel 316 are indicated in the Table 5-1 below:

**Table 5-1 The values of stress exponent (n)**

| TEMP. (K) | 873 | 923 | 973 | 1023 | 1073 | 1123 | Average |
|-----------|------|-----|-----|------|------|------|---------|
| Bar | 10.8 | 6.3 | 5.3 | 4.4 | 4.1 | 4.2 | 5.9 |
| Plate | 13.4 | 6.4 | 5.2 | 5.0 | 4.4 | 4.7 | 6.5 |
| Tube | 4.5 | 4.9 | 4.7 | 3.6 | - | - | 7.0 |

Conversely, the activation energy "$Q_c$" required for creep can be derived by plotting ln(t_f) against 1/RT at a constant stress, where the slopes of these plots correspond to the values of $Q_c$. Figure 5.3 is an example of SS316 bars.
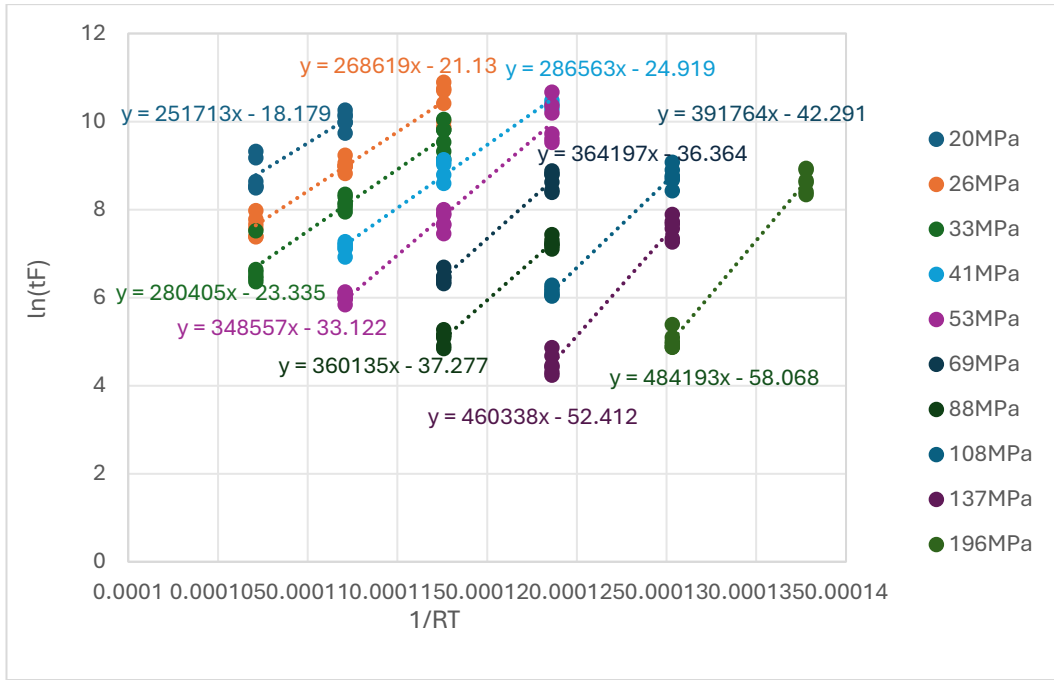
**Figure 5.3 The ln(t$_f$) against 1/RT plot determining the activation energies of SS316 bars.**

All the outcomes for activation energies of different 316 samples at various stresses are provided below at Table 5-2.

**Table 5-2 The values of activation energies (Q$_c$)**

| Stress (MPa) | 20 | 26 | 33 | 41 | 53 | 69 | 88 | 108 | 157 | 196 | Ave. |
|---|---|---|---|---|---|---|---|---|---|---|---|
| Bar (kJ/mol) | 252 | 269 | 280 | 287 | 349 | 364 | 360 | 392 | - | 484 | 350 |
| Plate (kJ/mol) | 319 | 356 | 352 | 328 | 373 | 404 | 424 | 406 | 570 | 546 | 408 |
| Tube (kJ/mol) | - | - | - | 285 | 223 | 303 | 395 | 382 | 429 | 484 | 323 |

From the outcomes, it is evident that the values of "n" and activation energy Q$_c$ exhibit considerable variations across different temperatures and stress conditions, respectively. The Power Law's assumption of these two variables as constants stands as a primary contributor to the diminished accuracy. The full dataset for 316 stainless steel bar specimens was used to calculate the parameters of the power law equation. This was achieved by applying a linear regression to the relationship between ln(tf),

149

ln(stress), and 1/RT. The resulting parameters were then substituted back into the original power law equation to predict the time to fracture, which was subsequently compared to the experimentally observed rupture times. The corresponding results are illustrated as depicted in the Figure 5.4, the predictive accuracy of SS316 plate is approximately 76.8%.
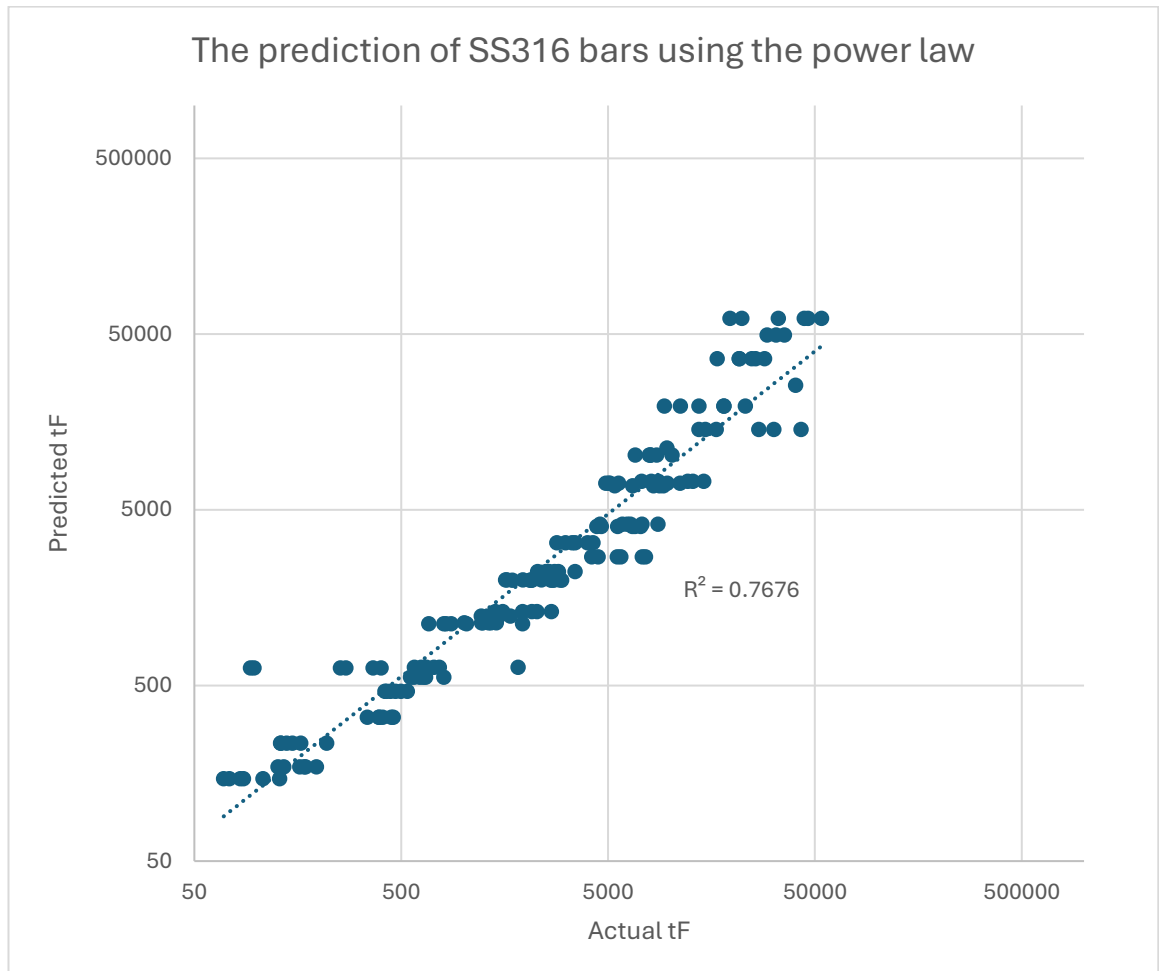


**Figure 5.4 The prediction plot estimated via the power law.**

The Power Law model serves as the foundation for several later models. However, its presentation of the variables stress exponent n and activation energy $Q_c$ as constants imposes significant constraints on its ability to accurately fit experimental data and provide precise predictions. The stress exponent value is commonly employed for the analysis of creep deformation mechanisms in metallic materials. The value of n for austenitic stainless steel typically ranges from 3 to 12[241]. The predicted n values obtained by the Power Law analysis exhibited little variations with respect to stress across the temperature range of 923K to 1123K, with the exception of the test temperature of 873K, when notable deviations were seen. It is worth noting that no

150

instances of power-law failure were observed during the analysis, indicating that the creep deformation mechanism consistently operates within the dislocation creep stage when considered using these traditional approaches. The observed reduction in the creep stress index from 6 to 4 as the creep temperature increases may be attributed to inherent microstructural changes within the alloy. Nevertheless, the determined average activation energies of 350kJ/mol for bar, 408kJ/mol for plate, and 323kJ/mol for tube exhibit significantly greater values compared to the austenitic self-diffusion activation energy of 270kJ/mol[242]. However, these values demonstrate a relatively small disparity among each other under low-stress conditions, indicating that the creep deformation observed at low stresses could potentially be attributed to crystal diffusion. Conversely, under high-stress conditions, it may be influenced by other deformation mechanisms leading to high activation energies. This finding provides more evidence for the inadequacy of the power law model in assuming a constant value for the activation energy.

## 5.1.2 The Larson-Miller prediction method

Larson and Miller[8] have contributed a significant tool to the realm of engineering design and lifespan prediction for high-temperature materials. While this equation retains an empirical nature, it holds widespread practical usage, particularly for initial life estimation and engineering design at elevated temperatures when detailed material data is lacking. The original LM equation is initially transformed into a linear form:

$$\log t = P_{LM}(1/T) - C_{LM}$$

**Eq. 5-4**

When stress is held constant, plotting $\log(t_f)$ against $1/T$ yields a slope equivalent to $P_{LM}$ and a y-intercept of $-C_{LM}$. As discussed in earlier, $C_{LM}$'s value is not constant, and its computed value from present data fluctuates between 11-29. Nonetheless, when seeking to fit all creep data to a master curve, it was observed that data fitting was more favourable with the value of 20 than with the actual $C_{LM}$ value. Consequently, the assumption of $C_{LM} = 20$ persisted in subsequent analyses and calculations. However, this assumption also contributed to the impact on the accuracy of the Larson-Miller model.

151
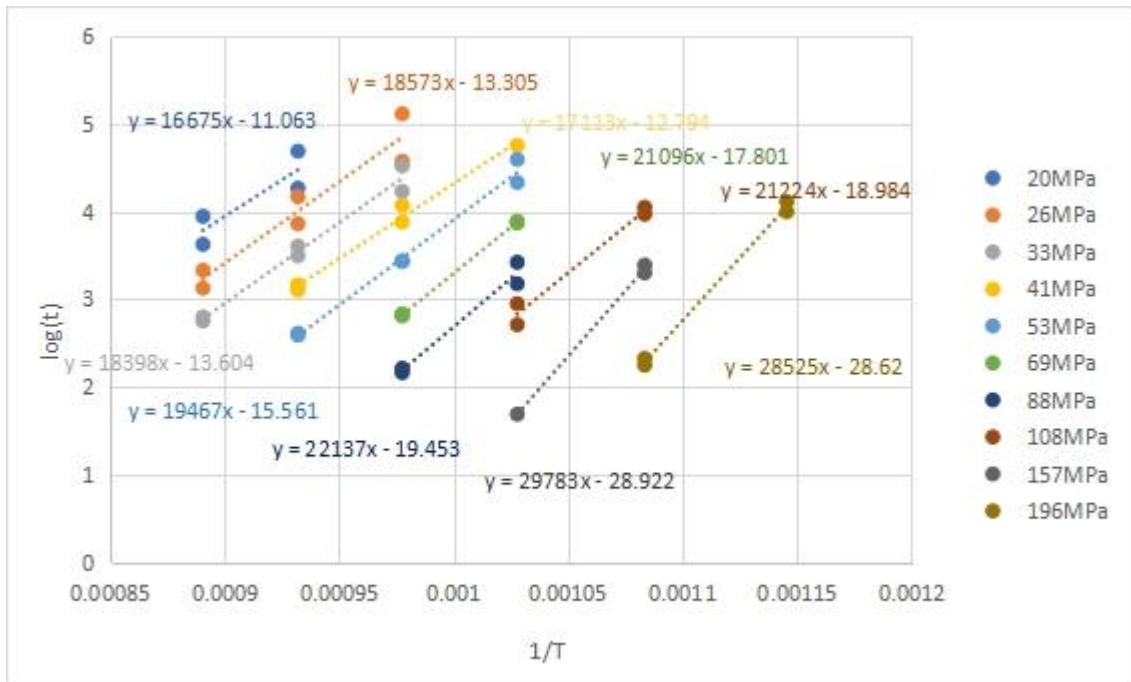
**Figure 5.5 log(t) against 1/T plot determining the parameters, i.e. $P_{LM}$ and $C_{LM}$, of the LM equation.**
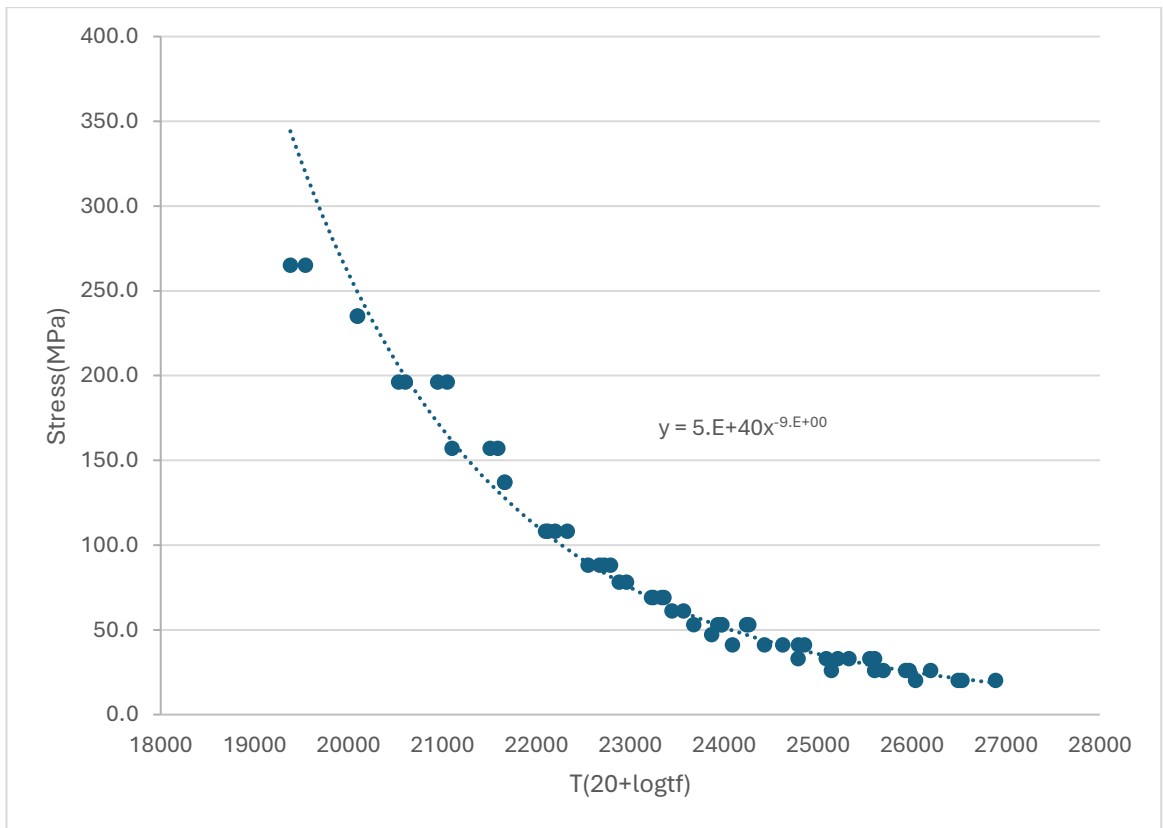


**Figure 5.6 Fitting data to a master curve with $C_{LM}=20$**

Upon applying the LM model to predict SS316, it was found to achieve approximately 77.8% accuracy, as depicted in the Figure 5.7.
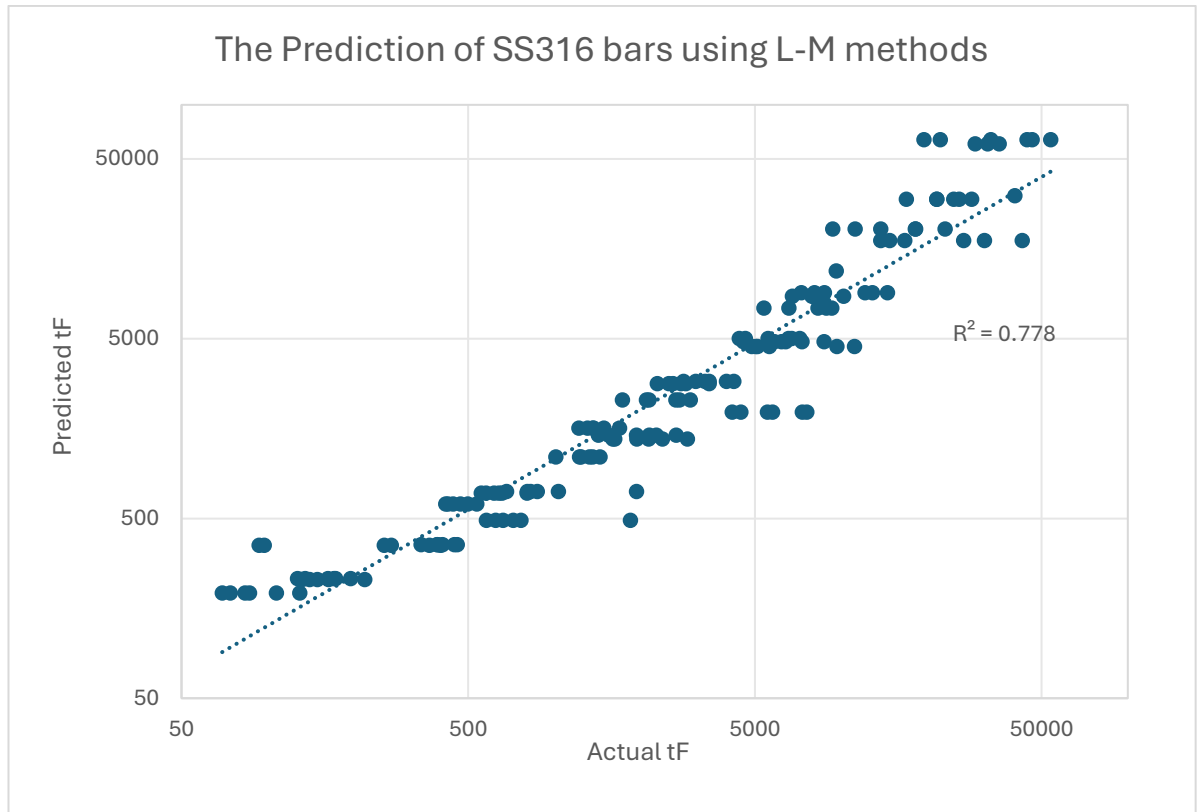


**Figure 5.7 The prediction plot estimated via the Larson-Miller methodology**

The Larson-Miller model is extensively employed in the field of engineering design. The constant, commonly referred to as $C_{LM}$, is considered a "fitting constant" in academic literature[92]. It is derived only from empirical data without any accompanying physical explanation and is frequently assigned a predetermined value. The number provided is usually 20. However, it is evident from Figure 5.5 that the $C_{LM}$ value exhibits distinct variability, not only across different alloys but also under the influence of various factors such as cold working, thermo-mechanical machining, phase transformations, and other structural modifications[95]. Additionally, phase transitions and other structural modifications can also impact the $C_{LM}$ value. Moreover, the parameters and constants derived in this context have not been associated with any observable physical events. This implies that the application of the Larson-Miller model to draw broader conclusions regarding creep behaviour is challenging.

### 5.1.3 Wilshire Equations

The Power Law model is a traditional method used to predict creep life, but its application to alloys like 316 stainless steel reveals significant limitations. The assumption of a constant stress exponent (n) and activation energy ($Q_c$) is not accurate across varying conditions, as seen in the variability of n values across temperatures and stresses (Table 4-2). This inconsistency highlights the need for a model that can account for these variations more effectively. In this study, the Power Law's inability to accurately predict creep behaviour, especially under the high-stress and high-temperature conditions explored, prompted the adoption of the Wilshire Equations. These equations, unlike the Power Law, allow for the dynamic determination of $Q_c^*$ by incorporating stress partitioning and temperature standardisation, thus offering a more flexible and accurate approach. In Wilshire Equation applications it is also generally expected that the creep life of engineering alloys at reasonable stresses is governed by the movement of dislocations rather than vacancy diffusion. As previously highlighted, should a mechanism change occur towards longer creep lives (often illustrated by a change from n = 4-6 to n = 1 based on power law approaches) then prediction of long-term data then from short term experiments would not be achievable. In a framework considering only dislocation creep prediction is possible provided behaviour changes are appropriately rationalised.

While the Larson-Miller method provides a practical framework for estimating the creep life of materials under high temperatures, it too suffers from limitations when applied to alloys with complex microstructures. The assumption of a constant fitting constant ($C_{LM}$) leads to reduced accuracy, particularly when applied to alloys like 316 stainless steels. The variability of $C_{LM}$ across different alloys and experimental conditions further undermines the reliability of the model. This underscores the need for a more comprehensive approach, which the Wilshire Equations aim to provide, by incorporating more material-specific variables and offering a greater degree of flexibility in predicting creep behaviour.

A more adaptable approach, the Wilshire Equations, address the limitations of traditional models such as the Power Law and Larson-Miller in accurately predicting creep behaviour across varying stress and temperature conditions. In particular, the Wilshire model calculates $Q_c^*$, the creep activation energy, by incorporating a

154

temperature-dependent tensile strength correction, distinguishing it from the traditional $Q_c$. By integrating material-specific factors such as ultimate tensile strength (UTS) and considering variations in deformation mechanisms across different stress regimes, the Wilshire Equations offer improved predictive accuracy. Furthermore, they are not a single equation based solely on rupture lives but encompass the minimum creep rates ($\dot{\varepsilon}_m$), the creep rupture time ($t_f$), and the time to reach various creep strain ($t_\varepsilon$). These advancements enable a more detailed understanding of creep behaviour, accounting for the complex interactions between stress, temperature, and microstructure.

After using the time to fracture equation of the Wilshire Equations to predict the SS316 bar, it was found that its accuracy could reach over 80%, as shown in the Figure 5.8.
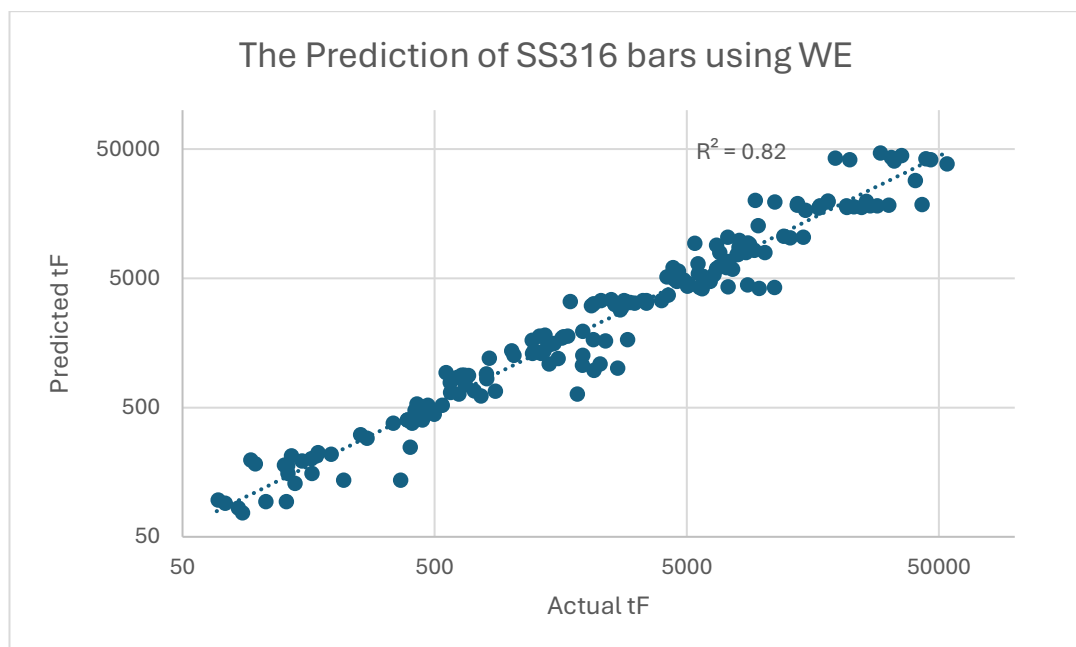


**Figure 5.8 The prediction plot estimated via the $t_f$ equation of Wilshire Equations.**

The Wilshire Equations have also proven to be an effective method for determining creep activation energy, as demonstrated in previous studies [15], [20], [21], [22], [23], [24], [59], [87], [88], [97], [99], [111], [113], [116], [117], [118], [243], [244]. Its applicability has been discussed in the literature review. Notably, a key study by Whittaker[87] revealed that activation energy varies significantly on either side of the breakpoint, indicating a clear transition in material behaviour. This finding was crucial in demonstrating that creep deformation mechanisms change across different stress

ranges, meaning creep behaviour cannot be fully described by a single activation energy value.

Further investigations, such as the one on 316 stainless steel by Whittaker et al[99], provided deeper insight into this issue, showing that activation energy depends on the microstructural features present in the material. Subsequently, the same author[19] then linked dislocation features to the $Q_c$* values, establishing a direct correlation between the movement of dislocations and the changes in activation energy. This finding was crucial in demonstrating how microstructural features, including dislocation behaviour, affect creep resistance.

Building on these insights, Birosca et al.[245] expanded on the role of grain boundaries in influencing creep behaviour, demonstrating that a significant portion of deformation occurs in the grain boundary region. Their study underscored the importance of grain boundary processes in determining the overall creep response of an alloy.

To explore these findings further, the three materials studied here were selected to represent alloys with different precipitate levels: 316 stainless steel, which has nearly no precipitates; Haynes 282, which contains low fraction of precipitates; and Inconel 713C, which has a high volume fraction of γ'. These materials were chosen to compare how varying levels of precipitates influence the creep behaviour and activation energy.

This selection of materials laid the foundation for re-analysing previously presented data, particularly the 316 stainless steel work. After the process of region splitting, it was found that the activation energy of 316 bar showed a variation from 153 to 298 KJ/mol below and above the yield strength (Figure 4.46), and the activation energy of 316 plates gave a similarly large variation from 181 to 298 kJ/mol (Figure 4.47). As previously noted, the self-diffusion energy of austenite is approximately 270 kJ/mol [242]. In the case of stainless steel 316, whether in bar or plate form, the calculated activation energies within the low-stress region are notably lower than this benchmark.

A similar trend has been documented in prior investigations of HK40 and HP40, where the calculated activation energies at lower stress region were significantly below the self-diffusion energies [117]. This phenomenon can be attributed to the coarse-grained structure and minimal precipitation found in both HK40/HP40 and stainless steel 316. In these materials, dislocations encounter little resistance to movement within grain

boundaries (as shown in Figure 5.9, the cavity of HK 40 tube formed along columnar grain boundaries), as there are limited impediments, there is no need to expend energy to generate new dislocations[59] or make cutting or climbing moves, resulting in relatively low energy requirements for dislocation motion.



**Figure 5.9 Cavity developed along the grain boundaries**[117]

In calculating the activation energies of 316 stainless steel using the Wilshire Equations, a sharp transition is seen at stresses at or near to the yield stress of the material. However, it is important to understand whether this transition occurs more gradually. To achieve a more comprehensive analysis of activation energy trends, an attempt was made to remove data from either the high or low-stress end of the range. After dividing the data into two sections based on high and low stress levels, the extraction of the most extreme data from each group begins. This process aims to explore how the activation energy changes with variations in the stress level ($\sigma/\sigma_{UTS}$), and how this influences the material's behaviour. The results, as depicted in the Figure 5.10 and Figure 5.11, reveal interesting trends. In the low-stress regime (Figure 5.10), when extracting data starting from the lower stress end, the activation energy exhibits a relatively gentle increase, with values ranging between 180 and 200 kJ/mol, due to the influence of data from more elevated stresses increases in influence. As the normalised stress approaches approximately 2.67, a notable turning point in activation energy is observed, after which the rate of increase becomes more significant—rising from 236 kJ/mol to 320 kJ/mol. Despite this inflection, the overall trend remains one of gradual change.

In contrast, under high-stress conditions (Figure 5.11), where data are extracted from the higher end of the stress range, the activation energy shows a declining trend, decreasing from 305 kJ/mol to 248 kJ/mol.
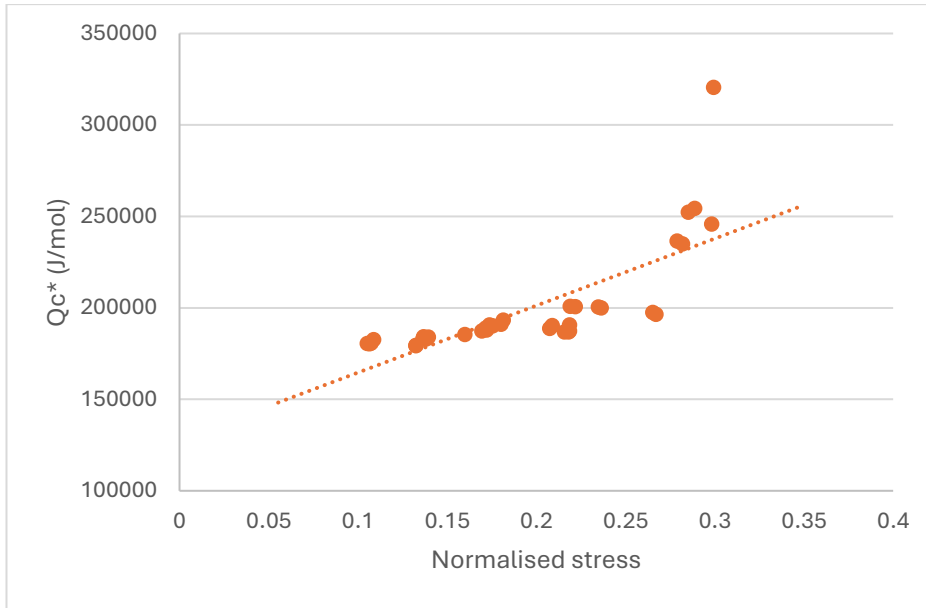
**Figure 5.10 Calculation of Qc\* based on the band of data where the upper limit is the yield stress and the lower limit is the value shown on the x-axis.**
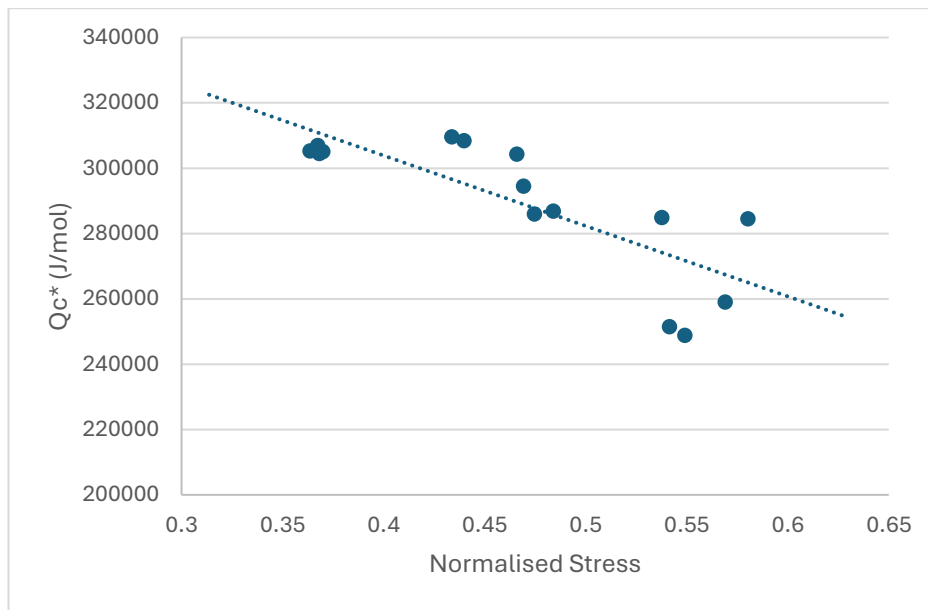


**Figure 5.11 Calculation of Qc\* based on the band of data where the lower limit is the yield stress and the upper limit is the value shown on the x-axis.**

The aforementioned alterations transpire gradually. A transition in behaviour seems to occur in a gradual manner, potentially commencing inside grains that are suitably aligned to facilitate this transition. The weaker grains beginning to yield, and as stress levels escalate, this yielding gradually spreads to incorporate broader regions of the material.

Haynes 282 also exhibited a distinct breakpoint in its activation energy, with values increasing from 277 kJ/mol to 427 kJ/mol, see Figure 4.50. Given the alloy's microstructural similarity to Waspaloy, it is hypothesised that dislocation entanglement and forest hardening mechanisms contributed to the observed rise in activation energy[19]. This behaviour will be further discussed after the TEM section of this chapter, where detailed microstructural analysis is conducted.

In contrast, IN713C, which also contains γ' precipitates but in different proportions, did not demonstrate a clear breakpoint in its activation energy when analysed using the Wilshire Equations, as shown in Figure 4.53 and Figure 4.54. This suggests that the activation energy for IN713C remained relatively stable across the stress range, with no substantial variation observed. The underlying mechanisms responsible for this behaviour, including the effects of gamma prime content and microstructural evolution, will again be explored in greater detail in the subsequent section with TEM analysis.

## 5.2  Microstructural Evolution and Creep Mechanisms

### 5.2.1  316 Stainless steels

Following the interrupted creep tests, a detailed microstructural investigation was carried out to clarify the deformation mechanisms operating during exposure. Transmission Electron Microscopy (TEM) was selected for this purpose, as it allows direct observation of dislocation arrangements, interactions with precipitates, and the formation of characteristic substructures. The analysis was undertaken at the University of Birmingham in collaboration with the Swansea team, providing high-resolution evidence to complement the mechanical data. These observations establish the link between the measured creep response and the microstructural changes, forming the basis for the discussion presented in this section.

At 600°C and 125MPa, TEM analysis has revealed a relatively homogeneous distribution of dislocations, along with some evidence of complete dislocations and cross slips as shown in Figure 5.12.
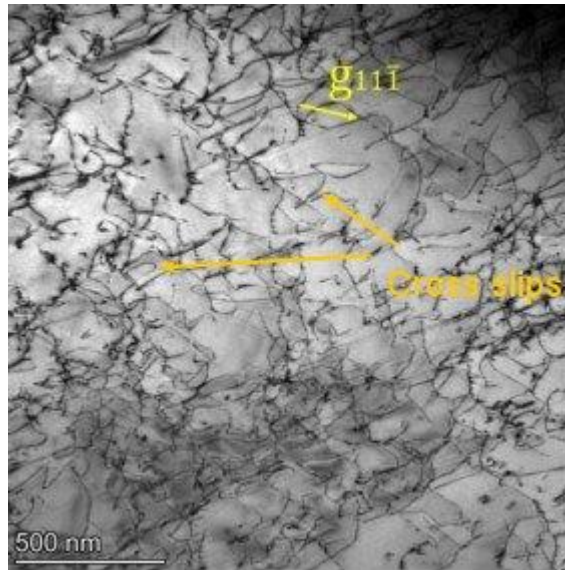
**Figure 5.12 TEM micrographs of SS316 after 600°C and 125MPa creep test showing complete dislocations and cross slips.**

Figure 5.13 depicts a more pronounced occurrence of stacking faults and extended partial dislocations. These structural characteristics arise from deviations in the atomic arrangement within the crystal lattice, resulting in modifications to the stacking sequence of specific atomic layers, ultimately giving rise to stacking faults. Conversely, the extended partial dislocations originate from the slipping and bending of dislocation lines within the crystal, where these lines function as nuclei for dislocation motion. Stacking fault energy (SFE) is a composition- and temperature-dependent property of crystalline materials and is widely recognised as a key parameter in determining deformation mechanisms—particularly in austenitic steels[246]. SFE is defined as the energy per unit area associated with the dissociation of a perfect dislocation into two Shockley partial dislocations. It can be considered similar to the surface tension of the separating section of the dislocation[247]. The magnitude of SFE significantly influences the resulting microstructure during deformation. At low SFE values ($\leq 15\,\mathrm{mJ\,m^{-2}}$), deformation is typically accompanied by martensite formation. At intermediate SFE levels (approximately $15\text{–}45\,\mathrm{mJ\,m^{-2}}$), deformation twinning tends to dominate, while at high SFE values ($\geq 45\,\mathrm{mJ\,m^{-2}}$), dislocation slip is the primary deformation mechanism[246], [248], [249]. Metals with low to moderate SFEs can readily form a high density of stacking faults during plastic deformation[250].

These stacking faults and extended partial dislocations wield notable influence over the material's performance. Initially, they have the potential to induce localised stress

160

concentrations, as the atomic arrangement undergoes modifications in these areas, introducing a measure of structural non-uniformity. Secondly, these dislocations and faults can influence the material's strength and ductility by potentially serving as crack initiation sites or augmenting dislocation density, thereby affecting the material's plastic deformation mechanisms.
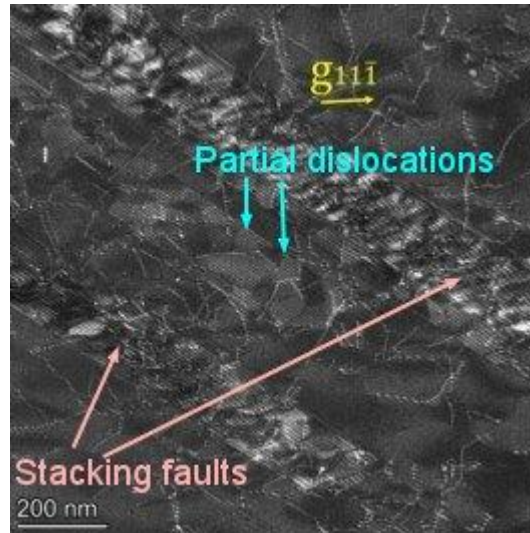


**Figure 5.13 TEM micrographs of SS316 after 600°C and 125MPa creep test showing partial dislocations and stacking faults.**

The presence of twins depicted in Figure 5.14 may be ascribed to minor lattice misalignments, leading to a degree of misorientation between neighbouring grains. These misorientations impact not only the local crystal structure but also influence the behaviour of dislocations and stacking faults. The varying levels of contrast observed among stacking faults, partial dislocations, and twins underscore the intricate nature of the interactions among dislocations, stacking faults, and twins.
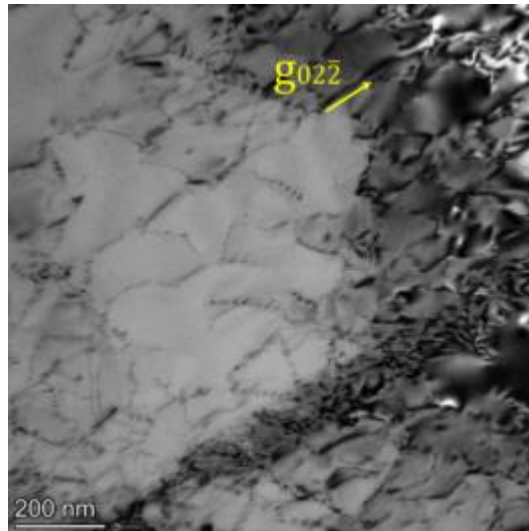
**Figure 5.14 TEM micrographs of SS316 after 600°C and 125MPa creep test showing twin boundaries.**

Creep testing at higher stress (275MPa) and the same temperature (600°C) led to a uniform distribution of low- to moderately-dense dislocations, as shown in Figure 5.15.
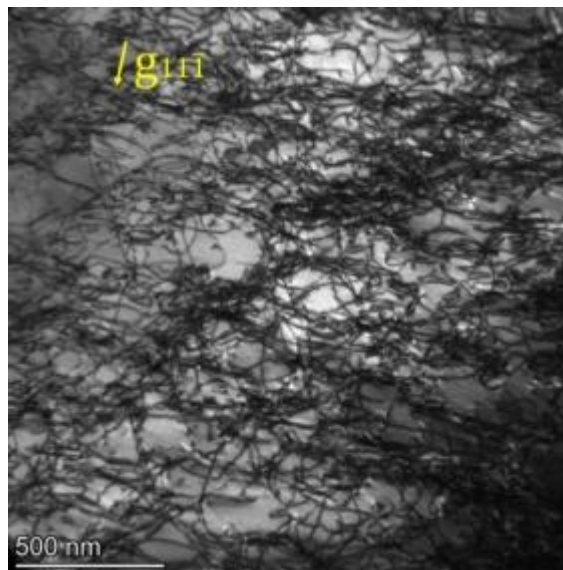


**Figure 5.15 TEM micrographs of SS316 after 600°C and 275MPa creep test showing dislocation network.**

The dislocation network displays heterogeneity, with specific regions exhibiting clear characteristics. This uneven distribution primarily arises from the reduced spacing between dislocations caused by the heightened stress levels. The heightened interactions among dislocations under high stress conditions not only curtail their mobility but also induce them to reorganize within localized regions, with the objective of alleviating stress concentrations. This reorganization gives rise to the creation of

162

boundaries between dislocations in neighbouring regions, resulting in a structure reminiscent of cellular formations, possibly indicative of dislocation cells. Higher magnification of Figure 5.16 show the heterogeneous dislocation distribution and dislocation cells more clearly.

Dislocation cell formation occurs as a result of intense dislocation interactions when the material is under high stress. This process helps relieve localized stress concentrations by strengthening the material, which ultimately reduces dislocation density. Generally, this behaviour contributes positively to the material's overall performance.
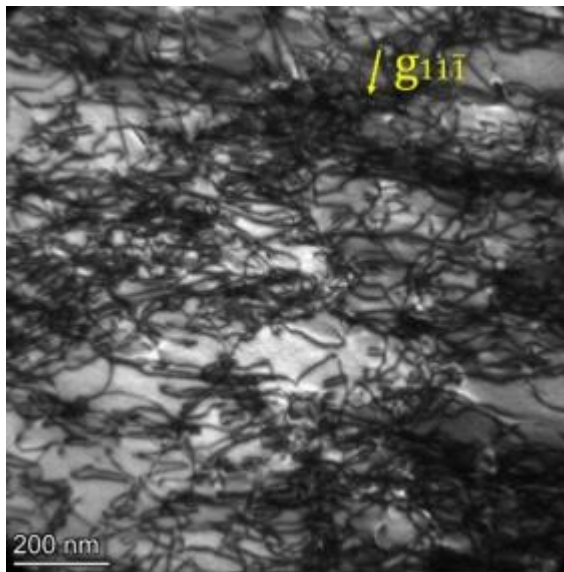


**Figure 5.16 TEM micrographs of SS316 after 600°C and 275MPa creep test showing heterogeneous dislocation.**

Additionally, it was observed that there were more partial dislocations present, but there was no significant increase in stacking faults and twinning in Figure 5.17.
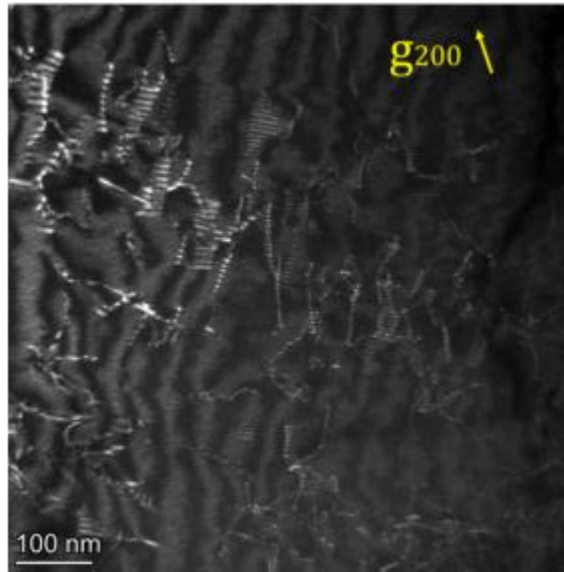
**Figure 5.17 TEM micrographs of SS316 after 600°C and 275MPa creep test showing partial dislocations.**

As previously detailed in Figure 4.23, further 316 stainless steel samples were creep tested at higher temperature (700 ℃) with stress of 100MPa, 125MPa, 175Mpa and 225MPa individually, and interrupted once it had been established that primary creep had ended. As shown in Figure 5.18, TEM results of 225MPa, the transmission electron microscopy analysis did not demonstrate a substantial presence of dislocation entanglement or strain hardening. In contrast, an increased number of deformation twins was reported by EBSD maps (Figure 4.26). Twinning is a distinct method of deformation, and previous research has revealed that dislocations can engage with twin borders in various manners inside face-centred cubic (fcc) materials[251]. Twins, characterized by high-angle coincident site lattice barriers, possess the ability to hinder the movement of dislocations and augment the mechanical strength of alloys. The increased stability of high-angle grain boundaries at increasing temperatures can be attributed to their lower energy state in comparison to other types of grain boundaries[252]. The study conducted by Jozaghi [253] examined the influence of deformation twins on the mechanical properties of austenitic stainless steels. The findings of this research demonstrated that the yield strength of 316 samples with a stratified twinned structure surpassed that of the non-twinned 316 samples, primarily due to the decreased mean free path of dislocations. 316 samples exhibiting a laminated twin structure were seen to display a notable enhancement in the level of yield strength, an increase in ultimate tensile strength (UTS), and no reduction in

164

ductility. This improvement can be attributed to the reduced mean free range of the dislocations.
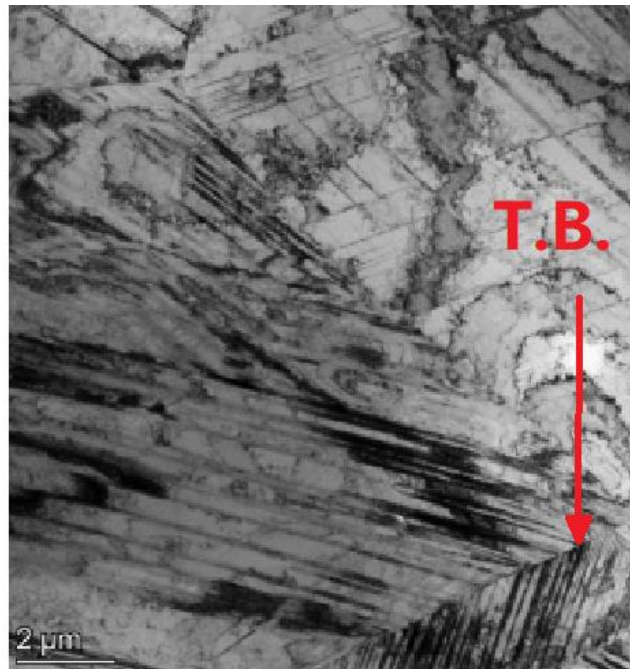


**Figure 5.18 TEM micrographs of SS316 after 700°C and 225MPa creep test showing twinning boundary.**

The use of transmission electron microscopy (TEM) investigation provides significant insights into the deformation behaviour of stainless steel 316 when subjected to creep conditions. The complicated deformation process is suggested by the interaction between dislocations and stacking faults as well as twins under the conditions of 600 °C and 125 MPa. Under these circumstances, the presence of dislocation slip processes is indicated by the even distribution of low-density dislocations.

At a temperature of 600 °C and at a stress of 275 MPa, the heightened density of dislocations resulted in intensified interactions and the emergence of structures resembling cells, which might potentially indicate the beginning phase of dislocation cells. Dislocation cell formation usually leads to matrix hardening [12].

Although twin bands were observed, the EBSD maps (Figure 4.25) indicate that their occurrence did not increase with higher test stress. This suggests that while twinning bands may influence dislocation behaviour, their effect is limited at 600°C. Instead, the formation of a cellular structure and a substantial increase in dislocation density were identified as the driving factors behind the activation energy surge at 275 MPa.

This differs from the anticipated increase in twins. Previous studies on dislocation structure evolution of stainless steels 301 and 316 L have also revealed the formation of dislocation cells, rather than twinning[254], [255]. In the investigation of the impact of dislocation cells on the thermal stability of austenitic stainless steels, Deng et al. [256] identified elemental segregation and lamellar dislocation energy as the primary factors influencing the formation of cell structures. The effect of dislocation cells on twinning was mentioned in the study of Karthik et al. [257] for laser powder-bed fusion processed CuSn alloy. They explained that the activation energy required for the nucleation and propagation of certain dislocations substantially increased in the prepared samples due to the presence of a fine dislocation cell structure, approximately 600 nm in size, and the elevation in stacking fault energy resulting from intracellular tin segregation. This suppression effectively inhibited the occurrence of deformation twinning.

However, at the temperature of 700°C, the observation of an elevated occurrence of deformation twin bands with increased testing stress indicates the potential effect of deformation processes associated with twinning under these particular circumstances. By combining the observations from EBSD maps (Figure 4.26) with calculations based on the Wilshire Equation, it can be inferred that the main determinant affecting the deformation behaviour of 316 stainless steel is not the interactions between dislocations, but rather the increased occurrence of twins that impede dislocation motion. This leads to a significant alteration in the activation energy required for deformation.

## 5.2.2 Haynes 282

The TEM analysis indicated the discrete presence of minute slip bands adorning the $\gamma$ matrix of Haynes 282 as shown in Figure 5.19. EDS images (Figure 5.20) manifested clusters that were characterised by a distinct absence of nickel (Ni) content but enriched by chromium (Cr) around $\gamma'$ precipitates – suggestive the potential formation of pores, with Cr—as an active element—aggregating in these regions prior to pore development. This inference is supported by the presence of faint dislocation lines surrounding the Cr-rich clusters. Given that $\gamma'$ precipitates are the result of precipitation

hardening, they are expected to hinder dislocation motion. It is therefore unsurprising that dislocations accumulate around those spherical precipitates. However, due to the relatively short test duration and relatively low stress, more extensive creep voids or cracks had not yet formed.
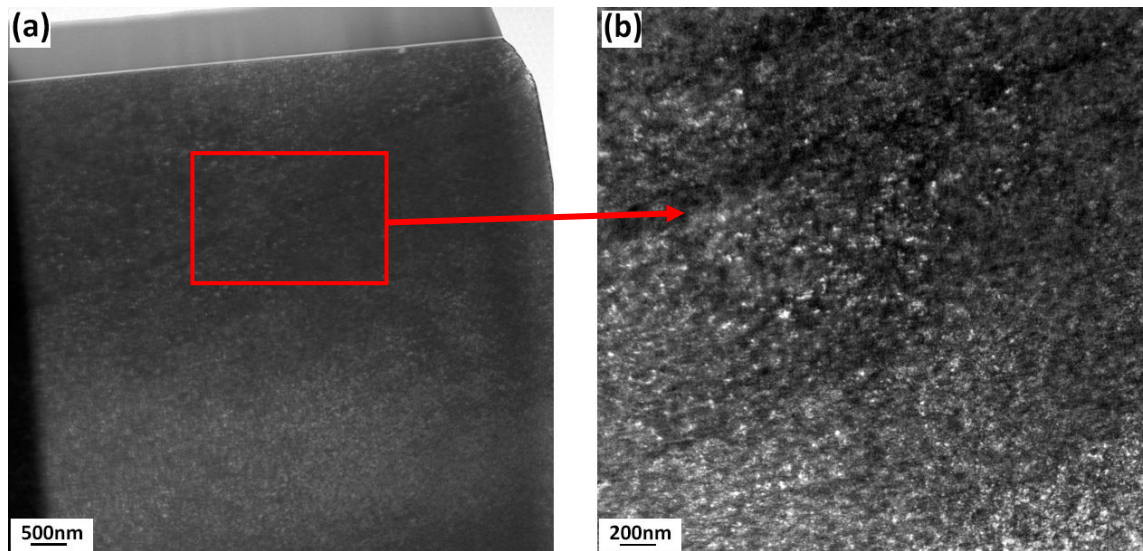


**Figure 5.19 TEM micrographs of H282 after 650℃, 500MPa creep test showing slip bands.**
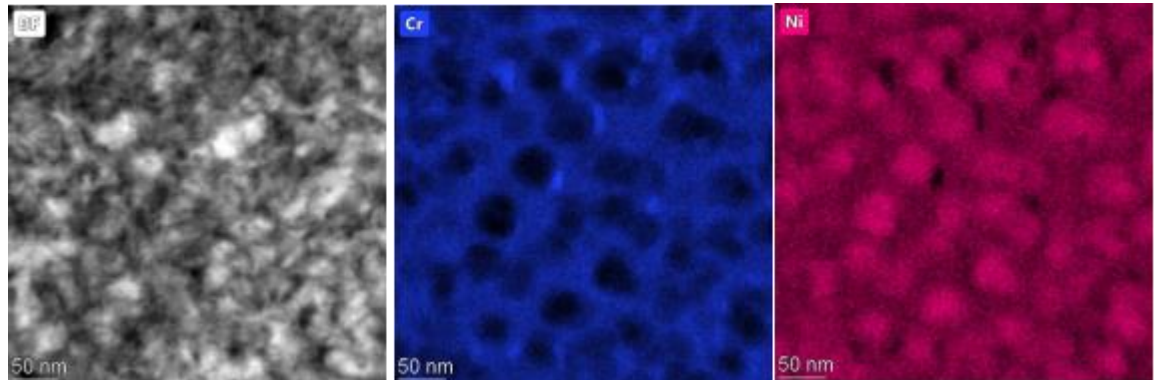


**Figure 5.20 EDS maps showing the enrichment of Cr around γ'.**

No apparent indication of dislocations severing the precipitated phase was detected by this study. Nevertheless, Shen [258] reported that dislocations can slip on octahedral slip planes and bypass the precipitates by forming Orowan loops. This mechanism produces a dislocation network around the γ′ phase, as illustrated in Figure 5.21.
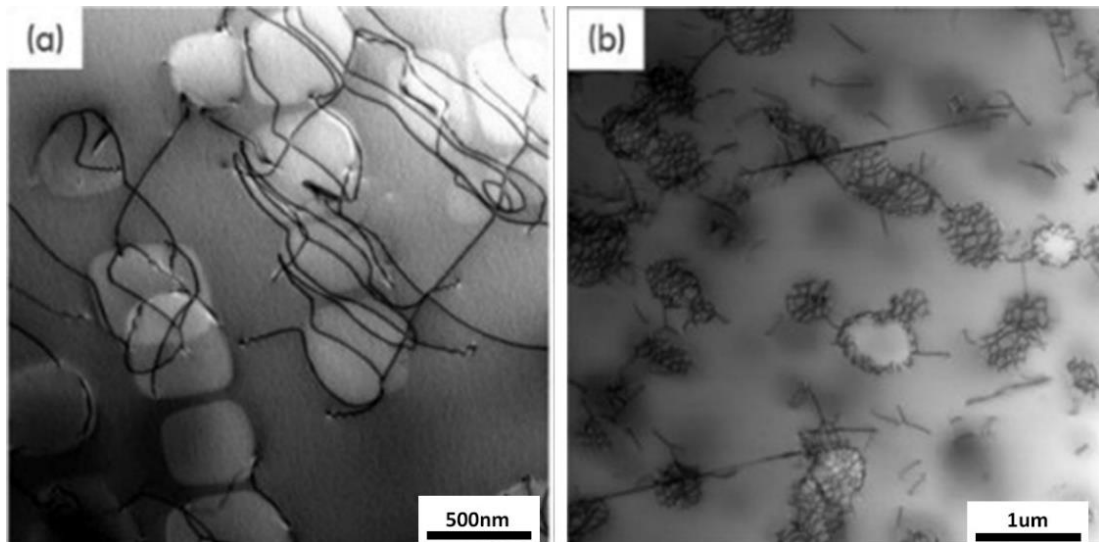
**Figure 5.21 The dislocation network in H282**[258].

Stepping into higher stress territory at 800MPa, the material undergoes creep fracture, leading to a substantial rise in dislocation density. However, these dislocations encountered resistance from $Cr_{23}C_6$ carbides located within grain boundaries. This interference was evidenced by observable dislocation accumulations near the carbides, characterized by a decrease in dislocation spacing towards the $Cr_{23}C_6$ carbides, and also culminating in dislocation entanglements. Most of these dislocations congregate near the grain boundaries, forming a phenomenon referred to as forest dislocations.
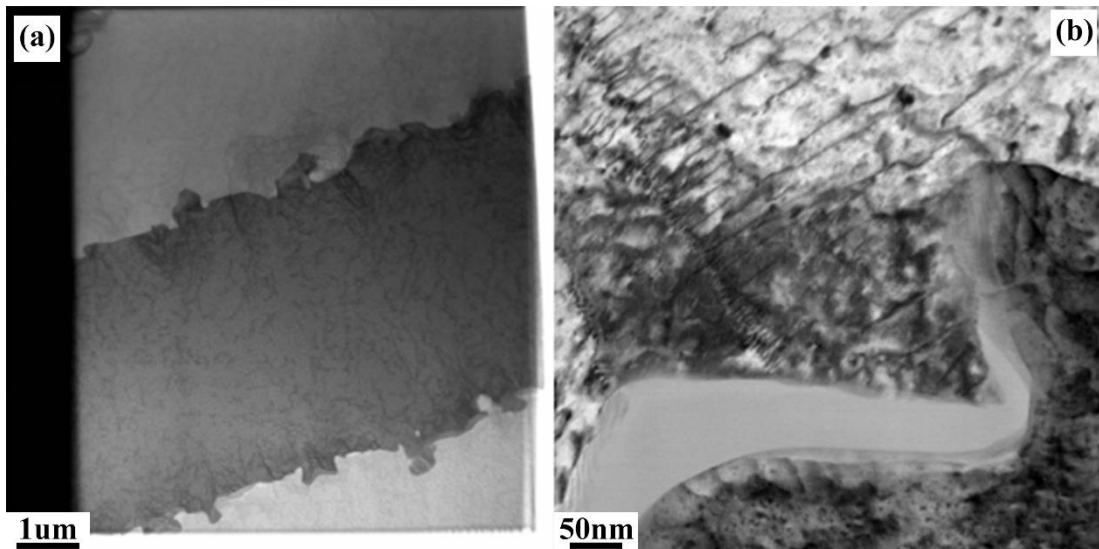


**Figure 5.22 TEM micrographs of H282 after 650℃, 800MPa creep test shown that dislocations were interrupted by grain boundaries.**

Haynes 282 exhibits a structural resemblance to Waspaloy, characterised by a low volume fraction of spherical γ' precipitates. Despite the limited data available for

168

Haynes 282 in this particular study and the suboptimal nature of the results, it is still possible to examine the activation energy of Haynes 282 within the framework of earlier investigations conducted on Waspaloy[19]. The first dislocations are stopped because of the presence of γ' precipitates, which serve as the precipitation hardening phase. The occurrence of dislocations is triggered by the process of Orowan looping around the smaller γ' and subsequently wrapping around or climbing over the larger γ'. Given the current state of dislocation density, it can be observed that the strain rate is mostly influenced by the rate of diffusion[259]. This assertion is substantiated by the computed creep activation energy value of 277kJ/mol[260]. As the stress intensifies, the dislocation density experiences a significant increase, potentially leading to the activation of several slip systems inside the crystal lattice. The distance between the dislocations that are formed from different sources is smaller than the distance between the dislocations and the precipitation phase. This implies that the occurrence of dislocations being severed or encompassing the precipitating phase is hindered prior to being severed or encompassed by dislocations that have multiplied through distinct slip systems. Furthermore, distinct dislocations can serve as impediments to one another[25], [261]. The presence of dislocations on secondary slip systems that intersect the primary slip system, commonly known as forest dislocations, is widely believed to be the primary hindrance to dislocation slip. When the phenomenon of dislocation slip encounters a forest dislocation, it might result in either the formation of a new dislocation, or the bypassing of the forest dislocation, allowing the dislocation to continue its growth. In both scenarios, there is an expenditure of more energy. During the phenomenon of slip, the density of dislocations within a forest hardened material undergoes an increase. This increase in density can be attributed to several factors such as an increase in the number of cut steps, the production of new dislocations, or the growth of existing dislocation lines. Consequently, this rise in dislocation density ultimately results in an increase in resistance inside the material. This phenomenon is also accountable for the rise in activation energy under conditions of elevated stressors.

### 5.2.3 Inconel 713C

IN713C sample was tested at 650℃ and 500MPa stress, and TEM analysis revealed the presence of a small number of dislocations surrounding the γ' precipitates, as

depicted in Figure 5.23. The presence of γ' hindered dislocation motion, even when it shared a coherent interface with the matrix. This behaviour can be attributed to the ordered crystal structure of γ', making it challenging for dislocations to penetrate the precipitate phase. The formidable impediment of γ' prompted the dislocations to follow the Orowan mechanism, bypassing γ' particles.
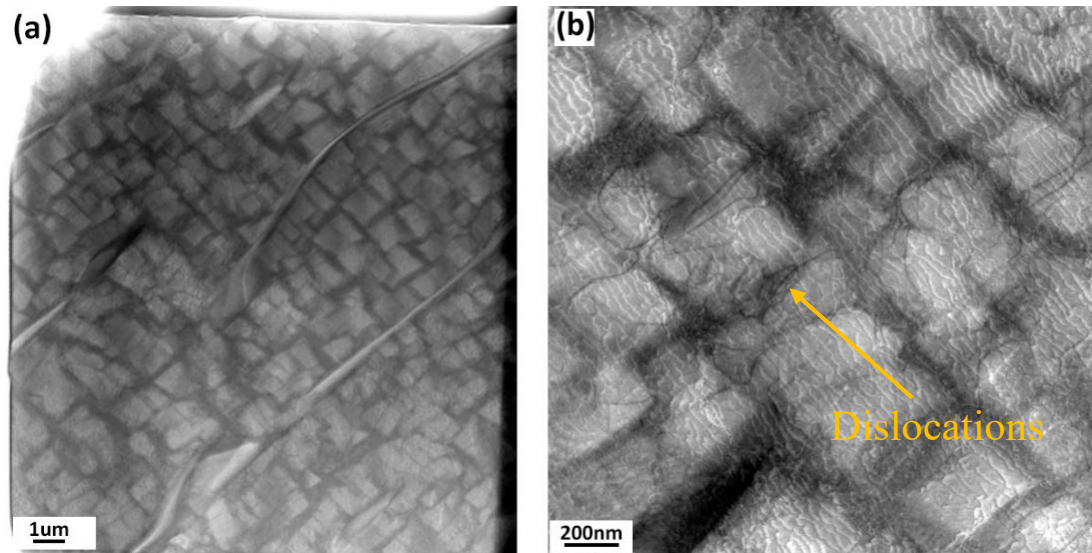


**Figure 5.23 TEM micrographs of IN713C after 650℃, 500MPa creep test showing how dislocation move inside the γ channel.**

IN713C sample which was tested at 650°C, 500MPa shows a large number of Ti, Mo and Nb rich needle-like particles with a volume fraction of about 11% within the selected area, suspected to be carbides or borides, as shown in Figure 5.24.
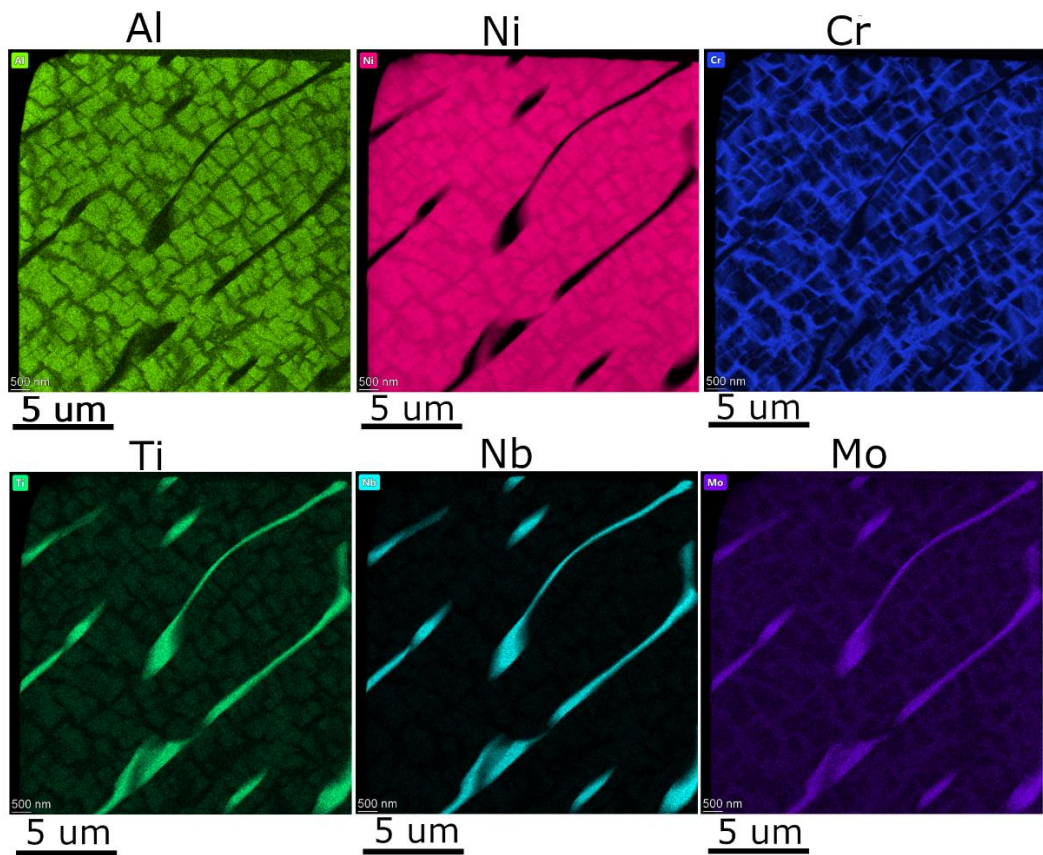
**Figure 5.24 Needle-shape carbides in IN713C.**

Past studies have shown that when a large number of fine-grained carbides precipitate within the grain and along grain boundaries and are uniformly distributed, they can impede dislocation motion and inhibit grain boundary slip[262]. However, large-sized carbides such as MC can easily generate stress concentration around and promote cracking along the carbide-matrix interface, and the interface between carbide and matrix is an easy channel for crack propagation[263]. Cracks and creep cavities have been generated at Figure 4.33 and Figure 4.35, and Figure 5.23(b) also illustrated that the dislocations are mostly clustered near or on the carbide. These prove that stress concentration is more likely to occur around the MC.

When the stress was increased to 800MPa, most of the γ' phase in the samples still maintained the intact cubic morphology, and no obvious carbides were found. This may be due to the fact that under high temperatures and high stress conditions, carbides may dissolve more readily or become localised at the grain boundaries, leading to a redistribution of carbides. Alternatively, the grains may undergo plastic deformation during creep and the carbides are subsequently stretched or twisted, thus affecting their

shape and distribution. It may also be due to the fact that MC-type carbides are predominantly distributed on the grain boundaries between the γ and γ' phases of the matrix, as reported by Zhang et al. [168]. Detailed observations of the carbides in most of the slices show that the core of the striated carbides is located at the boundary of the γ phase. However, the TEM lift-out size is only about 10 μm, which is much smaller than the grain size of IN713C, leading to the possibility that the selected region may not cover the grain boundary portion, resulting in missing carbides. Under high stress conditions, it can be found that most of the dislocations accumulate around γ', forming a kind of barrier that prevents the movement of other dislocations. This dislocation accumulation increases the density of dislocations and increases dislocation-dislocation interactions, thus making it more difficult for the material to deform plastically. It has also been proposed that the dislocation network can release lattice mismatch stresses, moderate stress concentrations, and delay dislocation shear into the γ' phase, which is conducive to maintaining grain boundary strength and improving the creep resistance of the alloy[264]. Although most of the dislocation activity is in the γ channel, the applied stress has induced shearing of the γ' precipitated phase.
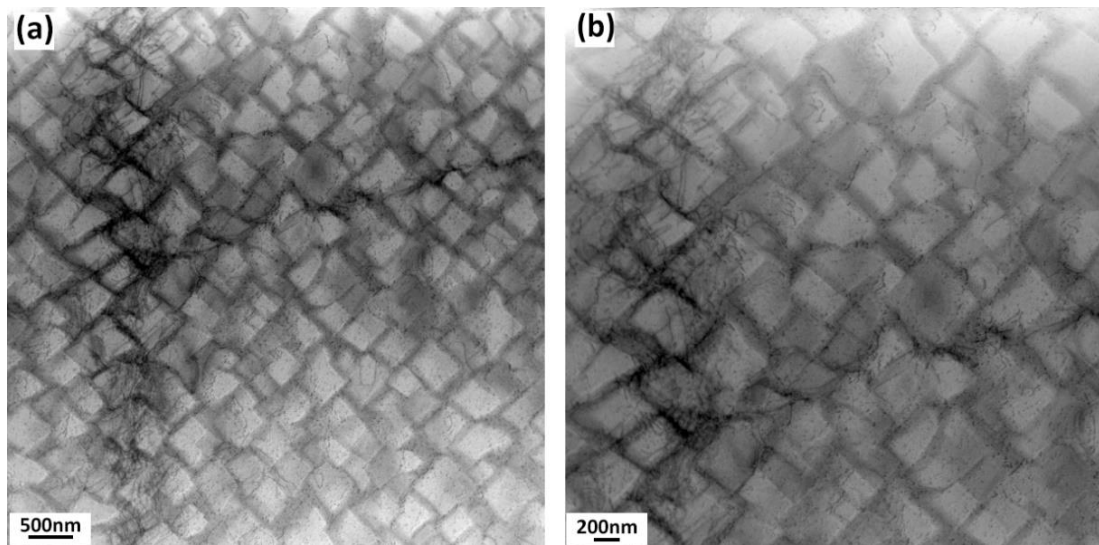


**Figure 5.25 TEM micrographs of IN713C after 650, 800MPa creep test showing the dislocations are confined to γ channels.**
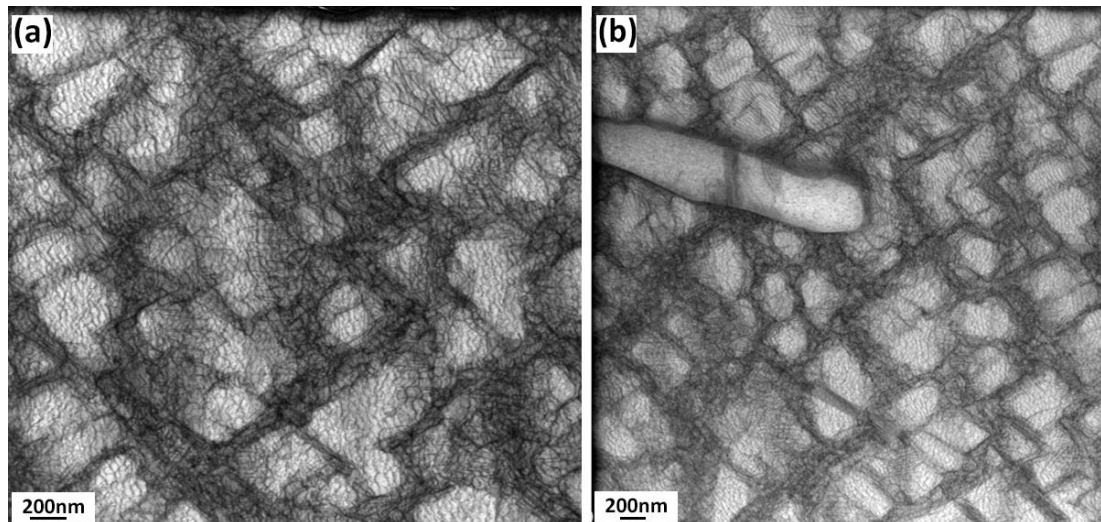
**Figure 5.26 TEM micrographs of IN713C after 750℃, 500MPa creep test**

Under the conditions of 750°C and 500MPa, γ' precipitates underwent microstructural evolution - the morphology and distribution of γ' phase particles significant changed. Initially uniform and cubic in shape, γ' precipitates tend to become increasingly irregular and coarser in appearance, although ImageJ analysis did not reveal any substantial increase in size. This alteration correspondingly diminished their capacity to curtail dislocation activity. Consequently, a substantial density of dislocations occurred near γ' precipitates, leading to climb motion. A conspicuous carbide formation was exclusively observed in the upper left corner of the image (Figure 5.27). Within this carbide, traces of dislocations and stacking faults were identified, as depicted in the Figure 5.26 (b). The γ' phase, influenced by the elevated temperature, underwent marked coarsening and lost its cubic morphology, yet it retained some capacity to hinder dislocations. These dislocations, despite their altered shape, continued to exert an inhibitory effect on others, resulting in a dense accumulation of dislocations surrounding the γ' phase.
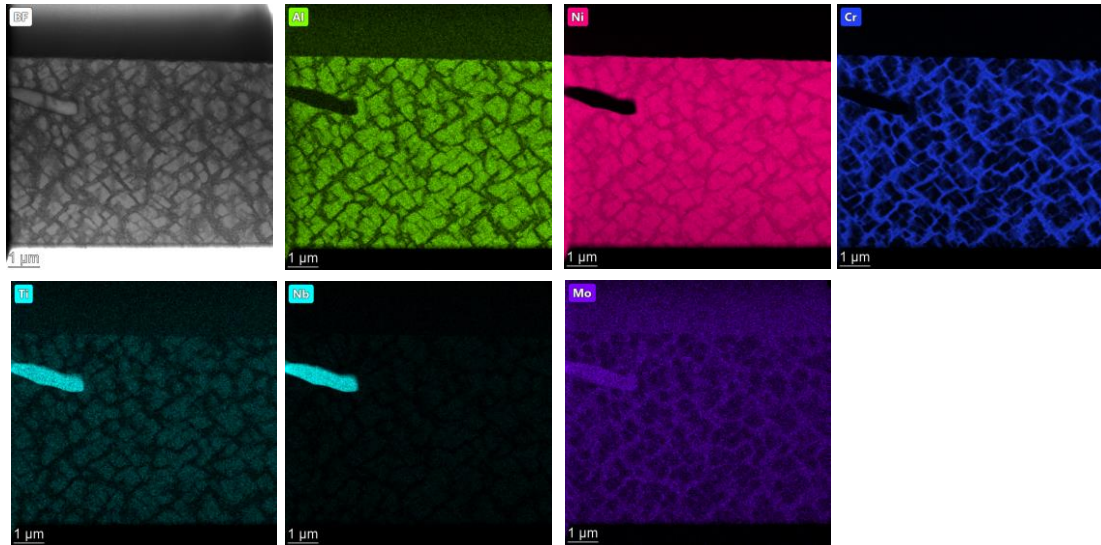
**Figure 5.27 EDS analysis illustrating the carbides on the top-left corner.**

TCP phase presence was detected in the untreated IN713C sample. The formation of this TCP phase is primarily attributed to the significant incorporation of high-melting-point alloying elements concentrated in the dendritic stem region. This elevated concentration results in a higher degree of supersaturation of solid solution elements within the γ matrix[169]. As the TCP phase forms, it consumes the solid solution strengthening elements, diminishing the alloy's solid solution strengthening effect and consequently reducing its strength. Furthermore, the lamellar TCP phase tends to create stress concentrations at interfaces during service, initiating and propagating cracks along these interfaces[265]. This, in turn, diminishes the alloy's tensile properties and fatigue resistance. Interestingly, no precipitation of the TCP phase was observed in either the selected SEM or TEM samples. Previous findings indicate that applying tensile stresses at elevated temperatures reduces TCP phase precipitation in CMSX alloys[266]. Similarly, another nickel-based single-crystal high-temperature alloy, DD11, exhibited a lower degree of elemental bias for rhenium and tungsten in the γ-phase after the stress-aging process, resulting in a reduced occurrence of TCP phase precipitation[267]. However, it is worth noting that stress may promote the precipitation of certain TCP phases, such as the μ phase[268]. In light of the experimental results on IN713C, it is preferable to suspect that tensile stress reduces the incidence of TCP phase precipitation.

In summary, the microstructure of the material undergoes substantial transformations under high-temperature conditions. Comparing the results of increasing the stress,

increasing the experimental temperature has a more prominent effect on the creep properties of the material.

In a previous study, Canton and Liu[269] conducted fatigue experiments on IN713C samples from the same batch, customised to exhibit three distinct grain structures: transition, equiaxed, and columnar, with significant differences in grain size. They found that equiaxed specimens exhibited longer fatigue life than the other structures, which was attributed to the dispersion of crack propagation in specimens with smaller grain sizes.

This finding contrasts with the results of the present creep study. As shown in Figure 4.29, equiaxed specimens display a higher creep rate and fracture earlier than those with transition grain structures under the same temperature and stress conditions. This discrepancy is likely due to the different damage mechanisms: creep voids and cracks are typically observed along carbides and grain boundaries. The higher grain boundary density in equiaxed specimens increases the likelihood of grain boundary cracking and eventual fracture.

However, EBSD results do not show obvious intergranular fracture paths, and in transition-structured specimens, fracture locations tend to appear in the off-columnar direction. This observation requires further investigation.

Liu[125] also reported that fatigue striations were primarily distributed within dendritic regions, with high dislocation densities concentrated between dendrites. Therefore, in this study, creep behaviour was also examined separately in dendritic and non-dendritic regions, and the comparison of the γ' are presented in Figure 5.28.
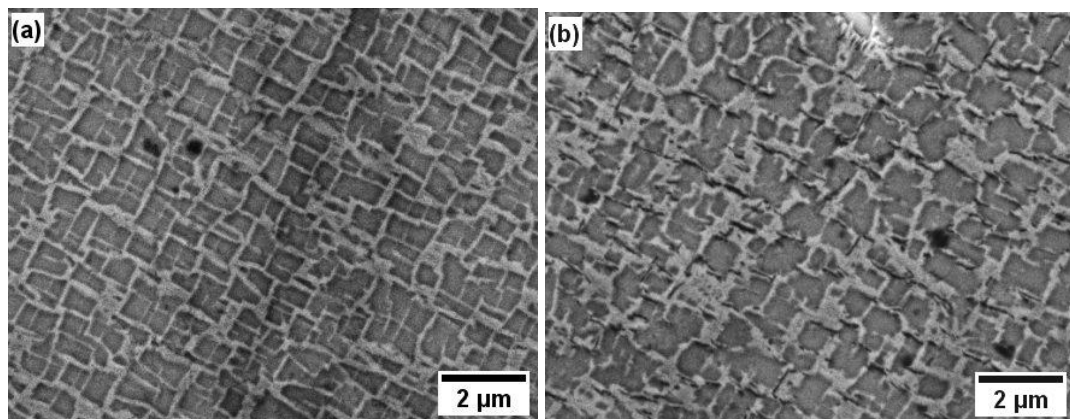


**Figure 5.28 SEM images showing different microstructure of γ' in (a) dendritic**

**area, (b) interdendritic area.**

It is evident that the γ′ precipitates in the dendritic regions exhibit a more regular and ordered cubic morphology. In contrast, within the interdendritic regions, the γ′ precipitates display considerable morphological variability. Although they retain a generally cubic form, their shape is irregular, and their local distribution is highly heterogeneous.

Furthermore, following creep testing at 650 °C and 650 MPa, small cracks were observed in the γ channels of interdendrite region, despite no macroscopic fracture and the examined region being located some distance from the middle of the tested zone. This is more clearly illustrated in the EDS analysis in Figure 5.29, where Cr-rich streaks that lack nickel can be seen within the γ channels, indicative of early stage of creep cracking.
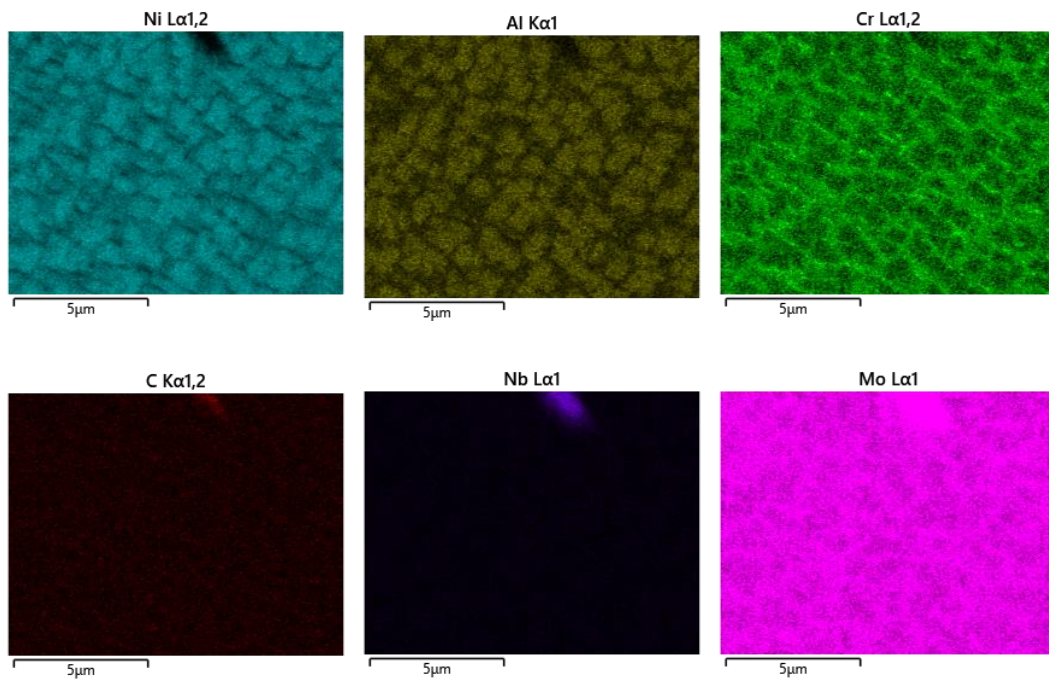


**Figure 5.29 EDS maps of γ′ from the interdendrite region.**

A representative grain boundary was selected for further analysis, and the corresponding EBSD maps are shown in Figure 5.30. The two grains exhibit similar colours in the IPF-Y map, suggesting a similar orientation in the Y-direction. This implies that the boundary between them is likely a low-angle grain boundary (LAGB).

Figure 5.30(e) shows the geometrically necessary dislocation (GND) density distribution calculated using the Channel 5 software. In contrast to Haynes 282, the dislocations—partially indicated by the brighter colours—are primarily concentrated within the grains rather than along the grain boundary. As evident from Figure 5.23(d), strain appears to accumulate within the dendritic structure, suggesting that dendritic and interdendritic regions act as barriers to dislocation motion, leading to localised dislocation pile-up, possibly more so than low-angle grain boundaries.
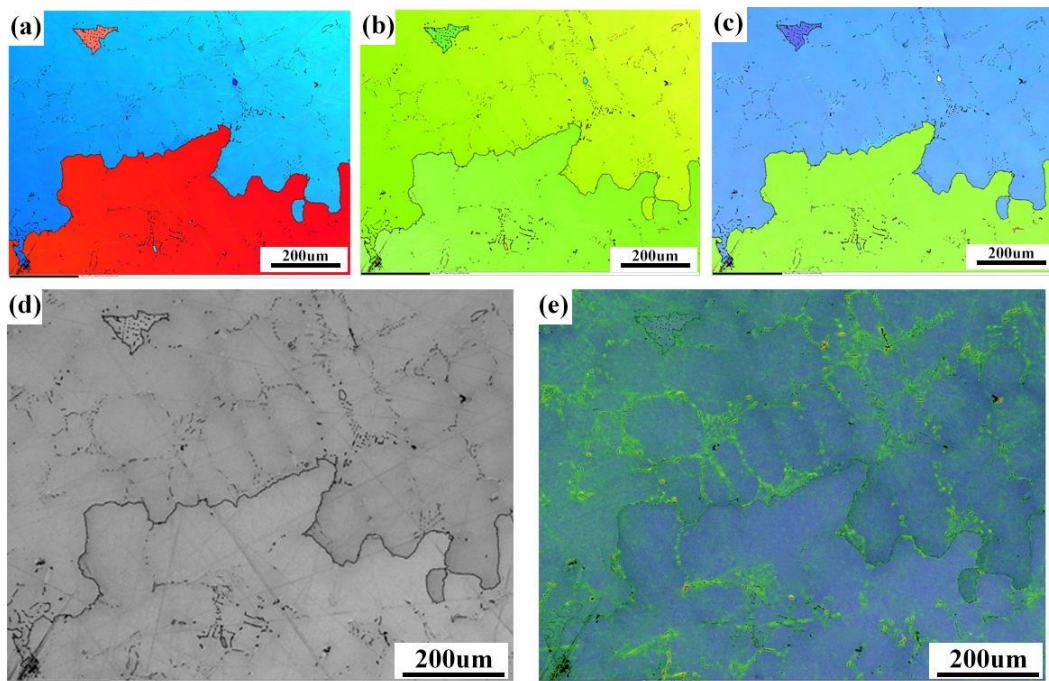


**Figure 5.30 EBSD maps of LAGB of a crept specimen tested at 650°C and 650MPa with (a) IPF X, (b) IPF Y, (c) IPF Z, (d) Band contrast, (d) GND map**

Another triple point junction was examined, as shown in Figure 5.31. The map reveals that the grains are distinctly coloured, indicating different crystallographic orientations. Only one region, highlighted by the pink box on Figure 5.31(a), shows a LAGB because of the similar colour, while the other boundaries exhibit significant colour contrast, indicating high-angle grain boundaries (HAGB). In this case, GNDs are clustered both in the dendritic boundaries and along grain boundaries. In some areas, dislocation accumulation at grain boundaries is even more pronounced than at the dendrite–interdendrite boundaries. These findings suggest that both dendritic structures and high-angle grain boundaries contribute significantly to impeding dislocation motion and promoting dislocation pile-up.

177
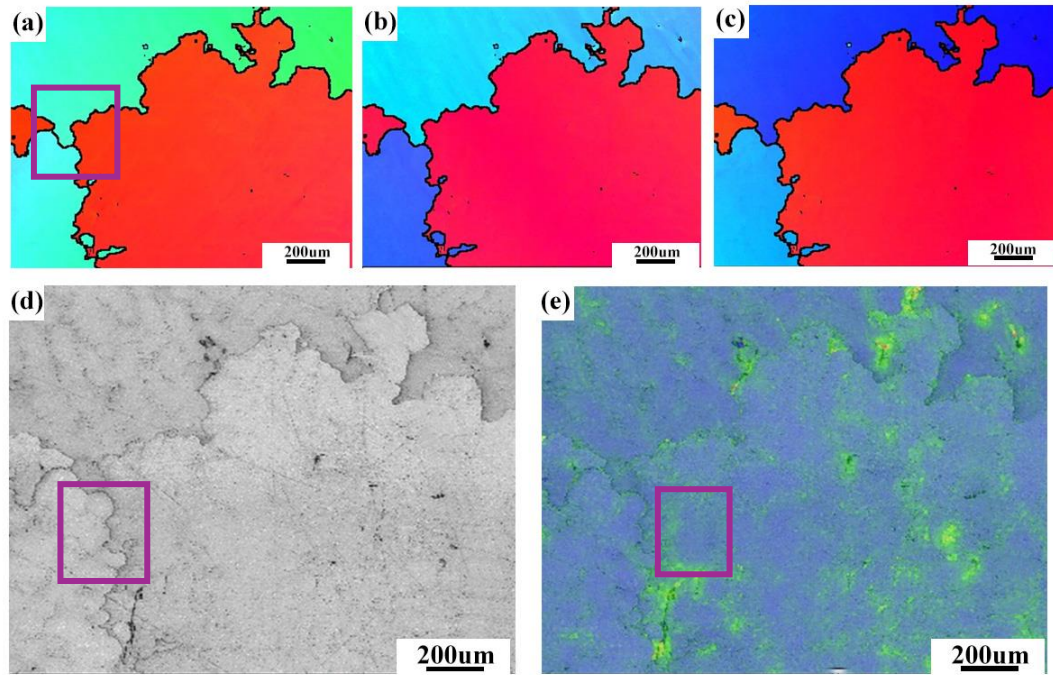
**Figure 5.31 EBSD maps of HAGB of a crept specimen tested at 650°C and 650MPa with (a) IPF X, (b) IPF Y, (c) IPF Z, (d) Band contrast, (d) GND map**

In summary, grain orientation influences both the misorientation angle of grain boundaries and the extent of dislocation activity.

The combined TEM and EBSD observations help explain why the creep activation energy of IN713C, as derived using the Wilshire equation, remains constant. Dislocation activity initially concentrates in the γ channels and around carbides, then becomes further obstructed by dendritic features and high-angle grain boundaries. Despite increasing applied stress, no fundamental shift occurs in the underlying deformation mechanism since it is these barriers rather than an increase in forest hardening above the yield stress, which continues to hinder dislocation mobility. As a result, the $Q_c*$ remains unchanged.

The microstructural investigation reveals that both nickel-based superalloys undergo dislocation interactions with the precipitated phase, hence influencing their creep behaviour. The γ' precipitates of IN713C and H282 exhibit a restrictive influence on dislocation movement under low stress conditions. Nevertheless, when the applied stress exceeds the yield strength (YS), as shown in Figure 5.32 (a), the restrictive effect of the cubic γ' phase in IN713C becomes more pronounced. As a result, dislocations are constrained to move primarily within the narrow γ channels. In contrast, the

dislocations in Haynes 282 tend to accumulate near the grain boundaries. This accumulation, along with the forest hardening caused by grain boundaries, carbides within the grain boundaries, and the entanglement of dislocations, contributes to the increased difficulty in further dislocation motion.
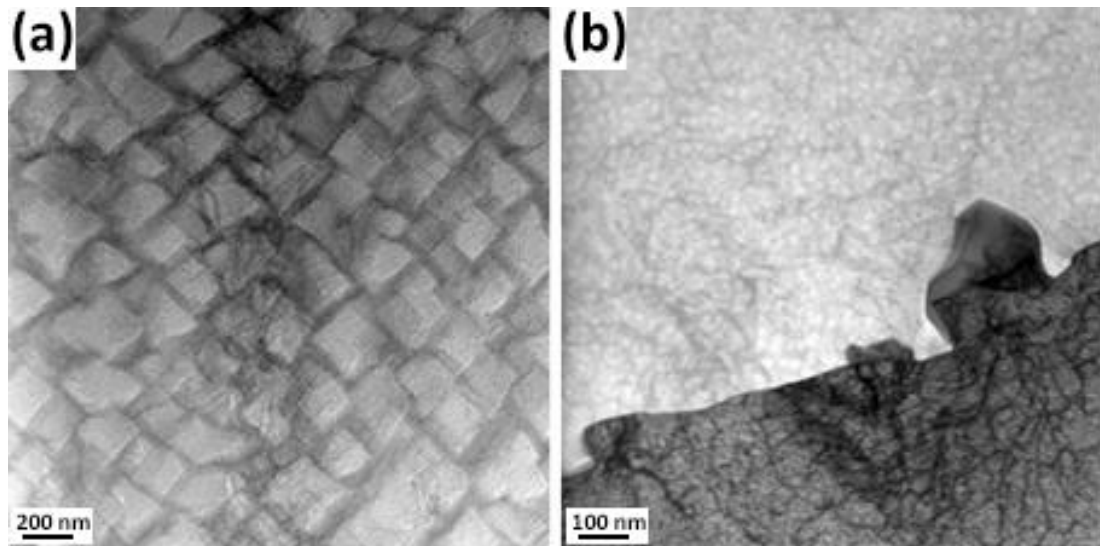


**Figure 5.32 TEM micrographs of nickel superalloys after 800MPa creep test (a) IN713C (b)H282**

In conjunction with the transmission electron microscopy (TEM) findings, it is evident that alterations in the cubic morphology of the $\gamma'$ precipitation hardening phase occur when the temperature is raised to 750 °C or the stress is increased to 800MPa. However, even at elevated temperatures the precipitation phase continues to exert a significant restraining influence on dislocations. Consequently, the majority of dislocations exhibit restricted movement within a narrow $\gamma$ channel, with only a minor fraction of dislocations engaging in shearing of the $\gamma'$ phase, as depicted in Figure 5.33. Due to the significantly elevated volume fraction of $\gamma'$ phase in IN713C, the penetration of dislocations into the $\gamma'$ phase is hindered, hence resulting in little alteration of the activation energy.
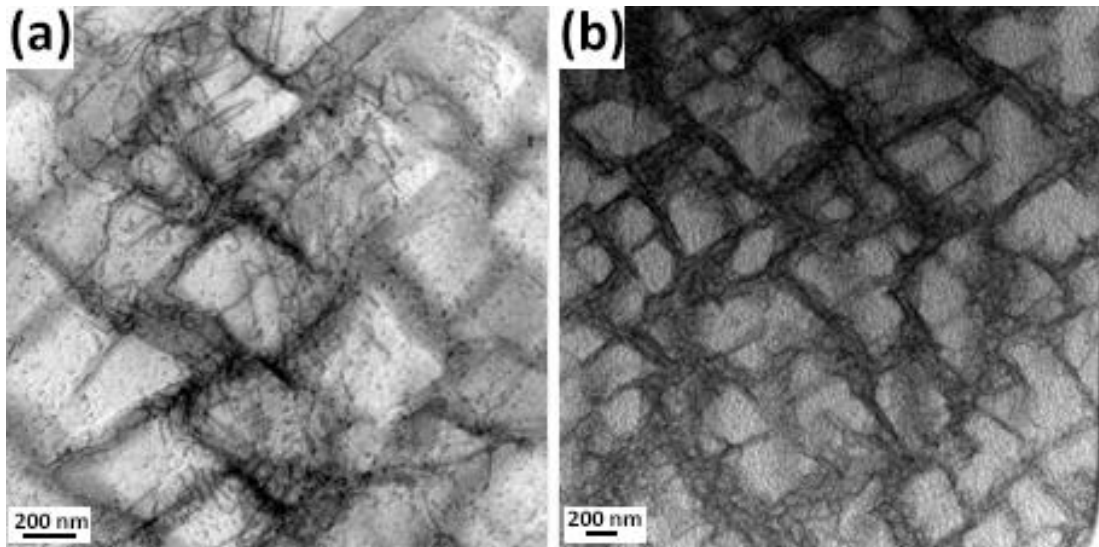
**Figure 5.33 TEM micrographs of IN713C (a) 650°C 800MPa, (b) 750°C 500MPa**

It is worth noting that the activation energy value of Haynes 282 is significantly higher in magnitude compared to that of IN713C. As a result of smaller grains, the greater number of grain boundaries in the Haynes 282 alloy serves to impede the mobility of dislocations. This gains further support from the transmission electron microscopy (TEM) image of Haynes 282. When examining specimens that have undergone creep fracture, a substantial build-up of dislocations near the grain boundaries becomes evident. Grain boundaries impede the movement of these dislocations, thus inhibiting actions like cutting or climbing along the grain boundaries.

## 5.3  Cyclic tests

The cyclic creep experiments conducted on 316 stainless steel provide valuable insights into how alternating stress and temperature conditions affect deformation mechanisms compared to conventional isothermal creep. Both cyclic tests, whether initiated at 600 °C/334 MPa or 700 °C/165 MPa, resulted in significantly shorter rupture lives than their constant-stress counterparts. This clearly indicates that cyclic conditions accelerate creep damage accumulation, primarily by repeatedly destabilising the microstructure during temperature and stress transitions.

A key feature of the cyclic tests is the emergence of a transient stage resembling a "pseudo-primary creep" after each cooling–heating cycle. The TEM evidence supports this phenomena. Figure 4.1 shows a microstructure featuring primary twins, which not

only serve as obstacles to dislocation motion but also act as sites for dislocation nucleation and accumulation. When dislocation density is low, dislocations are more likely to react with the twinning boundaries (TB), to be blocked by the TB, or to be absorbed by the TB through different dislocation reactions[270]. With increasing temperature, deformation initiates earlier in each grain, and more twin boundary/grain boundary junctions are activated, thereby providing additional dislocation sources and enhancing dislocation nucleation within grains[271]. TEM observations (Figure 5.16) indicate that at 600 °C, dislocation cells form in 316 stainless steel, suggesting a sufficiently high dislocation density to allow stress relaxation via dislocation glide. These dislocations accumulate and, over time, overcome the energy barrier associated with dislocation–TB interaction. As the temperature rises further, the number of dislocations increases significantly. Many of these dislocations become randomly oriented, entangled, and pinned at TBs, limiting further dislocation reactions and hindering penetration through the TB. To release the localised strain energy caused by dislocation accumulation, secondary twinning is activated via the emission of new dislocations across the TB[270]. As shown in Figure 4.26, the higher stress at 700 °C leads to the formation of additional twins, providing evidence that dislocation build-up may be relieved through twinning. This transition from dislocation activity to twinning could explain the observed increase in creep rate as the temperature rises from 600 °C to 700 °C.

Unexpectedly, however, a higher creep rate was also observed at lower temperatures during certain stages of cyclic loading. In a non-cyclic environment, cooling typically results in a reduced creep rate—as seen in the constant-stress creep tests, where the curve at 600 °C (green curve) lies below that at 700 °C (purple curve). Therefore, this unusual phenomenon prompted closer examination of the stress conditions. Normally, creep recovery due to internal stress relaxation during cooling leads to a temporary reduction in creep rate and potential reverse dislocation motion[272]. However, it has been reported that retrograde motion of dislocations under high internal stress can weaken dislocation barriers, thereby enhancing creep during subsequent reloading[273]. This phenomenon may explain the increase in creep rate following stress recovery under cyclic conditions, although the precise mechanisms require further investigation through detailed microscopic analysis.

From a broader perspective, these findings align with previous studies on cyclic creep of 316 stainless steel, which emphasise the strong influence of thermal cycling on creep rate and rupture life[215], [217], [218]. The results highlight the importance of considering cyclic conditions in service environments, such as power plant start-up and shutdown cycles, where components are frequently exposed to fluctuating thermal and mechanical loads. In such cases, cyclic creep can dominate over conventional creep, significantly reducing service life.

## 5.4 Summary

This chapter provides a comprehensive analysis of the creep behaviour of three alloys—316 stainless steel, Haynes 282, and Inconel 713C—focusing on activation energy ($Q_c$*) and its correlation with microstructural features. It highlights the limitations of traditional creep models such as the Power Law and Larson-Miller methods, which fail to account for the complex microstructures of high-performance alloys. The study shifts to the Wilshire Equations, which offer a more robust approach to predicting creep behaviour by considering stress partitioning and temperature standardisation.

The results demonstrate that the Wilshire Equations provide an accurate framework for determining $Q_c$*, offering a better understanding of how activation energy varies across different stress and temperature conditions. Significant differences in $Q_c$* values were observed among the alloys, with 316 stainless steel showing lower activation energies under low-stress conditions, Haynes 282 exhibiting a clear breakpoint in activation energy related to dislocation behaviour, and IN713C maintaining stable activation energy values due to the influence of γ' precipitates.

Microstructural analysis using TEM revealed that for 316 stainless steel, dislocation motion at 600°C and twinning boundaries at 700°C played key roles in influencing activation energy. Haynes 282 exhibited complex dislocation interactions with γ' precipitates at low stress, while IN713C's γ' phase significantly hindered dislocation motion, contributing to its stable creep resistance. The study further demonstrated that variations in microstructure, such as grain size and precipitate distribution, angle of

grain boundaries, dendritic structure etc. greatly affect the creep behaviour and activation energy of these materials.

Cyclic creep of SS316, based on the life-fraction hardening method, results in a shorter creep life compared to constant-stress creep. Additionally, the creep rate increases with rising temperature, which can be attributed to a transition in deformation mechanisms—from the formation of dislocation cells to the development of twin boundaries. The creep rate was observed to increase more with decreasing temperature. This may be explained by dislocation recovery processes reducing dislocation barriers, resulting in a higher creep rate during subsequent reloading.

The chapter concludes that the Wilshire Equations, by incorporating microstructural features, provide a more comprehensive understanding of creep mechanisms. This approach proves particularly useful for extrapolating creep behaviour in novel alloys and evaluating the role of microstructural evolution in high-temperature performance.

# 6. Conclusions

To investigate the creep behaviour of high-temperature alloys, this study meticulously examined three alloys with varying precipitate phase contents: 316, Haynes 282 (H282), and Inconel 713C (IN713C). The primary objective was to unravel the fundamental mechanisms governing creep and link them to the activation energy calculated through the Wilshire equation. This research substantiated the Wilshire equation's reliability in associating micromechanics with deformation mechanisms for creep behaviour prediction.

## 6.1  316 Stainless steels

Derivation from the Wilshire Equation shows that in 316 stainless steel, the apparent creep activation energy $Q_c*$ gradually increases from ~153 kJ/mol to ~298 kJ/mol as stress lower or exceeds the yield strength. This progressive variation reflects the evolving deformation mechanisms. At low temperatures, the creep activation energy is below the self-diffusion value of austenite, consistent with its coarse-grained, precipitate-free microstructure, which allows dislocations to move with little resistance. At 600 °C, TEM revealed the formation of dislocation cells, while EBSD at 700 °C demonstrated a marked increase in twin boundaries, indicating enhanced twinning with rising temperature and corresponding increases in $Q_c*$. Importantly, this change was gradual rather than abrupt, as demonstrated by systematically removing data at the lowest or highest stresses, suggesting that dislocation multiplication initially occurred in local regions before propagating throughout the material as stress increased to yield.

Cyclic creep tests were subsequently performed to examine these mechanisms in greater depth. Accelerated creep rates were observed under both 600 °C and 700 °C conditions. This acceleration was independent of loading sequence: whether high or low temperature was applied first, the response remained similar. At 600 °C, 316 formed high-density dislocation cells, which provided favourable sites for twin nucleation and growth; during cycling, the transition to 700 °C markedly accelerated the creep rate. Conversely, when cycling down from 700 °C to 600 °C, the creep rate

also increased, possibly due to dislocation recovery during unloading weakening the dislocation barrier and thereby facilitating easier motion during reloading.

## 6.2 Nickel-based Superalloys

For Haynes 282, Wilshire Equation fitting revealed a distinct breakpoint. Below the yield strength, $Q_c^*$ is ~277 kJ/mol, consistent with the self-diffusion energy of nickel. At higher stresses, however, $Q_c^*$ increases to ~427 kJ/mol. This behaviour corresponds to a change in dislocation interactions: at low stresses, $\gamma'$ precipitates strongly pin dislocations, while at high stresses dislocations accumulate near grain boundaries and become entangled, producing forest hardening and significantly raising the activation energy. These results are consistent with behaviour reported for Waspaloy and similar alloys, underscoring the role of moderate $\gamma'$ content in creep resistance through the interplay of precipitation strengthening and grain-boundary interactions.

In contrast, Inconel 713C exhibits stable high-temperature behaviour due to its high volume fraction of $\gamma'$. Tensile tests show a higher hardening rate at 750 °C than at 650 °C, yet with higher ultimate tensile strength (UTS). Wilshire analysis revealed that $Q_c^*$ remains essentially constant at ~269–270 kJ/mol across all stresses, with no evidence of breakpoints. TEM confirmed this, showing dislocation motion confined to narrow $\gamma$ channels, with creep governed by hindered slip rather than extensive dislocation rearrangement. $\gamma'$ strengthening dominates across all conditions, preventing the mechanism shifts observed in 316 and Haynes 282.

Grain morphology further influences creep resistance in IN713C. Columnar grains show the greatest resistance, while equiaxed grains with high boundary density deform most readily. Analysis of dislocation distributions indicates that in adjacent grains with small misorientation angles, geometrically necessary dislocations (GNDs) accumulate primarily in interdendritic regions, rather than on the grain boundaries themselves. In contrast, at larger misorientations, GNDs are distributed across both interdendritic and grain boundaries, with significant pile-up occurring on the latter. This suggests that dendrite boundaries, interdendritic boundaries, and high-angle grain boundaries all act as important barriers to dislocation motion, collectively controlling local creep behaviour.

185

## 6.3  Overall Remarks

Comparative fitting of the 316 datasets using the power-law, Larson–Miller, and Wilshire Equations confirmed that although all methods provide reasonable fits over limited ranges, the Wilshire Equation gives the most consistent predictive accuracy across alloys and stress conditions.

By combining predictive modelling with experimental observations, this study highlights the interconnected influence of precipitate fraction, grain morphology, and dislocation behaviour on creep resistance. Creep in 316 stainless steel is primarily governed by dislocation slip and twinning; in Haynes 282 by dislocation–precipitate interactions and forest hardening; and in Inconel 713C by $\gamma'$ strengthening and restricted dislocation glide. The Wilshire equation provides a robust framework linking these microstructural mechanisms with macroscopic creep behaviour. Verification of the model against microstructural evidence confirms its reliability and engineering significance: it enables accurate identification of mechanism-dependent regions and guides the selection of predictive equations under specific conditions. This in turn improves the extrapolation of creep life in new alloys and informs the design and optimisation of materials for high-temperature applications.

# 7. Future work

While this study has provided valuable insights into the creep behaviour of 316 stainless steel, Haynes 282, and Inconel 713C—highlighting the connection between creep activation energy in the Wilshire equation and transitions in dislocation behaviour—several areas remain for further investigation. These could significantly enhance our understanding of high-temperature deformation mechanisms in advanced alloys.

**1. Comprehensive TEM Characterisation under Cyclic Stress Conditions:**

This study observed the formation of dislocation cells and twinning structures in 316 stainless steel at 600 °C and 700 °C, respectively, which contributed to an increased cyclic creep rate at elevated temperatures. However, the observed increase in creep rate following the temperature reduction from 700 °C to 600 °C lacks microscopic characterisation. Future work should involve interrupting the cyclic creep tests after the initial 700 °C–600 °C transition, allowing a brief continuation of testing before removing the specimen for TEM analysis. This would enable detailed observation of the microstructural evolution responsible for this behaviour.

**2. Extension of the Cyclic Creep Testing Matrix:**

Although this study aimed to compare conditions with equivalent creep life under differing temperature and stress combinations, the two selected cases did not demonstrate significant contrasts in creep damage dominance. Future testing should consider comparing creep conditions with the same rupture life but differing damage mechanisms—for example, pairing higher-temperature/lower-stress conditions with lower-temperature/higher-stress conditions. This would help to see how primary and tertiary creep mechanisms behave under cyclic loading.

**3. Cyclic Creep Testing of Mechanism-Stable Materials:**

While 316 exhibits a clear transition in deformation mechanism, other materials such as Inconel 713C demonstrate a more stable mechanism dominated by dislocation activity only. Investigating such materials under cyclic creep conditions could help reveal whether changes in dislocation density alone influence cyclic behaviour, or

whether alternative mechanisms emerge under repeated thermal and mechanical cycling.

## 4. Extension of DIC Creep Testing and In-situ Observation:

The digital image correlation (DIC) creep experiments did not yield fully conclusive results. Although equiaxed specimens appeared to exhibit poorer creep resistance, EBSD analysis of fractured transition specimens indicated that failure often occurred in columnar regions. The DIC strain maps also showed significant localised deviations, but the microstructure at those specific locations could not be observed due to experimental limitations. Future work should incorporate in-situ microscopic techniques during DIC testing to monitor the evolution of microstructural features—particularly grain boundaries in columnar structures and the formation of creep cavities—under load.

## 5. Comparative Experiments on Nickel-Based Alloys:

Haynes 282 and Waspaloy possess very similar microstructures and both exhibit a significant increase in creep activation energy, as calculated using the Wilshire equation. This increase is attributed to a transition in dislocation behaviour—from bypassing spherical $\gamma'$ precipitates to entanglement with other dislocations, including forest dislocations. Under high-stress conditions, both alloys show creep activation energies exceeding 400 kJ/mol.

However, under low-stress conditions, Haynes 282 displays a creep activation energy of 276 kJ/mol, whereas Waspaloy exceeds 320 kJ/mol. The reason for this difference remains unclear and warrants further investigation in future studies.

# 8. Reference

[1]     R. Fouladi Fard, K. Naddafi, M. Yunesian, R. Nabizadeh Nodehi, M. H. Dehghani, and M. S. Hassanvand, 'The assessment of health impacts and external costs of natural gas-fired power plant of Qom', *Environmental Science and Pollution Research*, vol. 23, no. 20, pp. 20922–20936, Oct. 2016.

[2]     S. Basu and A. K. Debnath, 'Advanced Ultrasupercritical Thermal Power Plant and Associated Auxiliaries', *Power Plant Instrumentation and Control Handbook*, pp. 893–988, Jan. 2019.

[3]     A. Di Gianfrancesco, 'The fossil fuel power plants technology', *Materials for Ultra-Supercritical and Advanced Ultra-Supercritical Power Plants*, pp. 1–49, Jan. 2017.

[4]     W. Kotlarz and M. Witanowski, 'Turbine Engines Trend Development', *Journal of KONBiN*, vol. 51, no. 1, pp. 243–254, Mar. 2021.

[5]     R. P. Skelton, *High Temperature Fatigue*. Dordrecht: Springer Netherlands, 1987.

[6]     K. Sawada *et al.*, 'Catalog of NIMS creep data sheets', *Sci Technol Adv Mater*, vol. 20, no. 1, pp. 1131–1149, Dec. 2019.

[7]     S. M. Bagnall, D. L. Shaw, and J. C. Mason-Flucke, 'Implications of'Power by the Hour'on Turbine Blade Lifing', 2000.

[8]     F. R. Larson and J. Miller, 'A Time-Temperature Relationship for Rupture and Creep Stresses', *J Fluids Eng*, vol. 74, no. 5, pp. 765–771, Jul. 1952.

[9]     S. S. Manson and A. M. Haferd, 'A linear time-temperature relation for extrapolation of creep and stress-rupture data', Lewis Flight Propulsion Lab., NACA, 1953.

[10]    R. L. Orr, O. D. Sherby, and J. E. Dorn, 'Correlations of rupture data for metals at elevated temperatures', U.S. Atomic Energy Commission, Jul. 1953.

[11]    B. Wilshire and H. Burt, 'Long-term creep design data for forged 1Cr–1Mo–0.25V steel', *Strength Fract Complex*, vol. 4, no. 2, pp. 65–73, 2006.

[12]   S. G. R. Brown, R. W. Evans, and B. Wilshire, 'Creep strain and creep life prediction for the cast nickel-based superalloy IN-100', *Materials Science and Engineering*, vol. 84, no. C, pp. 147–156, Dec. 1986.

[13]   J. Weertman, 'Theory of Steady-State Creep Based on Dislocation Climb', *J Appl Phys*, vol. 26, no. 10, pp. 1213–1217, Oct. 1955.

[14]   P. Brozzo, 'Paper 67: A Method for the Extrapolation of Creep and Stress-Rupture Data of Complex Alloys', *Proceedings of the Institution of Mechanical Engineers, Conference Proceedings*, vol. 178, no. 1, pp. 6-77-6–85, Jun. 1963.

[15]   B. Wilshire, P. J. Scharning, and R. Hurst, 'A new approach to creep data assessment', *Materials Science and Engineering: A*, vol. 510–511, no. C, pp. 3–6, Jun. 2009.

[16]   M. T. Whittaker, M. Evans, and B. Wilshire, 'Long-term creep data prediction for type 316H stainless steel', *Materials Science and Engineering A*, vol. 552, pp. 145–150, Aug. 2012.

[17]   W. Harrison, M. Whittaker, and S. Williams, 'Recent Advances in Creep Modelling of the Nickel Base Superalloy, Alloy 720Li', *Materials*, vol. 6, no. 3, pp. 1118–1137, Mar. 2013.

[18]   M. T. Whittaker, W. J. Harrison, R. J. Lancaster, and S. Williams, 'An analysis of modern creep lifing methodologies in the titanium alloy Ti6-4', *Materials Science and Engineering: A*, vol. 577, pp. 114–119, Aug. 2013.

[19]   M. Whittaker, W. Harrison, C. Deen, C. Rae, and S. Williams, 'Creep Deformation by Dislocation Movement in Waspaloy', *Materials*, vol. 10, no. 1, p. 61, Jan. 2017.

[20]   Z. Abdallah, K. Perkins, and S. Williams, 'Advances in the Wilshire extrapolation technique—Full creep curve representation for the aerospace alloy Titanium 834', *Materials Science and Engineering: A*, vol. 550, pp. 176–182, Jul. 2012.

[21]   V. Cedro, C. Garcia, and M. Render, 'Use of the Wilshire equations to correlate and extrapolate creep data of HR6W and Sanicro 25', *Materials*, vol. 11, no. 9, pp. 1–30, 2018.

[22] V. Cedro III, C. Garcia, and M. Render, 'Use of the Wilshire equation to correlate and extrapolate creep rupture data of Incoloy 800 and 304H stainless steel', *Materials at High Temperatures*, vol. 36, no. 6, pp. 511–530, Nov. 2019.

[23] B. Wilshire and P. J. Scharning, 'Prediction of long term creep data for forged 1Cr–1Mo–0·25V steel', *Materials Science and Technology*, vol. 24, no. 1, pp. 1–9, 2008.

[24] B. Wilshire and P. J. Scharning, 'A new methodology for analysis of creep and creep fracture data for 9–12% chromium steels', *International Materials Reviews*, vol. 53, no. 2, pp. 91–104, 2008.

[25] C. S. Deen, 'Application of the Wilshire Equations to Nickel Disc Alloys , with an Investigation of the Dislocation Network', EngD thesis, Swansea University, 2015.

[26] M. Niinomi, 'Metallic biomaterials', *Journal of Artificial Organs*, vol. 11, no. 3, pp. 105–110, Sep. 2008.

[27] D. R. Askeland and P. P. Phule, *Essentials of Materials Science and Engineering*, 1st ed. Tsinghua University Press, 2004.

[28] J. P. Singh and S. Verma, 'Raw materials for terry fabrics', in *Woven Terry Fabrics*, Elsevier, 2017, pp. 19–28.

[29] R. Singh and R. Singh, 'Chapter 10 – Working with Metals', *Applied Welding Engineering*, pp. 99–102, 2016, Accessed: Aug. 21, 2025.

[30] R. N. Wright, 'Mechanical Properties of Wire and Related Testing', *Wire Technology*, pp. 127–155, 2011.

[31] J. W. Morris, 'Dislocation-controlled Plasticity of Crystalline Materials: Overview', *Encyclopedia of Materials: Science and Technology*, pp. 2245–2255, Jan. 2001.

[32] G. Gottstein, M. Goerdeler, and G. V. S. S. Prasad, 'Mechanical Properties: Plastic Behavior', *Encyclopedia of Condensed Matter Physics, Six-Volume Set*, vol. 3, pp. 298–305, Jan. 2005.

[33] M. Fattahi, C.-Y. Hsu, A. O. Ali, Z. H. Mahmoud, N. P. Dang, and E. Kianfar, 'Severe plastic deformation: Nanostructured materials, metal-based and polymer-based nanocomposites: A review', *Heliyon*, vol. 9, no. 12, p. e22559, Dec. 2023.

[34] R. W. Evans, B. Wilshire, and I. of Metals, *Creep of Metals and Alloys*. in Book (Metals Society). Institute of Metals, 1985.

[35] K. Takeishi, 'Evolution of Turbine Cooled Vanes and Blades Applied for Large Industrial Gas Turbines and Its Trend toward Carbon Neutrality', *Energies (Basel)*, vol. 15, no. 23, p. 8935, Nov. 2022.

[36] M. Bogdan, W. Zieliński, T. Płociński, and K. J. Kurzydłowski, 'Electron Microscopy Characterization of the High Temperature Degradation of the Aluminide Layer on Turbine Blades Made of a Nickel Superalloy', *Materials*, vol. 13, no. 14, p. 3240, Jul. 2020.

[37] R. W. Evans and B. Wilshire, *Introduction to creep*. in Matsci Series. Institute of Materials, 1993.

[38] F. Qayyum, M. Umar, J. Dölling, S. Guk, and U. Prahl, 'Mechanics of New-Generation Metals and Alloys', *Comprehensive Mechanics of Materials*, pp. 31–57, Jan. 2024.

[39] E. J. Mittemeijer, 'Recovery, Recrystallization and Grain Growth', in *Fundamentals of Materials Science*, Berlin, Heidelberg: Springer Berlin Heidelberg, 2010, pp. 463–496.

[40] A. Chatterjee, 'Effect of Microstructure and Crystallographic Texture on Mechanical Properties of Modified 9Cr-1Mo Steel', PhD thesis, May, 2018.

[41] W. Blum, 'Creep of crystalline materials: experimental basis, mechanisms and models', *Materials Science and Engineering: A*, vol. 319–321, pp. 8–15, Dec. 2001.

[42] Kodur, V. K. R., & Dwaikat, M. M. S. (2010). Effect of high temperature creep on the fire response of restrained steel beams. *Materials and Structures*, *43*(10), 1327–1341.

[43]    L. W. McKeen, 'Chapter 1 - Introduction to Plastics and Elastomers', in *The Effect of Creep and Other Time Related Factors on Plastics and Elastomers (Second Edition)*, 2009, pp. 1–31.

[44]    Frederick. H. Norton, *The creep of steel at high temperatures*. New York: McGraw-Hill book company, 1929.

[45]    S. Arrhenius, 'Über die Dissociationswärme und den Einfluss der Temperatur auf den Dissociationsgrad der Elektrolyte', *Zeitschrift für Physikalische Chemie*, vol. 4U, no. 1, Jan. 1889.

[46]    F. R. N. Nabarro, 'Do we have an acceptable model of power-law creep?', *Materials Science and Engineering: A*, vol. 387–389, no. 1-2 SPEC. ISS., pp. 659–664, Dec. 2004.

[47]    J. P. Poirier, *Creep of Crystals: High-Temperature Deformation Processes in Metals, Ceramics and Minerals*. in Cambridge Earth Science Series. Cambridge University Press, 1985.

[48]    W. Blum and P. Eisenlohr, 'Dislocation mechanics of creep', *Materials Science and Engineering: A*, vol. 510–511, no. C, pp. 7–13, Jun. 2009.

[49]    M. E. Kassner, 'New Developments in Understanding Harper–Dorn, Five-Power Law Creep and Power-Law Breakdown', *Metals (Basel)*, vol. 10, no. 10, p. 1284, Sep. 2020.

[50]    M. E. Kassner and R. Ermagan, 'Power Law Breakdown in the Creep in Single-Phase Metals', *Metals (Basel)*, vol. 9, no. 12, p. 1345, Dec. 2019.

[51]    B.-S. Lee, J.-M. Kim, J.-Y. Kwon, K.-J. Choi, and M.-C. Kim, 'A practical power law creep modeling of alloy 690 SG tube materials', *Nuclear Engineering and Technology*, vol. 53, no. 9, pp. 2953–2959, Sep. 2021.

[52]    H. J. Frost and M. F. Ashby, *Deformation-mechanism Maps: The Plasticity and Creep of Metals and Ceramics*. Franklin Book Company, Incorporated, 1982.

[53]    R. L. Coble, 'A Model for Boundary Diffusion Controlled Creep in Polycrystalline Materials', *J Appl Phys*, vol. 34, no. 6, pp. 1679–1682, Jun. 1963.

[54]    F. R. N. Nabarro, 'Steady-state diffusional creep', *Philosophical Magazine*, vol. 16, no. 140, pp. 231–237, Aug. 1967.

[55]    H. K. D. H. Bhadeshia, 'Mechanisms and Models for Creep Deformation and Rupture', *Comprehensive Structural Integrity*, pp. 2–25, Jan. 2003.

[56]    H. E. Friedrich and B. Mordike, *Magnesium technology*, vol. 212. Springer, 2006.

[57]    H. Yang, S. Gavras, and H. Dieringa, 'Creep Characteristics of Metal Matrix Composites', *Encyclopedia of Materials: Composites*, vol. 1, pp. 375–388, Jan. 2021.

[58]    T. E. Mitchell, J. P. Hirth, and A. Misra, 'Apparent activation energy and stress exponent in materials with a high Peierls stress', *Acta Mater*, vol. 50, no. 5, pp. 1087–1093, Mar. 2002.

[59]    B. Wilshire and A. J. Battenbough, 'Creep and creep fracture of polycrystalline copper', *Materials Science and Engineering: A*, vol. 443, no. 1–2, pp. 156–166, 2007.

[60]    V. Foldyna, Z. Kubon, A. Jakovová, and V. Vodárek, *Development of advanced high chromium ferritic steels*, vol. 667. Institute of Materials, 1997.

[61]    G. Fantozzi, J. Chevalier, C. Olagnon, and J. L. Chermant, 'Creep of Ceramic Matrix Composites', *Comprehensive Composite Materials*, pp. 115–162, Jan. 2000.

[62]    D. R. H. Jones and M. F. Ashby, 'Mechanisms of Creep, and Creep-Resistant Materials', in *Engineering Materials 1*, Elsevier, 2019, pp. 381–394.

[63]    M. F. Ashby, 'Mechanisms of Deformation and Fracture', Academic Press, 1983, pp. 117–177.

[64]    T. H. Courtney, *Mechanical behavior of materials*, 2nd ed. Boston: McGraw Hill, 2000.

[65]    H. F. Moore, B. B. Betty, and C. W. Dollins, 'Creep and fracture of lead and lead alloys: a report', *University of Illinois. Engineering Experiment Station. Bulletin*, vol. 272, 1935.

[66]    R. L. Bell and T. G. Langdon, 'An investigation of grain-boundary sliding during creep', *J Mater Sci*, vol. 2, no. 4, pp. 313–323, Jul. 1967.

[67]    R. C. Gifkins, A. Gittins, R. L. Bell, and T. G. Langdon, 'The dependence of grain-boundary sliding on shear stress', *J Mater Sci*, vol. 3, no. 3, pp. 306–313, May 1968.

[68]    T. G. Langdon, 'Grain boundary sliding revisited: Developments in sliding over four decades', *J Mater Sci*, vol. 41, no. 3, pp. 597–609, Feb. 2006.

[69]    W. Cui, J.-Q. Chen, L. U. Hao, and J.-M. Chen, 'Influence of grain boundary sliding on ductility-dip cracking of Ni-based alloy', *The Chinese Journal of Nonferrous Metals*, vol. 23, no. 5, pp. 1269–1274, 2013.

[70]    M. F. Ashby and B. F. Dyson, 'Creep damage mechanics and micromechanisms', pp. 3–30, Jan. 1984.

[71]    'Nucleation of Creep Cavity', *High Temperature Deformation and Fracture of Materials*, pp. 191–198, Jan. 2010.

[72]    R. Bullough and R. S. Nelson, 'Voids in irradiated metals', *Physics in Technology*, vol. 5, no. 1, pp. 29–67, Jan. 1974.

[73]    N. Akasaka, K. Hattori, S. Onose, and S. Ukai, 'Effect of temperature change on void swelling in P, Ti-modified 316 stainless steel', *Journal of Nuclear Materials*, vol. 271–272, pp. 370–375, May 1999.

[74]    S. L. Dudarev, A. A. Semenov, and C. H. Woo, 'Segregation of voids in a spatially heterogeneous dislocation microstructure', *Phys Rev B*, vol. 70, no. 9, p. 094115, Sep. 2004.

[75]    Q. Zeng *et al.*, 'Effect of Temperature and Grain Boundary on Void Evolution in Irradiated Copper: A Phase-Field Study', *Acta Metallurgica Sinica (English Letters)*, vol. 37, no. 9, pp. 1621–1632, Sep. 2024.

[76]    M. E. Kassner, 'Creep Fracture', *Fundamentals of Creep in Metals and Alloys, Second Edition*, pp. 221–246, Jan. 2008.

[77]    T. Tian, C. Ge, X. Li, Z. Hao, S. Peng, and C. Jia, 'Influences of a Hot-Working Process on the Microstructural Evolution and Creep Performance of a Spray-

Formed Nickel-Based Superalloy', *Metals (Basel)*, vol. 10, no. 4, p. 454, Mar. 2020.

[78]  R.W. Evans and B. Wilshire, *Creep of Metals and Alloys*. 1985.

[79]  N. Dudova, 'Creep and Deformation of Metals and Alloys at Elevated Temperatures', *Metals (Basel)*, vol. 11, no. 11, p. 1837, Nov. 2021.

[80]  J. K. Lai and A. Wickens, 'Microstructural changes and variations in creep ductility of 3 casts of type 316 stainless steel', *Acta Metallurgica*, vol. 27, no. 2, pp. 217–230, Feb. 1979.

[81]  J. Čadek, *Creep in Metallic Materials*. 1988.

[82]  M. E. Kassner and T. A. Hayes, 'Creep cavitation in metals', 2003.

[83]  I. W. Chen and A. S. Argon, 'Diffusive growth of grain-boundary cavities', *Acta Metallurgica*, vol. 29, no. 10, pp. 1759–1768, Oct. 1981.

[84]  S. E. Stanzl, A. S. Argon, and E. K. Tschegg, 'Diffusive intergranular cavity growth in creep in tension and torsion', *Acta Metallurgica*, vol. 31, no. 6, pp. 833–843, Jun. 1983.

[85]  L.-Q. Shen *et al.*, 'Observation of cavitation governing fracture in glasses', *Sci Adv*, vol. 7, no. 14, Apr. 2021.

[86]  E. Gariboldi and S. Spigarelli, 'Creep and High-Temperature Deformation of Metals and Alloys', *Metals (Basel)*, vol. 9, no. 10, p. 1087, Oct. 2019.

[87]  M. T. Whittaker and B. Wilshire, 'Advanced procedures for long-term creep data prediction for 2.25 chromium steels', *Metall Mater Trans A Phys Metall Mater Sci*, vol. 44, no. SUPPL. 1, Jan. 2013.

[88]  M. T. Whittaker and W. J. Harrison, 'Evolution of Wilshire equations for creep life prediction', *Materials at High Temperatures*, vol. 31, no. 3, pp. 233–238, Aug. 2014.

[89]  K. Ito, H. Yajima, and M. Arai, 'Creep Life Prediction Method by Using High-Temperature Indentation Creep Test', in *The 18th International Conference on Experimental Mechanics*, Basel Switzerland: MDPI, Jun. 2018, p. 450.

[90] B. Ma, X. Wang, G. Xu, J. Xu, and J. He, 'Prediction of Creep Curves Based on Back Propagation Neural Networks for Superalloys', *Materials*, vol. 15, no. 19, p. 6523, Sep. 2022.

[91] M. S and G. Succop, *Stress-Rupture Properties of Inconel 700 and Correlation on the Basis of Several Time-Temperature Parameters*. 1956.

[92] Z. Abdallah, V. Gray, M. Whittaker, and K. Perkins, 'A Critical Analysis of the Conventionally Employed Creep Lifing Methods', *Materials*, vol. 7, no. 5, pp. 3371–3398, Apr. 2014.

[93] F. C. Monkman and N. J. Grant, 'An empirical relationship between rupture life and minimum creep rate in creep-rupture tests', 1956.

[94] E. Pink, 'Physical significance and reliability of Larson–Miller and Manson–Haferd parameters', *Materials Science and Technology*, vol. 10, no. 4, pp. 340–346, Apr. 1994.

[95] J. G. Kaufman, Z. Long, and S. Ningileri, 'Application of time-temperature-stress parameters to high temperature performance of aluminium alloys', *Aluminum Alloys for Transportation, Packaging, Aerospace, and Other Applications*, pp. 137–146, 2007.

[96] J. Zhao, D. Li, and Y. Fang, 'Selection of Manson-Haferd Constants and Its Application on Rupture Life Prediction', 材料工程, vol. 6, pp. 30–34, 2009.

[97] B. Wilshire and P. J. Scharning, 'Creep and creep fracture of commercial aluminium alloys', *J Mater Sci*, vol. 43, no. 12, pp. 3992–4000, Jun. 2008.

[98] B. Burton and G. W. Greenwood, 'The Contribution of Grain-Boundary Diffusion to Creep at Low Stresses', *Metal Science Journal*, vol. 4, no. 1, pp. 215–218, Jan. 1970.

[99] M. T. Whittaker, M. Evans, and B. Wilshire, 'Long-term creep data prediction for type 316H stainless steel', *Materials Science and Engineering A*, vol. 552, pp. 145–150, Aug. 2012.

[100] M. T. Whittaker and B. Wilshire, 'Creep and creep fracture of 2.25Cr–1.6W steels (Grade 23)', *Materials Science and Engineering: A*, vol. 527, no. 18–19, pp. 4932–4938, Jul. 2010.

[101] N. A. Zharkova and L. R. Botvina, 'Estimate of the life of a material under creep conditions in the phase-transition theory', *Doklady Physics*, vol. 48, no. 7, pp. 379–381, Jul. 2003.

[102] I. M. Bernstein, *Diffusion creep in Zirconium and certain Zirconium alloys*. US Steel Corp., Monroeville, Pa., 1967.

[103] K. Kimura, 'Creep Rupture Strength Evaluation With Region Splitting by Half Yield', in *Volume 6A: Materials and Fabrication*, American Society of Mechanical Engineers, Jul. 2013.

[104] K. Kimura and K. Sawada, 'Creep rupture ductility of ferritic creep resistant steels', *Materials at High Temperatures*, vol. 39, no. 6, pp. 538–548, Nov. 2022.

[105] K. Kimura, H. Kushima, and K. Sawada, 'Long-term creep strength prediction of high Cr ferritic creep resistant steels based on degradation mechanisms', in *PARSONS 2003: Sixth International Charles Parsons Turbine Conference*, 2003, pp. 443–456.

[106] K. Kimura, K. Sawada, and H. Kushima, 'Creep Deformation, Rupture Strength, and Rupture Ductility of Grades T/P92 Steels', in *ASME 2014 Symposium on Elevated Temperature Application of Materials for Fossil, Nuclear, and Petrochemical Industries*, American Society of Mechanical Engineers, Mar. 2014, pp. 193–201.

[107] K. Kimura, K. Sawada, H. Kushima, and Y. Toda, 'Long-term Creep Strength of Creep Strength Enhanced Ferritic Steels', in *Challenges of Power Engineering and Environment*, Berlin, Heidelberg: Springer Berlin Heidelberg, 2007, pp. 1059–1065.

[108] K. Kimura, K. Sawada, H. Kushima, and K. Kubo, 'Effect of stress on the creep deformation of ASME Grade P92/T92 steels', *International Journal of Materials Research*, vol. 99, no. 4, pp. 395–401, Apr. 2008.

[109]  K. Kimura, K. Sawada, H. Kushima, and Y. Toda, 'Stress dependence of degradation and creep rupture life of creep strength enhanced ferritic steels', in *Pros. 5th Int. Conf. Adv. Mater. Techn. Fossil Power Plant*, 2007.

[110]  V. Gray and M. Whittaker, 'The changing constants of creep: A letter on region splitting in creep lifing', *Materials Science and Engineering A*, vol. 632, pp. 96–102, Apr. 2015.

[111]  C. Deen, M. T. Whittaker, W. Harrison, C. M. F. Rae, and S. J. Williams, 'Relating fundamental creep mechanisms in Waspaloy to the Wilshire equations', *MATEC Web of Conferences*, vol. 14, p. 15001, Aug. 2014.

[112]  M. Evans, 'Constraints Imposed by the Wilshire Methodology on Creep Rupture Data and Procedures for Testing the Validity of Such Constraints: Illustration Using 1Cr-1Mo-0.25V Steel', *Metall Mater Trans A Phys Metall Mater Sci*, vol. 46, no. 2, pp. 937–947, 2015.

[113]  B. Wilshire and P. J. Scharning, 'Long-term creep life prediction for a high chromium steel', *Scr Mater*, vol. 56, no. 8, pp. 701–704, Apr. 2007.

[114]  T. A. Williams, M. Evans, S. J. Williams, and S. E. John, 'Modification of the Wilshire strain equation: an application to RR1000', *Materials Science and Technology (United Kingdom)*, vol. 37, no. 6, pp. 592–606, 2021.

[115]  M. T. Whittaker, M. Evans, and B. Wilshire, 'Long-term creep data prediction for type 316H stainless steel', *Materials Science and Engineering: A*, vol. 552, pp. 145–150, Aug. 2012.

[116]  M. L. Santella *et al.*, 'Predicting the creep-rupture lifetime of a cast austenitic stainless steel using Larson-Miller and Wilshire parametric approaches', *International Journal of Pressure Vessels and Piping*, vol. 205, Oct. 2023.

[117]  M. Whittaker, B. Wilshire, and J. Brear, 'Creep fracture of the centrifugally-cast superaustenitic steels, HK40 and HP40', *Materials Science and Engineering A*, vol. 580, pp. 391–396, Sep. 2013.

[118]  V. Cedro, C. Garcia, and M. Render, 'Use of the Wilshire equations to correlate and extrapolate creep data of Inconel 617 and Nimonic 105', *Materials*, vol. 11, no. 12, Dec. 2018.

[119] V. Cedro, C. Garcia, and M. Render, 'Use of the Wilshire Equations to Correlate and Extrapolate Creep Data of HR6W and Sanicro 25', *Materials*, vol. 11, no. 9, p. 1585, Sep. 2018.

[120] M. Evans, 'The importance of creep strain in linking together the Wilshire equations for minimum creep rates and times to various strains (including the rupture strain): an illustration using 1CrMoV rotor steel', *J Mater Sci*, vol. 49, no. 1, pp. 329–339, Jan. 2014.

[121] M. Evans, 'A Re-Evaluation of the Causes of Deformation in 1Cr-1Mo-0.25V Steel for Turbine Rotors and Shafts Based on iso-Thermal Plots of the Wilshire Equation and the Modelling of Batch to Batch Variation', *Materials*, vol. 10, no. 6, p. 575, May 2017.

[122] M. Evans, 'The importance of creep strain in linking together the Wilshire equations for minimum creep rates and times to various strains (including the rupture strain): An illustration using 1CrMoV rotor steel', *J Mater Sci*, vol. 49, no. 1, pp. 329–339, 2014.

[123] M. Evans, 'Incorporating specific batch characteristics such as chemistry, heat treatment, hardness and grain size into the Wilshire equations for safe life prediction in high temperature applications: An application to 12Cr stainless steel bars for turbine blades', *Appl Math Model*, vol. 40, no. 23–24, pp. 10342–10359, Dec. 2016.

[124] M. Evans, 'Incorporating the Wilshire equations for time to failure and the minimum creep rate into a continuum damage mechanics for the creep strain of Waspaloy', *Materials at High Temperatures*, vol. 39, no. 2, pp. 133–148, 2022.

[125] G. Liu, S. Winwood, K. Rhodes, and S. Birosca, 'The effects of grain size, dendritic structure and crystallographic orientation on fatigue crack propagation in IN713C nickel-based superalloy', *Int J Plast*, vol. 125, no. May, pp. 150–168, Feb. 2020.

[126] K. Shin, J. Kim, M. Terner, B. Kong, and H. Hong, 'Effects of heat treatment on the microstructure evolution and the high-temperature tensile properties of Haynes 282 superalloy', *Materials Science and Engineering: A*, vol. 751, no. February, pp. 311–322, Mar. 2019.

[127] A. J. Hassan, B. Cheniti, B. Belkessa, T. Boukharouba, D. Miroud, and N.-E. Titouche, 'Tensile joint strength characterizations for Cr-Ni-Mo steel (AISI 316) during direct drive friction welding process', *The International Journal of Advanced Manufacturing Technology*, vol. 128, no. 11–12, pp. 5621–5633, Oct. 2023.

[128] A. H. Advani *et al.*, 'Deformation effects on interfacial carbide precipitation and chromium-depletion in type 304 stainless steel', *Scripta Metallurgica et Materialia*, vol. 27, no. 12, pp. 1759–1764, Dec. 1992.

[129] F. Nový, V. Zatkalíková, O. Bokůvka, and K. Miková, 'Gigacycle Fatigue Endurance of Marine Grade Stainless Steels with Corrosion Pits', *Periodica Polytechnica Transportation Engineering*, vol. 41, no. 2, p. 99, 2013.

[130] G. Sasikala, S. L. Mannan, M. D. Mathew, and K. B. Rao, 'Creep deformation and fracture behavior of types 316 and 316L(N) stainless steels and their weld metals', *Metallurgical and Materials Transactions A*, vol. 31, no. 4, pp. 1175–1185, Apr. 2000.

[131] G. Lien, 'Experience with Stainless Steels in Utility Power Plants', *Advances in the Technology of Stainless Steels and Related Alloys*, pp. 132–146, 1965.

[132] Y. Kawaguchi, N. Nakamura, and S. Yusa, 'Fatigue damage evaluation of stainless steel pipes in nuclear power plants using positron annihilation lineshape analysis', *Nippon Kinzoku Gakkai-Shi*, vol. 66, no. 7, Jul. 2002.

[133] AZO Materials, 'Grade 316 Stainless Steel: Properties, Fabrication and Applications', https://www.azom.com/article.aspx?ArticleID=2868.

[134] A. Chamanfar, S. M. Chentouf, M. Jahazi, and L. P. Lapierre-Boire, 'Austenite grain growth and hot deformation behavior in a medium carbon low alloy steel', *Journal of Materials Research and Technology*, vol. 9, no. 6, pp. 12102–12114, Nov. 2020.

[135] Y. S. Lee, W. Kim, Y. Lee, and W. S. Ryu, 'Effect of Grain Size on Creep Properties of Type 316LN Stainless Steel', 2001.

[136] N. Solomon and I. Solomon, 'Deformation induced martensite in AISI 316 stainless steel', *Revista de Metalurgia (Madrid)*, vol. 46, no. 2, pp. 121–128, Mar. 2010.

[137] W. Li, L. Meng, S. Wang, H. Zhang, X. Niu, and H. Lu, 'Plastic deformation behavior and strengthening mechanism of SLM 316L reinforced by micro-TiC particles', *Materials Science and Engineering: A*, vol. 884, p. 145557, Sep. 2023.

[138] D. Wang, L. Wang, X. Feng, B. Zhang, X. Yong, and G. Zhang, 'Creep Properties of Pre-deformed F316 Stainless Steel', *Cailiao Yanjiu Xuebao/Chinese Journal of Materials Research*, vol. 33, no. 7, pp. 497–504, Jul. 2019.

[139] W. S. Park, S. W. Yoo, M. H. Kim, and J. M. Lee, 'Strain-rate effects on the mechanical behavior of the AISI 300 series of austenitic stainless steel under cryogenic environments', *Mater Des*, vol. 31, no. 8, pp. 3630–3640, 2010.

[140] W. Wang, W. Yan, K. Yang, Y. Shan, and Z. Jiang, 'Temperature dependence of tensile behaviors of nitrogen-alloyed austenitic stainless steels', *J Mater Eng Perform*, vol. 19, no. 8, pp. 1214–1219, Nov. 2010.

[141] E. I. Samuel, B. K. Choudhary, and K. Bhanu Sankara Rao, 'Influence of temperature and strain rate on tensile work hardening behaviour of type 316 LN austenitic stainless steel', *Scr Mater*, vol. 46, no. 7, pp. 507–512, Apr. 2002.

[142] T. S. Byun, N. Hashimoto, and K. Farrell, 'Temperature dependence of strain hardening and plastic instability behaviors in austenitic stainless steels', *Acta Mater*, vol. 52, no. 13, pp. 3889–3899, Aug. 2004.

[143] L. Sun, S. He, K. Liu, and E. Zhang, 'Microstructure Evolution of 316 Stainless Steel During Tensile Process', *Iron Steel Vanadium Titanium*, vol. 39, no. 4, pp. 142–151, 2018.

[144] I. Nikulin, R. Kaibyshev, and V. Skorobogatykh, 'High temperature properties of an austenitic stainless steel', in *Journal of Physics: Conference Series*, Institute of Physics Publishing, 2010.

[145] S. L. Mannan and P. Rodriguez, 'Effect of grain size on creep rate in type 316 stainless steel at 873 and 973 K', *Metal Science*, vol. 17, no. 2, pp. 63–69, Feb. 1983.

[146] D. G. Morris and D. R. Harries, 'Creep and rupture in Type 316 stainless steel at temperatures between 525 and 900°C Part III: Precipitation behaviour', *Metal Science*, vol. 12, no. 11, pp. 542–549, Nov. 1978.

[147] B. Zhang, H. Yu, H. Jing, L. Xu, and L. Zhao, 'Study on creep properties of deposited weld metal in nuclear class 316H pipe', *Hanjie Xuebao/Transactions of the China Welding Institution*, vol. 40, no. 12, pp. 97–101, Dec. 2019.

[148] Y. Cheng and Q. Gao, 'Effects of Precreep on the Microstructure of 316 Stainless Steels', *Foundry Technology*, vol. 39, no. 09, pp. 2075–2077, 2018.

[149] S. Song, Q. Kan, Y. Liu, C. Bao, X. Lu, and X. Zhang, 'Tensile and creep behavior of 316L austenite stainless steel at elevated temperatures: experiment and crystal plasticity modeling', *Acta Mechanica Sinica/Lixue Xuebao*, vol. 40, no. 2, Feb. 2024.

[150] R. Yoda, T. Yokomaku, and N. Tsuji, 'Plastic deformation and creep damage evaluations of type 316 austenitic stainless steels by EBSD', *Mater Charact*, vol. 61, no. 10, pp. 913–922, Oct. 2010.

[151] L. Esposito, N. Bonora, and G. De Vita, 'Creep modelling of 316H stainless steel over a wide range of stress', *Procedia Structural Integrity*, vol. 2, pp. 927–933, Jan. 2016.

[152] C. M. Davies, N. P. O'Dowd, D. W. Dean, K. M. Nikbin, and R. A. Ainsworth, 'Failure assessment diagram analysis of creep crack initiation in 316H stainless steel', *International Journal of Pressure Vessels and Piping*, vol. 80, no. 7–8, pp. 541–551, Jul. 2003.

[153] H. K. D. H. Bhadeshia, 'Nickel Based Superalloys', http://www.phase-trans.msm.cam.ac.uk/2003/Superalloys/superalloys.html.

[154] C. T. Sims, 'A History of Superalloy Metallurgy', pp. 399–419.

[155] B. Geddes, H. Leon, and X. Huang, *Superalloys: Alloying and Performance*. ASM International, 2010.

[156] H. K. D. H. Bhadeshia, 'Recrystallisation of practical mechanically alloyed iron-base and nickel-base superalloys', *Materials Science and Engineering: A*, vol. 223, no. 1–2, pp. 64–77, Feb. 1997.

[157] E. O. Ezugwu, 'High Speed Machining of Aero-Engine Alloys', 2004, *Brazilian Society of Mechanical Sciences and Engineering*.

[158] A. King, 'Tactics and strategies for the future', *Critical Materials*, pp. 235–254, Jan. 2021.

[159] I. A. Choudhury and M. A. El-Baradie, 'Machinability of nickel-base super alloys: a general review', 1998.

[160] R. C. Reed, '2 The physical metallurgy of nickel and its alloys', *The Superalloys: Fundamentals and Applications*, pp. 33–120, 2006.

[161] R. C. Reed, *The Superalloys: Fundamentals and Applications*. Cambridge University Press, 2008.

[162] N. Zhou *et al.*, 'Computer simulation of phase transformation and plastic deformation in IN718 superalloy: Microstructural evolution during precipitation', *Acta Mater*, vol. 65, pp. 270–286, Feb. 2014.

[163] Joseph. R. Davis, *Metals Handbook Desk Edition*. ASM International, 1998.

[164] E. F. Bradley, *Superalloys: A Technical Guide*. in Technical guide series. ASM International, 1988.

[165] J. A. Hawk, T.-L. Cheng, J. S. Sears, P. D. Jablonski, and Y.-H. Wen, 'Gamma Prime Stability in Haynes 282: Theoretical and Experimental Considerations', *J Mater Eng Perform*, vol. 24, no. 11, pp. 4171–4181, Nov. 2015.

[166] G. Liu, L. Kong, S. Ruan, and S. Birosca, 'Microstructure and phases structure in nickel-based superalloy IN713C after solidification', *Mater Charact*, vol. 182, p. 111566, Dec. 2021.

[167] T. M. Pollock and S. Tin, 'Nickel-Based Superalloys for Advanced Turbine Engines: Chemistry, Microstructure and Properties', *J Propuls Power*, vol. 22, no. 2, pp. 361–374, Mar. 2006.

[168] Z. Zhang *et al.*, 'Multiscale characterization of the 3D network structure of metal carbides in a Ni superalloy by synchrotron X-ray microtomography and ptychography', *Scr Mater*, vol. 193, pp. 71–76, Mar. 2021.

[169] Ł. Rakoczy, B. Rutkowski, M. Grudzień-Rakoczy, R. Cygan, W. Ratuszek, and A. Zielińska-Lipiec, 'Analysis of γ′ Precipitates, Carbides and Nano-Borides in Heat-Treated Ni-Based Superalloy Using SEM, STEM-EDX, and HRSTEM', *Materials*, vol. 13, no. 19, p. 4452, Oct. 2020.

[170] J. Belan, 'GCP and TCP Phases Presented in Nickel-base Superalloys', *Mater Today Proc*, vol. 3, no. 4, pp. 936–941, 2016.

[171] V. Bartow, 'Axel Fredrick Cronstedt', *J Chem Educ*, vol. 30, no. 5, p. 247, May 1953.

[172] J. R. Davis and A. S. M. I. H. Committee, *Nickel, Cobalt, and Their Alloys*. in ASM specialty handbook. ASM International, 2000.

[173] I. Baker, 'Nickel-Based Superalloys', in *Fifty Materials That Make the World*, no. September 2015, Cham: Springer International Publishing, 2018, pp. 131–136.

[174] F. Daniel León-Cázares, 'On the plastic deformation behaviour of nickel-based superalloys: low cycle fatigue and stress orientation effects', 2019.

[175] S. Tian, J. Zhang, T. Jin, H. Yang, Y. Xu, and Z. Hu, 'Internal stress and effect factors for single crystal nickel-based superalloys during steady state creep', *Journal of Aeronautical Materials*, vol. 18, no. 3, pp. 16–21, 1998.

[176] R. A. Ricks, A. J. Porter, and R. C. Ecob, 'The growth of gamma prime precipitates in nickel-base superalloys', *Acta Metallurgica*, vol. 31, pp. 43–53, 1983.

[177] H. Matysiak *et al.*, 'The microstructure degradation of the in 713C nickel-based superalloy after the stress rupture tests', *J Mater Eng Perform*, vol. 23, no. 9, pp. 3305–3313, 2014.

[178] Z. Zhu and K. Yao, *Engineering Materials*, Fifth Edit. Tsinghua University Press, 2011.

[179] M. T. Jovanovic, B. Lukic, Z. Miskovic, I. Bobic, I. Cvijovic, and B. Dimcic, 'Processing and Some Applications of Nickel , Cobalt and Titanium-Based Alloys', *Association of Metallurgical Engineers of Serbia*, vol. 13, no. 2, pp. 91–106, 2007.

[180] R. Royce, *The Jet Engine*. Wiley, 2015.

[181] R. J. Smith, G. J. Lewi, and D. H. Yates, 'Development and application of nickel alloys in aerospace engineering', *Aircraft Engineering and Aerospace Technology*, vol. 73, pp. 138–147, 2001.

[182] 'Engineering Properties of ALLOY 713C'.

[183] 'INCONEL 713'. [Online]. Available: http://fountainheadalloys.com/inconel-713_inconel-713c_in713c_alloy-713lc_uns-n07713_ams-5377/

[184] E. Orowan, 'Fracture and strength of solids', *Reports on Progress in Physics*, vol. 12, no. 1, p. 309, Jan. 1949.

[185] S. Zhao, X. Xie, G. D. Smith, and S. J. Patel, 'Gamma prime coarsening and age-hardening behaviors in a new nickel base superalloy', *Mater Lett*, vol. 58, no. 11, pp. 1784–1787, Apr. 2004.

[186] J. R. Brinegar, J. R. Mihalisin, and J. VanderSluis, 'The Effects of Tantalum for Columbium Substitutions in Alloy 713C', in *Superalloys 1984 (Fifth International Symposium)*, TMS, 1984, pp. 53–61.

[187] R. G. Garlick and C. E. Lowell, 'Alloy composition effects on oxidation products of VIA, B-1900, 713C, and 738X: A high temperature diffractometer study', 1973.

[188] A. A. Vicente, J. R. S. Moreno, J. A. S. TenÓRio, A. B. Botelho, A. T. F. A. Santos, and C. R. Espinosa, 'Comparison of behaviour to oxidation at high

temperature of two superalloys: Inconel 713c and IC-50', *Oxidation Communications*, vol. 41, no. 2, pp. 195–204, 2018.

[189] M. Azadi, A. Marbout, S. Safarloo, M. Azadi, M. Shariat, and M. H. Rizi, 'Effects of solutioning and ageing treatments on properties of Inconel-713C nickel-based superalloy under creep loading', *Materials Science and Engineering: A*, vol. 711, no. November 2017, pp. 195–204, Jan. 2018.

[190] M. Kvapilova, P. Kral, J. Dvorak, and V. Sklenicka, 'High temperature creep behaviour of cast nickel-based superalloys inc 713 lc, b1914 and mar-m247', *Metals (Basel)*, vol. 11, no. 1, pp. 1–16, Jan. 2021.

[191] C. He, L. Liu, T. Huang, wenchao Yang, J. Zhang, and H. Fu, 'Dislocations in Ni-based Single Crystal Superalloys and Their Influence on Creep Behavior', *Materials Reports*, vol. 33, no. 9, pp. 2918–2928, 2019.

[192] H. Farahani, P. Melali, and M. Divandari, 'Study the Effects of Casting Revert–Virgin Alloy with Different Portion of Return (Revert) Materials on Microstructure, Mechanical Properties, and Creep Resistance of Inconel 713LC', *International Journal of Metalcasting*, 2024.

[193] Haynes® International Inc., 'Haynes International - Our Milestones'. [Online]. Available: https://www.haynesintl.com/company-information/our-heritage/our-milestones

[194] Haynes® International Inc., 'Haynes® 282® Alloy, Datasheet', 2006, [Online]. Available: http://www.haynesintl.com/pdf/h3173.pdf

[195] R. Hood, S. L. Soo, D. K. Aspinwall, P. Andrews, and C. Sage, 'Twist drilling of haynes 282 superalloy', *Procedia Eng*, vol. 19, no. 0, pp. 150–155, 2011.

[196] D. L. Klarstrom, L. M. Pike, and V. R. Ishwar, 'Nickel-base alloy solutions for ultrasupercritical steam power plants', *Procedia Eng*, vol. 55, pp. 221–225, 2013.

[197] R. Purgert, J. Phillips, H. Hendrix, J. Shingledecker, and J. Tanzosh, 'Materials for Advanced Ultra-supercritical (A-USC) Steam Turbines-A-USC Component Demonstration Pre-FEED Final Technical Report', 2016.

[198] K. L. Kruger, 'HAYNES 282 alloy', in *Materials for Ultra-Supercritical and Advanced Ultra-Supercritical Power Plants*, Elsevier, 2017, pp. 511–545.

[199] X. Song, L. Tang, and Z. Chen, 'Characteristics and applications of a new Ni-based superalloy Haynes 282', *Materials Review A: Overview*, vol. 30, no. 6, pp. 116–120, 2016.

[200] R. Sitek *et al.*, 'The Impact of Plastic Deformation on the Microstructure and Tensile Strength of Haynes 282 Nickel Superalloy Produced by DMLS and Casting', *Materials*, vol. 15, no. 21, Nov. 2022.

[201] N. Kim *et al.*, 'Microstructural evolution and creep behavior of the weld interface between 10% cr steel and haynes 282 filler metal', *Metals (Basel)*, vol. 11, no. 5, May 2021.

[202] P. M. Kelly, 'The effect of particle shape on dispersion hardening', *Scripta Metallurgica*, vol. 6, no. 8, pp. 647–656, Aug. 1972.

[203] L. Wang *et al.*, 'Effect of heterogeneous microstructure on the tensile and creep performances of cast Haynes 282 alloy', *Materials Science and Engineering: A*, vol. 828, p. 142099, Nov. 2021.

[204] L. M. Pike, 'HAYNES® 282TM Alloy: A New Wrought Superalloy Designed for Improved Creep Strength and Fabricability', in Turbo Expo: Power for Land, Sea, and Air, vol. Volume 4: 2006, pp. 1031–1039.

[205] C. J. Boehlert and S. C. Longanbach, 'A comparison of the microstructure and creep behavior of cold rolled HAYNES® 230 alloyTM and HAYNES® 282 alloyTM', *Materials Science and Engineering A*, vol. 528, no. 15, pp. 4888–4898, Jun. 2011.

[206] M. L. Santella *et al.*, 'Effects of applied stress and grain size on creep-rupture lifetime prediction for Haynes 282 alloy', *Materials Science and Engineering: A*, vol. 838, p. 142785, Mar. 2022.

[207] Y. Li, H. Yu, G. Zhang, J. Li, and X. Wu, 'Effect of Tensile Strain Dwell on the Low Cycle Fatigue Behavior of DD6 Nickel-Based Single Crystal Super-alloy at High Temperature', *Gas Turbine Experiment and Research*, vol. 18, no. 1, pp. 14–16, 2005.

[208] X. Chen, L. Zhu, W. Liu, X. Zhao, and L. Lang, 'Numerical predictions of low cyclic fatigue and creep-fatigue behavior of P92 steel under non-isothermal-mechanical loading', *International Journal of Pressure Vessels and Piping*, vol. 206, p. 105074, Dec. 2023.

[209] G. zheng KANG, J. ZHANG, Y. fang SUN, and Q. hua KAN, 'Uniaxial Time-Dependent Ratcheting of SS304 Stainless Steel at High Temperatures', *Journal of Iron and Steel Research, International*, vol. 14, no. 1, pp. 53–59, Jan. 2007.

[210] P. Zhao and F. Z. Xuan, 'Ratchetting behavior of advanced 9–12% chromium ferrite steel under creep-fatigue loadings', *Mechanics of Materials*, vol. 43, no. 6, pp. 299–312, Jun. 2011.

[211] W.-G. Kim, J.-Y. Park, I. M. W. Ekaputra, S.-J. Kim, and J. Jang, 'Cyclic creep behaviour under tension–tension loading cycles with hold time of modified 9Cr–1Mo steel', *Materials at High Temperatures*, vol. 31, no. 3, pp. 249–257, Aug. 2014.

[212] W.-G. Kim, J.-Y. Park, I. M. W. Ekaputra, S.-J. Kim, and J. Jang, 'Influence of Hold Time and Stress Ratio on Cyclic Creep Properties Under Controlled Tension Loading Cycles of Grade 91 Steel', *Nuclear Engineering and Technology*, vol. 49, no. 3, pp. 581–591, Apr. 2017.

[213] K. Huang *et al.*, 'Study on Cyclic Bearing Capacity of Suction Pile Based on Equivalent Cyclic Creep Model', *Sustainability (Switzerland)*, vol. 14, no. 22, Nov. 2022.

[214] D. Liu, D. J. Pons, and E. H. Wong, 'The unified creep-fatigue equation for stainless steel 316', *Metals (Basel)*, vol. 6, no. 9, Sep. 2016.

[215] K. T. Chang, K. Z. Z. Lee, P. T. Yeh, C. M. Chang, and J. Y. Yu, 'Creep behavior of cemented sand investigated under cyclic loading', *Environ Earth Sci*, vol. 80, no. 23, Dec. 2021.

[216] D. G. Morris and D. R. Harries, 'The cyclic creep behaviour of Type 316 stainless steel', *J Mater Sci*, vol. 13, no. 5, pp. 985–996, May 1978.

[217] A. Sarkar, A. Nagesha, P. Parameswaran, R. Sandhya, and M. D. Mathew, 'Transition in Failure Mechanism Under Cyclic Creep in 316LN Austenitic

Stainless Steel', *Metallurgical and Materials Transactions A*, vol. 45, no. 7, pp. 2931–2937, Jun. 2014.

[218] A. Sarkar, A. Nagesha, R. Sandhya, and M. D. Mathew, 'Effect of mean stress and stress amplitude on the ratcheting behaviour of 316LN stainless steel under dynamic strain aging regime', *Materials at High Temperatures*, vol. 29, no. 4, pp. 351–358, Dec. 2012.

[219] G. Kang, Y. Dong, H. Wang, Y. Liu, and X. Cheng, 'Dislocation evolution in 316L stainless steel subjected to uniaxial ratchetting deformation', *Materials Science and Engineering: A*, vol. 527, no. 21–22, pp. 5952–5961, Aug. 2010.

[220] C. Gaudin and X. Feaugas, 'Cyclic creep process in AISI 316L stainless steel in terms of dislocation patterns and internal stresses', *Acta Mater*, vol. 52, no. 10, pp. 3097–3110, Jun. 2004.

[221] W. J. Harrison, M. T. Whittaker, and C. Deen, 'Creep behaviour of Waspaloy under non-constant stress and temperature', *Materials Research Innovations*, vol. 17, no. 5, pp. 323–326, Aug. 2013.

[222] T. O. Erinosho, K. A. Venkata, M. Mostafavi, D. M. Knowles, and C. E. Truman, 'Influence of prior cyclic plasticity on creep deformation using crystal plasticity modelling', *Int J Solids Struct*, vol. 139–140, pp. 129–137, May 2018.

[223] I. Abarkan, A. Khamlichi, and R. Shamass, 'A Numerical Analysis on the Cyclic Behavior of 316 FR Stainless Steel and Fatigue Life Prediction', in *The 2nd International Electronic Conference on Applied Sciences*, Basel Switzerland: MDPI, Oct. 2021, p. 28.

[224] D. Molnár, X. Sun, S. Lu, W. Li, G. Engberg, and L. Vitos, 'Effect of temperature on the stacking fault energy and deformation behaviour in 316L austenitic stainless steel', *Materials Science and Engineering: A*, vol. 759, pp. 490–497, Jun. 2019.

[225] K. Sekido *et al.*, 'Data Sheets on the Elevated-Temperature Properties of 18Cr-12Ni-Mo Stainless Steel Bars for General Application (SUS 316-B)', 1988.

[226] 'Data Sheets on the Elevated-Temperature Properties of 18Cr-12Ni-Mo Stainless Steel Plates for Reactor Vessels (SUS 316-HP)'.

[227] H. Hongo *et al.*, 'Data Sheets on the Elevated-Temperature Properties of 18Cr-12Ni-Mo Stainless Steel Tubes for Boilers and Heat Exchangers (SUS 316H TB)', 2000.

[228] A. B. Schroeder, E. T. A. Dobson, C. T. Rueden, P. Tomancak, F. Jug, and K. W. Eliceiri, 'The <scp>ImageJ</scp> ecosystem: Open-source software for image visualization, processing, and analysis', *Protein Science*, vol. 30, no. 1, pp. 234–249, Jan. 2021.

[229] Q. Zhang *et al.*, 'Enhanced tensile ductility and strength of electrodeposited ultrafine-grained nickel with a desired bimodal microstructure', *Materials Science and Engineering: A*, vol. 701, pp. 196–202, Jul. 2017.

[230] M. V. Canté, J. E. Spinelli, N. Cheung, and A. Garcia, 'The correlation between dendritic microstructure and mechanical properties of directionally solidified hypoeutectic Al-Ni alloys', *Metals and Materials International*, vol. 16, no. 1, pp. 39–49, Feb. 2010.

[231] C. H. Konrad, M. Brunner, K. Kyrgyzbaev, R. Völkl, and U. Glatzel, 'Determination of heat transfer coefficient and ceramic mold material parameters for alloy IN738LC investment castings', *J Mater Process Technol*, vol. 211, no. 2, pp. 181–186, Feb. 2011.

[232] T. M. Pollock and S. Tin, 'Nickel-Based Superalloys for Advanced Turbine Engines: Chemistry, Microstructure and Properties', *J Propuls Power*, vol. 22, no. 2, pp. 361–374, Mar. 2006.

[233] G. Malakondaiah and R. Rama, 'Effect of grain size, grain shape and subgrain size on high temperature creep behaviour.', *Def Sci J*, vol. 35, no. 2, pp. 201–217, 1985.

[234] B. Jordi and S. Cant, 'Mechanical and Microstructural Characterisations of IN713C Nickel-Based Superalloy', 2018.

[235] M. Cieśla, F. Binczyk, and M. Mańka, 'Impact of Surface and Volume Modification of Nickel Superalloys IN-713C and MAR-247 on High Temperature Creep Resistance', *Archives of Foundry Engineering*, vol. 12, no. 4, pp. 17–24, Dec. 2012.

[236] Y. Wen and W. Yunxin, 'Effects of Temperature and Pressure on Elastic Properties of Single Crystal Aluminum in Different Crystal Orientations', *physica status solidi (b)*, vol. 257, no. 12, Dec. 2020.

[237] Ł. Rakoczy, B. Rutkowski, M. Grudzień-Rakoczy, R. Cygan, W. Ratuszek, and A. Zielińska-Lipiec, 'Analysis of γ′ Precipitates, Carbides and Nano-Borides in Heat-Treated Ni-Based Superalloy Using SEM, STEM-EDX, and HRSTEM', *Materials*, vol. 13, no. 19, p. 4452, Oct. 2020.

[238] P. J. Zhou, J. J. Yu, X. F. Sun, H. R. Guan, and Z. Q. Hu, 'Role of yttrium in the microstructure and mechanical properties of a boron-modified nickel-based superalloy', *Scr Mater*, vol. 57, no. 7, pp. 643–646, Oct. 2007.

[239] T. M. Smith *et al.*, 'The effect of composition on microstructure and properties for additively manufactured superalloy 718', *J Alloys Compd*, vol. 873, p. 159789, Aug. 2021.

[240] M. Xie, 'Effect of C content on the microstructures and mechanical properties of laser additive manufactured Ni-base superalloys', *Heliyon*, vol. 9, no. 5, p. e16111, May 2023.

[241] S. Latha, M. D. Mathew, P. Parameswaran, K. Bhanu Sankara Rao, and S. L. Mannan, 'Creep behaviour of 14Cr-15Ni-Ti stainless steel at 923K', *Materials Science and Engineering A*, vol. 527, no. 20, pp. 5167–5174, Jul. 2010.

[242] M. Gómez and S. F. Medina, 'Role of microalloying elements in the microstructure of hot rolled steels', 2011.

[243] B. Wilshire and P. J. Scharning, 'Extrapolation of creep life data for 1Cr-0.5Mo steel', *International Journal of Pressure Vessels and Piping*, vol. 85, no. 10, pp. 739–743, Oct. 2008.

[244] S. J. Williams, M. R. Bache, and B. Wilshire, '25 Year Perspective Recent developments in analysis of high temperature creep and creep fracture behaviour', *Materials Science and Technology*, vol. 26, no. 11, pp. 1332–1337, Nov. 2010.

[245] S. Birosca *et al.*, 'The dislocation behaviour and GND development in a nickel based superalloy during creep', *Int J Plast*, vol. 118, no. July 2018, pp. 252–268, Jul. 2019.

[246] J. Lu *et al.*, 'Stacking fault energies in austenitic stainless steels', *Acta Mater*, vol. 111, pp. 39–46, Jun. 2016.

[247] W. F. Hosford, *Mechanical Behavior of Materials*. 2010.

[248] B. C. De Cooman, Y. Estrin, and S. K. Kim, 'Twinning-induced plasticity (TWIP) steels', *Acta Mater*, vol. 142, pp. 283–362, Jan. 2018.

[249] Y. F. Shen, X. X. Li, X. Sun, Y. D. Wang, and L. Zuo, 'Twinning and martensite in a 304 austenitic stainless steel', *Materials Science and Engineering: A*, vol. 552, pp. 514–522, Aug. 2012.

[250] X. Wu, Y. T. Zhu, M. W. Chen, and E. Ma, 'Twinning and stacking fault formation during tensile deformation of nanocrystalline Ni', *Scr Mater*, vol. 54, no. 9, pp. 1685–1690, May 2006.

[251] S. Ni *et al.*, 'The effect of dislocation density on the interactions between dislocations and twin boundaries in nanocrystalline materials', *Acta Mater*, vol. 60, no. 6–7, pp. 3181–3189, Apr. 2012.

[252] J. W. Christian and S. Mahajan, 'Deformation twinning', *Prog Mater Sci*, vol. 39, no. 1–2, pp. 1–157, Jan. 1995.

[253] T. Jozaghi, P. Samimi, Y. Chumlyakov, and I. Karaman, 'Role of thermally-stable deformation twins on the high-temperature mechanical response of an austenitic stainless steel', *Materials Science and Engineering: A*, vol. 845, p. 143199, Jun. 2022.

[254] S. N. Monteiro, L. F. C. Nascimento, N. T. Simonassi, E. S. Lima, A. S. de Paula, and F. de O. Braga, 'High temperature work hardening stages, dynamic strain aging and related dislocation structure in tensile deformed AISI 301 stainless steel', *Journal of Materials Research and Technology*, vol. 7, no. 4, pp. 571–577, Oct. 2018.

[255] M. Gerland, R. Alain, B. Ait Saadi, and J. Mendez, 'Low cycle fatigue behaviour in vacuum of a 316L-type austenitic stainless steel between 20 and 600°C—Part II: Dislocation structure evolution and correlation with cyclic behaviour', *Materials Science and Engineering: A*, vol. 229, no. 1–2, pp. 68–86, Jun. 1997.

[256] P. Deng *et al.*, 'On the Thermal Stability of Dislocation Cellular Structures in Additively Manufactured Austenitic Stainless Steels: Roles of Heavy Element Segregation and Stacking Fault Energy', *JOM*, vol. 72, no. 12, pp. 4232–4243, Dec. 2020.

[257] G. M. Karthik, E. S. Kim, A. Zargaran, P. Sathiyamoorthi, S. G. Jeong, and H. S. Kim, 'Role of cellular structure on deformation twinning and hetero-deformation induced strengthening of laser powder-bed fusion processed CuSn alloy', *Addit Manuf*, vol. 54, p. 102744, Jun. 2022.

[258] C. Shen, V. Gupta, S. Huang, M. Soare, P. Zhao, and Y. Wang, 'Modeling Long-term Creep Performance for Welded Nickel-base Superalloy Structures for Power Generation Systems', Pittsburgh, PA, and Morgantown, WV (United States), Feb. 2017.

[259] F. X. liu, A. C. F. Cocks, and E. Tarleton, 'Dislocation dynamics modelling of the creep behaviour of particle-strengthened materials', *Proceedings of the Royal Society A: Mathematical, Physical and Engineering Sciences*, vol. 477, no. 2250, Jun. 2021.

[260] G. Neumann and V. Tölle, 'Monovacancy and divacancy contributions to self-diffusion in face-centred cubic metals reanalysis for copper, silver, gold, nickel and platinum', *Philosophical Magazine A: Physics of Condensed Matter, Structure, Defects and Mechanical Properties*, vol. 54, no. 5, pp. 619–629, 1986.

[261] S. Queyreau, G. Monnet, and B. Devincre, 'Orowan strengthening and forest hardening superposition examined by dislocation dynamics simulations', *Acta Mater*, vol. 58, no. 17, pp. 5586–5595, Oct. 2010.

[262] F. Wang, S. Zhu, S. Zhu, X. Ren, Y. Tan, and J. Zhang, 'Effect of boundary carbide on creep crack growth in Fe-Cr15-Ni25 alloy', *ACTA METALLURGICA SINICA*, vol. 27, no. 4, pp. 54–58, 1991.

[263] Y. Gu, S. Yang, P. Zhao, J. Qu, and Y. Chen, 'Solidification segregation and carbide precipitation behavior of nickel-based superalloy GH4738', *China Metallurgy*, vol. 31, no. 7, pp. 13–21, 2021.

[264] Q. Yue, L. Liu, W. Yang, T. Huang, J. Zhang, and H. Fu, 'Stress dependence of dislocation networks in elevated temperature creep of a Ni-based single crystal superalloy', *Materials Science and Engineering: A*, vol. 742, pp. 132–137, Jan. 2019.

[265] T. Sugui, W. Minggang, L. Tang, Q. Benjiang, and X. Jun, 'Influence of TCP phase and its morphology on creep properties of single crystal nickel-based superalloys', *Materials Science and Engineering: A*, vol. 527, no. 21–22, pp. 5444–5451, Aug. 2010.

[266] M. Zhang, 'Microstructural evolution and electron microscopic in situ study of the nickel-based single crystal high temperature alloy CMSX-4', 2023.

[267] C. Liu *et al.*, 'Effects of Stressed Aging on TCP Phase Precipitation Behaviour of DD11 Single Crystal Superalloy', 机械工程材料, vol. 42, no. 6, pp. 36–41, 2018.

[268] K. Cheng, 'Precipitation behavior and role of μ phase in several Re-containing single crystal superalloys', 2009.

[269] G. Liu, J. S. Cantó, S. Birosca, S. Wang, and Y. Zhao, 'A study of high cycle fatigue life and its correlation with microstructural parameters in IN713C nickel-based superalloy', *Materials Science and Engineering: A*, vol. 877, p. 145161, Jun. 2023.

[270] S. Ni *et al.*, 'The effect of dislocation density on the interactions between dislocations and twin boundaries in nanocrystalline materials', *Acta Mater*, vol. 60, no. 6–7, pp. 3181–3189, Apr. 2012.

[271] I. Shabib and R. E. Miller, 'A molecular dynamics study of twin width, grain size and temperature effects on the toughness of 2D-columnar nanotwinned copper', *Model Simul Mat Sci Eng*, vol. 17, no. 5, p. 55009, Jun. 2009.

[272] D. G. Morris and D. R. Harries, 'The cyclic creep behaviour of Type 316 stainless steel', 1978.

[273]  J. T. Evans and R. N. Parkins, 'Creep induced by load cycling in a C-Mn steel', *Acta Metallurgica*, vol. 24, no. 6, pp. 511–515, Jun. 1976.